

博士論文

**Development of Three-Dimensional Electromagnetic
Analysis Method using Thin Plate Approximation
for REBCO Superconducting Coils and
its Application to Coupled Analysis with Heat Transfer**
(REBCO 超電導コイルを対象とする薄板近似を用いた
三次元電磁界解析手法の開発及び伝熱との連成解析)

令和 2 年 12 月 1 日提出

指導教員 大崎博之教授

東京大学大学院工学系研究科

電気系工学専攻

37-167299

銭 可楨

Contents

Chapter 1.	Introduction	1
1.1	Background	1
1.2	Introduction to Superconductors	2
1.2.1	Type I & Type II Superconductors	3
1.2.2	High Temperature Superconductors	5
1.2.3	REBCO Coated Conductors	6
1.3	Numerical Methods for Electromagnetic Analyses.....	7
1.3.1	Equivalent Circuit Models.....	8
1.3.2	Finite Difference Method	9
1.3.3	Finite Element Method	9
1.4	HTS Electromagnetic Characteristics Modelling.....	13
1.4.1	Critical State Models	13
1.4.2	E - J Power Law	17
1.4.1	Kim Model.....	18
1.5	Research Objectives	19
1.6	Outline of this Thesis	20
Chapter 2.	3D Electromagnetic Analysis Method.....	22
2.1	Analysis Conditions & Governing Equation.....	22
2.2	Coordinate Transformation & Orthogonal Curvilinear Coordinate System.....	23
2.3	Discretization & Coordinate Transformation.....	24
2.4	Node Equation.....	28
2.5	HTS Electromagnetic Characteristics Modelling.....	31
2.6	Metal Overlayer Modelling.....	31
2.7	Electric Circuit Model & Boundary Conditions	32
2.8	Analysis Flowchart & Advantages.....	33
Chapter 3.	Verifications and Case Studies of 3D Electromagnetic Analysis	35
3.1	Verifications	35
3.1.1	Verification with JMAG	35
3.1.2	Verification with Theoretical Formula.....	38
3.2	Case Study: Solenoid REBCO Coil for Magnet Application.....	43
3.2.1	Analysis Conditions.....	43
3.2.2	Influence of Current Changing Speed on Field Stability.....	46
3.2.3	Influence of Excitation Pattern on Field Stability	48
3.2.4	Detailed Electromagnetic Analysis of Demagnetization Excitation Method ...	50

3.3	Case Study: Saddle-shaped REBCO Coil for Accelerator Application.....	62
3.3.1	Analysis Conditions.....	62
3.3.2	Modelling of Saddle-shaped Coil End.....	65
3.3.3	Investigation on Current density distribution	66
3.3.4	Investigation on Magnetic Field Distribution.....	75
Chapter 4.	3D Heat Transfer Analysis Method	103
4.1	Analysis Objects and Governing Equation	103
4.2	Galerkin Discretization with Hexahedron First-order Elements.....	107
4.3	Model of Liquid Nitrogen Cooling Effect.....	113
4.4	Coupled Analysis Flowchart	114
4.5	Verification of the Coupled Analysis	116
Chapter 5.	Case Studies of Electromagnetic and Heat Transfer Coupled Analysis	117
5.1	Case Study: REBCO Coil for Resistive SFCL Application	117
5.1.1	Analysis Conditions.....	117
5.1.2	REBCO Coil with Uniform J_C Distribution	118
5.1.3	REBCO Coil with Local J_C Degradation.....	121
5.2	Case Study: REBCO Coil for Magnet Application.....	122
5.2.1	Analysis Conditions.....	122
5.2.2	Influence of Heat Input Power on Quench	123
5.2.3	Influence of Time Constant of Current Decrease on Quench.....	125
5.2.4	Influence of Heat Input Area on Quench.....	127
Chapter 6.	Conclusion.....	131
	References.....	134
	List of Publications	140
	Acknowledgements	142

Chapter 1. Introduction

1.1 Background

The RE (rare earth) $\text{Ba}_2\text{Cu}_3\text{O}_x$ (REBCO)-coated conductor has shown its advantages in various applications such as high field magnet, accelerator, superconducting fault current limiter (SFCL), etc., because of its high critical temperature, critical current density, axial tensile stress, and heat capacity [1]–[6]. The developments of such applications using REBCO-coated conductors have become increasingly active in recent years since the commercialization of long-length REBCO-coated conductors. However, some problems are still hindering the practical use of REBCO coils such as quench, AC loss, cooling, cost, and so on.

Experimental and numerical approach are the main method to study such problems to find the solutions. Although experiments are essential to study the actual physical phenomena and to conclusively verify a certain idea, it is still difficult to measure all the accurate and detailed information such as the current density, electric field, magnetic field, temperature, etc. at a certain point because of the limitation of the measurement technology. Hence, the numerical analysis is necessary and useful in today's research, and has contributed greatly with the detailed analysis [7]–[12].

In the research of applications using REBCO-coated conductors, the electromagnetic and thermal behaviors are two of the most important aspects. Because the REBCO-coated conductors have to be cooled to superconductive, and the electromagnetic characteristics of superconductors are functions of the temperature, while the temperature is also affected by the conductor's Joule heat. To study the electromagnetic and thermal behaviors, numerical simulation using equivalent circuit models, finite element method (FEM), etc. has been proposed and widely utilized. Equivalent circuit model of electric circuit elements (and thermal equivalent circuit elements in some cases) is a very fast numerical solution to simulate simple applications of REBCO-coated conductors [13], [10], [14], meanwhile, the improvement of analysis accuracy, which depends on the parameters of the equivalent circuit, is still a problem especially in the cases with complicated structures. Finite elements method is the most developed and widely used method today, allowing the use of different formulations for electromagnetic analysis: \mathbf{A} - V (\mathbf{A} : magnetic vector potential; V : electric scalar potential) [15], \mathbf{T} - Ω (\mathbf{T} : current vector potential; Ω : magnetic scalar potential) [16], [17], \mathbf{H} (\mathbf{H} : magnetic field) [18], and \mathbf{E} (\mathbf{E} : electric field) [19]. Among them, the \mathbf{T} - Ω formulation has shown better convergence in both two-dimensional (2D) and three-dimensional (3D) situations, although extra variables are needed at each node [15], [7]. Some methods, such as the thin plate approximation [16], [17] and the fast multipole method [20], were proposed to reduce variables and computation load. Because of the importance of thermal analysis, some electromagnetic and heat transfer coupled analysis tools up to 2D have been developed in some

research [11], [21]. However, performing a 3D electromagnetic and heat transfer coupled analysis is still difficult, because the operating characteristics of REBCO-coated conductors are extremely non-linear and strongly affected by temperature, then the convergence could significantly deteriorate in 3D problems. Therefore, it is necessary to develop a practical 3D electromagnetic analysis method and couple the electromagnetic and heat transfer analysis together for more accurate and useful numerical analyses.

1.2 Introduction to Superconductors

Superconductivity has a long history since the first discovery by H. Kamerlingh Onnes in 1911 [22]. Kamerlingh Onnes observed that the electrical resistance of some metals like mercury, lead, etc. disappeared within a narrow temperature range around a critical temperature T_C . Perfect conductivity was the first logical characteristic of superconductivity, and then perfect diamagnetism in such materials was the second logical characteristic that discovered by Meissner and Ochsenfeld in 1933 [23]. Perfect diamagnetism is the phenomenon that a superconductor only allows the applied magnetic flux penetrating within a distance of λ which is called the penetration depth, and completely ejects the flux in the other region. Perfect diamagnetism is also well known as the Meissner effect. Hence, critical temperature T_C , critical magnetic field H_C , and critical current density J_C are usually used to characterize a superconductor (Figure 1.1). The shaded area indicates that the material is in the superconducting state. The critical conditions for the superconducting state of a material can be defined by these three parameters.

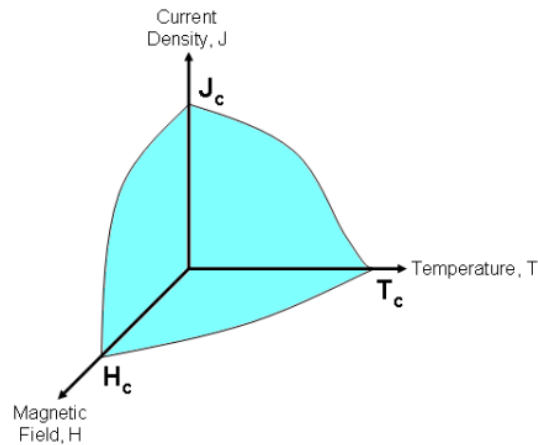


Fig. 1.1. Critical temperature T_C , critical magnetic field H_C , and critical current density J_C define the critical conditions for the superconductivity.

By the end of the 1960s, remarkable achievements in theoretical research had been made and

became the theoretical basis of today's research, such as the Meissner effect [23], the London equations [24], and BCS (Bardeen–Cooper–Schrieffer) theory [25], [26].

1.2.1 Type I & Type II Superconductors

According to different properties, superconductors can be divided into two classes: Type I and Type II. In 1957, Alexei Alexeyevich Abrikosov suggested another class of superconductors with different properties from the previous ones [27]. Hence, the previous ones were called “Type I” superconductors and the new ones were called “Type II” superconductors.

The Meissner effect below H_C is one of the main characteristics of Type I superconductors which is introduced in the previous paragraph. In the case of Type I superconductors, the superconductor will transit to the normal state and allow the penetration of the magnetic flux when the applied magnetic field exceeds H_C . However, low current carrying capacity is the disadvantage of Type I superconductors because of Ampere's law and the Meissner effect.

As to type II superconductors, a “mixed state” is observed, which has a higher and lower critical magnetic field, H_{C1} and H_{C2} respectively, instead of the complete expulsion of flux at $H < H_C$ (Fig. 1.2). In the case of applied magnetic field that lower than H_{C1} , the superconductor is in the superconducting state and ejects the field, meanwhile, in the case of applied magnetic field that higher than H_{C2} , the superconductor is in the normal state, which is the same as Type I superconductors. However, the mixed state is a unique characteristic of Type II superconductors, in which the magnetic flux partially penetrates the superconductor in the form of vortices, as shown in Fig. 1.3. These vortices are limited to minuscule tubelike regions with the diameter in the order of the coherence length ξ (the spatial distance of superconductors' electron pair coupling). When the applied magnetic field strengthens to H_{C2} , the superconducting area between vortices reduces to 0, in the meantime, a continuous transition from superconducting state towards the normal state with an increase in the resistivity can be observed. Because of the much higher H_{C2} in comparison with H_C , Type II superconductors' current carrying capacity is much larger than Type I superconductors.

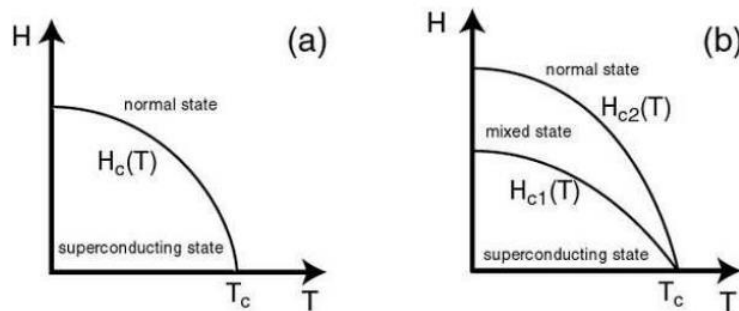


Fig. 1.2. Critical magnetic field as a function of temperature for (a) Type I superconductors and (b) Type II superconductors [28].

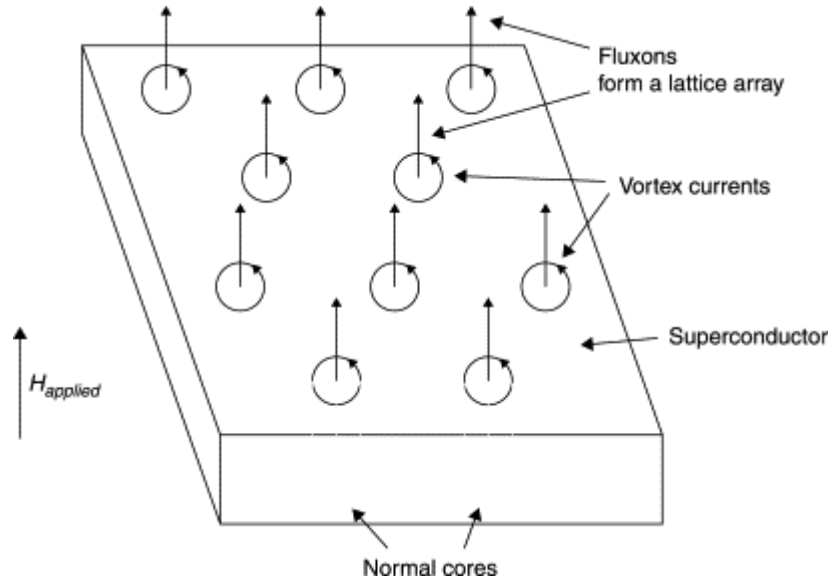


Fig. 1.3. Mixed state of Type II superconductors [29].

Type I superconductors commonly consist of metals and metalloids such as mercury (Hg), lead (Pb), indium (In), tin (Sn), and aluminum (Al), which have relatively lower conductivity at room temperature. Type I superconductors are also the main part of low temperature superconductors (LTS) for their low critical temperature. On the other hand, Type II superconductors usually consist of metallic compounds and alloys except for vanadium, technetium and niobium. The class of Type II superconductors include some LTS, high temperature superconductors (HTS), and some other superconductors like magnesium diboride (MgB₂). Figure 1.4 summarizes the history of the discovery of some well-known superconductors with the equivalent examples of certain temperatures for reference.

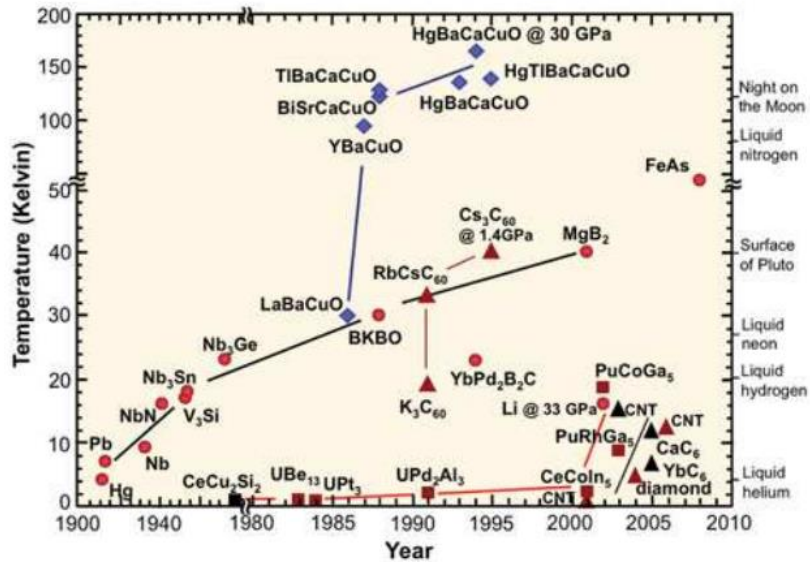


Fig. 1.4. Critical temperatures and years of discovery for different superconductors [30].

1.2.2 High Temperature Superconductors

After Bednorz and Muller discovered LSCO ($\text{La}_{2-x}\text{Sr}_x\text{CuO}_2$) the first high temperature superconductor (HTS) in 1986 [31], more and more high temperature superconductors have been discovered. LSCO consists of layered materials dominated by copper oxide planes, called Perovskites, which critical temperature is higher than 100 K. HTS commonly refer to the superconductors that T_C is over around 23–30 K.

YBCO ($\text{YBa}_2\text{Cu}_3\text{O}_{7-x}$) is one of the most famous HTS superconductor which was discovered by M. K. Wu, etc. in 1987 [32]. It is also well-known as the second generation (2G) HTS as it is the second HTS that used in conducting wires as the conducting layer. It created a new era for practical use of liquid nitrogen as a coolant and broadened the range of practical applications, because its critical temperature is near 92 K that is higher than the boiling point of liquid nitrogen. Other superconductors discovered before this usually use helium or hydrogen as coolant which show the boiling points as 4.2 K and 20 K respectively and are both more expensive and difficult to obtain than liquid nitrogen. After the discovery of YBCO, other rare-earth elements were also found to be able to substitute the yttrium such as lanthanum, samarium, neodymium, and so on. Then the family of chemical compounds using rare-earth and shares the similar structure are called REBCO (Rare-earth barium copper oxide) superconductors. As an advantage, REBCO superconductors have shown capability to sustain stronger magnetic field than other superconductors.

1.2.3 REBCO Coated Conductors

After active developments in manufacturing, more and more companies have realized the supplies of long-length REBCO-based HTS tape: SuperPower, American Superconductor (AMSC), Fujikura, and so on. Commercialization of long-length tapes made it possible to produce cables and coils for large scale applications, such as cables, motors, generators, and so on.

Different manufacturing techniques have been developed in such companies, such as RABiTS/MOD (rolling assisted biaxially textured substrate/metalorganic deposition), IBAD/MOCVD (ion beam assisted deposition/metal organic chemical vapor deposition), etc. Figure 1.5 illustrates an overview of the RABiTS/MOD technology developed by AMSC [33]. The buffer layers, which consist of a 75 nm Y_2O_3 seed layer, a 75 nm YSZ barrier layer, and a 75 nm CeO_2 cap layer, are deposited by high-rate reactive sputtering onto a metal alloy (Ni-W for example) substrate. Furthermore, the rare earth doped YBCO precursor film is slot-die coated onto the buffered substrate, and further, capped with an Ag layer, then oxygenated, and laminated between two metallic stabilizer strips (usually brass or copper). As to IBAD/MOCVD technology, a stack of buffer layers is sputtered to produce the biaxial texture for the YBCO layer, which is deposited using MOCVD. Then, a thin silver layer is sputtered for protection and better electrical contact. In some applications, silver can be completely electroplated to surround the wire.

The general configurations of REBCO tapes from different companies are similar even though different manufacturing processes are utilized. Figure 1.6 illustrates the configuration of SuperPower's YBCO-based tape which commonly consists of a substrate, a buffer layer, a REBCO superconductor layer, a silver overlayer, and sometimes a stabilizer. Specific material and thickness of each layer can be different depending on the manufacturer. REBCO tape is highly anisotropic, and the magnetic fields that perpendicular to the tape's wide surface significantly influence tape's performance because of REBCO's crystalline structure and the thin but flat shape of the tape.

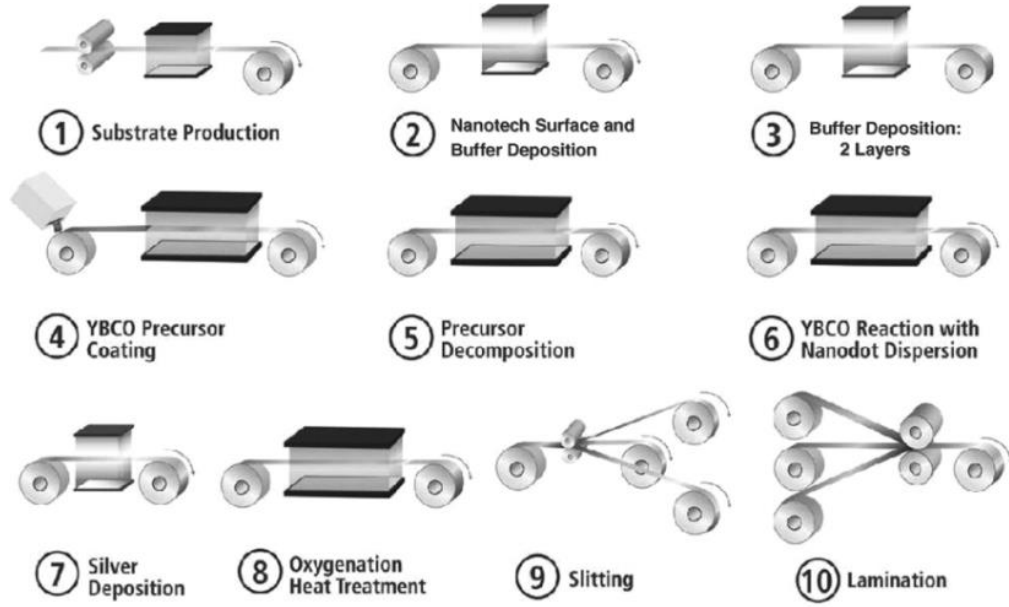


Fig. 1.5. Overview of RABiTS/MOD manufacturing process for HTS wire developed by AMSC [33].

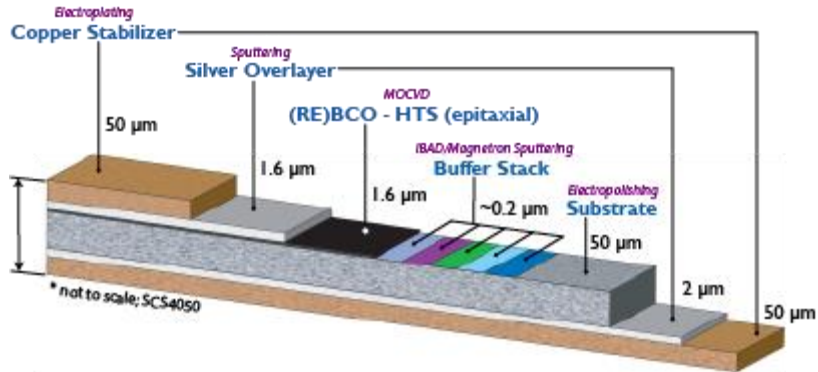


Fig. 1.6. SuperPower REBCO tape configuration [34].

1.3 Numerical Methods for Electromagnetic Analyses

Experimental and numerical approaches are the main method to study such problems to find the solutions. Although experiments are essential to study the actual physical phenomena and to conclusively verify a certain idea, it is still difficult to measure all the accurate and detailed information such as the current density, electric field, magnetic field, temperature, etc. at a certain point because of the limitation of the measurement technology. Hence, the numerical analysis is necessary and useful in today's research, and has contributed greatly with the detailed analysis [7], [12]. To study the electromagnetic behaviors, numerical simulation using equivalent circuit models, finite difference method (FDM), finite element method (FEM), etc. has been proposed and widely utilized. Equivalent circuit model of electric circuit elements is a very fast numerical

solution to simulate simple applications of REBCO-coated conductors [13], [10], [14], meanwhile, the improvement of analysis accuracy, which depends on the parameters of the equivalent circuit, is still a problem especially in the cases with complicated structures. Finite elements method is the most developed and widely used method today, allowing the use of different formulations for electromagnetic analysis: A - V (A : magnetic vector potential; V : electric scalar potential) [15], T - Ω (T : current vector potential; Ω : magnetic scalar potential) [16], [17], H (H : magnetic field) [18], and E (E : electric field) [19]. Among them, the T - Ω formulation has shown better convergence in both two-dimensional (2D) and three-dimensional (3D) situations, although extra variables are needed at each node [15], [7].

1.3.1 Equivalent Circuit Models

A lot of research on electrical systems (such as CERN magnets) have been conducted which utilized equivalent circuit models of non-linear resistivities, inductances, and capacitances [13], [10], [14]. Here the author introduces a similar approach proposed by Witzeling [35] that has been used by many research teams to analyze simple samples, and verified to be first and practical. In this approach, the superconductors are treated as an array of parallel wires as shown in Fig. 1.7.

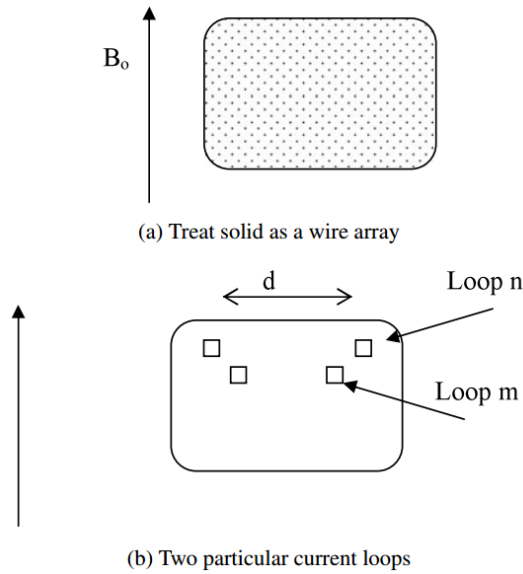


Fig. 1.7. Superconductors are treated as an array of parallel wires [7].

The electromagnetic field in loop n of width d is the sum of the induced voltages from the other loops' field and the external field. Then, we can get the relation below from Kirchhoff's equation assuming that the currents in each loop n and other loops m are I_n and I_m .

$$I_n R_n = \dot{B}_0 d + \sum_m \dot{I}_m M_{mn} \quad (1.1)$$

where the currents in each loop n and other loops m are I_n and I_m , M_{mn} is the mutual inductance between loops n and m .

When modelling superconductors, it can be modelled as a nonlinear resistivity or treated as a constant value 0 or I_C .

1.3.2 Finite Difference Method

This method is easy for understanding and programming. In this method, the domain is split into squares with values A at each node i , and turn differentials into differences as below in the case of forward finite difference method.

$$\left(\frac{\partial A}{\partial x}\right)_i = \frac{A(x_{i+1}) - A(x_i)}{x_{i+1} - x_i} \quad (1.2)$$

Then, differential equations can be derived to simultaneous equations using the variables A_n . For Maxwell's equations, we get a sparse matrix of $[A]$ along the diagonal and the resulting equations can be solved by many software. The disadvantage of this method is its limitation in the domain geometry as it can only to deal with problems with simple geometry such as rectangles. Hence, FDM has been superseded by FEM which has similar characteristics but better flexibility on complicated configurations.

1.3.3 Finite Element Method

Finite element method is the most general and developed method that utilized for analyzing problems using conventional materials. The basis of this method is the minimization of an integrated function over all region, which for electromagnetism has the dimensions of energy, and in some cases can be interpreted as the free energy of the system [7]. The calculus of variations indicates the process for a function of space being minimized by deriving a set of differential equations. However, the method is much more general for equations concerned with hysteresis and irreversibility, for which we cannot invoke the physical principle of minimizing the energy, and can still provide a function which results in the required solution after minimized [7].

In this method, the domain is split into finite meshes with simple shape such as triangular and so on. Then the differential equations are derived into a scalar integral and minimized to require the solution. Fig. 1.8 shows an example in a two-dimensional area.

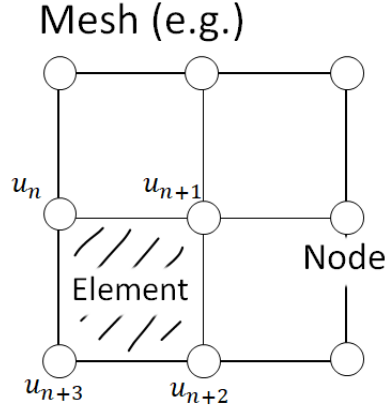


Fig. 1.8. An example for finite elements method in two-dimensional area.

In conventional FEM, the variable u_n are defined at node n , whereas the variables are defined at edge in the cases of edge element finite element method. A differential equation is assumed as below.

$$\frac{\partial^2 u}{\partial x^2} + \frac{\partial^2 u}{\partial y^2} + C = 0 \quad (1.3)$$

Galerkin method is usually used for discretization as below.

$$\int_V [N]^u \left(\frac{\partial^2 u}{\partial x^2} + \frac{\partial^2 u}{\partial y^2} + C \right) dV = 0 \quad (1.4)$$

where N is the interpolation function, φ is the basis vector of u ($u = [N]\{\varphi\}$). Then the equation can be derived as below with Gauss-Green's theorem.

$$-\int_V \left(\frac{\partial [N]^u}{\partial x} \frac{\partial [N]}{\partial x} + \frac{\partial [N]^u}{\partial y} \frac{\partial [N]}{\partial y} \right) dV + \int_V C [N]^u dV = 0 \quad (1.5)$$

After applying the derivation to each element, the governing equation then can be described with the coefficient matrix as below.

$$[A]^e \{\varphi\}^e = f^e \quad (1.6)$$

$$\begin{pmatrix} * & \cdots & 0 \\ \vdots & \ddots & \vdots \\ 0 & \cdots & * \end{pmatrix} \begin{pmatrix} u_1 \\ \vdots \\ u_N \end{pmatrix} = [f] \quad (1.7)$$

Finally, the solution can be required by solving the matrix equation above. To solve the equation, direct method and iterative method are the main methods. Direct methods attempt to solve the problem by a finite sequence of operations. Because of the absence of rounding errors, direct methods can calculate the exact solution with no convergence problem, meanwhile, it requires high memory storage and computational load. In contrast, iterative methods use an initial value to generate a sequence of solutions with improving approximate accuracy for a class of problems, in which the n -th approximation is derived from the previous ones. In the cases of sparse matrixes,

iterative methods show advantage with lower memory storage requirement and lower computational load. Therefore, it is often the only choice for nonlinear equations and is also useful even for linear problems involving many variables (sometimes of the order of millions), where direct methods would be prohibitively expensive.

The advantage of FEM is that various kinds of minimization techniques can be independently developed and applied to the problem by decoupling the original problem from the minimization in the cases of various situations [7]. Furthermore, the meshes based on the nodes of triangular or more complex forms enable the analyses in more complex geometries. On the other hand, the high computational load is still a problem for complex and large-scale analyses.

In FEM, \mathbf{A} - V (\mathbf{A} : magnetic vector potential; V : electric scalar potential), \mathbf{T} - Ω (\mathbf{T} : current vector potential; Ω : magnetic scalar potential), \mathbf{H} (\mathbf{H} : magnetic field) are the common formulations in analyzing superconducting problems.

A. \mathbf{A} - φ formulation

\mathbf{A} - φ formulation uses \mathbf{A} (magnetic vector potential, $\nabla \times \mathbf{A} = \mathbf{B}$) and φ (electric scalar potential) as the variables. The governing equation can be derived as below.

Firstly, the Ampere's law can be derived using \mathbf{A} as below.

$$\nabla \times \left(\frac{1}{\mu} \nabla \times \mathbf{A} \right) = \mathbf{J} \quad (1.8)$$

Then, the Faraday's law can be derived as

$$\nabla \times \mathbf{E} + \frac{\partial}{\partial t} \nabla \times \mathbf{A} = \nabla \times \left(\mathbf{E} + \frac{\partial}{\partial t} \mathbf{A} \right) = 0 \quad (1.9)$$

$$\mathbf{E} + \frac{\partial}{\partial t} \mathbf{A} = -\nabla \varphi \quad (1.10)$$

where φ is the electric scalar potential.

Then, we can use Maxwell's equation $\nabla \times \mathbf{H} = \mathbf{J}$ to get the first equation

$$\nabla \times \left(\frac{1}{\mu} \nabla \times \mathbf{A} \right) = -\sigma \frac{\partial}{\partial t} \mathbf{A} - \sigma \nabla \varphi \quad (1.11)$$

Furthermore, we can get the second equation since $\nabla \cdot \mathbf{J} = 0$

$$\nabla \sigma \left(\frac{\partial \mathbf{A}}{\partial t} + \nabla \varphi \right) = 0 \quad (1.12)$$

Equation (1.11) is the governing equation used in the \mathbf{A} - φ formulation and (1.12) is condition to be met. These equations are able to be solved by common commercial software. In addition, using \mathbf{A} as the variable has the advantage that the magnetic lines of force in 2D Cartesian geometry can be required by contouring \mathbf{A} .

The electrostatic potential φ can be ignored in some situations depending on the position and

direction of the current that generated by the applied magnetic field. Both φ and (1.12) can be ignored in the case that the currents can flow along the applied electric field lines without encountering a boundary which also means no electrostatic charges needed. However, surface charges and φ should be taken into consideration if a boundary exists where the current is bent.

In A - φ formulation, basically 4 variables need to be calculated in the governing equation, meanwhile, the number of variables is reduced to 3 in the region with 0 resistance. Furthermore, the number can be reduced to 2 in the case that axial symmetry is assumed and the circumferential component B_ϕ of magnetic field is 0 because only circumferential component A_ϕ needs to be considered. Therefore, good convergence can be acquired in solving common nonlinear problems.

B. T - Ω formulation

This formulation has similar form to A - φ formulation but utilizes different variables: \mathbf{T} (current vector potential) and Ω (magnetic scalar potential). First, we can define a vector potential by $\nabla \times \mathbf{T} = \mathbf{J}$ and $\nabla \cdot \mathbf{J} = 0$. Then, because $\nabla \times \mathbf{H} = \mathbf{J}$ we can get

$$\nabla \times (\mathbf{H} - \mathbf{T}) = 0 \quad (1.13)$$

$$\mathbf{H} - \mathbf{T} = -\nabla \Omega \quad (1.14)$$

where Ω is the magnetic scalar potential and can be related to magnetic surface poles, which is similar to the way surface charges determine φ in the A - φ formulation.

Finally, the Maxwell–Faraday equation is derived as below with (1.14)

$$\nabla \times \nabla \times \mathbf{T} = -\sigma \mu \frac{\partial}{\partial t} (\mathbf{T} - \nabla \Omega) \quad (1.15)$$

Equation (1.15) is the governing equation of T - Ω formulation. Additionally, the current streamlines in 2D Cartesian geometry can be acquired by contouring \mathbf{T} .

A - φ formulation and T - Ω formulation seem similar in the most general cases, however, the term concerning Ω can be omitted, then, the T - Ω formulation becomes identical to formulations only using \mathbf{H} (or \mathbf{B}) as variable [36], [37]. This also leads to a considerable advantage over the A - φ formulation because extra variables and corresponding equations can significantly increase the computational load.

C. H formulation

When ignoring the term of displacement current, namely assume that $\nabla \times \mathbf{H} = \mathbf{J}$, the Ampere's law can be derived with $\mathbf{J} = \sigma \mathbf{E}$ as below

$$\nabla \times (\sigma^{-1} \nabla \times \mathbf{H}) = \nabla \times \mathbf{E} \quad (1.16)$$

Then we can get the governing equation of H formulation based on the Maxwell–Faraday equation as (1.17)

$$\nabla \times (\sigma^{-1} \nabla \times \mathbf{H}) = -\frac{\partial}{\partial t}(\mu \mathbf{H}) \quad (1.17)$$

\mathbf{H} formulation is easy for practical use because the number of variables is always 3 and no electromagnetic four-potential is considered here. Furthermore, good convergence was observed because of its simple processing for variables. Hence, it is widely utilized in commercial software [38]. On the other hand, there are still problems such as that the computational load is relatively high because the number of variables cannot be reduced, and it cannot deal with the problems with zero resistance.

1.4 HTS Electromagnetic Characteristics Modelling

High temperature superconductors (HTS) have shown their potential and advantages in many engineering applications because of their unique properties. To optimize the design of a system that utilizing superconductors, it is important to understand and predict the electromagnetic behaviors of the superconductors [39]. However, the computation of HTS materials' quantitative electromagnetic characteristics is quite complex because of their highly non-linear current-voltage relationship.

To simulate such HTS electromagnetic behaviors, two classes of models have been developed: microscopic models and macroscopic models. Microscopic models focus on the superconductors' exact physical properties, meanwhile macroscopic models utilize simplified phenomena of physical properties to simulate the superconductors' behaviors. Microscopic models are usually based on the London model, the BCS and Ginzburg-Landau theories, and so on. On the other hand, to model the non-linear resistivity of a superconductor, macroscopic models are commonly based on critical state models, such as the Bean [40] and Kim [41], [42] models, as well as a nonlinear current-voltage relationship, such as the E - J power law [43]–[45]. Because of their good balance in accuracy and computational time, macroscopic models are the most common models in the engineering design of large-scale devices using superconductors. Some of them will be introduced in this sector.

The value of the critical current density J_C is partly determined by the properties of a specific superconductor including the type of twinning, granularity, material, concentration of defect centers, and so on. On the other hand, J_C also depends on the temperature, magnetic, and sometimes the strain as shown previously in Fig. 1.1. Strain usually occurs during cooling and warming up especially for a twisted or bent superconductor.

1.4.1 Critical State Models

As introduced in previous sectors, HTS materials are all Type II superconductors, in which

magnetic flux penetrates in the form of vortices (or discrete fluxons). Cooper pairs, namely the super-electrons, flow around the vortices to shield it from the superconducting region. These vortices always penetrate the superconductors initially from the edges. Meanwhile, their motion inward is always hindered by pinning centers which are the irregularities within the material's microstructure, such as non-superconducting precipitates, various lattice defects, dislocations, grain boundaries, and so on. In other words, the vortices in the pinning center generates interaction force to trap the magnetic flux. The magnetization of a Type II superconductor can be reversible, and magnetic field cannot be easily trapped without such pinning centers. However, once the Lorentz force exceeds the pinning force, a vortex will pass the pinning center and the magnetization will be reversed.

A critical state model (CSM) is usually utilized to simulate such behavior of vortices. CSMs are based on the macroscopic behavior of superconducting materials, which indicates the relationship between current density and magnetic field and is observed from experiments. Under a low applied current or magnetic field, the outer layer of the superconductor is considered to be in a "critical state". The critical state occurs in the case that the applied magnetic field exceeds the lower critical value H_{C1} . Circulating shield current is generated by the penetrating magnetic flux vortices, and then stop the applied current/field from penetrating more inward, namely, the penetration depth depends on the magnitude of the applied current/field.

Bean suggested a practical CSM to describe the J_C of type II superconductors which has been widely used [40]. Bean summarized this model based on his studies of ferromagnetic materials. Domain-like structure of the current density is suggested in his model and J_C is assumed to be dependent on magnetic field even in modified models. His model significantly simplifies the calculations of losses. The CSM models are widely used to calculate J_C from magnetic hysteresis loops of Type II superconductors, because it provides relatively accurate solutions for most simple practical cases in consideration of the magnetic field dependance of critical current density.

The related Maxwell's equations are as below without displacement current.

$$\nabla \times \mathbf{H} = \mathbf{J} \quad (1.18)$$

$$\nabla \times \mathbf{E} = -\frac{d\mathbf{B}}{dt} \quad (1.19)$$

where $\mathbf{B} = \mu_0 \mathbf{H}$ which is a good approximation for practical applications where $H_{C1} < H < H_{C2}$, and $\nabla \cdot \mathbf{J} = 0$ because no time-varying free charge distributions are considered here.

Once current flows in the superconductor, a Lorentz force is applied to the magnetic field vortices as $\mathbf{F} = \mathbf{J} \times \mathbf{B}$. In the case of a big enough Lorentz force, the vortices can be moved by the force at velocity \mathbf{v} . Such movement further induces an electric field as $\mathbf{E} = \mathbf{B} \times \mathbf{v}$ which is parallel to $\mathbf{B} \times (\mathbf{J} \times \mathbf{B})$. In the case that \mathbf{B} is perpendicular to \mathbf{J} , which is commonly true for 2D models, then \mathbf{E} is parallel to \mathbf{J} . Thus,

$$\mathbf{E} = \rho(J)\mathbf{J} \quad (1.20)$$

where $\rho(J)$ is the non-linear resistivity function of the superconductors, and $J = |\mathbf{J}|$. In addition, the superconductor's current density cannot exceed the critical value J_C in all the states in CSMs.

Bean Model

Bean's model [40] is the simplest one among all CSMs and it determines the magnitude of the superconductor's current density to be either 0 or $\pm J_C$. Namely, the electric field is assumed to be non-vanishing with current density. Moreover, the superconductor is considered to enter the critical state when the current flows through. On the other hand, the current density is considered to be zero in regions of the superconductor with no electric field experienced.

After an external magnetic field applied, the field initially starts to penetrate at the outer edges of the superconductor. The penetration depth mainly depends on the magnitude of J_C and external field. In the case of no vortex pinning, J_C is 0 and any external field can fully penetrate the superconductor with vortices moving. In the cases of vortex pinning, a gradient of vortex density defines J_C which is maintained by the pinning.

Therefore, two main assumptions are suggested for the Bean model as below:

1. The electric field \mathbf{E} is parallel to the current density \mathbf{J} ;
2. A current of J_C flows in the region where the superconductor is in the critical state.

$$\begin{aligned} J(x) &= \pm J_C & (\text{if } |E(x)| \neq 0) \\ J(x) &= 0 & (\text{if } |E(x)| = 0) \end{aligned} \quad (1.21)$$

The current distribution is the same in under both AC and DC current which share the same value of the peak magnitude. A “full penetration” occurs when the shielding currents, which is generated by transport current or external field, is large enough and the current region reaches the center of the superconductor. Losses in the changing transport current or external field depend on both the applied field's direction and the penetration depth.

For instance, Fig. 1.9 shows a superconducting slab with infinite length applied with an external magnetic field. The slab's thickness is $2a$ and the external magnetic field B_0 is applied in the z -direction. Then the induced shielding current density J is considered to flow in the y -direction between the front and back surfaces [46]. Different states based on the Bean model in this case is shown in Fig. 1.10. B^* is the characteristic field [46] or full-penetration field which is defined by $B^* = \mu_0 J_C a$. The Bean model is also capable to describe the electromagnetic behaviors in the cases of transport current, and both magnetic field and transport current. In addition, the calculated shielding current and transport current can be superposed to each other.

The Bean model was then modified by Kim [41] and Anderson [42] to take the influence of local magnetic field on the critical current density into consideration. This is introduced in the following section.

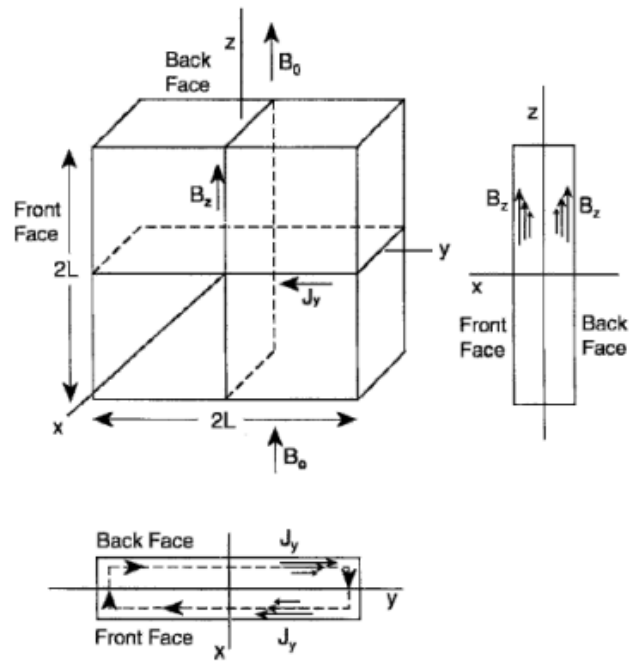


Fig. 1.9. An example for superconducting slab in externally applied magnetic field [46].

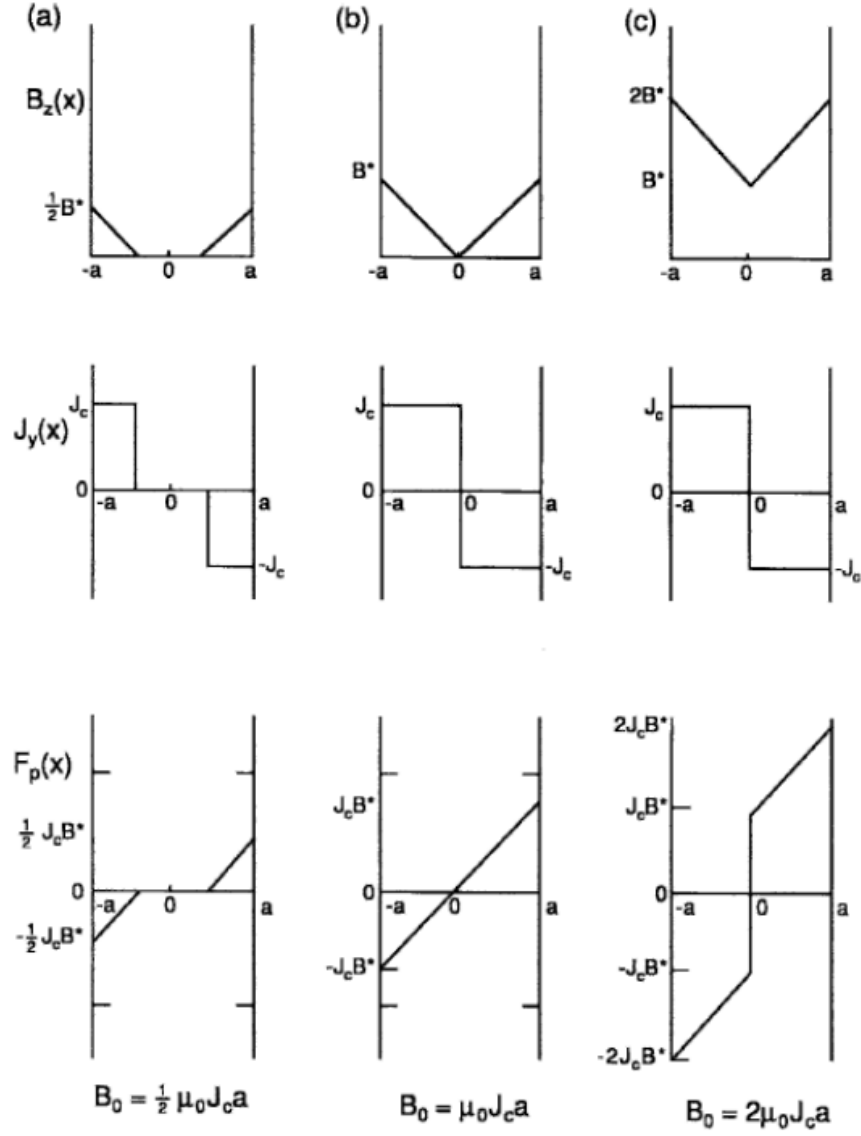


Fig. 1.10. Different states of internal magnetic field $B_z(x)$, current density $J_y(x)$, and pinning force $F_p(x)$ with different magnitudes of applied magnetic field B_0 : (a) $B_0/\mu_0 J_c a = 1/2$, (b) $B_0/\mu_0 J_c a = 1$, and (c) $B_0/\mu_0 J_c a = 2$ using the Bean model [46].

1.4.2 E - J Power Law

In the Bean model, a step relationship between the current density and electric field is assumed in the superconductor. It is based on a well-defined value of J_c which is also a function of the magnetic field. This has been verified effective in simulating LTS and some HTS [43]. However, it was revealed insufficient for some other HTS materials. Anderson proposed flux creep theory especially for the transient phase where this relationship is not discontinuous [42]. According to this theory, in the cases that the current is lower than I_c , the magnetic flux slowly moves and

generates an electric field and losses due to thermal activation. Then, Rhyner, etc. suggested the following E - J power law in [43], which is called n -value model that is now commonly utilized to describe the non-linear characteristics.

$$E = E_0 \left(\frac{J}{J_0} \right)^n \quad (1.22)$$

where J_C is a measured value of current density at a defined electrical field E_0 which is commonly 10^{-4} V/m.

N -value model has been verified to have good agreement with the experimental V - I curves of many HTS under DC current, and n is an important parameter which depends on the material's specific properties. The extreme cases of $n = 1$ and $n = \infty$ correspond to the linear Ohm's law ($E = \rho J$) and the Bean model ($J = 0$ or $\pm J_C$), respectively. A superconductor shows strong flux creep with n under 10, and critical line between HTS and LTS's n values is around 50. Figure 1.11 summarizes the E - J relationship described by n -value model with certain n values and the Bean model ($n = \infty$).

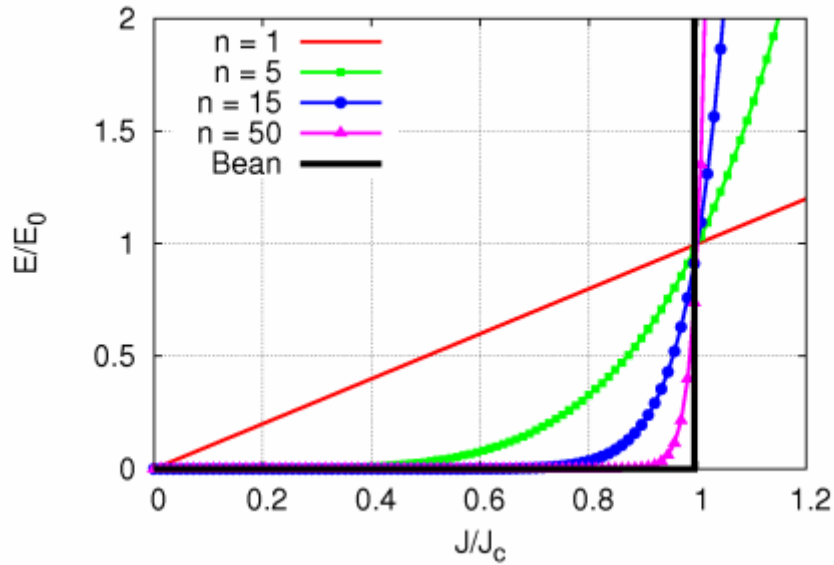


Fig. 1.11. E - J relationship described by the n -value model from $n = 1$ (linear) to $n = \infty$ (the Bean model).

1.4.1 Kim Model

Kim [41] and Anderson [42] revealed that the critical current I_C of Type II superconductors shows a strong dependence on temperature and applied magnetic field. An empirical relationship is summarized as

$$J_C(B) = \frac{\alpha(T)}{B_0 + B} = \frac{J_{C0}(T)}{1 + \frac{B}{B_0}} \quad (1.23)$$

where B_0 is a constant that depends on the material's property, and $J_{C0} = \alpha(T)/B_0$. The dependence of α with temperature was also proposed:

$$\alpha = \frac{1}{d}(a - bT) \quad (1.24)$$

where d strongly depends on the material's microstructure, and $a, b \leq T_C$. (1.25) and (1.26) show the dependence of the critical current density J_C and the power index n on B .

$$J_C(B) = \frac{J_{C0}}{1 + \frac{|B_y|}{B_0}} \quad (1.25)$$

$$n(B) = \frac{n_{C0}}{1 + \frac{|B_y|}{B_0}} \quad (1.26)$$

where only the y -component of B , which is parallel to the z -axis, is considered, J_{C0} and n_{C0} are the critical current density and power index under self-field, B_0 is a constant that obtained from the I_C - B experimental curve. This model enables a more accurate analysis of HTS electromagnetic behaviors, especially for cases with both current and magnetic field applied.

The Kim model is further extended with factor k and B_0 for a more accurate approximation of J_C in the cases that the superconductor is subjected to both perpendicular and parallel magnetic field [47], [48].

$$J_C(|B_x|, |B_y|) = \frac{J_{C0}}{1 + \frac{\sqrt{k^2|B_x|^2 + |B_y|^2}}{B_0}} \quad (1.27)$$

This was recently extended again to consider the dependance of J_C on the angular and magnitude of magnetic field as $J_C(B, \theta)$ [49], [50].

1.5 Research Objectives

In consideration of the advantages in applying REBCO coils, the objective of this research is to develop a versatile three-dimensional electromagnetic analysis method that can applies to various of cases with reduced computation load, furthermore, apply the method to coupled analysis with heat transfer to investigate the transient electromagnetic and thermal behaviors of REBCO coils, such as screening current, hotspot phenomenon, and so on.

Then, verifications for the correctness and accuracy of the proposed three-dimensional electromagnetic analysis method are necessary. Moreover, case studies of 3D electromagnetic problems and 3D electromagnetic and thermal coupled problems are conducted to study the capability of the developed analysis program.

1.6 Outline of this Thesis

In Chapter 2, the author introduces the proposed three-dimensional electromagnetic analysis method using finite elements method and thin plate approximation for REBCO-coated conductors and coils. Thin plate approximation and coordinate transformation (from Cartesian coordinates system to orthogonal curvilinear coordinate system) are utilized to realize the electromagnetic analysis of REBCO coils, which have 3D structures, in 2D calculation space. The governing electromagnetic equation is given by $\nabla \times (\rho \nabla \times \mathbf{T}) = -\partial \mathbf{B} / \partial t$ (\mathbf{T} : current vector potential; ρ : electric resistivity; \mathbf{B} : magnetic flux density), where \mathbf{T} is defined by $\mathbf{J} = \nabla \times \mathbf{T}$ (\mathbf{J} : current density). Additionally, a nonlinear E - J relation (E : electric field) as well as the temperature dependence is used for modelling the electromagnetic characteristic of superconductors.

In Chapter 3, verifications and two case studies are conducted with the developed analysis program that based on the proposed three-dimensional electromagnetic analysis method. Firstly, verifications are conducted by comparing the analysis results with theoretical formula and commercial simulation software JMAG. Good agreement is observed which verifies the correctness and accuracy of the proposed analysis method. Next, two case studies based on the three-dimensional electromagnetic analysis are conducted and indicate the capability of the developed electromagnetic analysis tool to analyze various electromagnetic characteristics of REBCO coils in any shape. One is an analysis of a solenoid REBCO coil for magnet application, which requires high magnetic field as well as high stability and homogeneity of the field. The author has modelled a solenoid REBCO coil and assumed some different patterns of excitation to study the magnet field stability and homogeneity with detailed distribution of magnetic field, screening current induced field, current density, and screening current density. The other case study is an analysis of a saddle-shaped REBCO coil for accelerator application, which requires accurate and homogeneous magnetic field with the frequently changing coil current. The author has modelled a saddled-shaped REBCO coil and assumed the change pattern of coil current to study the space magnetic field distribution and the influence of screening current with detailed distribution of magnetic field, screening current induced field, current density, and screening current density.

In Chapter 4, the author introduces the three-dimensional heat transfer analysis method as well as the electromagnetic and heat transfer coupled analysis. In the heat transfer analysis, the 3D structure of REBCO coils is modeled and the temperature change is calculated under the condition of Joule heating, heat conduction, heat transfer, and cooling characteristics. In addition, the temperature dependence of thermal characteristics is also considered in the analysis.

In Chapter 5, two case studies based on electromagnetic and heat transfer coupled analysis are conducted to study the quench phenomenon in certain applications. One is an analysis of a REBCO coil for resistive type SFCL application, in which quench is a problem because high

resistance is generated to limit the overcurrent through the SN transition with a significant temperature rise. The author has analyzed the transient electromagnetic and thermal behaviors of two solenoid REBCO coils under overcurrent: one with uniform critical current density (J_C) distribution and the other with local J_C degradation. The other case study is an analysis of a REBCO coil for magnet application, in which a quench usually occurs after an external energy input during the normal operation or the excitation process. The author has analyzed the influence of different energy input power, area, and different time constants of current decrease on the quench of a solenoid REBCO coil, as well as the electromagnetic and thermal behaviors before and after the quench.

Chapter 6 summarizes the background and the achievements of this research, and discusses potential direction of research in this area in the future.

Chapter 2. 3D Electromagnetic Analysis Method

2.1 Analysis Conditions & Governing Equation

The target of the proposed three-dimensional electromagnetic analysis method is REBCO coated conductors and coils in any practical shape. A practical shape of REBCO coils necessarily has a bend radius over about some centimeters because of the dramatic performance degradation when the bent bend radius is lower than that. Therefore, in consideration of the thickness of the conducting layer, which is only some μm , the thin plate approximation is available for the analysis. Furthermore, in this thesis, no ferromagnetic materials are assumed in the model, namely, only REBCO coated conductors or coils are considered and modelled here.

The finite element method based on current vector potential \mathbf{T} is used for the electromagnetic analysis [16], [17]. The current vector potential is used to calculate the current density which is then used to calculate the magnetic field by the Biot-Savart law, and no ferromagnetic materials are assumed here, therefore, the magnetic scalar potential Ω (defined by $\mathbf{H} - \mathbf{T} = -\nabla\Omega$) is unnecessary and omitted here. The governing equation of current vector potential \mathbf{T} defined by $\mathbf{J} = \nabla \times \mathbf{T}$ (\mathbf{J} : current density) is then given by the following equations:

$$\nabla \times (\rho \nabla \times \mathbf{T}) = -\frac{\partial \mathbf{B}}{\partial t} \quad (2.1)$$

$$\mathbf{B} = \frac{\mu_0}{4\pi} \int_V \frac{\mathbf{J} \times \mathbf{r}}{r^3} dV \quad (2.2)$$

$$\nabla \times (\rho \nabla \times \mathbf{T}) = -\frac{\mu}{4\pi} \frac{\partial}{\partial t} \iiint_V \frac{(\nabla \times \mathbf{T}) \times \mathbf{r}}{r^3} dV - \frac{\partial \mathbf{B}_0}{\partial t} \quad (2.3)$$

where ρ is the electric resistivity, \mathbf{B} is the magnetic flux density, \mathbf{B}_0 is the externally applied magnetic field. The governing equation (2.3) can be obtained by inserting (2.1) into the Biot-Savart law (2.2). In consideration of the very thin superconductor layer, the current flow can be assumed to be parallel to the coated conductor, and a thin plate approximation can be applied in this research (Fig. 2.1). Therefore, the current density in the conductor is dominated by the component of \mathbf{T} that is normal to the surface. In addition, the transport current of the conductor can be determined by the boundary condition of \mathbf{T} [51]. Furthermore, because of the thin plate approximation, this method is currently unavailable for some types of REBCO coils with current flowing in the direction that perpendicular to the wide surface such as non-insulation coils.

To summarize the analysis conditions, this proposed analysis method is capable of simulating REBCO coated conductors and coils in any practical shapes with no ferromagnetic materials. However, it is currently unavailable for such types of REBCO coils with current flowing in the direction that perpendicular to the wide surface as non-insulation coils.

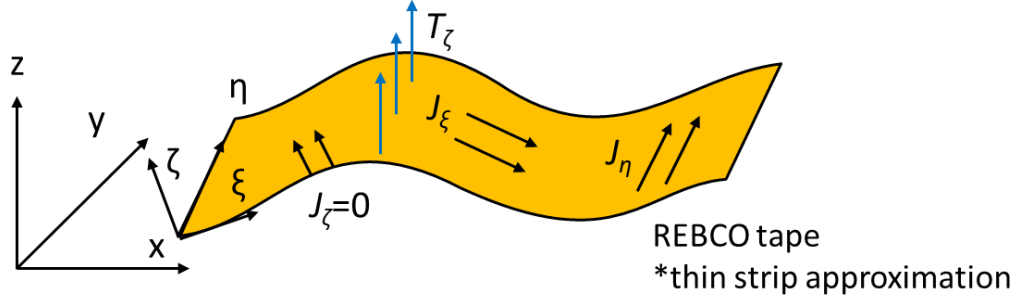


Fig. 2.1. Thin strip approximation of REBCO-coated conductor: J_x, J_y, J_z are the current densities and \mathbf{T} is the current vector potential.

2.2 Coordinate Transformation & Orthogonal Curvilinear Coordinate System

To decrease the computational load, coordinate transformation is applied to the governing equations. The governing equations are given and calculated in the orthogonal curvilinear coordinate system (ξ, η, ζ) , which is set to follow the surface of REBCO tape (Fig. 2.2). The ξ -axis is along the longitudinal direction of REBCO tape, the η -axis is along the widthwise direction, and the ζ -axis is normal to the surface of REBCO tape. Therefore, after utilizing the coordinate transformation and the thin plate approximation, the variables (T_x, T_y, T_z) in the (x, y, z) coordinate system can be reduced to only T_ζ in the orthogonal curvilinear coordinate system.

Furthermore, in coordinate transformation, scale factors (h_ξ, h_η, h_ζ) are needed and they are defined in (2.4)–(2.6) as the constants of proportionality of different coordinate [52], [53].

$$h_\xi = \left| \frac{\partial \mathbf{r}}{\partial \xi} \right| = \left| \frac{\partial x}{\partial \xi} \mathbf{e}_x + \frac{\partial y}{\partial \xi} \mathbf{e}_y + \frac{\partial z}{\partial \xi} \mathbf{e}_z \right| = \sqrt{\left(\frac{\partial x}{\partial \xi} \right)^2 + \left(\frac{\partial y}{\partial \xi} \right)^2 + \left(\frac{\partial z}{\partial \xi} \right)^2} \quad (2.4)$$

$$h_\eta = \left| \frac{\partial \mathbf{r}}{\partial \eta} \right| = \left| \frac{\partial x}{\partial \eta} \mathbf{e}_x + \frac{\partial y}{\partial \eta} \mathbf{e}_y + \frac{\partial z}{\partial \eta} \mathbf{e}_z \right| = \sqrt{\left(\frac{\partial x}{\partial \eta} \right)^2 + \left(\frac{\partial y}{\partial \eta} \right)^2 + \left(\frac{\partial z}{\partial \eta} \right)^2} \quad (2.5)$$

$$h_\zeta = \left| \frac{\partial \mathbf{r}}{\partial \zeta} \right| = \left| \frac{\partial x}{\partial \zeta} \mathbf{e}_x + \frac{\partial y}{\partial \zeta} \mathbf{e}_y + \frac{\partial z}{\partial \zeta} \mathbf{e}_z \right| = \sqrt{\left(\frac{\partial x}{\partial \zeta} \right)^2 + \left(\frac{\partial y}{\partial \zeta} \right)^2 + \left(\frac{\partial z}{\partial \zeta} \right)^2} \quad (2.6)$$

where $\partial \mathbf{r}$ is the derivative of position vector \mathbf{r} and can be expressed as below:

$$d\mathbf{r} = dx\mathbf{e}_x + dy\mathbf{e}_y + dz\mathbf{e}_z = \frac{\partial \mathbf{r}}{\partial \xi} d\xi \mathbf{e}_\xi + \frac{\partial \mathbf{r}}{\partial \eta} d\eta \mathbf{e}_\eta + \frac{\partial \mathbf{r}}{\partial \zeta} d\zeta \mathbf{e}_\zeta = h_\xi d\xi \mathbf{e}_\xi + h_\eta d\eta \mathbf{e}_\eta + h_\zeta d\zeta \mathbf{e}_\zeta$$

Here, (h_ξ, h_η, h_ζ) are functions of (ξ, η, ζ) but are assumed to be constant in each element after discretization.

Then, the governing equation (2.3) can be expressed in orthogonal curvilinear coordinate system as below.

Firstly, we focus on the right side of the governing equation (2.3). $(\nabla \times \mathbf{T})$ can be calculated in the orthogonal curvilinear coordinate as below:

$$\nabla \times \mathbf{T} = \begin{vmatrix} \frac{\xi}{h_\eta h_\zeta} & \frac{\eta}{h_\zeta h_\xi} & \frac{\zeta}{h_\xi h_\eta} \\ \frac{\partial}{\partial \xi} & \frac{\partial}{\partial \eta} & \frac{\partial}{\partial \zeta} \\ h_\xi T_\xi & h_\eta T_\eta & h_\zeta T_\zeta \end{vmatrix} \quad (2.5)$$

Only ζ -direction component is considered because of the thin plate approximation. So, $(\nabla \times \mathbf{T})$ and the first term in the right side of governing equation (2.3) can be written as below:

$$\begin{aligned} [\nabla \times \mathbf{T}]_\zeta &= \frac{1}{h_\eta h_\zeta} \left(\frac{\partial h_\zeta T_\zeta}{\partial \eta} \right) \xi - \frac{1}{h_\zeta h_\xi} \left(\frac{\partial h_\zeta T_\zeta}{\partial \xi} \right) \eta = J_\xi \xi + J_\eta \eta \\ \left[-\frac{\mu}{4\pi} \frac{\partial}{\partial t} \iiint_V \frac{(\nabla \times \mathbf{T}) \times \mathbf{r}}{r^3} dV \right]_\zeta &= -\frac{\mu}{4\pi} \frac{\partial}{\partial t} \iint_S \left(\frac{(\nabla \times \mathbf{T}) \times \mathbf{r}}{r^3} \right) h_\xi h_\eta d\xi d\eta \end{aligned} \quad (2.6)$$

Secondly, we turn to the left side of the governing equation (2.3). Because (h_ξ, h_η, h_ζ) are treated as constants in each element when utilizing FEM and only ζ -direction component is considered for the thin plate approximation, the left side can be expressed as below:

$$\begin{aligned} [\nabla \times (\rho \nabla \times \mathbf{T})]_\zeta &= \frac{\rho}{h_\xi h_\eta} \left[\frac{\partial \frac{h_\eta}{h_\zeta h_\xi} \left(-\frac{\partial h_\zeta T_\zeta}{\partial \xi} \right)}{\partial \xi} - \frac{\partial \frac{h_\xi}{h_\eta h_\zeta} \left(\frac{\partial h_\zeta T_\zeta}{\partial \eta} \right)}{\partial \eta} \right] \\ &= -\frac{\rho}{h_\xi h_\eta} \left[\frac{\partial \left(\frac{h_\eta}{h_\xi} \frac{\partial T_\zeta}{\partial \xi} \right)}{\partial \xi} + \frac{\partial \left(\frac{h_\xi}{h_\eta} \frac{\partial T_\zeta}{\partial \eta} \right)}{\partial \eta} \right] \\ &= -\rho \left(\frac{1}{h_\xi^2} \frac{\partial^2 T_\zeta}{\partial \xi^2} + \frac{1}{h_\eta^2} \frac{\partial^2 T_\zeta}{\partial \eta^2} \right) \end{aligned} \quad (2.7)$$

Consequently, the governing equation can be written as (2.8).

$$\rho \left(\frac{1}{h_\xi^2} \frac{\partial^2 T_\zeta}{\partial \xi^2} + \frac{1}{h_\eta^2} \frac{\partial^2 T_\zeta}{\partial \eta^2} \right) - \frac{\mu h}{4\pi} \frac{\partial}{\partial t} \iint_S \left(\frac{(\nabla \times \mathbf{T}) \times \mathbf{r}}{r^3} \right) h_\xi h_\eta d\xi d\eta - \frac{\partial \mathbf{B}_0 \cdot \boldsymbol{\zeta}}{\partial t} = 0 \quad (2.8)$$

2.3 Discretization & Coordinate Transformation

Galerkin method with triangle elements and a linear interpolation formula is used for discretization. Refer to reference [51], [54] for the detail of triangle elements and the numerical integration in such elements. Based on the governing equation, a node equation can be given as G_i^* :

$$\begin{aligned} G_i^* &= \rho \iint_{S^{(e)}} N_i \left(\frac{1}{h_\xi^2} \frac{\partial^2 T_\zeta}{\partial \xi^2} + \frac{1}{h_\eta^2} \frac{\partial^2 T_\zeta}{\partial \eta^2} \right) h_\xi h_\eta d\xi d\eta \\ &\quad - \iint_{S^{(e)}} N_i \left[\frac{\mu}{4\pi} \frac{\partial}{\partial t} \iint_{S_v'} \left(\frac{(\nabla \times \mathbf{T}) \times \mathbf{r}}{r^3} \right) h_\xi' h_\eta' d\xi d\eta \right] h_\xi h_\eta d\xi d\eta \end{aligned}$$

$$- \iint_{S^{(e)}} N_i \frac{\partial \mathbf{B}_0 \cdot \boldsymbol{\zeta}}{\partial t} h_\xi h_\eta d\xi d\eta = 0 \quad (2.9)$$

where N_i is the interpolation function, $S^{(e)}$ is the calculation area around node i , S'_v is the integral area for magnetic field calculation using Biot–Savart law.

Firstly, we focus on the first term on the right. After applying the following transformation,

$$\frac{\partial}{\partial \xi} \left(N_i \frac{\partial T_\zeta}{\partial \xi} \right) = \frac{\partial N_i}{\partial \xi} \left(\frac{\partial T_\zeta}{\partial \xi} \right) + N_i \frac{\partial}{\partial \xi} \left(\frac{\partial T_\zeta}{\partial \xi} \right) \quad (2.10)$$

The first term can be transformed as below.

$$\begin{aligned} & \rho \iint_{S^{(e)}} N_i \left(\frac{1}{h_\xi^2} \frac{\partial^2 T_\zeta}{\partial \xi^2} + \frac{1}{h_\eta^2} \frac{\partial^2 T_\zeta}{\partial \eta^2} \right) h_\xi h_\eta d\xi d\eta \\ &= \rho \iint_{S^{(e)}} \left[\frac{1}{h_\xi^2} \frac{\partial}{\partial \xi} \left(N_i \frac{\partial T_\zeta}{\partial \xi} \right) + \frac{1}{h_\eta^2} \frac{\partial}{\partial \eta} \left(N_i \frac{\partial T_\zeta}{\partial \eta} \right) \right] h_\xi h_\eta d\xi d\eta \\ & \quad - \rho \iint_{S^{(e)}} \left[\frac{1}{h_\xi^2} \frac{\partial N_i}{\partial \xi} \left(\frac{\partial T_\zeta}{\partial \xi} \right) + \frac{1}{h_\eta^2} \frac{\partial N_i}{\partial \eta} \left(\frac{\partial T_\zeta}{\partial \eta} \right) \right] h_\xi h_\eta d\xi d\eta \end{aligned} \quad (2.11)$$

The Kelvin–Stokes theorem can be applied to the first term on the right.

$$\iint_S \nabla \times \mathbf{F} \cdot d\mathbf{S} = \oint_C \mathbf{F} \cdot d\mathbf{r} \quad (2.12)$$

In addition, the Kelvin–Stokes theorem also can be using in the orthogonal curvilinear coordinate system, and only the ζ -direction component needs to be considered.

$$(\nabla \times \mathbf{F})_\zeta = \frac{1}{h_\xi} \frac{\partial F_\eta}{\partial \xi} - \frac{1}{h_\eta} \frac{\partial F_\xi}{\partial \eta} \quad (2.13)$$

where F_ξ and F_η are defined as below.

$$F_\xi = -\frac{N_i}{h_\eta} \frac{\partial T_\zeta}{\partial \eta} \quad (2.17)$$

$$F_\eta = \frac{N_i}{h_\xi} \frac{\partial T_\zeta}{\partial \xi} \quad (2.16)$$

$$\oint_C \mathbf{F} \cdot d\mathbf{r} = \oint_C N_i \left(\frac{1}{h_\xi} \frac{\partial T_\zeta}{\partial \xi} h_\eta d\eta - \frac{1}{h_\eta} \frac{\partial T_\zeta}{\partial \eta} h_\xi d\xi \right) \quad (2.15)$$

Hence, the first term can be transformed as below after applying the Kelvin–Stokes theorem. Furthermore, it results in 0 because the contour C of the integral area is closed and it is treated as a natural boundary.

$$\begin{aligned} & \iint_{S^{(e)}} \left[\frac{1}{h_\xi^2} \frac{\partial}{\partial \xi} \left(N_i \frac{\partial T_\zeta}{\partial \xi} \right) + \frac{1}{h_\eta^2} \frac{\partial}{\partial \eta} \left(N_i \frac{\partial T_\zeta}{\partial \eta} \right) \right] h_\xi h_\eta d\xi d\eta \\ &= \iint_{S^{(e)}} \nabla \times \mathbf{F} \cdot d\mathbf{S} = \oint_C \mathbf{F} \cdot d\mathbf{r} = \oint_C N_i \left(\frac{1}{h_\xi} \frac{\partial T_\zeta}{\partial \xi} h_\eta d\eta - \frac{1}{h_\eta} \frac{\partial T_\zeta}{\partial \eta} h_\xi d\xi \right) = 0 \end{aligned} \quad (2.18)$$

Then, we get G_i as below.

$$\begin{aligned}
G_i = -G_i^* = & \rho \iint_{S^{(e)}} \left[\frac{1}{h_\xi^2} \frac{\partial N_i}{\partial \xi} \left(\frac{\partial T_\zeta}{\partial \xi} \right) + \frac{1}{h_\eta^2} \frac{\partial N_i}{\partial \eta} \left(\frac{\partial T_\zeta}{\partial \eta} \right) \right] h_\xi h_\eta d\xi d\eta \\
& + \iint_{S^{(e)}} N_i \left[\frac{\mu}{4\pi} \frac{\partial}{\partial t} \iint_{S'_v} \left(\frac{(\nabla \times \mathbf{T}) \times \mathbf{r}}{r^3} \right) h'_\xi h'_\eta d\xi d\eta \right] h_\xi h_\eta d\xi d\eta \\
& + \iint_{S^{(e)}} N_i \frac{\partial \mathbf{B}_0 \cdot \boldsymbol{\zeta}}{\partial t} h_\xi h_\eta d\xi d\eta = 0
\end{aligned} \tag{2.19}$$

G_i is the integral over the entire calculation region and is calculated by summing up all the value of each element with numerical integration. In that process, N_i is calculated as N_{ie} that is separately determined in each element. Additionally, the value of N_{ie} is 0 in the elements that do not share the node ie . Therefore, G_i only needs to be calculated within the elements in the area R_i that shares the node ie as below.

$$\begin{aligned}
G_i = & \sum_{R_i} \left\{ \rho \iint_{S^{(e)}} \left[\frac{1}{h_\xi^2} \frac{\partial N_i}{\partial \xi} \left(\frac{\partial T_\zeta}{\partial \xi} \right) + \frac{1}{h_\eta^2} \frac{\partial N_i}{\partial \eta} \left(\frac{\partial T_\zeta}{\partial \eta} \right) \right] h_\xi h_\eta d\xi d\eta \right\} \\
& + \sum_{R_i} \left\{ \iint_{S^{(e)}} N_i \left[\frac{\mu}{4\pi} \frac{\partial}{\partial t} \iint_{S'_v} \left(\frac{(\nabla \times \mathbf{T}) \times \mathbf{r}}{r^3} \right) h'_\xi h'_\eta d\xi d\eta \right] h_\xi h_\eta d\xi d\eta \right\} \\
& + \sum_{R_i} \left(\iint_{S^{(e)}} N_i \frac{\partial \mathbf{B}_0 \cdot \boldsymbol{\zeta}}{\partial t} h_\xi h_\eta d\xi d\eta \right) = 0
\end{aligned} \tag{2.20}$$

Secondly, we turn to the second term on the right side of G_i where magnetic field, that generated by the current flowing in the area S'_v , is calculated in the area $S^{(e)}$. Additionally, only ζ -direction component of the magnetic field is calculated because of the thin plate approximation.

The orthogonal curvilinear coordinate system is defined in each element when utilizing the finite element method. Hence, the current density is based on the orthogonal curvilinear coordinate system in the area S'_v and the magnetic field is based on another orthogonal curvilinear coordinate system in the area $S^{(e)}$, and transformation is necessary for the calculation. Here, we proposed the solution as below.

Firstly, we calculate the current density by $\nabla \times \mathbf{T}$ in the orthogonal curvilinear coordinate system in the area S'_v . Then, coordinate transformation to the (x, y, z) coordinate system is applied to the current density and the magnetic field is calculated in the (x, y, z) coordinate system. Finally, we apply another coordinate transformation to the magnetic field and get the magnetic field in the orthogonal curvilinear coordinate system in the area $S^{(e)}$. The detailed process is described below.

To transform a vector \mathbf{A} between different coordinate systems, a transformation matrix $[a_{ij}]$ is defined as below.

$$\begin{pmatrix} \xi \\ \eta \\ \zeta \end{pmatrix} = \begin{pmatrix} a_{11} & a_{12} & a_{13} \\ a_{21} & a_{22} & a_{23} \\ a_{31} & a_{32} & a_{33} \end{pmatrix} \begin{pmatrix} \mathbf{x} \\ \mathbf{y} \\ \mathbf{z} \end{pmatrix} \quad (2.21)$$

where $(\mathbf{x}, \mathbf{y}, \mathbf{z})$ and (ξ, η, ζ) are the basis vectors in the (x, y, z) coordinate system and orthogonal curvilinear coordinate system. $[a_{ij}]$ can be calculated as below in the way $\mathbf{x} \cdot \xi = \mathbf{x} \cdot (a_{11}\mathbf{x} + a_{12}\mathbf{y} + a_{13}\mathbf{z}) = a_{11}$.

$$\begin{aligned} a_{11} &= \mathbf{x} \cdot \xi & a_{12} &= \mathbf{y} \cdot \xi & a_{13} &= \mathbf{z} \cdot \xi \\ a_{21} &= \mathbf{x} \cdot \eta & a_{22} &= \mathbf{y} \cdot \eta & a_{23} &= \mathbf{z} \cdot \eta \\ a_{31} &= \mathbf{x} \cdot \zeta & a_{32} &= \mathbf{y} \cdot \zeta & a_{33} &= \mathbf{z} \cdot \zeta \end{aligned} \quad (2.22)$$

Therefore, the transformation between the (x, y, z) coordinate system and orthogonal curvilinear coordinate system is as below.

$$\begin{pmatrix} A_\xi \\ A_\eta \\ A_\zeta \end{pmatrix} = \begin{pmatrix} a_{11} & a_{12} & a_{13} \\ a_{21} & a_{22} & a_{23} \\ a_{31} & a_{32} & a_{33} \end{pmatrix} \begin{pmatrix} A_x \\ A_y \\ A_z \end{pmatrix} \quad (2.23)$$

$$\begin{pmatrix} A_x \\ A_y \\ A_z \end{pmatrix} = \begin{pmatrix} a_{11} & a_{21} & a_{31} \\ a_{12} & a_{22} & a_{32} \\ a_{13} & a_{23} & a_{33} \end{pmatrix} \begin{pmatrix} A_\xi \\ A_\eta \\ A_\zeta \end{pmatrix} \quad (2.24)$$

With the transformation matrix, the current density can be transformed to the (x, y, z) coordinate system as below.

$$\nabla \times \mathbf{T} = J_\xi \xi + J_\eta \eta = J_x \mathbf{x} + J_y \mathbf{y} + J_z \mathbf{z} \quad (2.25)$$

$$\begin{pmatrix} J_x \\ J_y \\ J_z \end{pmatrix} = \begin{pmatrix} a_{11} & a_{21} & a_{31} \\ a_{12} & a_{22} & a_{32} \\ a_{13} & a_{23} & a_{33} \end{pmatrix} \begin{pmatrix} J_\xi \\ J_\eta \\ 0 \end{pmatrix} \quad (2.26)$$

where $[a_{ij}]$ differs in each element.

Then, magnetic field is calculated in the (x, y, z) coordinate system.

$$\mathbf{J} \times \mathbf{r} = \begin{vmatrix} \mathbf{x} & \mathbf{y} & \mathbf{z} \\ J_x & J_y & J_z \\ r_x & r_y & r_z \end{vmatrix} = (J_y r_z - J_z r_y) \mathbf{x} - (J_x r_z - J_z r_x) \mathbf{y} + (J_x r_y - J_y r_x) \mathbf{z} \quad (2.27)$$

Finally, the magnetic field is transformed to the orthogonal curvilinear coordinate system in the area $S^{(e)}$ and we get the ζ -direction component as below.

$$\begin{aligned} \frac{(\mathbf{J} \times \mathbf{r})_\zeta}{r^3} &= \frac{a'_{31}}{r^3} (J_y r_z - J_z r_y) - \frac{a'_{32}}{r^3} (J_x r_z - J_z r_x) + \frac{a'_{33}}{r^3} (J_x r_y - J_y r_x) \\ &= \frac{a'_{31}}{r^3} [(a_{12} J_\xi + a_{22} J_\eta) r_z - (a_{13} J_\xi + a_{23} J_\eta) r_y] - \frac{a'_{32}}{r^3} [(a_{11} J_\xi + a_{21} J_\eta) r_z - (a_{13} J_\xi + a_{23} J_\eta) r_x] \\ &\quad + \frac{a'_{33}}{r^3} [(a_{11} J_\xi + a_{21} J_\eta) r_y - (a_{12} J_\xi + a_{22} J_\eta) r_x] \end{aligned}$$

$$= \frac{[(a'_{32}a_{13} - a'_{33}a_{12})r_x + (a'_{33}a_{11} - a'_{31}a_{13})r_y + (a'_{31}a_{12} - a'_{32}a_{11})r_z]J_\xi}{r^3} + [(a'_{32}a_{23} - a'_{33}a_{22})r_x + (a'_{33}a_{21} - a'_{31}a_{23})r_y + (a'_{31}a_{22} - a'_{32}a_{21})r_z]J_\eta/r^3 \quad (2.28)$$

where $[a_{ij}]$ is the transformation matrix in the area S'_v and $[a'_{ij}]$ is the transformation matrix in the area $S^{(e)}$.

Considering

$$J_\xi = \frac{1}{h_\eta} \left(\frac{\partial T_\zeta}{\partial \eta} \right) \quad (2.29)$$

$$J_\eta = -\frac{1}{h_\xi} \left(\frac{\partial T_\zeta}{\partial \xi} \right) \quad (2.30)$$

the equation can be simplified as below.

$$\begin{aligned} & \frac{(\mathbf{J} \times \mathbf{r})_\zeta}{r^3} \\ &= \frac{[(a'_{32}a_{13} - a'_{33}a_{12})r_x + (a'_{33}a_{11} - a'_{31}a_{13})r_y + (a'_{31}a_{12} - a'_{32}a_{11})r_z]}{h_\eta r^3} \left(\frac{\partial T_\zeta}{\partial \eta} \right) \\ & - \frac{[(a'_{32}a_{23} - a'_{33}a_{22})r_x + (a'_{33}a_{21} - a'_{31}a_{23})r_y + (a'_{31}a_{22} - a'_{32}a_{21})r_z]}{h_\xi r^3} \left(\frac{\partial T_\zeta}{\partial \xi} \right) \\ &= a_\eta \left(\frac{\partial T_\zeta}{\partial \eta} \right) + a_\xi \left(\frac{\partial T_\zeta}{\partial \xi} \right) \\ & G_i = \sum_{R_i} \left\{ \rho \iint_{S^{(e)}} \left[\frac{1}{h_\xi^2} \frac{\partial N_i}{\partial \xi} \left(\frac{\partial T_\zeta}{\partial \xi} \right) + \frac{1}{h_\eta^2} \frac{\partial N_i}{\partial \eta} \left(\frac{\partial T_\zeta}{\partial \eta} \right) \right] h_\xi h_\eta d\xi d\eta \right\} \\ & + \sum_{R_i} \left\{ \iint_{S^{(e)}} N_i \left[\frac{\mu}{4\pi} \frac{\partial}{\partial t} \iint_{S'_v} \left[a_\eta \left(\frac{\partial T_\zeta}{\partial \eta} \right) + a_\xi \left(\frac{\partial T_\zeta}{\partial \xi} \right) \right] h'_\xi h'_\eta d\xi d\eta \right] h_\xi h_\eta d\xi d\eta \right\} \\ & + \sum_{R_i} \left(\iint_{S^{(e)}} N_i \frac{\partial \mathbf{B}_0 \cdot \boldsymbol{\zeta}}{\partial t} h_\xi h_\eta d\xi d\eta \right) = 0 \quad (2.31) \end{aligned}$$

where

$$a_\eta = \frac{[(a'_{32}a_{13} - a'_{33}a_{12})r_x + (a'_{33}a_{11} - a'_{31}a_{13})r_y + (a'_{31}a_{12} - a'_{32}a_{11})r_z]}{h_\eta r^3} \quad (2.32)$$

$$a_\xi = -\frac{[(a'_{32}a_{23} - a'_{33}a_{22})r_x + (a'_{33}a_{21} - a'_{31}a_{23})r_y + (a'_{31}a_{22} - a'_{32}a_{21})r_z]}{h_\xi r^3} \quad (2.33)$$

2.4 Node Equation

Eventually, we develop the node equation from G_i .

Firstly, after substituting $T^{(e)} = \sum_{j=1}^3 N_{je} T_{je} = N_{1e} T_{1e} + N_{2e} T_{2e} + N_{3e} T_{3e}$ for the first term on the right,

$$\begin{aligned}
& \iint_{S^{(e)}} \left[\frac{1}{h_\xi^2} \frac{\partial N_i}{\partial \xi} \left(\frac{\partial T_\zeta}{\partial \xi} \right) + \frac{1}{h_\eta^2} \frac{\partial N_i}{\partial \eta} \left(\frac{\partial T_\zeta}{\partial \eta} \right) \right] h_\xi h_\eta d\xi d\eta \\
&= \iint_{S^{(e)}} \sum_{j=1}^3 \left(\frac{1}{h_\xi^2} \frac{\partial N_{ie}}{\partial \xi} \frac{\partial N_{je}}{\partial \xi} + \frac{1}{h_\eta^2} \frac{\partial N_{ie}}{\partial \eta} \frac{\partial N_{je}}{\partial \eta} \right) T_{je} h_\xi h_\eta d\xi d\eta
\end{aligned} \tag{2.34}$$

where (T_{1e}, T_{2e}, T_{3e}) are the value of three nodes of each element and (N_{1e}, N_{2e}, N_{3e}) are defined as below.

$$N_{ie} = \frac{1}{2\Delta^{(e)}} (b_{ie} + c_{ie}\xi + d_{ie}\eta) \tag{2.35}$$

$$\frac{\partial N_{ie}}{\partial \xi} = \frac{c_{ie}}{2\Delta^{(e)}} \quad \frac{\partial N_{ie}}{\partial \eta} = \frac{d_{ie}}{2\Delta^{(e)}} \tag{2.36}$$

where $\Delta^{(e)}$ is the element area in the orthogonal curvilinear coordinate system and

$$b_{ie} = \xi_{je}\eta_{ke} - \xi_{ke}\eta_{je} \tag{2.37}$$

$$c_{ie} = \eta_{je} - \eta_{ke} \tag{2.38}$$

$$d_{ie} = \xi_{ke} - \xi_{je} \tag{2.39}$$

In consideration of $\iint_{S^{(e)}} d\xi d\eta = \Delta^{(e)}$, the first term can be developed as below.

$$\begin{aligned}
& \iint_{S^{(e)}} \left[\frac{1}{h_\xi^2} \frac{\partial N_i}{\partial \xi} \left(\frac{\partial T_\zeta}{\partial \xi} \right) + \frac{1}{h_\eta^2} \frac{\partial N_i}{\partial \eta} \left(\frac{\partial T_\zeta}{\partial \eta} \right) \right] h_\xi h_\eta d\xi d\eta \\
&= \iint_{S^{(e)}} \sum_{j=1}^3 \left[\frac{1}{h_\xi^2} \frac{c_{ie}}{2\Delta^{(e)}} \frac{c_{je}}{2\Delta^{(e)}} + \frac{1}{h_\eta^2} \frac{d_{ie}}{2\Delta^{(e)}} \frac{d_{je}}{2\Delta^{(e)}} \right] T_{je} h_\xi h_\eta d\xi d\eta \\
&= \sum_{j=1}^3 \frac{1}{4\Delta^{(e)}} \left(\frac{h_\eta}{h_\xi} c_{ie} c_{je} + \frac{h_\xi}{h_\eta} d_{ie} d_{je} \right) T_{je}
\end{aligned} \tag{2.41}$$

Secondly, as to second term on the right, Gauss–Legendre quadrature is utilized for numerical integration.

$$\iint_{S^{(e)}} N_i \left[\frac{\mu}{4\pi} \frac{\partial}{\partial t} \iint_{S_v'} \left[a_\eta \left(\frac{\partial T_\zeta}{\partial \eta} \right) + a_\xi \left(\frac{\partial T_\zeta}{\partial \xi} \right) \right] h'_\xi h'_\eta d\xi d\eta \right] h_\xi h_\eta d\xi d\eta \tag{2.42}$$

The following part can be developed as below

$$\begin{aligned}
& \iint_{S_v'} \left[a_\eta \left(\frac{\partial T_\zeta}{\partial \eta} \right) + a_\xi \left(\frac{\partial T_\zeta}{\partial \xi} \right) \right] h'_\xi h'_\eta d\xi d\eta \\
&= \iint_{S_v'} \left[a_\eta \sum_{j=1}^3 \frac{d_{je}}{2\Delta^{(e)'}} T_{je} + a_\xi \sum_{j=1}^3 \frac{c_{je}}{2\Delta^{(e)'}} T_{je} \right] h'_\xi h'_\eta d\xi d\eta \\
&= \frac{1}{2\Delta^{(e)'}} \sum_{j=1}^3 T_{je} \iint_{S_v'} (a_\eta d_{je} + a_\xi c_{je}) h'_\xi h'_\eta d\xi d\eta
\end{aligned} \tag{2.43}$$

where $\Delta^{(e)'}$ is the element area in the orthogonal curvilinear coordinate system in the area S_v' .

Then the second term can be developed using Gauss–Legendre quadrature as below.

$$\begin{aligned}
& \iint_{S^{(e)}} N_i \left[\frac{\mu}{4\pi} \frac{\partial}{\partial t} \iint_{S_v'} \left[a_\eta \left(\frac{\partial T_\zeta}{\partial \eta} \right) + a_\xi \left(\frac{\partial T_\zeta}{\partial \xi} \right) \right] h'_\xi h'_\eta d\xi d\eta \right] h_\xi h_\eta d\xi d\eta \\
&= \frac{h_\xi h_\eta}{3} \Delta^{(e)} \left[\frac{\mu}{4\pi} \frac{\partial}{\partial t} \sum_{v=1}^L \frac{1}{2\Delta^{(e)'}} \sum_{j=1}^3 T_{je} \iint_{S_v'} (a_\eta d_{je} + a_\xi c_{je}) h'_\xi h'_\eta d\xi d\eta \right] \\
&= \frac{h_\xi h_\eta}{3} \Delta^{(e)} \frac{\partial}{\partial t} \left[\sum_{v=1}^L \frac{\mu}{8\pi\Delta^{(e)'}} \sum_{j=1}^3 T_{je} \iint_{S_v'} (a_\eta d_{je} + a_\xi c_{je}) h'_\xi h'_\eta d\xi d\eta \right] \quad (2.44)
\end{aligned}$$

Consequently, the node equation is developed as below.

$$\begin{aligned}
G_i &= \sum_{R_i} \left\{ \rho \iint_{S^{(e)}} \left[\frac{1}{h_\xi^2} \frac{\partial N_i}{\partial \xi} \left(\frac{\partial T_\zeta}{\partial \xi} \right) + \frac{1}{h_\eta^2} \frac{\partial N_i}{\partial \eta} \left(\frac{\partial T_\zeta}{\partial \eta} \right) \right] h_\xi h_\eta d\xi d\eta \right\} \\
&+ \sum_{R_i} \left\{ \iint_{S^{(e)}} N_i \left[\frac{\mu}{4\pi} \frac{\partial}{\partial t} \iint_{S_v'} \left[a_\eta \left(\frac{\partial T_\zeta}{\partial \eta} \right) + a_\xi \left(\frac{\partial T_\zeta}{\partial \xi} \right) \right] h'_\xi h'_\eta d\xi d\eta \right] h_\xi h_\eta d\xi d\eta \right\} \\
&+ \sum_{R_i} \left(\iint_{S^{(e)}} N_i \frac{\partial \mathbf{B}_0 \cdot \boldsymbol{\zeta}}{\partial t} h_\xi h_\eta d\xi d\eta \right) \\
&= \sum_{R_i} \left[\sum_{j=1}^3 \frac{\rho}{4\Delta^{(e)}} \left(\frac{h_\eta}{h_\xi} c_{ie} c_{je} + \frac{h_\xi}{h_\eta} d_{ie} d_{je} \right) T_{je} \right] \\
&+ \sum_{R_i} \left\{ \frac{h_\xi h_\eta}{3} \Delta^{(e)} \frac{\partial}{\partial t} \left[\sum_{v=1}^L \frac{\mu h'_\xi h'_\eta}{8\pi\Delta^{(e)'}} \sum_{j=1}^3 (a_\eta d_{je} + a_\xi c_{je}) T_{je} \right] \right\} \\
&+ \sum_{R_i} \left(\frac{h_\xi h_\eta}{3} \Delta^{(e)} \frac{\partial \mathbf{B}_0 \cdot \boldsymbol{\zeta}}{\partial t} \right) = 0 \quad (2.45)
\end{aligned}$$

where

$$a_\eta = \frac{[(a'_{32}a_{13} - a'_{33}a_{12})r_x + (a'_{33}a_{11} - a'_{31}a_{13})r_y + (a'_{31}a_{12} - a'_{32}a_{11})r_z]}{h_\eta r^3} \quad (2.46)$$

$$a_\xi = -\frac{[(a'_{32}a_{23} - a'_{33}a_{22})r_x + (a'_{33}a_{21} - a'_{31}a_{23})r_y + (a'_{31}a_{22} - a'_{32}a_{21})r_z]}{h_\xi r^3} \quad (2.47)$$

The governing equation then can be described with the coefficient matrix as below.

$$[R]\{T\} + [M]\left\{\frac{\partial T}{\partial t}\right\} + \left\{\frac{\partial B_0}{\partial t}\right\} = 0 \quad (2.48)$$

Furthermore, backward difference approximation is utilized for the time derivative term and the equation to be solved is as below.

$$\left[[R]_{k-1} + \frac{1}{\Delta t} [M] \right] \{T\}_k = \frac{1}{\Delta t} [M] \{T\}_{k-1} - \left\{ \frac{\partial B_0}{\partial t} \right\} \quad (2.49)$$

where (k) is the current time step to be calculated and $(k-1)$ is the previous time step.

2.5 HTS Electromagnetic Characteristics Modelling

N-value model is used here to describe the E - J relationship of the superconductor as (2.50). Then, the resistivity can be derived as (2.51).

$$E = E_0 \left(\frac{J}{J_c} \right)^n \quad (2.50)$$

$$\rho_s = \frac{E_0}{J_c} \left(\frac{J}{J_c} \right)^{n-1} \quad (2.51)$$

Furthermore, the n -value is observed to decrease slowly when the current density exceeds J_c , hence, the current density dependency of n -value is also modelled as below according to the experimental results of previous research [51]. The n -value is assumed to be constant when $i \leq 1$, and to be as (2.52) when $i > 1$.

$$n = n_0 + \frac{1}{\pi} \left\{ \tan^{-1}[d(i - e)] + \frac{\pi}{2} \right\} (a \exp[-bi] + c) \quad \text{for } i > 1 \quad (2.52)$$

$$i = \frac{J}{J_c} \quad (2.53)$$

2.6 Metal Overlayer Modelling

A metal overlayer is always coated on the superconducting layer in REBCO coated conductors. It is necessary to model this overlayer because the current will flow through this layer when SN transition occurs in the superconducting layer and the resistivity rises. Because the thickness of the overlayer is as thin as the superconducting layer, the thin plate approximation is still available here. Hence, the overlayer and the superconducting layer are assumed to be in parallel and modelled as an equivalent conducting layer. The equivalent resistivity ρ is defined as below.

$$\rho = \frac{\rho_m \rho_s (t_m + t_s)}{\rho_m t_s + \rho_s t_m} \quad (2.54)$$

where ρ_s and ρ_m are the resistivity of superconducting layer and metal overlayer respectively, t_s and t_m are the thickness of superconducting layer and metal overlayer respectively. Then, the current density and resistivity in the superconducting layer can be derived as below.

$$J_s = \frac{\rho_m (t_m + t_s)}{\rho_m t_s + \rho_s t_m} J \quad (2.55)$$

$$\rho_s = \frac{E_c}{J_c} \left(\frac{J}{J_c} \frac{\rho_m(t_m + t_s)}{\rho_m t_s + \rho_s t_m} \right)^{n-1} \quad (2.56)$$

Newton-Raphson method is utilized to calculate the resistivity ρ in (2.54). Refer to reference [51] for more detail.

2.7 Electric Circuit Model & Boundary Conditions

Boundary conditions for $\{T\}$ are necessary to solve the governing equation (2.49), and can be determined with the circuit current I as (2.57) and Fig. 2.2.

$$\begin{aligned} I &= \int_S \mathbf{J} \cdot \mathbf{n} dS = \int_S (\nabla \times \mathbf{T}) \cdot \mathbf{n} dS \\ &= \oint_{\text{Boundary}} \mathbf{T} \cdot d\mathbf{s} \end{aligned} \quad (2.57)$$

The current equals to the contour integration of \mathbf{T} along the boundary of the cross-section of the overlayer and superconducting layer. For example, \mathbf{T} at the upper side and bottom side can be decided as I/h and 0, respectively, where h is the total thickness of the overlayer and superconducting layer. Then, the left and right side are assumed as free boundary where the current flow in perpendicular to the boundary.

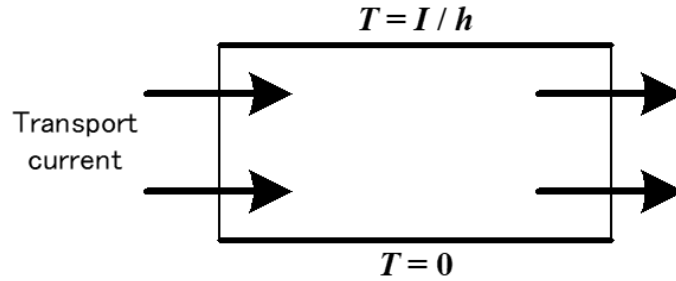


Fig. 2.2. Boundary condition for $\{T\}$.

Furthermore, the electric circuit is modelled as Fig. 2.3, and then the circuit current I can be calculated by (2.58).

$$V = R_{REBCO} I + R_c I + L_c \frac{dI}{dt} \quad (2.58)$$

where V is the source voltage, I is the circuit current, R_{REBCO} is REBCO coil's resistance, R_c is the circuit resistance, L_c is the circuit inductance.

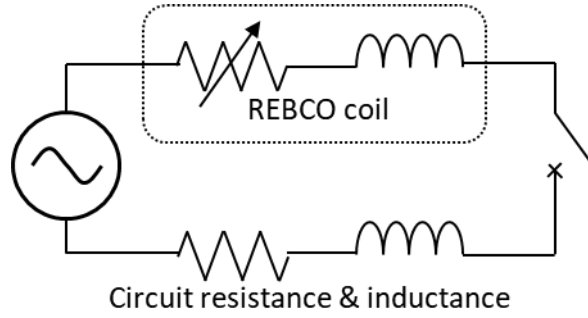


Fig. 2.3. Electric circuit model.

2.8 Analysis Flowchart & Advantages

Fig. 2.3 shows the schematic flowchart of the electromagnetic analysis. A program using Fortran language is developed for the analysis. The steps showed in red frames are the different steps from traditional 3D electromagnetic analysis using T - Ω formulation. This analysis is capable for any practical shapes of REBCO coated conductors and coils while extra processing and computation load is needed to calculate the scale factors and transformation matrix, as well as the coefficient matrix in orthogonal curvilinear coordinates. However, the overall memory usage and computational load are reduced because of less variables and smaller coefficient matrices. Furthermore, the solution convergence is also better than traditional 3D electromagnetic analysis, because the analysis is actually solving a 2D problem in the computation which has been verified to have better convergence than 3D problems [15].

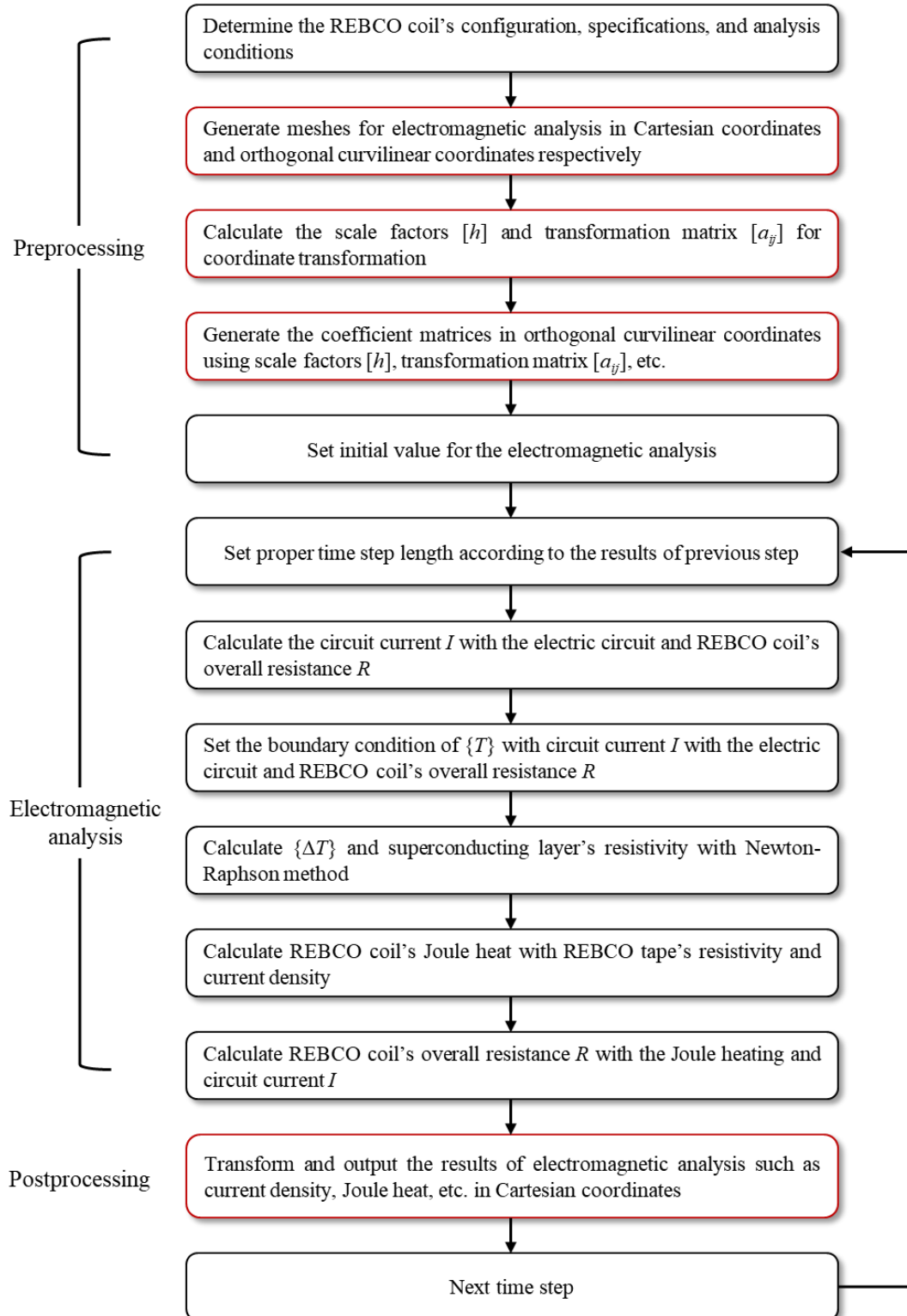


Fig. 2.2. Schematic flowchart of the electromagnetic analysis.

Chapter 3. Verifications and Case Studies of 3D

Electromagnetic Analysis

3.1 Verifications

Two verifications are conducted to verify the correctness and accuracy of the proposed three-dimensional electromagnetic analysis method. One verifies the correctness and accuracy of the 3D electromagnetic analysis with the commercial software JMAG. The other verifies correctness and accuracy of the proposed method in analyzing the electromagnetic characteristics of superconductors with the theoretical formula suggested in reference[55]–[57]. The analysis result of current density distribution is compared for verification.

3.1.1 Verification with JMAG

A one-turn copper coil, which is actually a ring, is modeled in the developed electromagnetic analyzed program and JMAG. The transient current density distribution under the AC circuit current is studied. A slight bias of the current density distribution in the tape widthwise direction is expected because of the changing magnetic field that generated by the current. The model of this coil and the electric circuit are shown in Fig. 3.1.1. The specifications of copper coil and circuit are summarized in Table 3.1.1.

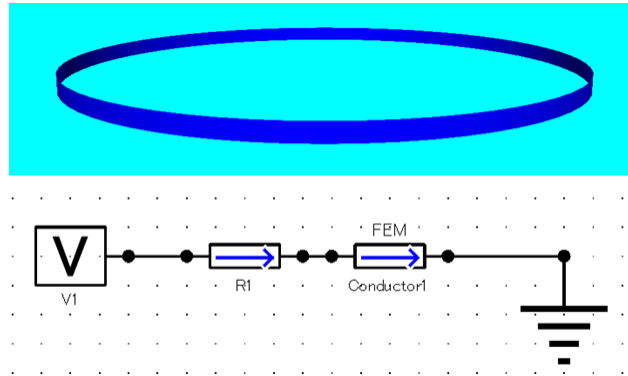
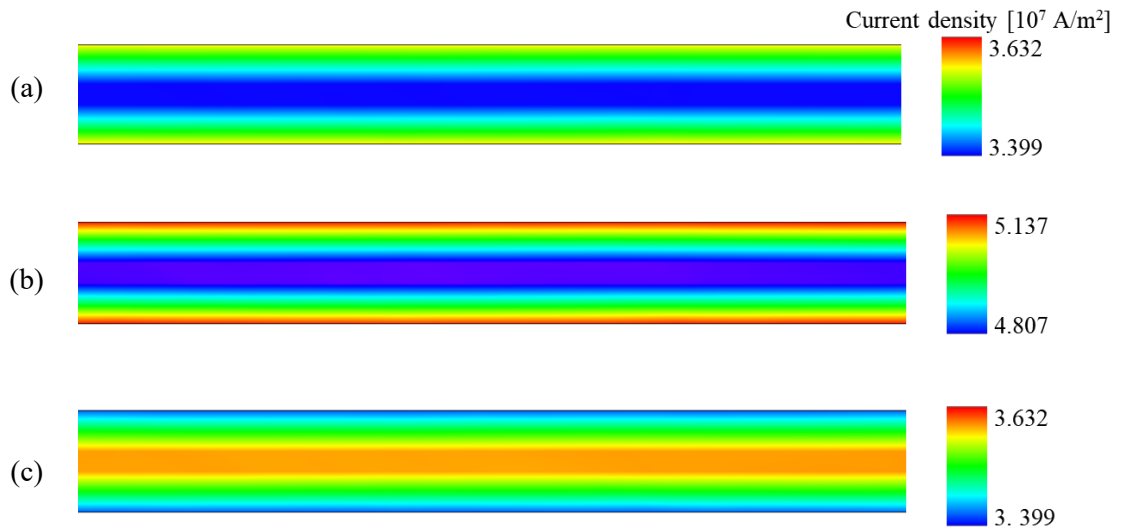


Fig. 3.1.1. One-turn copper coil model and schematic diagram of the electric circuit.

TABLE 3.1.1
SPECIFICATIONS OF COPPER COIL AND CIRCUIT FOR VERIFICATION.

Properties	Values
Copper coil	1 turn
Thickness of copper tape	0.1 mm
Diameter	0.318 m
Tape width	10 mm
Voltage	50 V @50 Hz
R1	1 Ω

According to the analysis results (Fig. 3.2 and 3.3), almost the same bias of current density distribution is observed in both analyses which is caused by the induced current because of the changing magnetic field generated by the current. When the current rises (e.g. at 2.5 ms), the induced current enhances the current at the edges of tape. On the other hand, the induced current would enhance the current at the middle of tape when the current decreases (e.g. at 7.5 ms). Furthermore, the detailed numbers of maximum and minimum current density are compared in Table 3.2 which shows the maximum difference is about 4.26%, and show good agreement between these two models. The reason of the difference between these two results is considered because that the thin plate approximation is utilized in the proposed method whereas it is not available in JMAG.



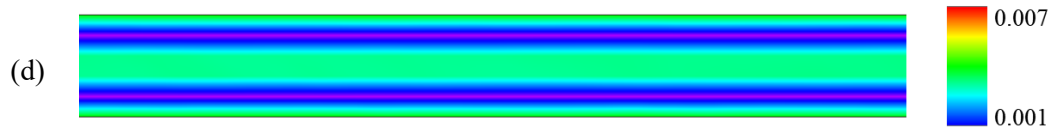
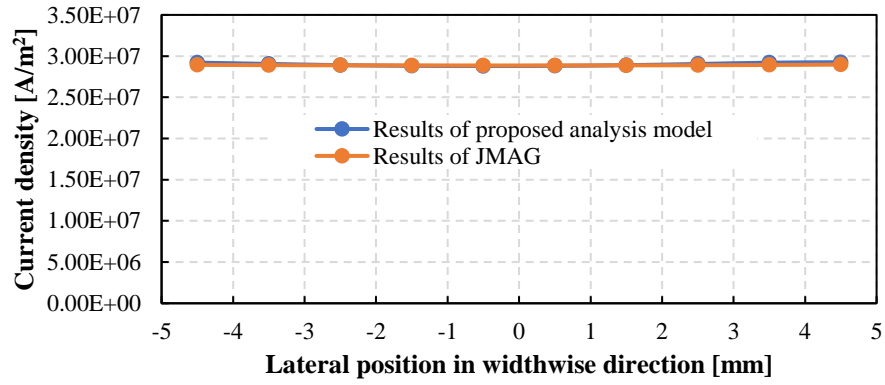
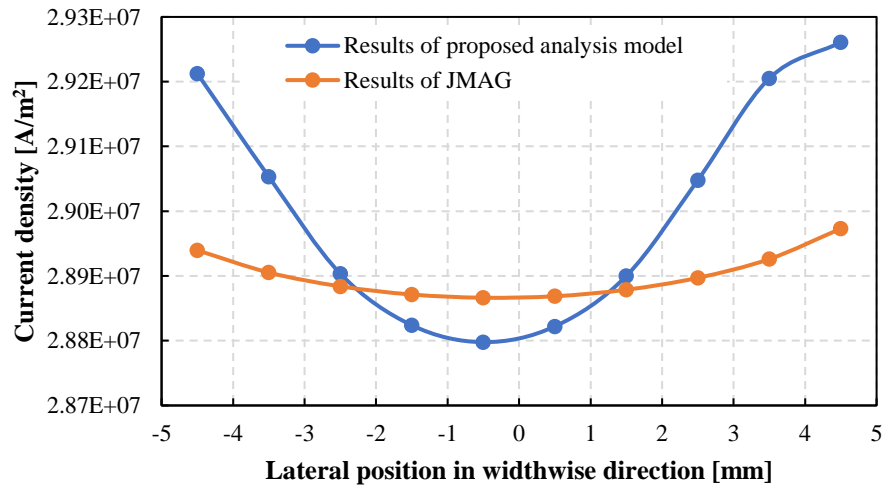


Fig. 3.1.2. Current density distribution of part of the one-turn copper coil at different phases of the sine wave alternating current: (a) $\pi/4$, (b) $\pi/2$, (c) $3\pi/4$, (d) π .



(a)



(b)

Fig. 3.1.3. Current density distribution in widthwise direction in the middle of the one-turn copper coil at the phase of $\pi/5$.

TABLE 3.1.2
CURRENT DENSITY CALCULATED IN JMAG AND THE DEVELOPED PROGRAM.

Phase	Current density from J-MAG [10^7 A/m ²]		Current density from this research [10^7 A/m ²]		Difference. in Min. value	Difference. in Max. value
	Min.	Max.	Min.	Max.		
	value	value	value	value		
$\pi/5$	2.888	2.895	2.825	3.019	2.23%	4.11%
$2\pi/5$	4.676	4.679	4.572	4.886	2.27%	4.24%
$3\pi/5$	4.676	4.678	4.572	4.886	2.27%	4.26%
$4\pi/5$	2.888	2.892	2.825	3.019	2.23%	4.21%

In addition, the number of elements and computation time are also compared. About 1.2 million 3D tetrahedron elements are generated in the JMAG analysis, which include 10 thousand elements for the conductor and the others for the air region. By contrast, only 2.5 thousand triangular elements are generated in the developed 3D electromagnetic analysis. The computation time of the JMAG analysis and the developed 3D electromagnetic analysis is around 46 minutes and 2 minutes respectively. The overall computational time of the developed 3D electromagnetic analysis is reduced, even though extra processing and computation load is needed for preprocessing and postprocessing. Although this comparison is far from definitive, it reveals the advantage of the proposed 3D electromagnetic analysis method in reducing variables, memory usage, and computational load.

3.1.2 Verification with Theoretical Formula

A long straight superconducting thin tape was modeled in the developed electromagnetic analysis program to compare with a theoretical formula suggested by Brandt [56], [57]. He realized that demagnetizing effects are crucial in most practical applications where flat superconductors are used in a perpendicular field, hence, proposed analytic formulas for superconducting thin tapes that carry currents in a perpendicular magnetic field. The superconducting thin tape is a good approximation for the superconducting layer in a superconducting coated conductor, and the theoretical analysis results are commonly used as a reference to verify FEM models' results of. A summary of the theoretical analysis is presented below.

For a tape of width $2a$ (in x -axis) and thickness d (in y -axis) (Fig. 3.1.4) and a transport current with magnitude I_0 , Brandt shows that

$$J(x) = \frac{2J_C d}{\pi} \arctan \left(\sqrt{\frac{a^2 - b^2}{b^2 - x^2}} \right) \text{ for } |x| < b$$

$$= J_C d \text{ for } b < |x| < a$$

where b is the penetration depth given by $b = a\sqrt{1 - (I_0/I_C)^2}$, the transport current $I_0 = 2J_C d\sqrt{a^2 - b^2}$, and critical current $I_C = 2aJ_C d$.

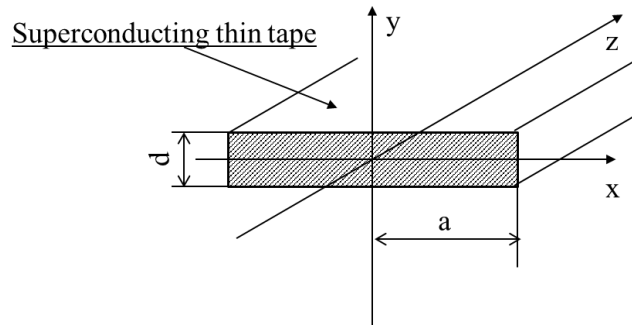


Fig. 3.1.4. Schematic diagram of a long straight superconducting thin tape.

Therefore, a straight superconducting thin tape is modelled and the current density distribution in its widthwise direction is analyzed for verification with the equation. The specifications of the tape are summarized in Table 3.1.3.

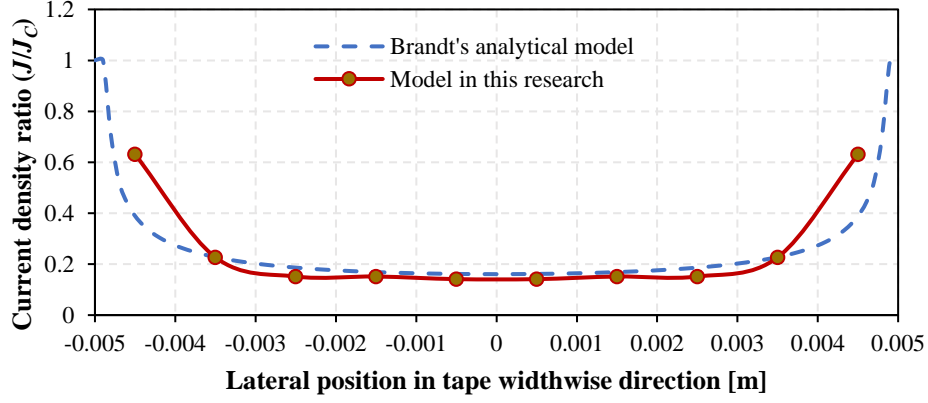
TABLE 3.1.3

SPECIFICATIONS OF STRAIGHT SUPERCONDUCTING THIN TAPE FOR VERIFICATION.

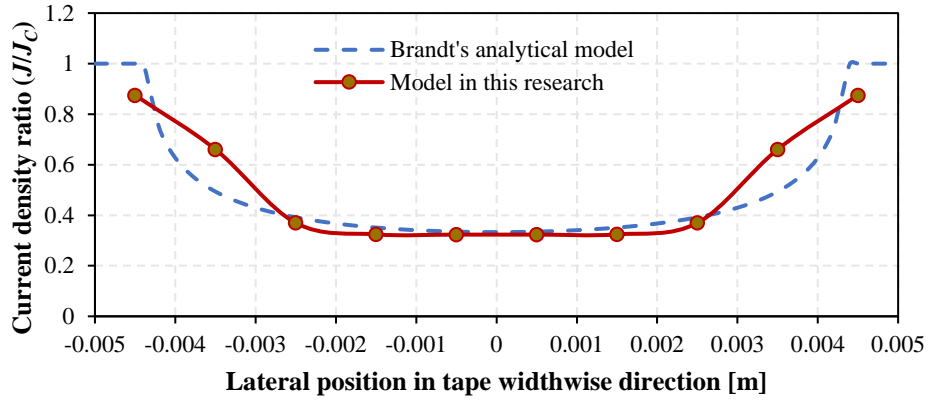
Properties	Values
Tape width	1 cm
Tape length	1 m
Superconductor layer thickness	1 μm
Critical current $I_C@77\text{ K}$	390 A
n value	30(20, 40, 50)
Operating current	$0.25I_C, 0.5I_C, 0.75I_C$

First, n-value is assumed to be 30 and the tape model is equally divided into 10 meshes in the widthwise direction. The current density distribution is shown in Fig. 3.1.5. The results of current density in the middle part of the tape show good agreement whereas the results close to the edges are quite different. The reason is considered to be the rough meshes, hence the number of meshes in the widthwise direction is increased to 24 and the width gets narrower when it is closer to the tape edge. Then, the results of the current density distribution are shown in Fig. 3.1.6. A better

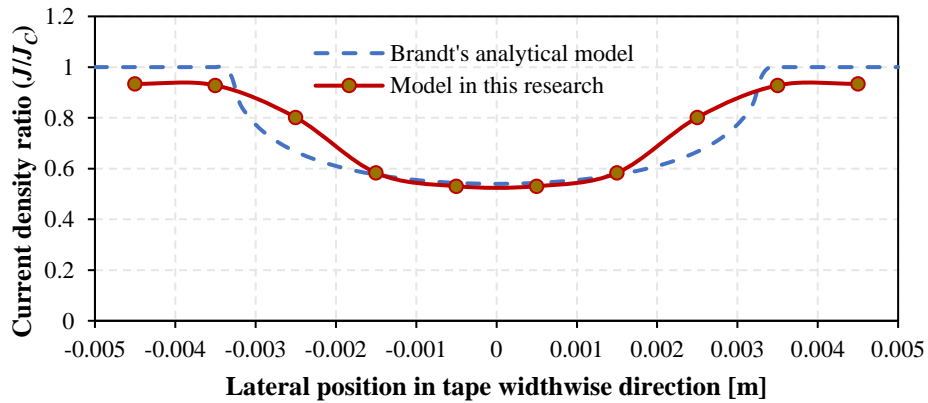
agreement is observed this time. However, the current density at the tape edge is still lower than J_C .



(a)

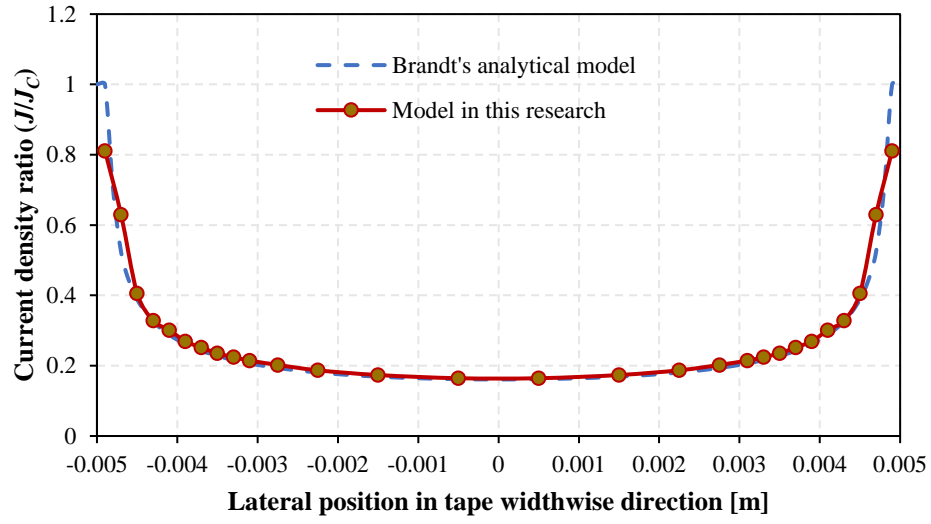


(b)

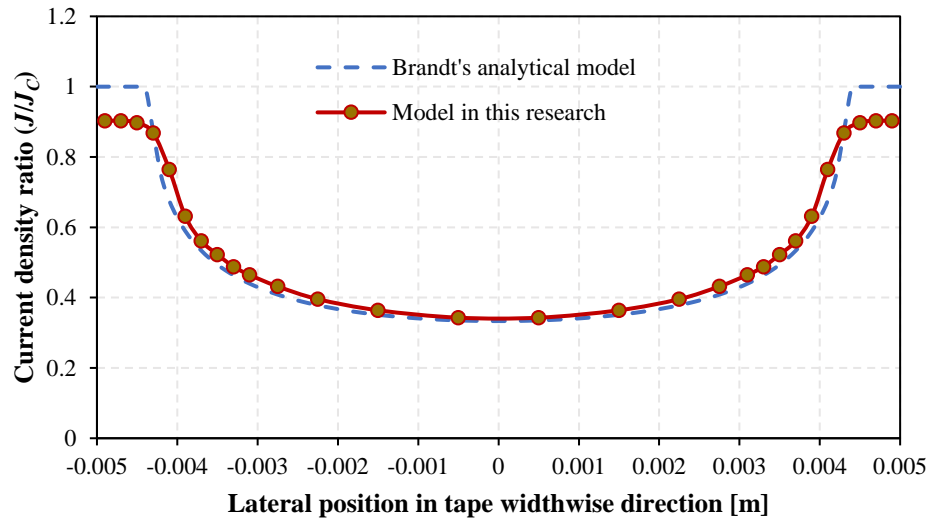


(c)

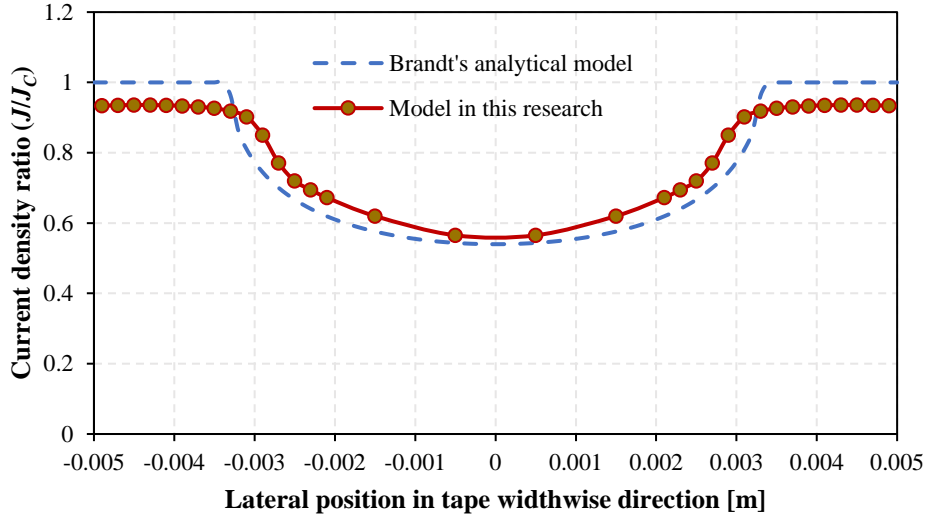
Fig. 3.1.5. Current density distribution in tape widthwise direction from Brandt's model and the proposed method with 10 uniform meshes under operating current: (a) $0.25I_C$, (b) $0.5I_C$, (c) $0.75I_C$.



(a)



(b)



(c)

Fig. 3. 1.6. Current density distribution in tape widthwise direction from Brandt's model and the proposed method with 24 various meshes under operating current: (a) $0.25I_C$, (b) $0.5I_C$, (c) $0.75I_C$.

To study the reason of the difference between the two results, various n -values are assumed and the results are summarized in Fig. 3.1.7. The higher n -value, the higher current density at tape edges. The reason is that higher n -value makes the n -value model of the superconducting characteristic closer to the ideal (or simplified) model that used in Brandt's equations. Brandt's equations have a better approximation in the cases of constant current which is lower than I_C . However, it is incapable of simulating transient behaviors especially with current over I_C . On the other hand, the n -value model has been verified to have good practicability and accuracy in transient analysis.

Therefore, the correctness and accuracy of the proposed electromagnetic analysis method in simulating superconductors are verified, although the current density at the tape edge is still lower than J_C which is mainly due to the different modelling for superconducting characteristics instead of the electromagnetic analysis method itself.

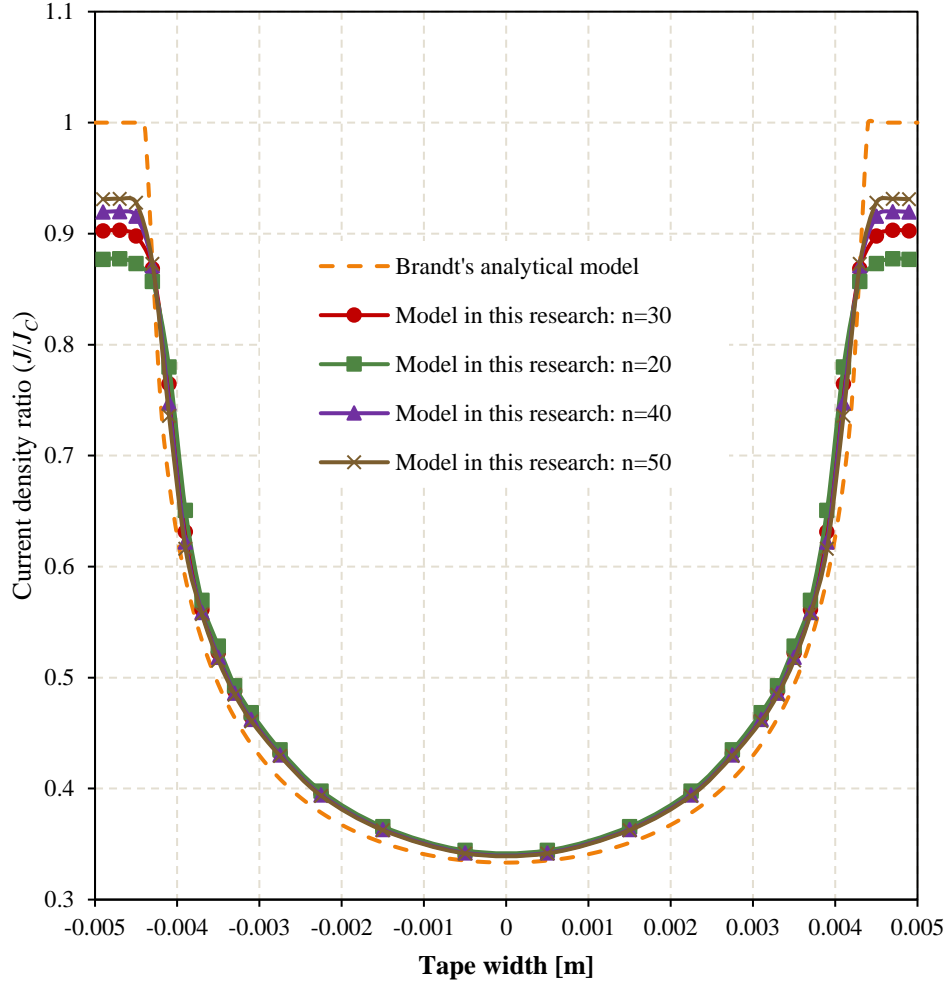


Fig. 3.1.6. Current density distribution in tape widthwise direction from Brandt's model and the proposed method with various n -value setting: 20, 30, 40, and 50.

3.2 Case Study: Solenoid REBCO Coil for Magnet Application

3.2.1 Analysis Conditions

Magnet use is an important application for the superconductors to sustain high circuit current under high magnetic field. Recently, REBCO coils has shown its high potential in such application for very high magnetic field generation and large temperature margins. High magnetic field as well as high stability and homogeneity of the field is required for designing a proper magnet coil. However, the magnetization phenomenon in the REBCO-coated conductors is one of the major problems that hinders the practical use because of its negative influence on the magnetic field quality. In this case study, we have modelled a solenoid REBCO coil for magnet application and assumed some different patterns of excitation to study the magnet field stability and homogeneity

with our proposed 3D electromagnetic analysis method. Detailed results of magnetic field, screening current induced field, and current density distribution are studied here.

The specifications of the solenoid REBCO coil is summarized in Table 3.2.1 and the schematic layout is shown in Fig. 3.2.1. Three types of excitation are assumed here: normal excitation, overshoot method[58], [59], and demagnetization method[60]. Fig. 3.2.2(a) is the normal excitation in which the circuit current is increased to the operating current 30 A in a specific speed then keeps constant. In this analysis, we assumed 4 patterns of the current changing speed from 0.05 A/s to 1.0 A/s to study the influence of the changing speed on the field stability. Fig. 3.2.2(b) is the overshoot method in which the circuit current is firstly increased to an overshooting value 110% of operating current and then decreased to the operating current. Fig. 3.2.2(c) is the demagnetization method in which demagnetization is conducted after the first excitation, then the circuit current is increased to an overshooting value, and finally decreased to the operating current. Fig. 3.2.2(d) and (e) are two variants of the demagnetization method in which the demagnetization times and level are varied to study their influence on the field stability. In addition, the current changing speed in overshoot method and demagnetization method is set as 0.1 A/s.

The screening current induced field is estimated according to the following procedure[58]. Firstly, a coil constant C_c [T/A], that defined by the coil current and magnetic field, can be calculated by measuring the magnetic field without any screening current. Here, it can be realized by applying a small enough current (1 A) to the REBCO coil in the normal state. In this case, the current flows uniformly in the copper layer. Then, we can calculate the magnetic field B_c by (1) that generated by the operating current I_c but without the influence of screening current. Finally, the screening field B_s can be calculated by (2). Moreover, the screening current density also can be calculated in the same way.

$$B_c = C_c \times I_c \quad (1)$$

$$B_s = B_0 - B_c \quad (2)$$

where B_0 is the actually measured magnetic field that got from the analysis results and generated by the operating current including the screening current.

TABLE 3.2.1

SPECIFICATIONS OF SOLENOID REBCO COIL FOR MAGNETIC APPLICATION

Properties	Values
REBCO coil	SuperPower Inc. SCS4050
Turns of coil	5
Coil diameter	10 cm
Coil pitch	1.5 cm
Cooling method	Immersion cooling in liquid nitrogen
Cooling temperature	77.3 K
Critical current at 77.3 K, self-field	156 A
Ag over-layer thickness	2 μm
Copper stabilizer thickness	20 μm
Coated conductor width	4 mm
Operating current	30 A

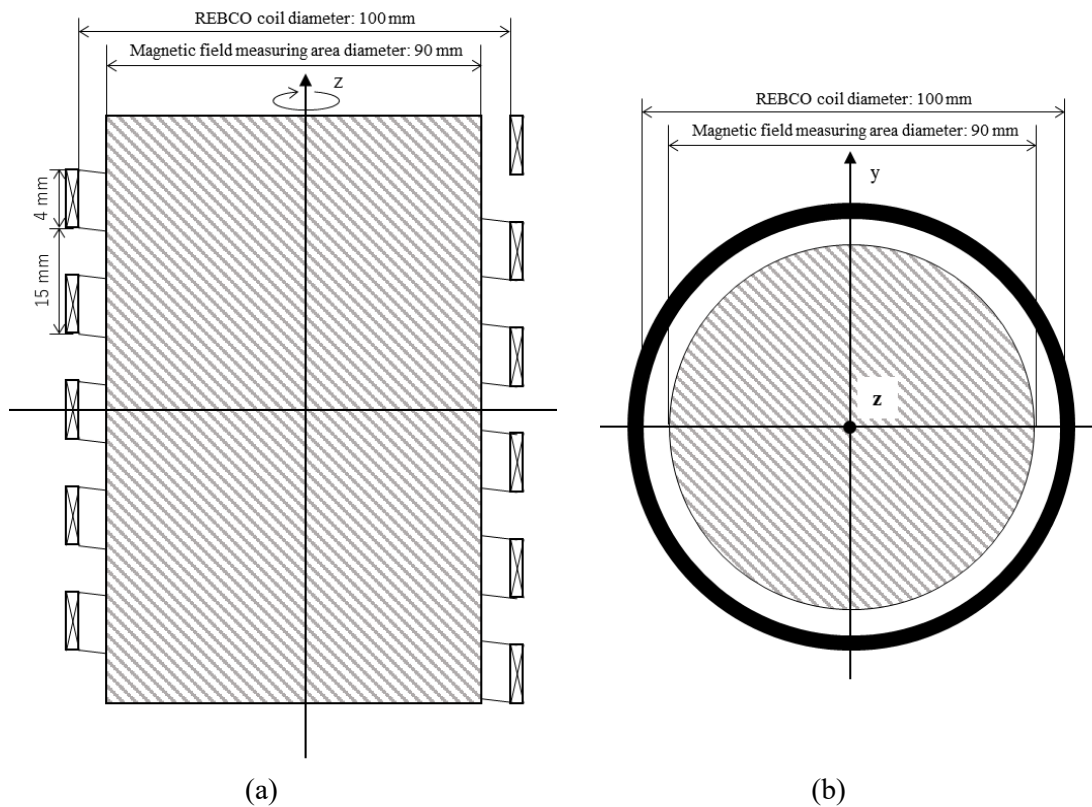


Fig. 3.2.1. Schematic layout of the solenoid REBCO coil with magnetic field measuring area:
 (a) Cross-section and (b) top view.

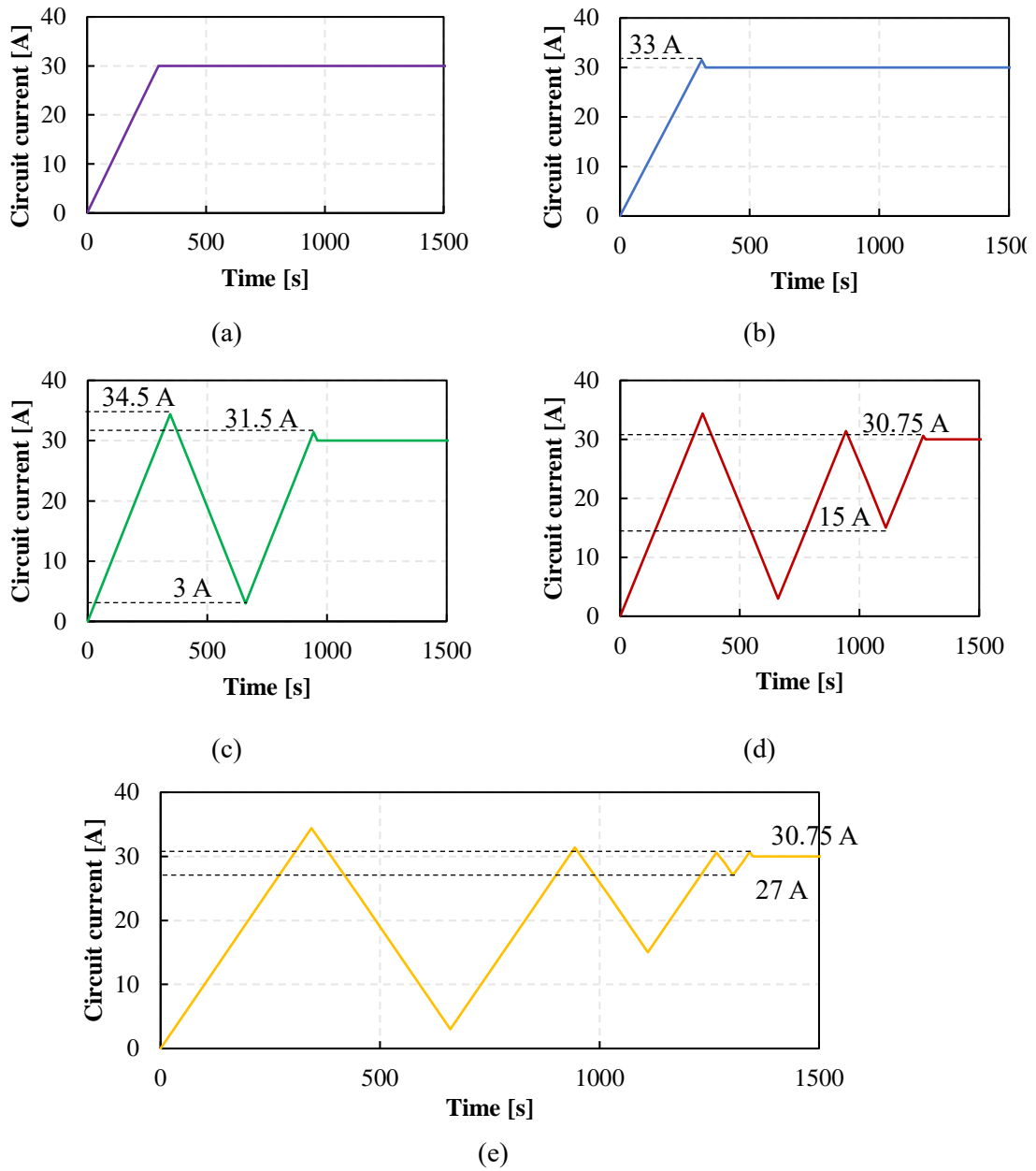
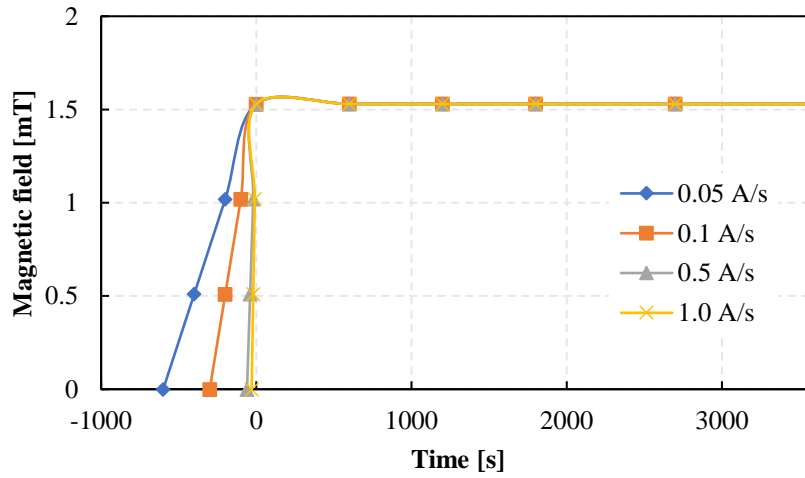


Fig. 3.2.2. Schematic illustration of the excitation current patterns. (a) Normal excitation; (b) Overshoot excitation method; (c) Demagnetization excitation method pattern I; (d) Demagnetization excitation method pattern II; (e) Demagnetization excitation method pattern III.

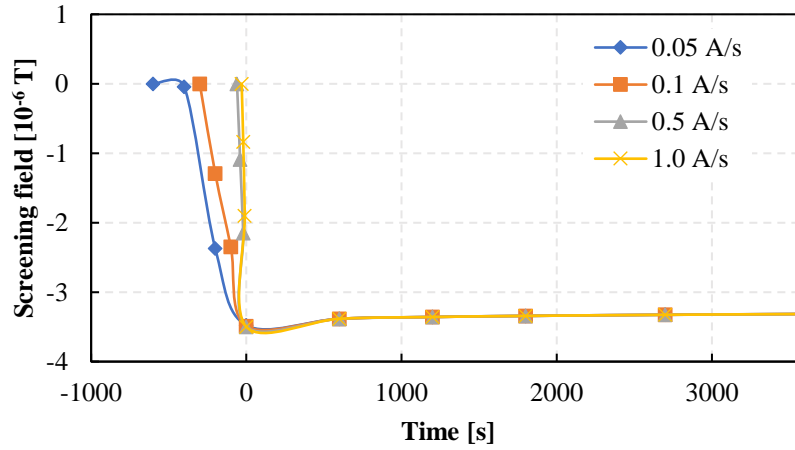
3.2.2 Influence of Current Changing Speed on Field Stability

The z-direction component of center magnetic field (located in $z = 0$, $r = 0$) and screening current induced field that excited by normal excitation with different speed is shown in Fig. 3.2.3. The temporal stability numbers, that defined as the change from 30 minutes after the excitation

to 60 minutes after the excitation, are also summarized in Table 3.2.2. The screening current induced field increases together with the excitation and keeps nearly constant after the excitation. The results show that lower current changing speed would lead to a relatively better field stability, but it has little influence in the cases that the changing speed is higher than 0.5 A/s. In consideration of the field stability and the efficiency of excitation, improvement should be conducted in the excitation method instead of simply slowing down the current changing speed. In the following analysis, the current changing speed is assumed to be 0.1 A/s.



(a)



(b)

Fig. 3.2.3. Z-direction component of (a) magnetic field and (b) screening current induced field in the center of the coil ($z = 0$, $r = 0$) that excited by normal excitation with different current changing speed 0.05 A/s, 0.1 A/s, 0.5 A/s, and 1.0 A/s. Excitation ends at time = 0 s.

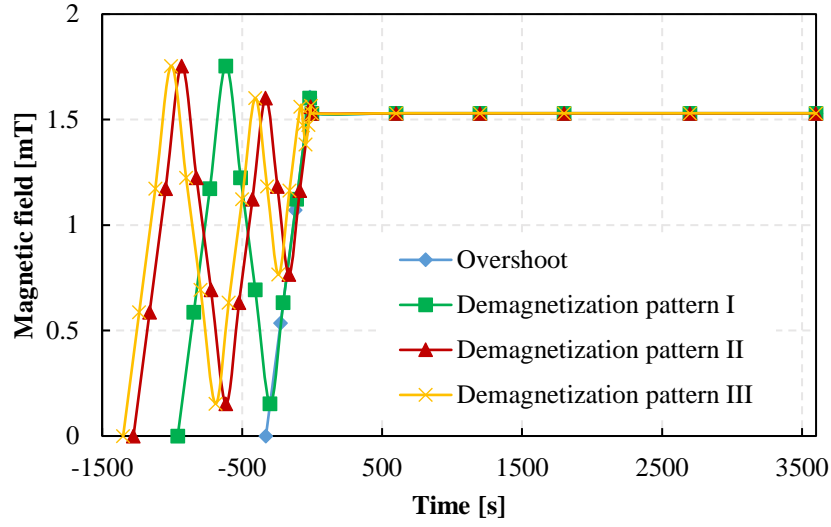
TABLE 3.2.2
TEMPORAL STABILITY OF THE CENTER MAGNETIC FIELD FOR EACH CURRENT CHANGING
SPEED

Currently changing speed [A/s]	0.05	0.1	0.5	1.0
Centre magnetic field change [ppm/h] (z-direction component)	35.76	35.85	35.92	35.93

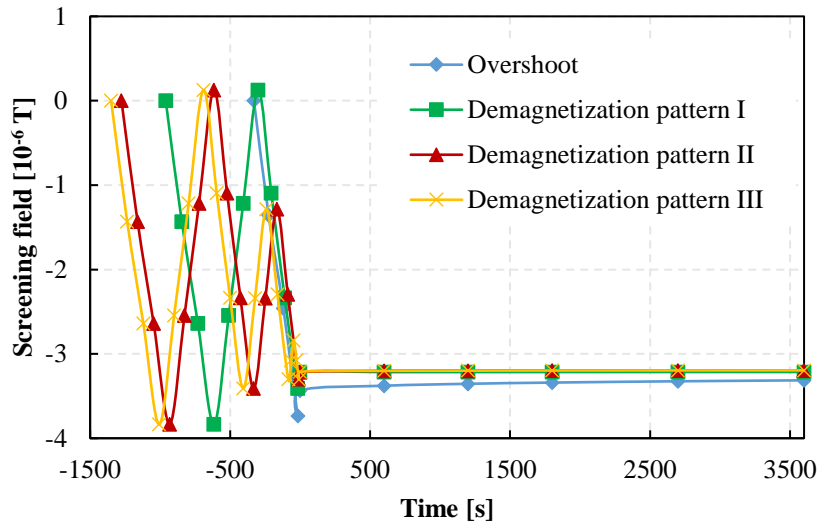
3.2.3 Influence of Excitation Pattern on Field Stability

The z-direction component of center magnetic field and screening current induced field that excited by overshoot method and demagnetization method are shown in Fig. 3.2.4. The temporal stability numbers, that defined as the change from 30 minutes after the excitation to 60 minutes after the excitation, are also summarized in Table 3.2.3. In comparison with the normal excitation, the overshoot method shows its advantage in improving the field stability. Above them, the demagnetization method improves the field stability to another level. The temporal stability numbers are lowered to one tenth even one thirtieth in the case of pattern I. The screening current induced field changes together with the excitation process and keeps nearly constant after excitation. The screening current induced field in the case of demagnetization method results in about 96% of that in the case of overshoot method.

The results of three patterns of demagnetization method show that more times of demagnetization may not necessarily improve the field stability. The screening current induced field is approximately 0.5% lower, but the temporal stability numbers almost double in the case of pattern II and III in comparison with pattern I. In this analysis, the simplest pattern of demagnetization shows the best performance, moreover, further research can be conducted on the demagnetization method for optimization.



(a)



(b)

Fig. 3.2.4. Z-direction component of (a) magnetic field and (b) screening current induced field in the center of the coil ($z = 0$, $r = 0$) that excited by overshoot method and three patterns of demagnetization method. Excitation ends at time = 0 s.

TABLE 3.2.3

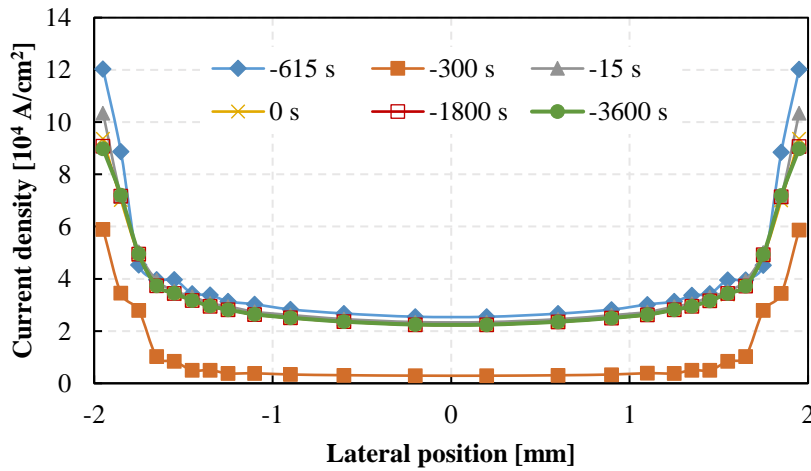
TEMPORAL STABILITY OF THE CENTER MAGNETIC FIELD FOR EACH EXCITATION PATTERN

Excitation pattern	Overshoot	Demagnetiza tion pattern I	Demagnetiza tion pattern II	Demagnetiza tion pattern III
Centre magnetic field change (z-direction component) [ppm/h]	34.52	1.05	2.04	1.95

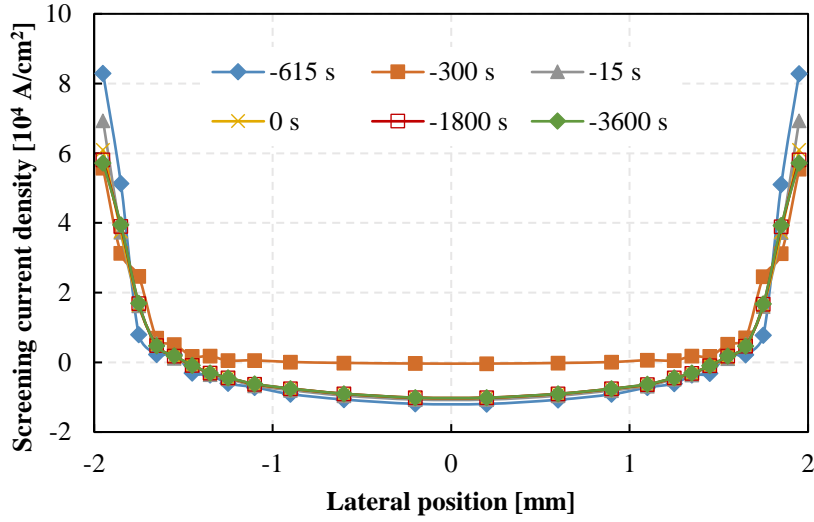
3.2.4 Detailed Electromagnetic Analysis of Demagnetization Excitation Method

Here, we focus on the detailed results from the 3D electromagnetic analysis. The case of demagnetization excitation method pattern I is chosen because of its outstanding performance.

Firstly, the change of lateral current density distribution in the tape widthwise direction is shown in Fig. 3.2.5. The measurements position is in the middle of the REBCO coil to reduce the influence of the coil ends on the current density distribution. The current concentrates to the edges of the REBCO tape because of the screening current as well as low operating current which is much lower than the critical current. The demagnetization is verified effective in reducing the screening current density which is reduced up to near 27% after the demagnetization at the edge of the REBCO tape. The screening current density at the edge of the REBCO tape is firstly $8.3 \times 10^4 \text{ A/cm}^2$ at the end of the first excitation at -615 s, then after decreasing and increasing the coil current it becomes $6.9 \times 10^4 \text{ A/cm}^2$ at -15 s, and finally it becomes even lower to $6.1 \times 10^4 \text{ A/cm}^2$ after the demagnetization excitation at 0 s. Lower screening current results in a better stability.



(a)



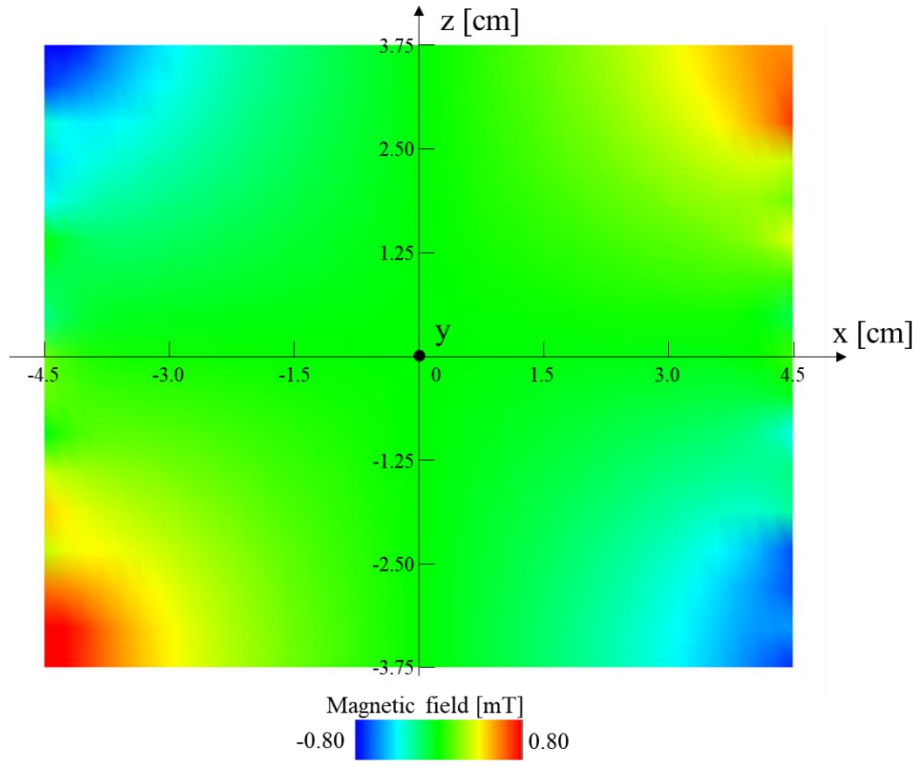
(b)

Fig. 3.2.5. (a) Lateral current density distribution and (b) screening current density distribution in the middle of the REBCO coil during and after the excitation with demagnetization method pattern I.

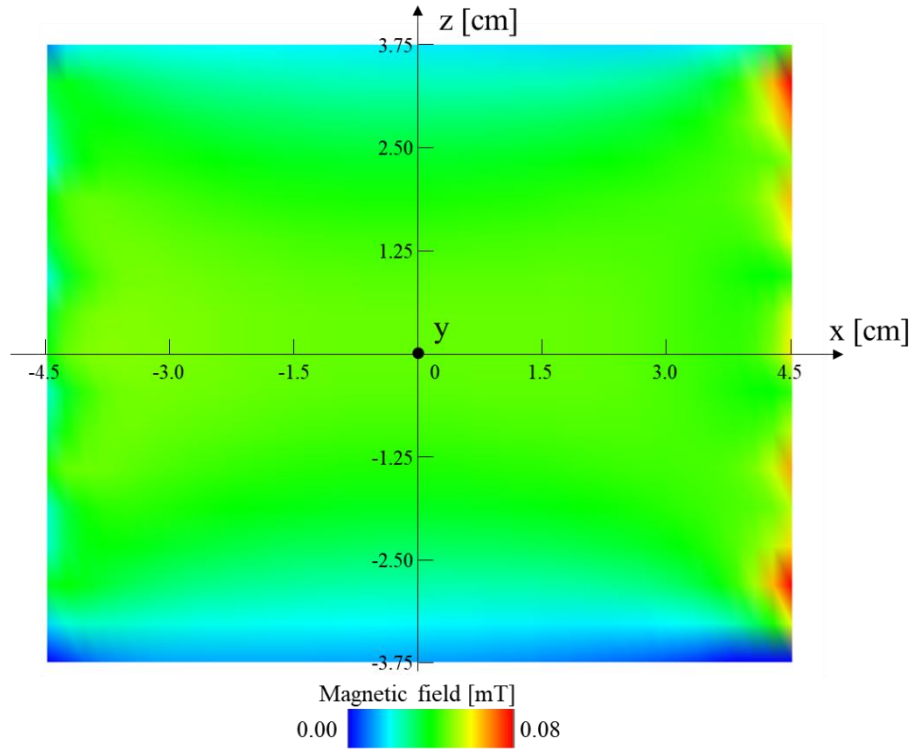
The x-direction, y-direction, and z-direction components of magnetic field in the cross-section area inside the REBCO coil 60 minutes after the excitation with demagnetization method pattern I are shown in Fig. 3.2.6. The cross-section is in the central axis plane which is the xz plane at $y = 0$. The x-direction and y-direction components, which especially appear at the corners and edges that close to the coil and coil ends, are both much smaller than the z-direction component. The z-direction component is the main parameter in the design of a magnet and it shows the best homogeneity in the center of the coil. Although the z-direction close to the REBCO tape is higher than that in the center, the inhomogeneity of x-direction and y-direction components become a problem. Hence, the center space is commonly utilized for magnet use because of its good homogeneity.

To study the homogeneity, the z-direction component of the magnetic field is normalized by B_C/B_{center} in the radial position, where B_C is the local magnetic field, is B_{center} the center magnetic field at $z = 0, r = 0$). The results are shown in Fig. 3.2.7. When $z = 0$ cm, the change of z-direction component is under 1% within a radius of 9 mm and under 5% within a radius of 20 mm. When z is higher or lower, the z-direction component becomes lower: the change is under 1% within a height of 10 mm and under 5% within a height of 16 mm. Furthermore, the x-direction, y-direction, and z-direction components of the magnetic field in the radial position inside the REBCO coil at $z = 0$ cm, $z = -0.94$ cm, and $z = -1.41$ cm are shown in Fig. 3.2.8 for reference. The x-direction and y-direction components are much smaller than the z-direction component (less than 1/30) at

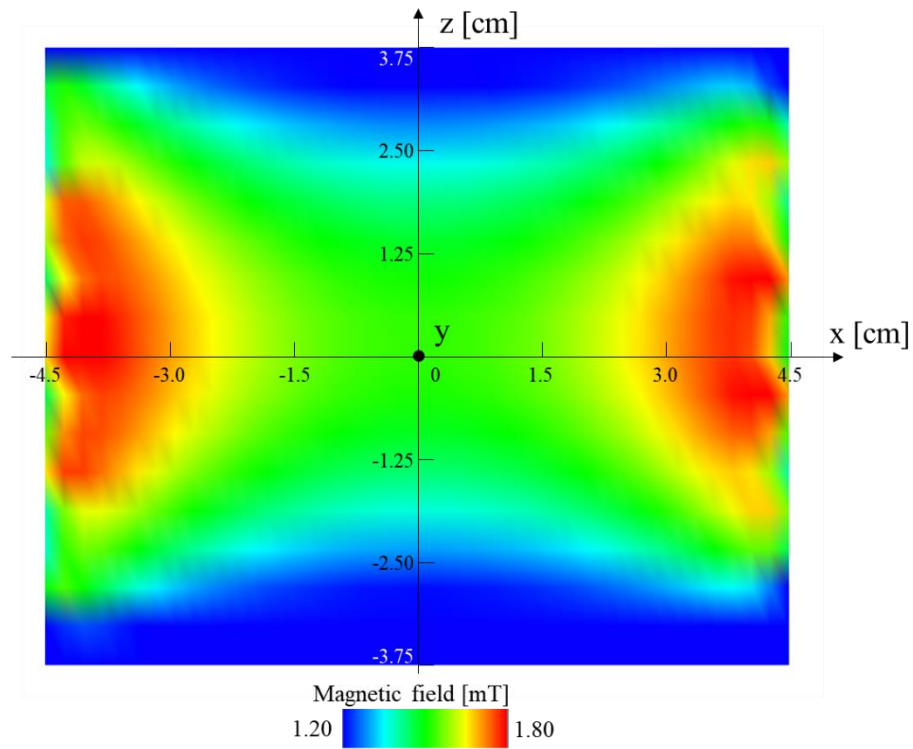
$z = 0$ cm. When z is higher or lower, the z -direction component becomes smaller while the x -direction and y -direction components become bigger, which declines the homogeneity level.



(a)



(b)



(c)

Fig. 3.2.6. (a) X-direction component, (b) y-direction component, and (c) z-direction component of the magnetic field in the cross-section area inside the REBCO coil at $y = 0$ 60

minutes after the excitation with demagnetization method pattern I.

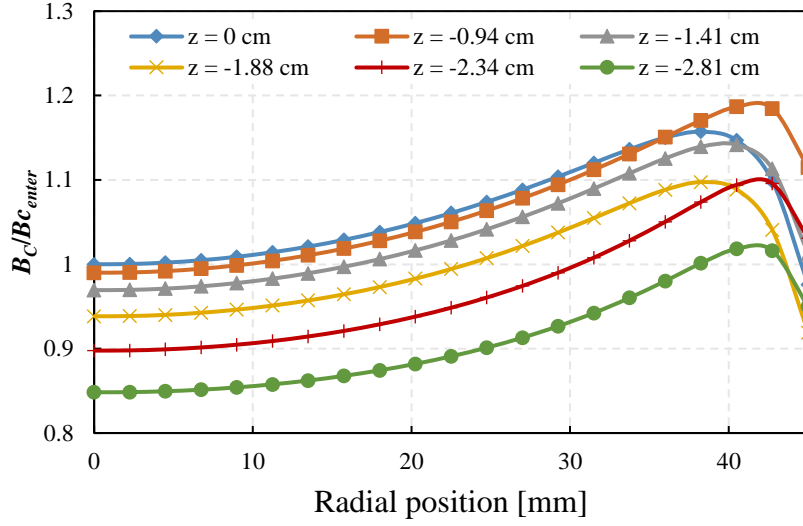
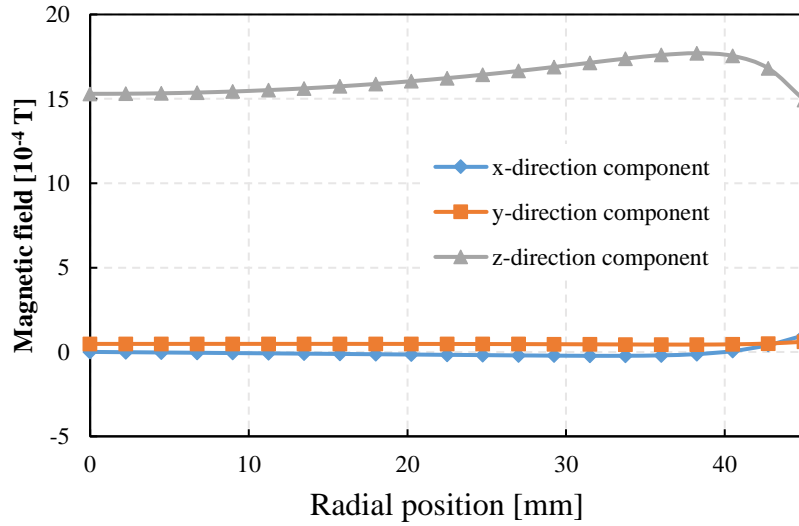
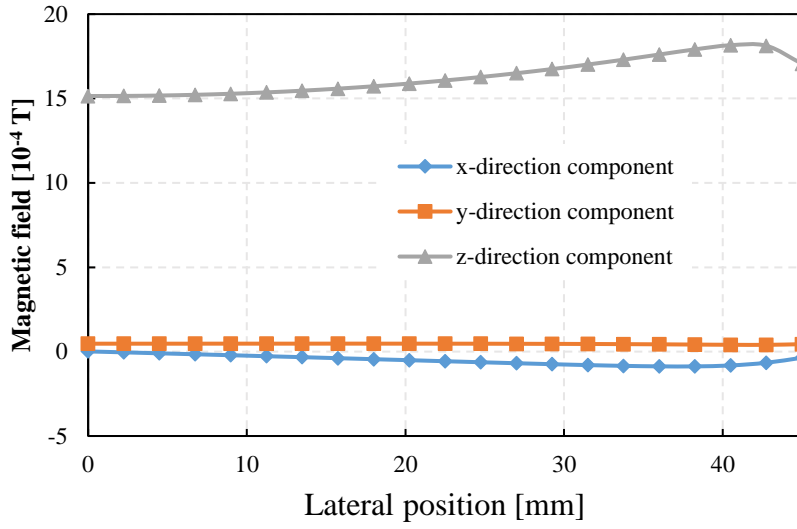


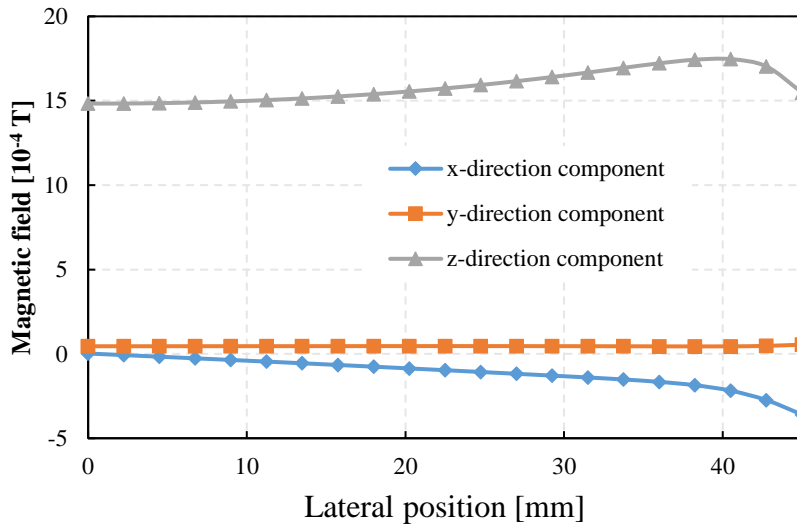
Fig. 3.2.7. Normalized z-direction component of magnetic field (B_C/B_{center} , where B_C is the local magnetic field, is B_{center} the center magnetic field at $z = 0$, $r = 0$) in the radial position inside the REBCO coil 60 minutes after the excitation with demagnetization method pattern I at different z .



(a)



(b)

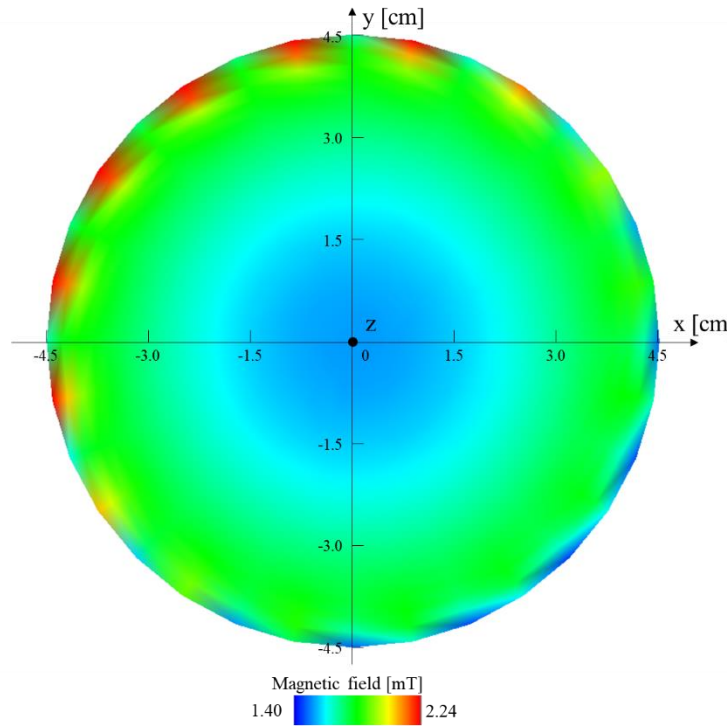


(c)

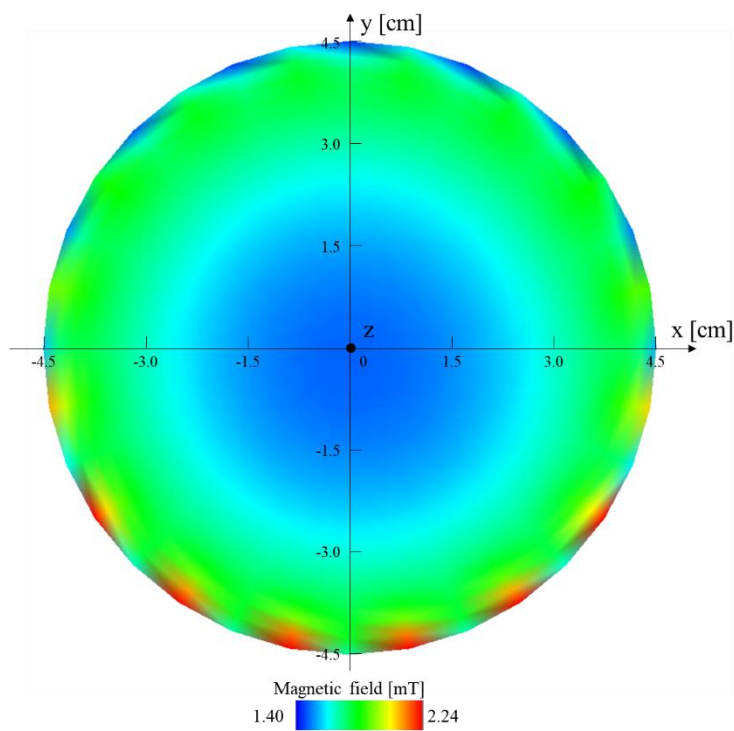
Fig. 3.2.8. X-direction, y-direction, and z-direction components of the magnetic field in the radial position inside the REBCO coil 60 minutes after the excitation with demagnetization method pattern I at (a) $z = 0$ cm, (b) $z = -0.94$ cm, and (c) $z = -1.41$ cm.

Some further information about the magnetic field distribution is indicated in Fig. 3.2.9, 3.2.10, and 3.2.11. Fig. 3.2.9 shows the z-direction component of the magnetic field in the cross-section area inside the REBCO coil 60 minutes after the excitation with demagnetization method pattern I at $z = 0$ cm, -0.94 cm, -1.41 cm, and -1.875 cm. We can find the influence of the REBCO tape on the magnetic field close to the tape. The z-direction component in the central area becomes smaller when z is higher and lower than 0. Moreover, the x-direction and y-direction components

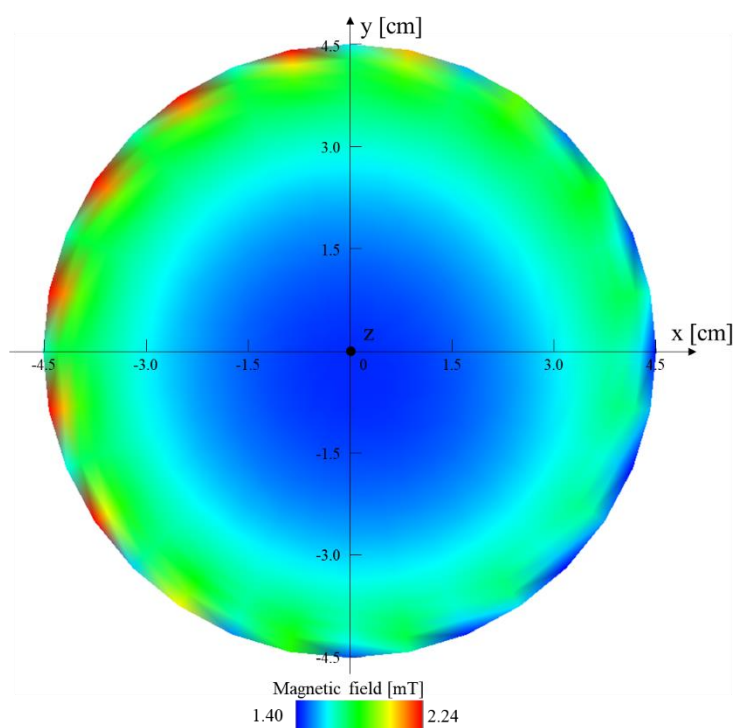
distribution are shown in Fig. 3.2.10 and 11. They indicate that the x-direction and y-direction components become bigger when z is higher and lower than 0. Especially, the x-direction component changes more significantly in x-direction, while the y-direction component changes more significantly in y-direction. It explains why the y-direction component is smaller than the x-direction component in Fig. 3.2.8 because the results shown in Fig. 3.2.8 are based on the xz plane in which $y = 0$. Although the homogeneity of the assumed solenoid coil needs to be improved when compared to the actual magnet coils which are carefully designed, the analysis results have indicated the detailed magnetic field distribution and the relatively homogeneous space within which the change of magnetic field is under 1% or 5%. The results also show the capability of the 3D electromagnetic analysis method in analysing detailed electromagnetic behaviors for coil design.



(a)



(b)



(c)

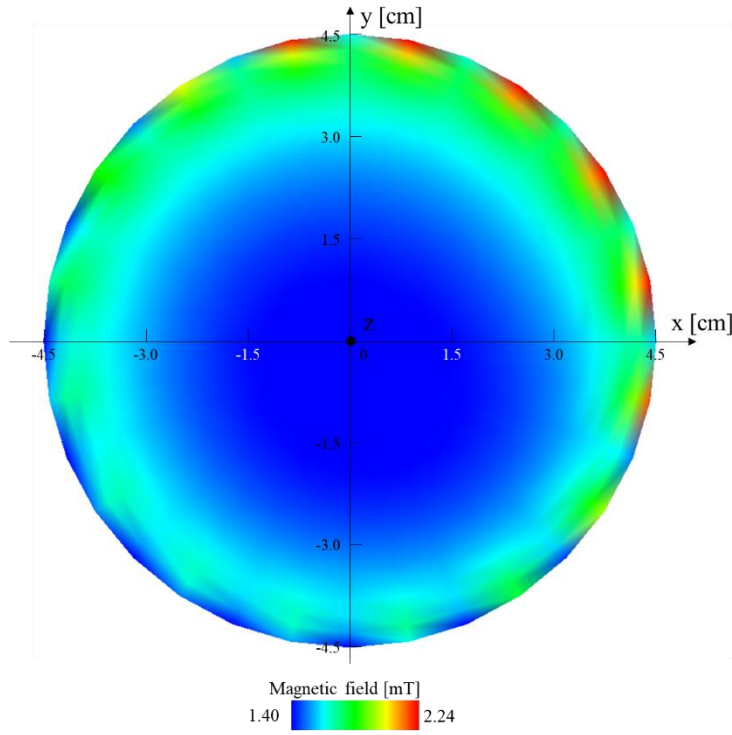
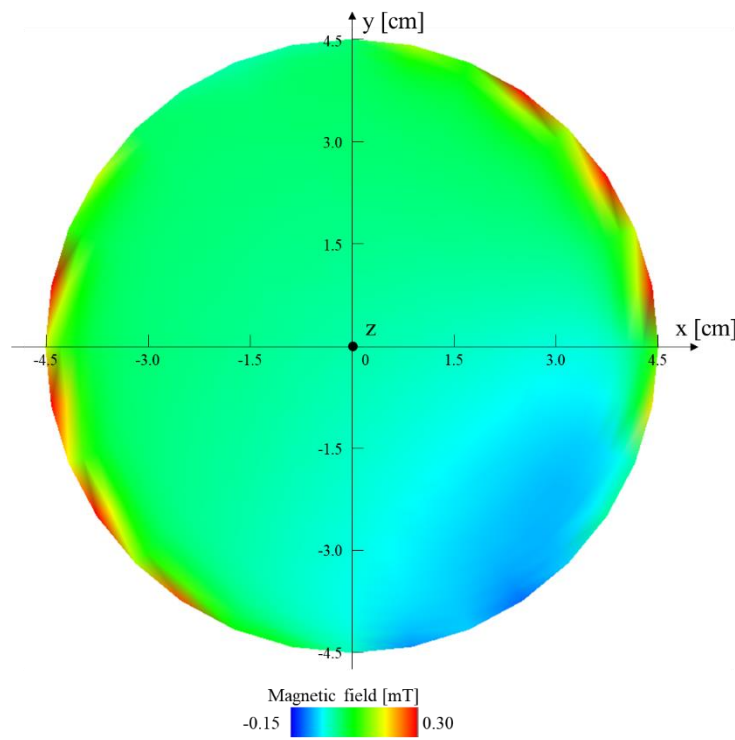
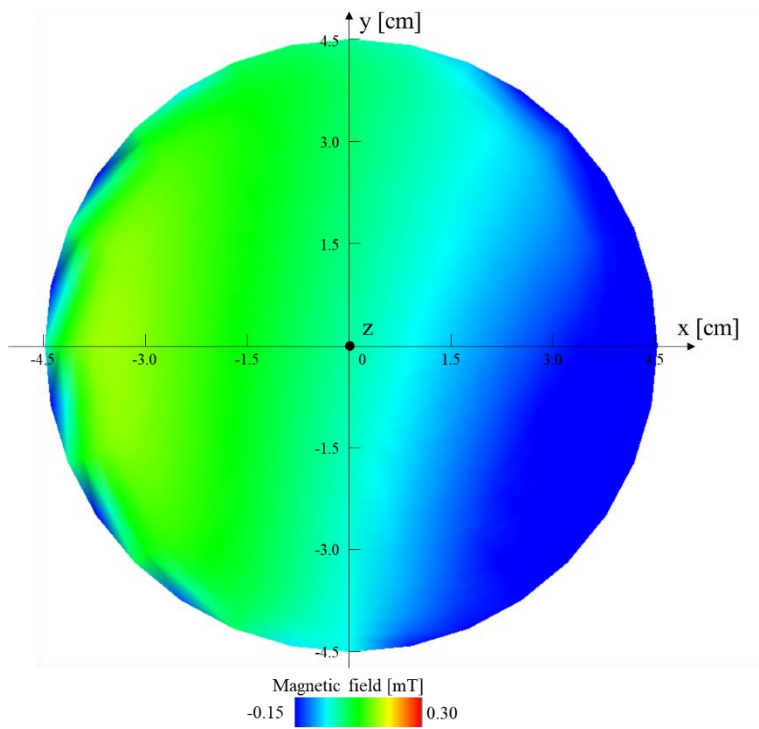


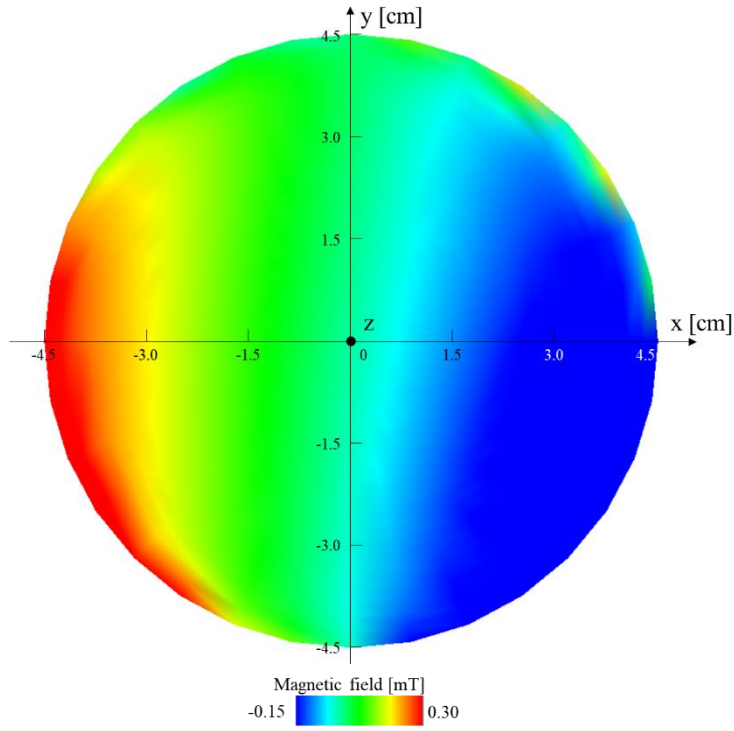
Fig. 3.2.9. Z-direction component of the magnetic field in the cross-section area inside the REBCO coil 60 minutes after the excitation with demagnetization method pattern I at (a) $z = 0$ cm, (b) $z = -0.94$ cm, (c) $z = -1.41$ cm, and (d) $z = -1.875$ cm.



(a)

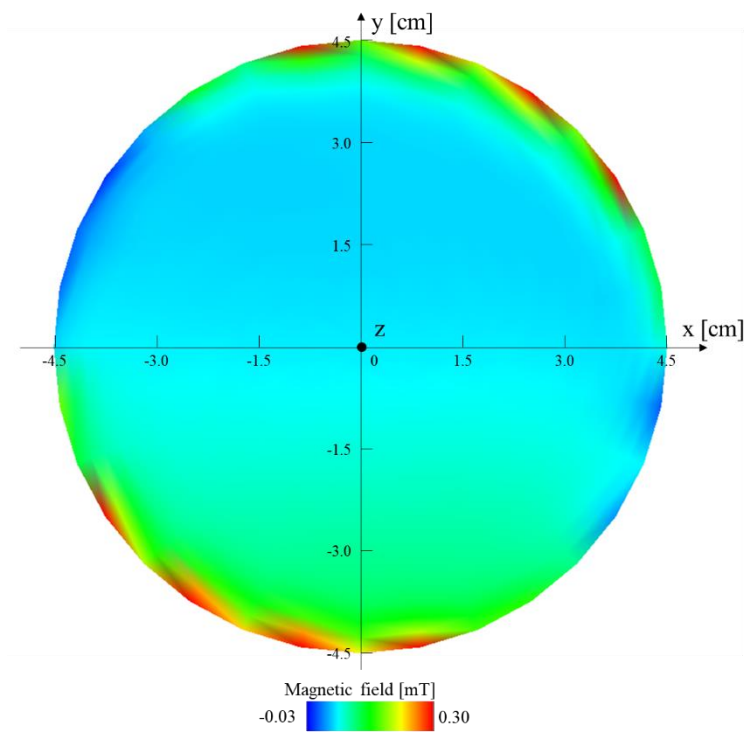


(b)

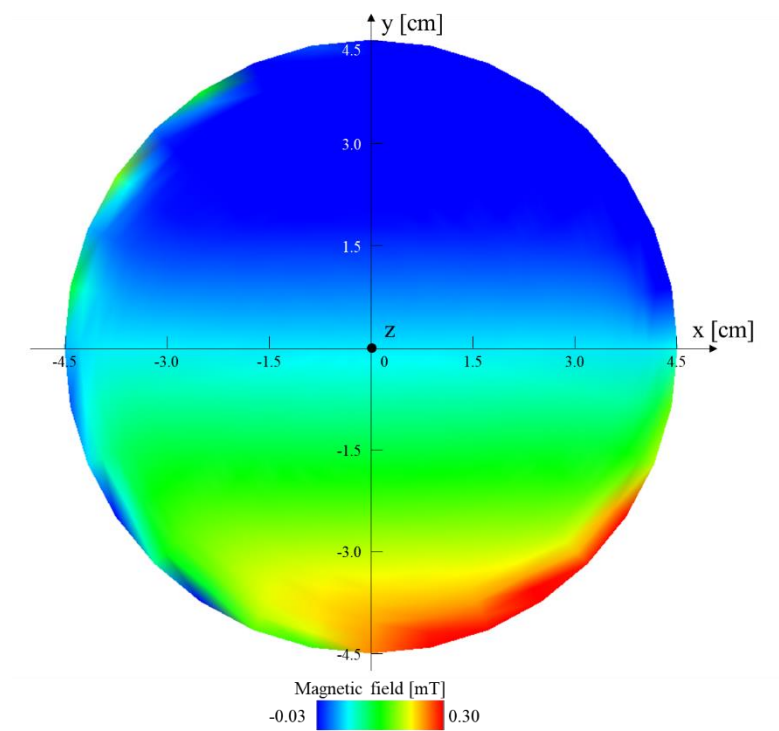


(c)

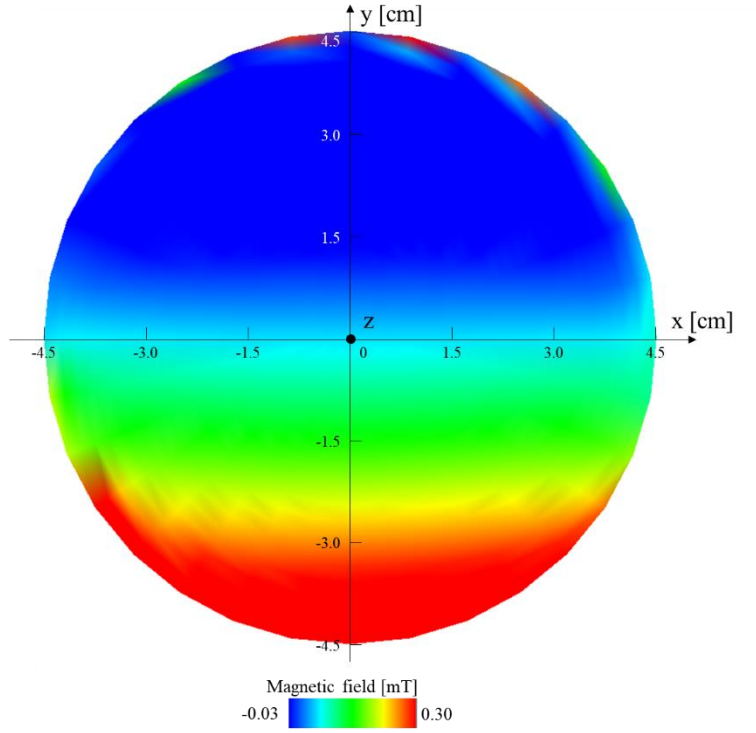
Fig. 3.2.10. X-direction component of the magnetic field in the cross-section area inside the REBCO coil 60 minutes after the excitation with demagnetization method pattern I at (a) $z = 0$ cm, (b) $z = -0.94$ cm, and (c) $z = -1.41$ cm.



(a)



(b)



(c)

Fig. 3.2.11. Y-direction component of the magnetic field in the cross-section area inside the REBCO coil 60 minutes after the excitation with demagnetization method pattern I at (a) $z = 0$ cm, (b) $z = -0.94$ cm, and (c) $z = -1.41$ cm.

3.3 Case Study: Saddle-shaped REBCO Coil for Accelerator Application

3.3.1 Analysis Conditions

A particle accelerator is a machine that uses electromagnetic fields to propel charged particles to very high speed and energy, and to contain them in well-defined beams. After the first invention, accelerators have been widely utilized for basic research in particle physics [61]–[63]. Recently, its application to cancer treatments has attracted worldwide attention [64], [65]. The heavy charged particles such as baryons are used to accurately deliver cancer-killing energy to tumors with negligible damage to the bodily functions. Hence, this method can significantly improve the treatment efficacy and the quality of patients' lives. However, the huge size and mass of the device, especially for the rotating gantry, are still a problem that hinders the spread.

The application of high temperature superconductors (HTS) is considered to be a good solution to this problem [66], [67]. In comparison with low temperature superconductors (LTS), HTS has

the advantages in low cooling cost, high thermal stability, and high magnetic field generation. Therefore, the developments of accelerator application using REBCO-coated conductor coils have become increasingly active in recent years. In such application, high accuracy of the changing magnetic field is required to accurately accelerating the particles and targeting at a specific area. The frequently changing coil current and magnetic field result in a high screening current [67], [68], hence, detailed analysis of the screening current and screening current induced field as well as the study of solution is necessary to design the REBCO coils.

In this case study, we have modelled a saddled-shaped REBCO coil and assumed the pattern of coil current to study the distribution of space magnetic field and screening current induced field with our proposed 3D electromagnetic analysis method. Detailed distribution of magnetic field, screening current induced field, and current density are studied here.

The specifications of the saddle-shaped coil are summarized in Table 3.3.1 and the schematic layout is shown in Fig. 3.3.1. A cosine-theta shape coil is modelled here. The pattern of coil current is shown in Fig. 3.3.2 which is based on and simplified as that of the magnet of the rotating gantry [69]. The ramp-up and ramp-down rates of current are 2 A/s and -2 A/s, and the duration after reaching 200 A, 150 A, and 100 A is 300 s, 10 s, and 10 s.

TABLE 3.3.1
SPECIFICATIONS OF SADDLE-SHAPED REBCO COIL FOR ACCELERATOR APPLICATION

Properties	Values
REBCO coil	SuperPower Inc. SCS4050
Turns of coil	1
Length of straight part	500 mm
Length of entire coil	620 mm
Radius of winding mandrel	500 mm
Parameter a of baseline	60 mm
Parameter b of baseline	40 mm
Additional twist θ_t^*	0
Total conductor length	1.33 m
Cooling temperature	30 K
Critical current at 77.3 K, self-field	600 A
Ag over-layer thickness	2 μm
Copper stabilizer thickness	20 μm
Coated conductor width	4 mm
Operating current	200 A

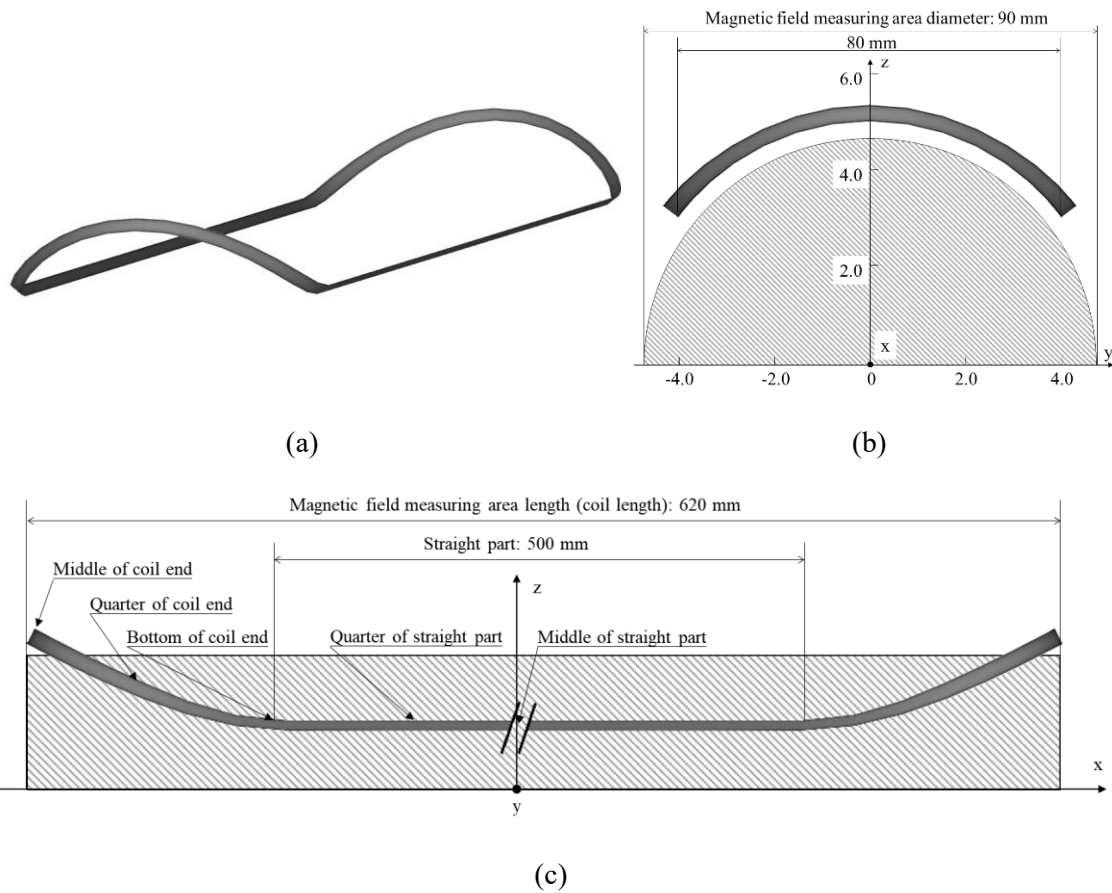


Fig. 3.3.1. Schematic layout of the saddle-shaped REBCO coil with magnetic field measuring area: (a) Bird's eye view, (b) side view, and (c) front view.

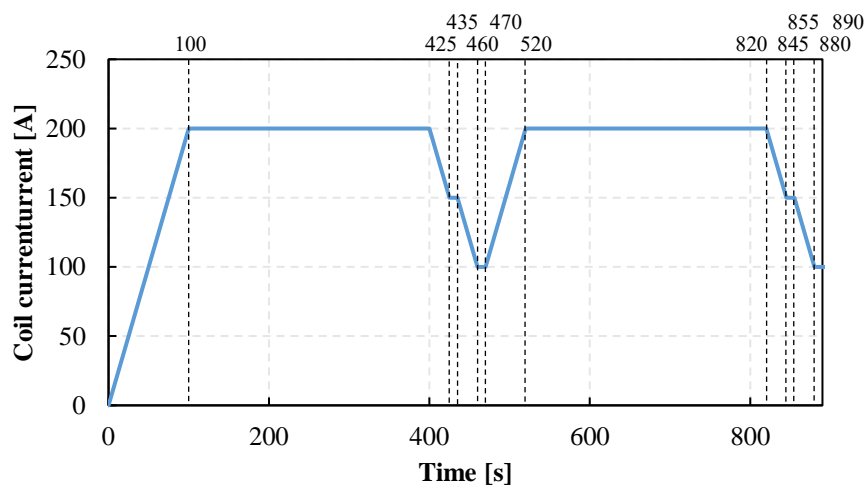


Fig. 3.3.2. Schematic illustration of the coil current pattern.

3.3.2 Modelling of Saddle-shaped Coil End

Because of the unique shape of the saddle-shaped coil end, an optimized design is required to reduce the strain on the REBCO tape for a better performance. Therefore, an integrated design approach, that used at CERN for the design and optimization of superconducting accelerator magnets, is utilized here. For detailed mathematical theory, refer to reference [70], [71]. The modelling process is as below.

Frenet–Serret equations (1)–(3) are used to generate strip surface.

$$\frac{d}{ds} \begin{pmatrix} \mathbf{t} \\ \mathbf{n} \\ \mathbf{b} \end{pmatrix} = \begin{pmatrix} 0 & \kappa & 0 \\ -\kappa & 0 & \tau \\ 0 & -\tau & 0 \end{pmatrix} \begin{pmatrix} \mathbf{t} \\ \mathbf{n} \\ \mathbf{b} \end{pmatrix} \quad (1)$$

$$\kappa = \frac{d\mathbf{t}}{ds} \cdot \mathbf{n} \quad (2)$$

$$\tau = -\frac{d\mathbf{b}}{ds} \cdot \mathbf{n} \quad (3)$$

where \mathbf{t} corresponds to the tangent of the base curve, \mathbf{n} is the normal vector that perpendicular to the tape surface, \mathbf{b} is the binormal vector that perpendicular to \mathbf{n} and \mathbf{t} , κ is the curvature, and τ is the torsion.

Firstly, a baseline should be defined, and here we define it as an ellipse on a cylinder (4) and (5). The baseline $r(\varphi)$ is then defined as (6) where φ is the parameter.

$$\left(\frac{x}{a}\right)^2 + \left(\frac{y}{b}\right)^2 = 1 \quad (4)$$

$$z = \sqrt{r^2 - y^2} \quad (5)$$

$$r(\varphi): \begin{cases} x = a \sin \varphi \\ y = b \cos \varphi \\ z = \sqrt{r^2 - (b \cos \varphi)^2} \end{cases} \quad (6)$$

Secondly, $(\mathbf{t}, \mathbf{n}, \mathbf{b})$ and κ, τ can be calculated as below.

$$\mathbf{t} = \frac{d\mathbf{r}}{d\varphi} = \frac{\mathbf{r}'(\varphi)}{\|\mathbf{r}'(\varphi)\|} \quad (7)$$

$$\mathbf{n} = \frac{\frac{d\mathbf{t}}{d\varphi}}{\left\|\frac{d\mathbf{t}}{d\varphi}\right\|} = \frac{\mathbf{r}'(\varphi) \times (\mathbf{r}''(\varphi) \times \mathbf{r}'(\varphi))}{\|\mathbf{r}'(\varphi) \times (\mathbf{r}''(\varphi) \times \mathbf{r}'(\varphi))\|} \quad (8)$$

$$\mathbf{b} = \mathbf{t} \times \mathbf{n} = \frac{\mathbf{r}'(\varphi) \times \mathbf{r}''(\varphi)}{\|\mathbf{r}'(\varphi) \times \mathbf{r}''(\varphi)\|} \quad (9)$$

$$\kappa = \frac{d\mathbf{t}}{ds} \cdot \mathbf{n} = \frac{\|\mathbf{r}'(\varphi) \times \mathbf{r}''(\varphi)\|}{\|\mathbf{r}'(\varphi)\|^3} \quad (10)$$

$$\tau = -\frac{d\mathbf{b}}{ds} \cdot \mathbf{n} = \frac{\mathbf{r}'(\varphi) \cdot (\mathbf{r}''(\varphi) \times \mathbf{r}'''(\varphi))}{\|\mathbf{r}'(\varphi) \times \mathbf{r}''(\varphi)\|^2} \quad (11)$$

Then, tape surface can be determined by the baseline $r(\varphi)$ and the generator vectors \mathbf{g} .

$$\mathbf{g} = \tau \mathbf{t} + \kappa \mathbf{b} \quad (12)$$

Additionally, to avoid the discontinuity in the connection between the coil end and straight part, applying an additional twist θ_t^* around \mathbf{t} is a solution. Consequently, $(\mathbf{t}, \mathbf{n}, \mathbf{b})$ can be calculated as below.

$$\mathbf{t}^* = \mathbf{t} \quad (13)$$

$$\mathbf{n}^* = \mathbf{n} \cos \theta_t^* + \mathbf{b} \sin \theta_t^* \quad (14)$$

$$\mathbf{b}^* = \mathbf{b} \cos \theta_t^* - \mathbf{n} \sin \theta_t^* \quad (15)$$

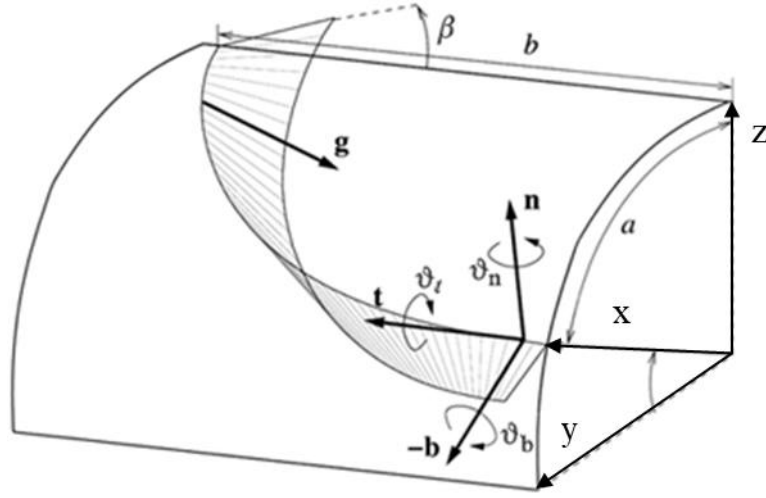


Fig. 3.3.3. Schematic layout of the saddle-shaped coil end. A strip bent along a baseline drawn on a cylinder of radius r , together with the generator lines of the developable surface[70].

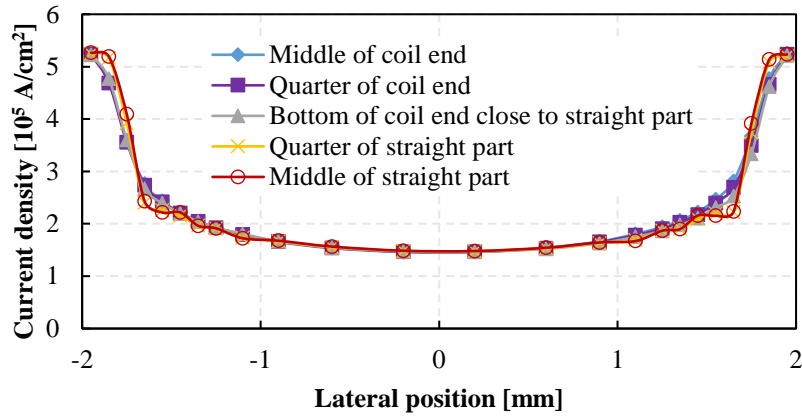
3.3.3 Investigation on Current density distribution

Firstly, we focus on the current density distribution in the widthwise direction at certain locations of the saddle-shaped REBCO coil. Because of the symmetry of the coil, we pick up five position as the typical position to study the current density distribution: middle of the coil end, quarter of the coil end, bottom of the coil end close to straight part, quarter of straight part, and middle of the straight part (Fig. 3.3.1(c)). In addition, lateral position -2 mm is the inside edge close to the center of the coil, while 2 mm is the outside edge away from the center.

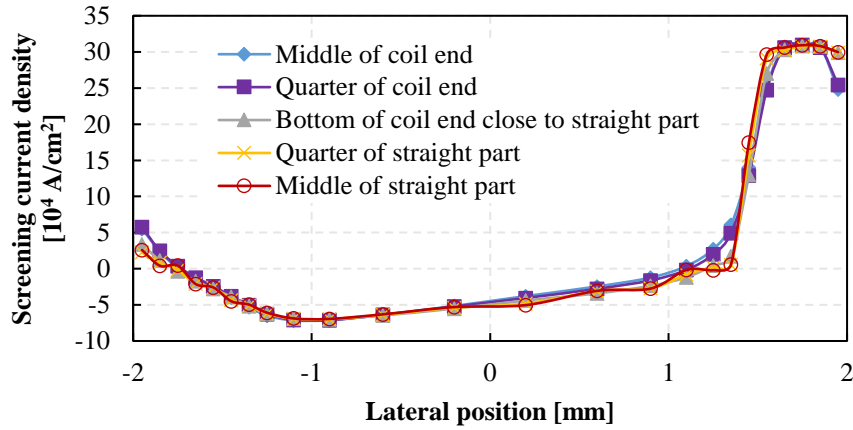
Fig. 3.3.4–3.3.10 indicate the lateral current density distribution and screening current density distribution in the widthwise direction of the REBCO tape at 100 s, 400 s, 425 s, 460 s, 520 s, 845 s, and 880 s. The start time and end time of the duration of 300 s as well as the start time of the duration of 10 s are picked up as the typical time to study the behaviors of current density distribution.

At 100 s, the first time the coil current increases to 200 A, Fig. 3.3.4 shows a typical lateral current density distribution that the current density increases from both edges of the REBCO tape.

When the lateral position moves from edge to the center, the current density in the coil end decreases more than that in the straight part, namely, the current density is more averaged in the coil end part because of the stronger and more complicated magnetic field. As to the screening current density distribution, the plus screening current concentrates to the edge in the plus lateral position, while the minus screening current is relatively averaged in the rest part. At 400 s, 300 s duration after the coil current reaches 200 A, we find that the current density distribution is slowly averaged in the tape widthwise direction because of the decreasing screening current. Moreover, the difference between the current density distribution in straight part and coil end part also becomes smaller.

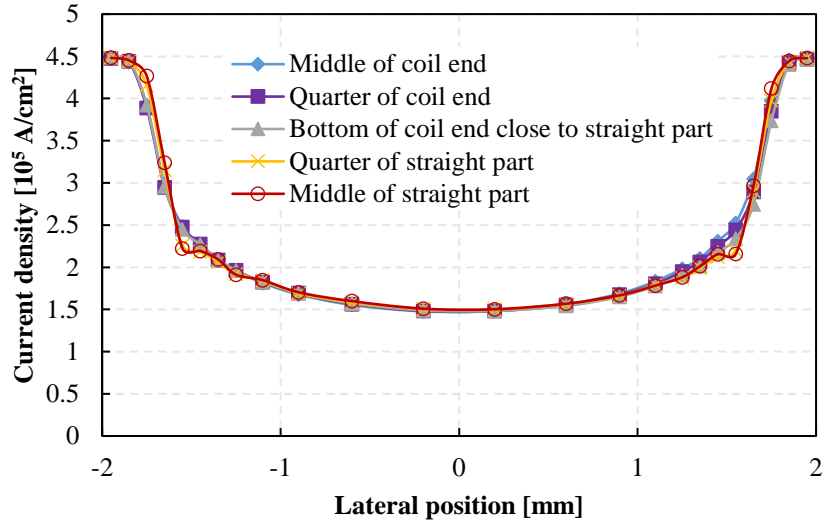


(a)

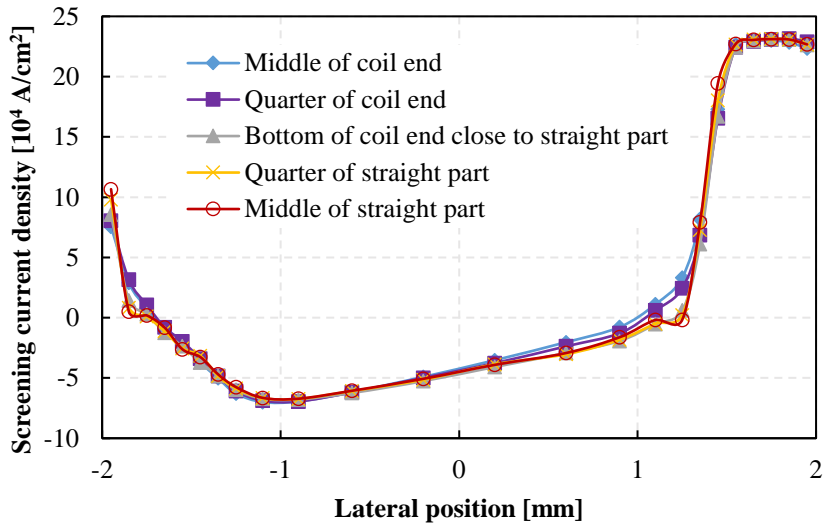


(b)

Fig. 3.3.4. (a) Lateral current density distribution and (b) screening current density distribution in at different position of the REBCO coil at 100 s.



(a)



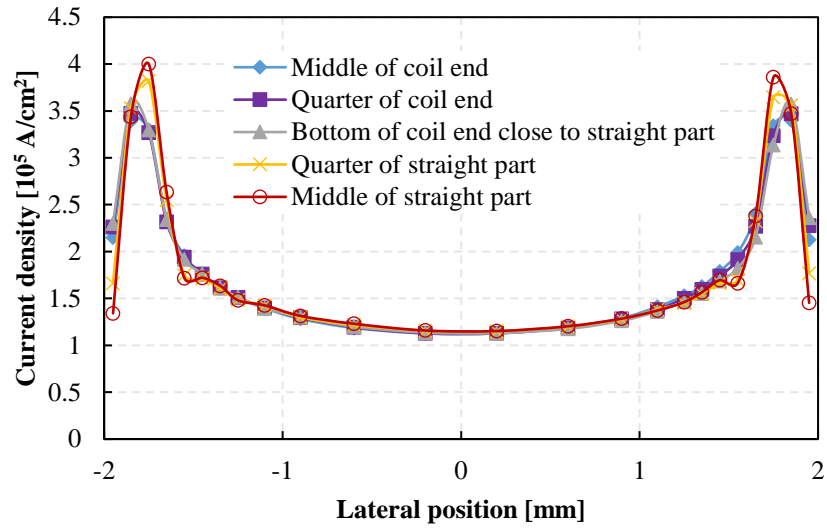
(b)

Fig. 3.3.5. (a) Lateral current density distribution and (b) screening current density distribution in at different position of the REBCO coil at 400 s.

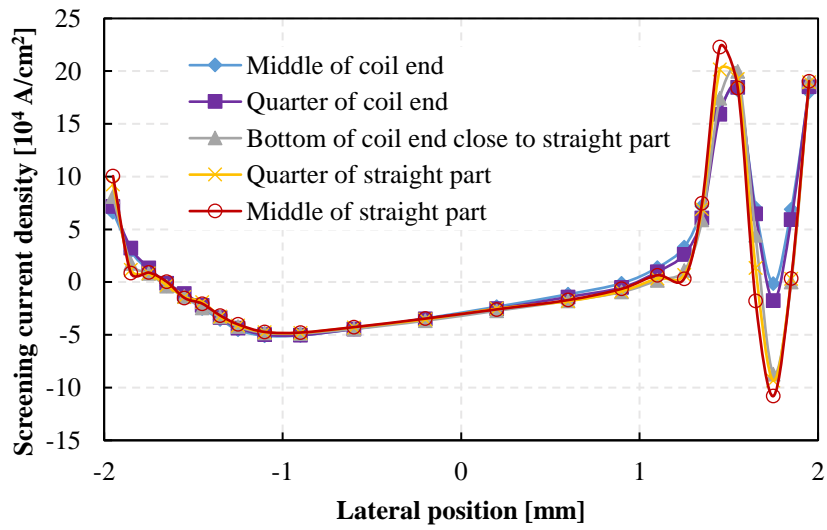
At 425 s, the coil current decreases to 150 A in 25 s and the current density at both edges of the tape decreases first. The maximum current density appears near the lateral position of ± 1.75 mm. As to the screening current density distribution, a fluctuation appears near the plus edge of the tape in comparison with the distribution at 400 s. The fluctuation indicates a new route of screening current flowing which may make the magnetic field more complicated. In addition, the results at 435 s are omitted here because the change in the 10 s duration is negligible.

At 460 s, the coil current decreases to 100 A in 25 s, and the current density at both edges of

the tape drops more and even becomes minus in the straight part of the coil. As to the screening current density distribution, more minus screening current as well as more averaged plus screening current is observed.

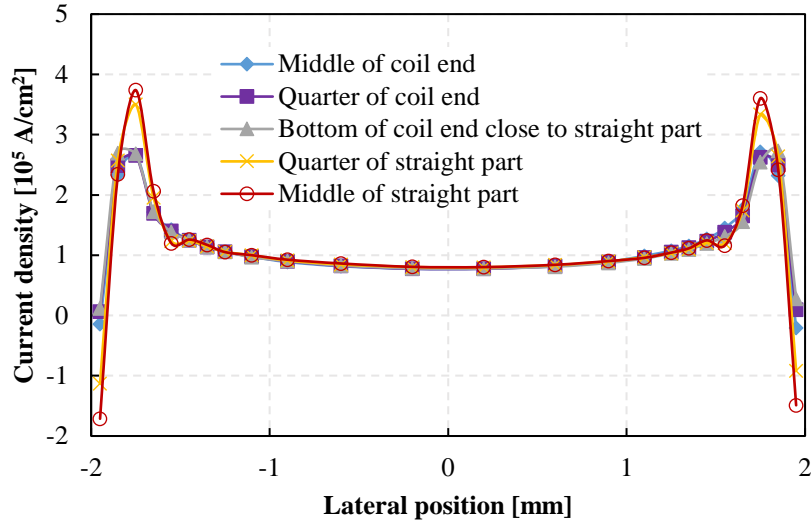


(a)

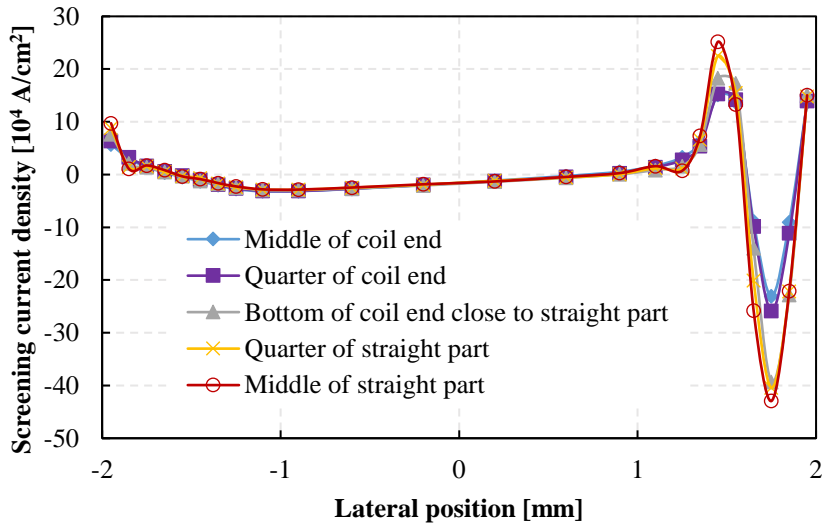


(b)

Fig. 3.3.6. (a) Lateral current density distribution and (b) screening current density distribution in at different position of the REBCO coil at 425 s.



(a)



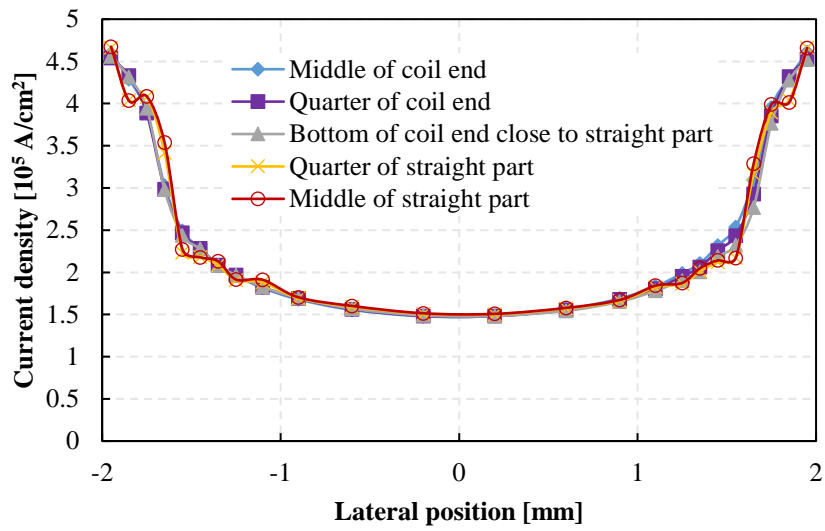
(b)

Fig. 3.3.7. (a) Lateral current density distribution and (b) screening current density distribution in at different position of the REBCO coil at 460 s.

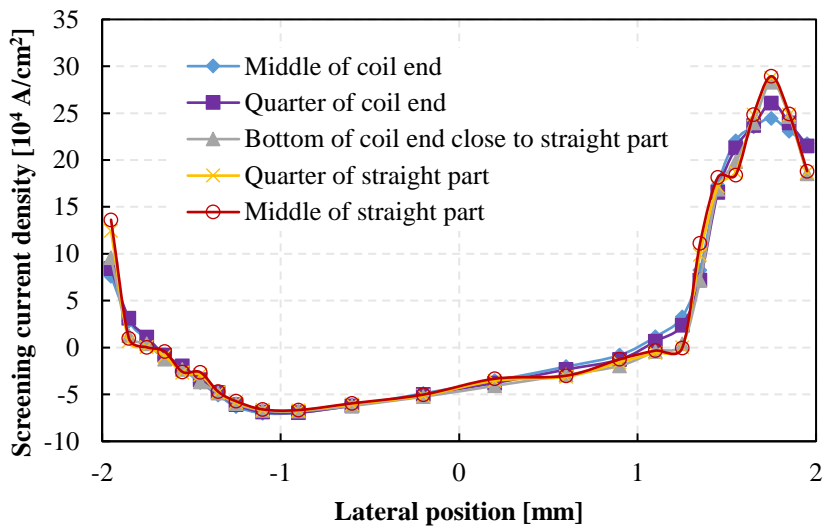
At 520 s, the second time the coil current increased to 200 A, the current density distribution is close to that at 100 s, whereas the current density at both edges becomes lower. Local peaks of the current density near the lateral position of ± 1.75 mm are observed especially in the straight part of the coil. The screening current density distribution near the plus edge of the tape also differs from that at 100 s and shows the influence of excitation history. In addition, the results at 820 s is omitted here because the change in the duration of 300 s is similar to the previous one.

At 845 s and 880 s, the distribution of current density and screening current density are similar

to those at 425 s and 460 s separately, but the magnitude of the current density and screening current density in the straight part become greater because of the influence of excitation history.

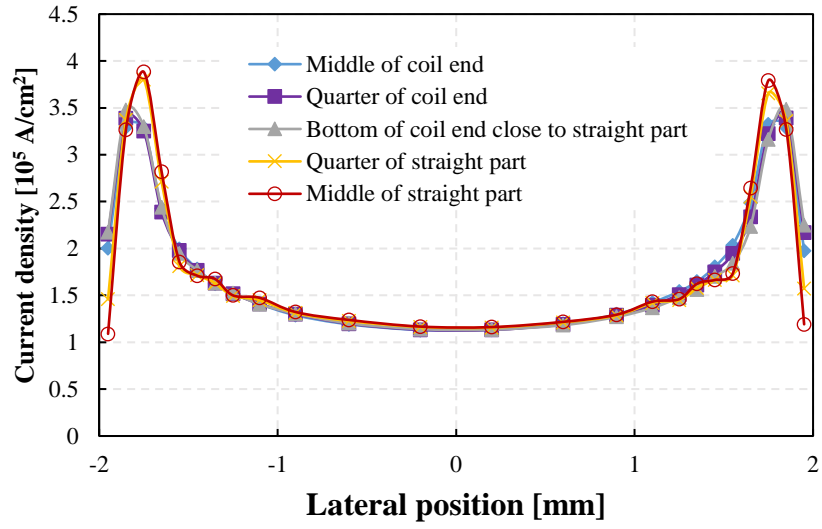


(a)

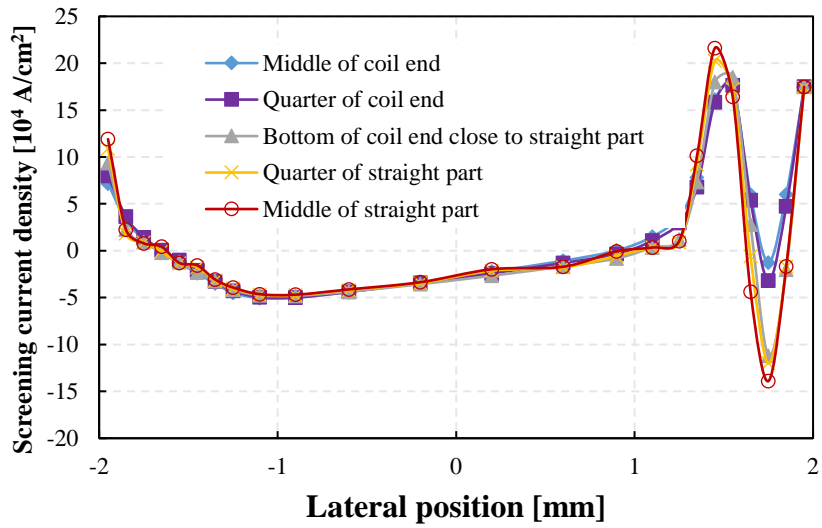


(b)

Fig. 3.3.8. (a) Lateral current density distribution and (b) screening current density distribution in at different position of the REBCO coil at 520 s.

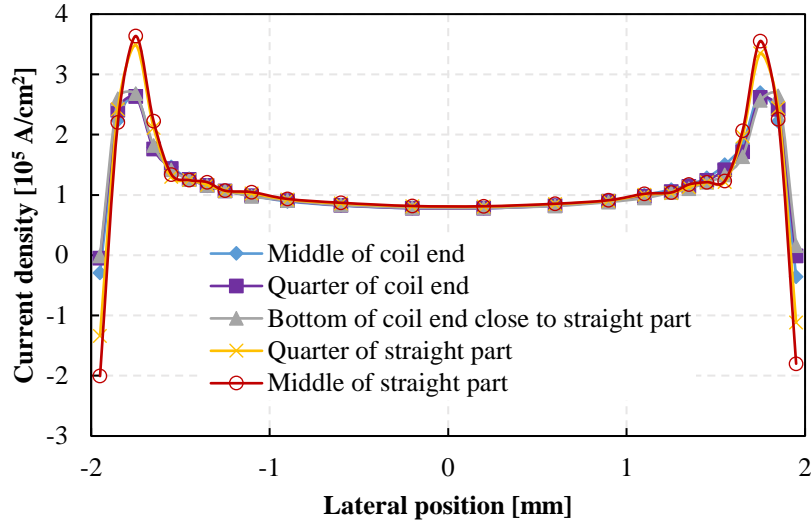


(a)

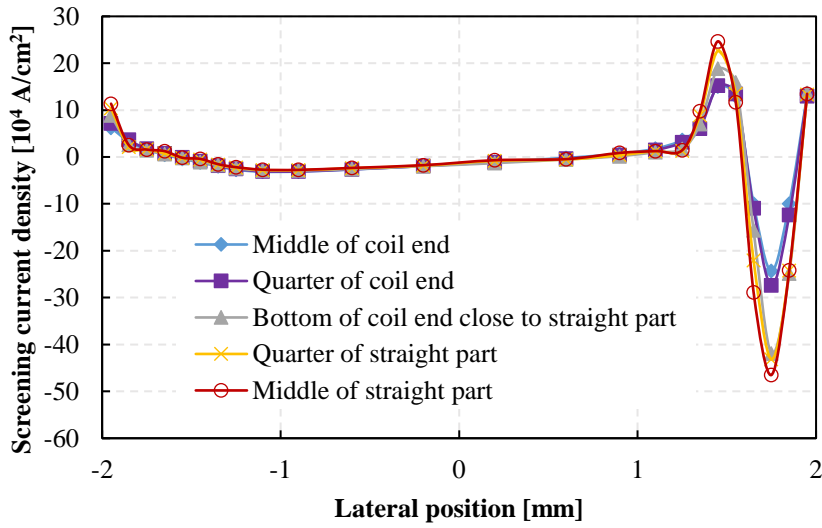


(b)

Fig. 3.3.9. (a) Lateral current density distribution and (b) screening current density distribution in at different position of the REBCO coil at 845 s.



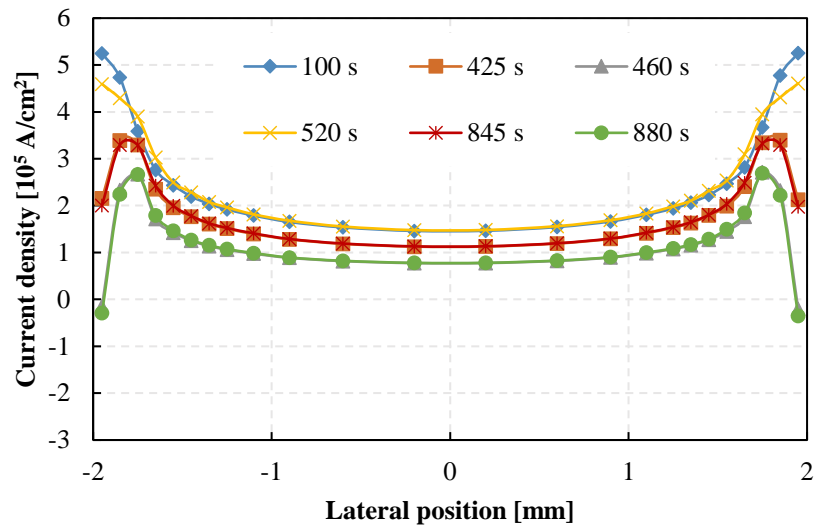
(a)



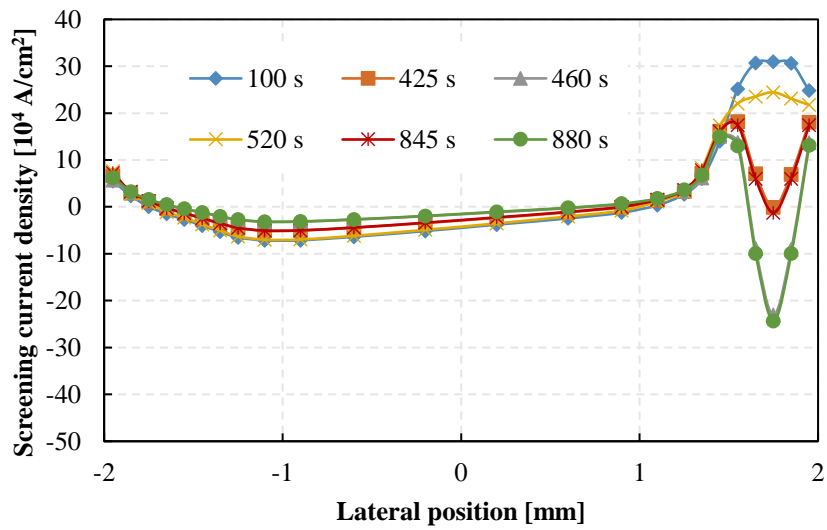
(b)

Fig. 3.3.10. (a) Lateral current density distribution and (b) screening current density distribution in at different position of the REBCO coil at 880 s.

For a clearer understanding of the change in the current density, the distribution of lateral current density and screening current density in the middle of the coil end and the straight part at certain times is shown in Fig. 3.3.11 and 3.3.12. The development of fluctuation of screening current density distribution near the outside edge of the tape can be observed. Note that the magnitude of screening current density in the straight part is greater than that in the coil end because of stronger and more complicated magnetic field in the coil end part. It also results in the more distinct difference in the lateral current density distribution.

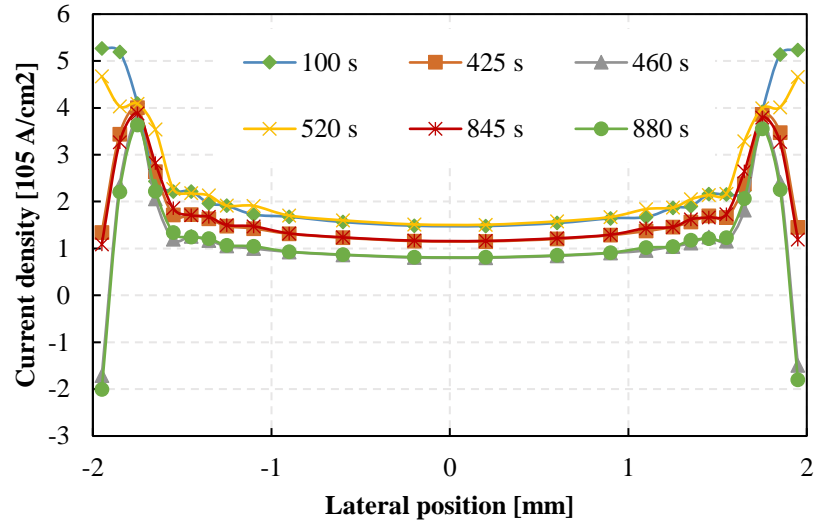


(a)

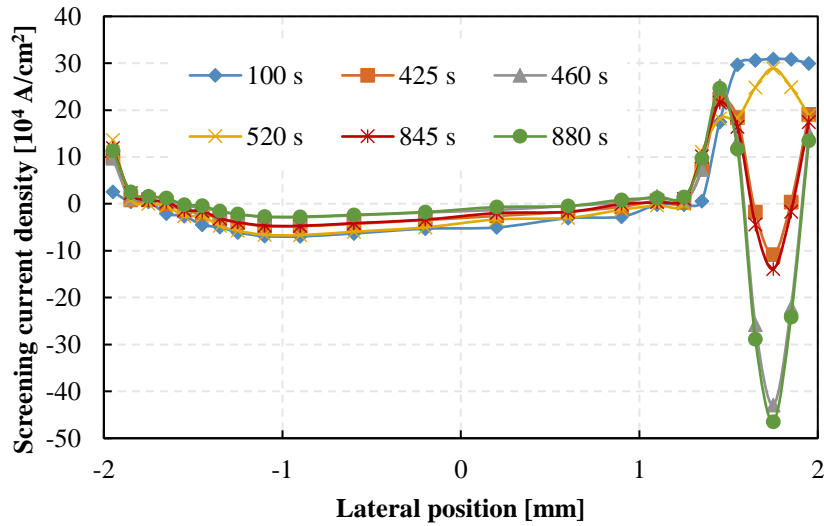


(b)

Fig. 3.3.11. (a) Lateral current density distribution and (b) screening current density distribution in the middle of coil end of the REBCO coil at certain times.



(a)



(b)

Fig. 3.3.12. (a) Lateral current density distribution and (b) screening current density distribution in the middle of straight part of the REBCO coil end at certain times.

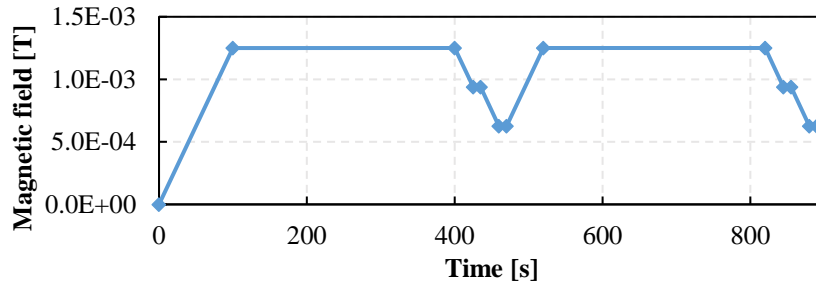
3.3.4 Investigation on Magnetic Field Distribution

Next, the magnetic field distribution is investigated in this sector.

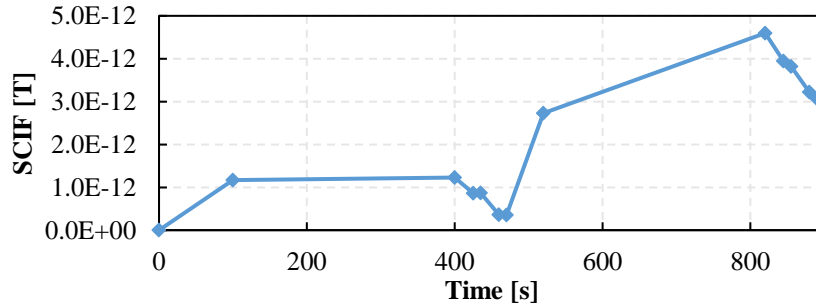
At first, Fig. 3.3.13 indicates the z-direction component of magnetic field, as well as the x-direction, y-direction, and z-direction component of screening current induced field (SCIF), at the center of the REBCO coil ($x = 0$, $y = 0$, $z = 0$). The change of magnetic field shows good conformity with the change of coil current, meanwhile, the SCIF shows different behaviors. In general, the magnitude of z-direction component is around 400 times bigger than that of y-

direction component which is about 100 times bigger than that of x-direction component. The difference is mainly due to the configuration of the saddle-shaped coil. The pair of long straight part mainly generates the z-direction component instead of the y-direction component, meanwhile, the x-direction component is mainly generated by the coil end parts which is far away from the center position.

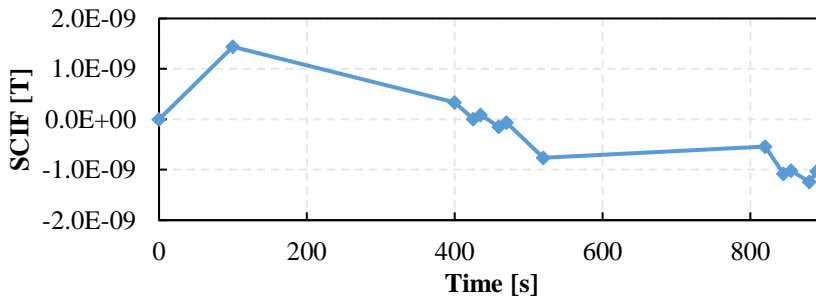
Then, Fig. 3.3.14 and 3.3.15 show the distribution of x-direction, y-direction, and z-direction components of magnetic field in the xy plane ($z = 0$) at certain times for an intuitive impression. It is found that the overall magnetic field distribution pattern is similar at different times except for the magnitude, while the magnitude seems to be in proportion to the value of coil current. Furthermore, x-direction, y-direction, and z-direction components of the magnetic field show different distribution from each other. The x-direction component enlarges in the area of the coil ends. The y-direction component enlarges near the +y-axis and -y-axis edges of the measuring area close to the straight part of the coil. The z-direction component enlarges in the central area.



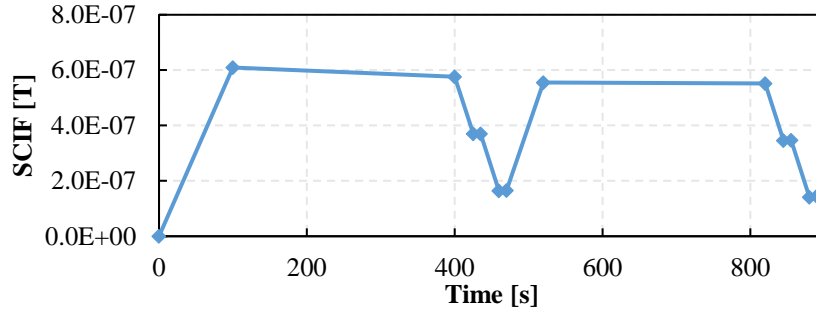
(a)



(b)

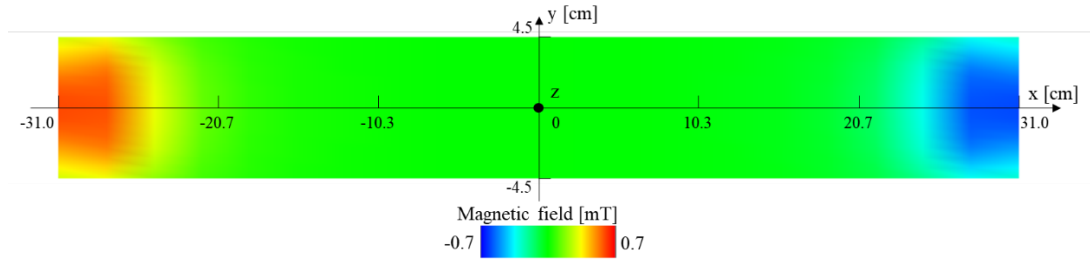


(c)

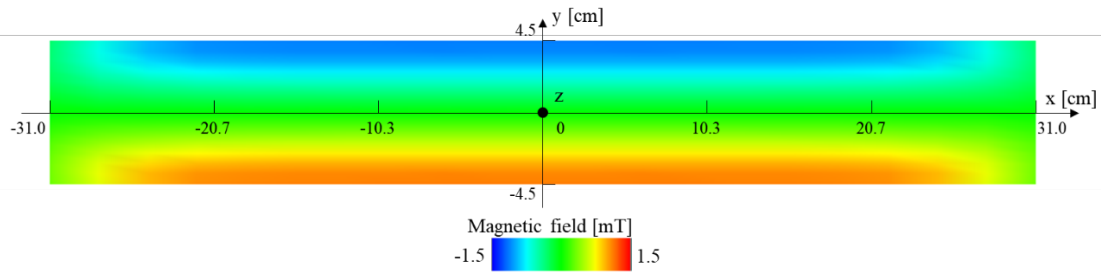


(d)

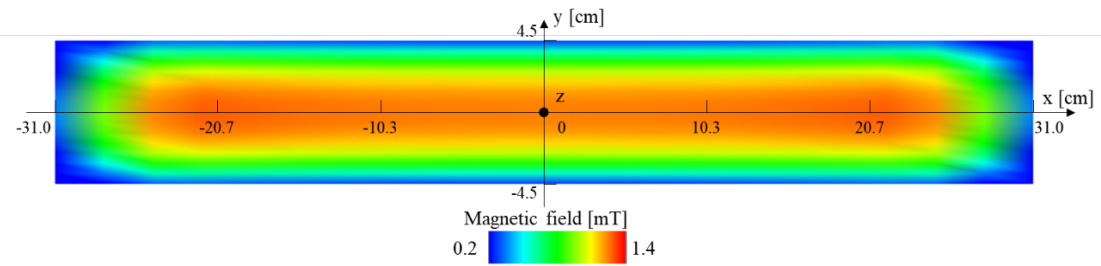
Fig. 3.3.13. (a) Z-direction component of magnetic field, (b) x-direction component, (c) y-direction component, and (d) z-direction component of screening current induced field (SCIF) at the center of the REBCO coil ($x = 0$, $y = 0$, $z = 0$).



(a)



(b)



(c)

Fig. 3.3.14. (a) X-direction component, (b) y-direction component, (c) z-direction component of magnetic field in the xy plane ($z = 0$) at 100 s.

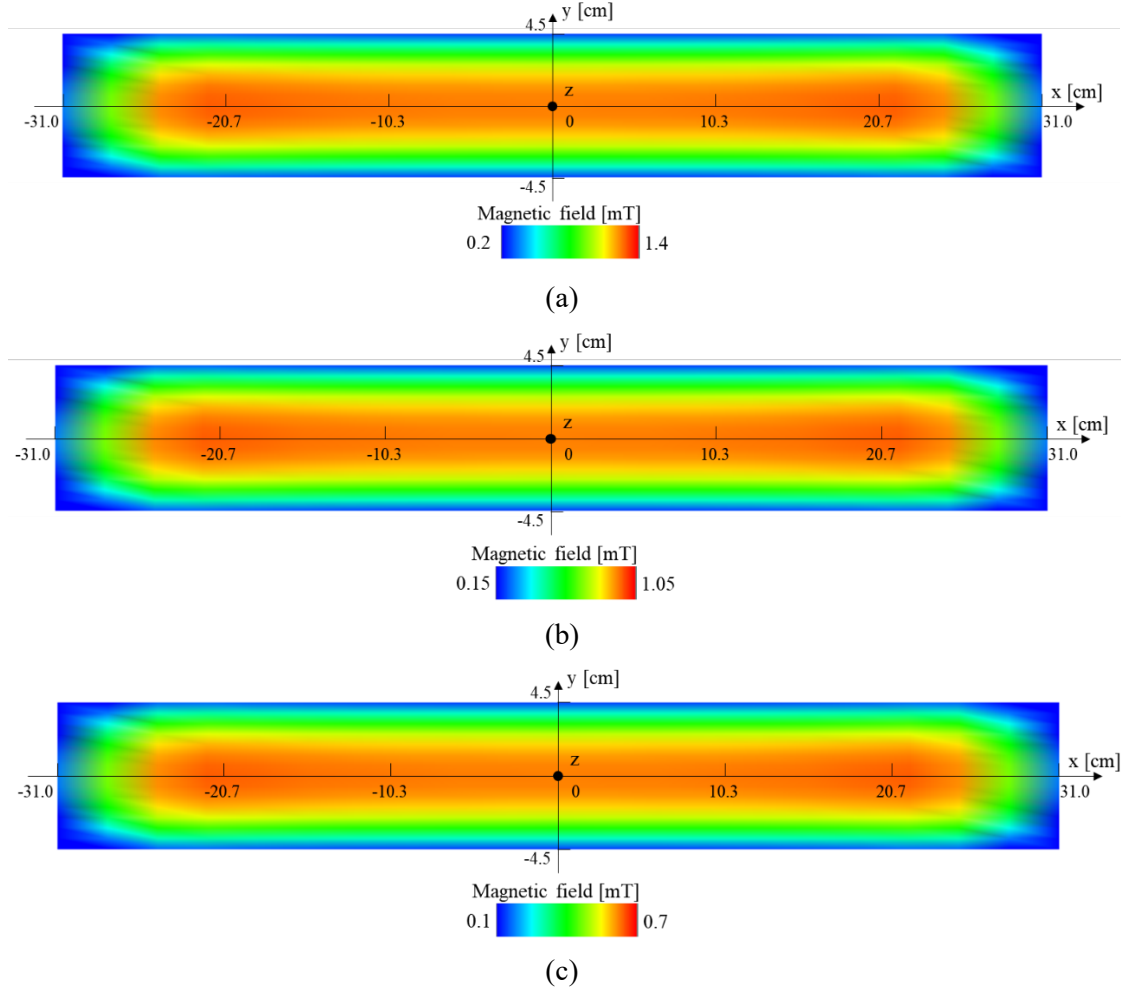
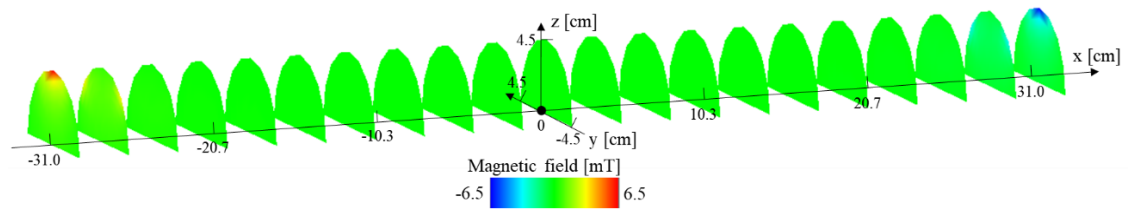
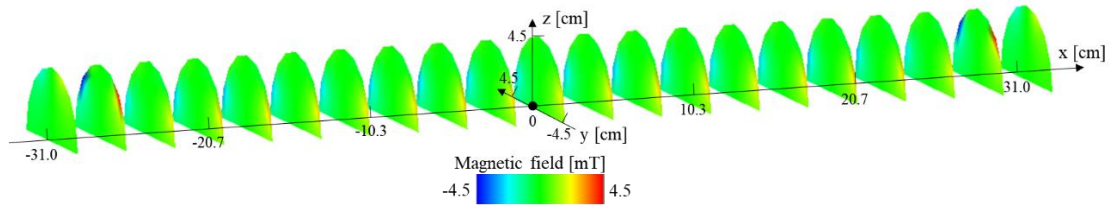


Fig. 3.3.15. Z-direction component of magnetic field in the xy plane ($z = 0$) at (a) 520 s, (b) 845 s, (c) 880 s.

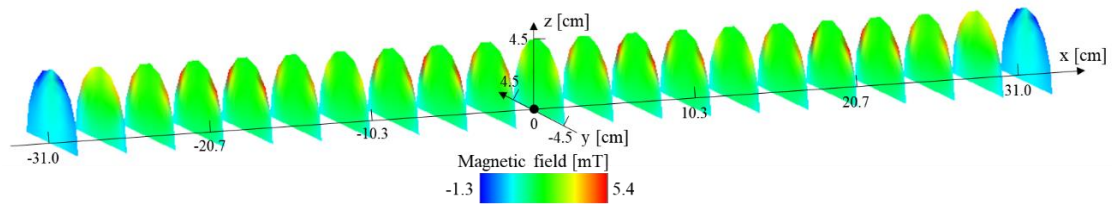
To study the spatial magnetic field distribution, Fig. 3.3.16–3.3.18 summarize the magnetic field distribution in yz plane at different position along the x-axis. The results at time of 100 s, 425 s, and 460 s are picked up here to study the distribution at the ends of current increase and decreases. The magnitude of the magnetic field is approximately proportion to the coil current. Moreover, the x-direction component mainly increases in the area of coil ends, while the y-direction component increases in both the coil end parts and straight part close to the REBCO tape. The z-direction component also increases significantly in the area close to the coil in the straight part, but decreases rapidly when it is away from the straight part in the coil end part.



(a)

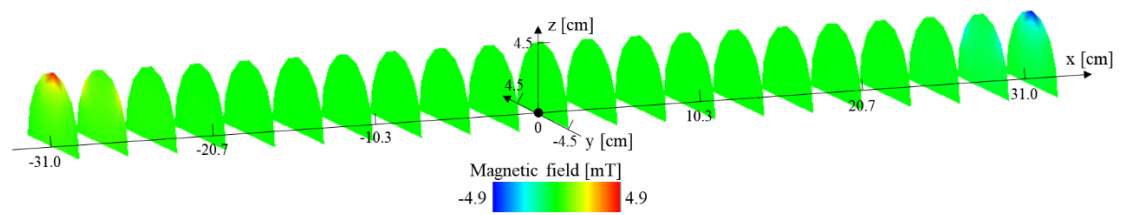


(b)

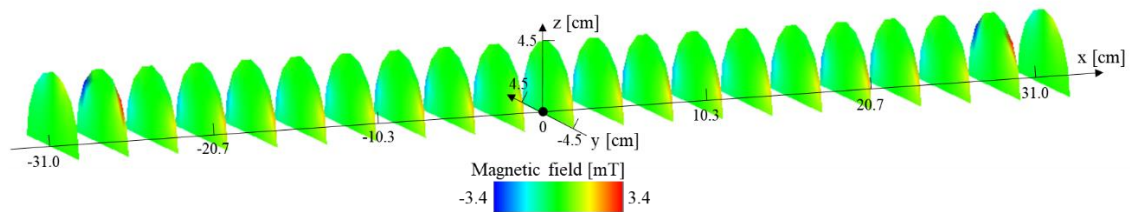


(c)

Fig. 3.3.16. (a) X-direction component, (b) y-direction component, (c) z-direction component of magnetic field in the field measuring space at 100 s.



(a)



(b)

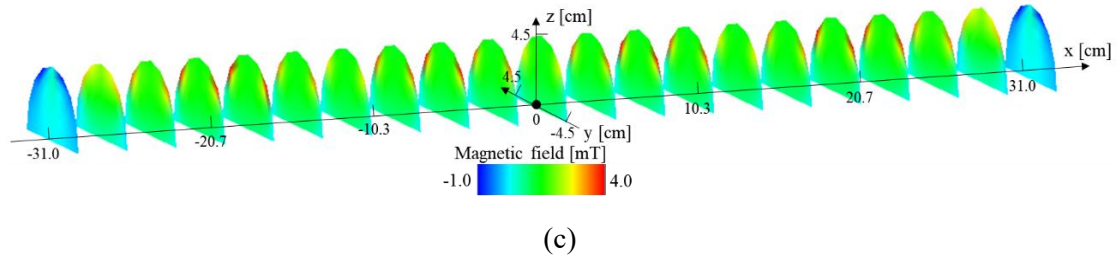


Fig. 3.3.17. (a) X-direction component, (b) y-direction component, (c) z-direction component of magnetic field in the field measuring space at 425 s.

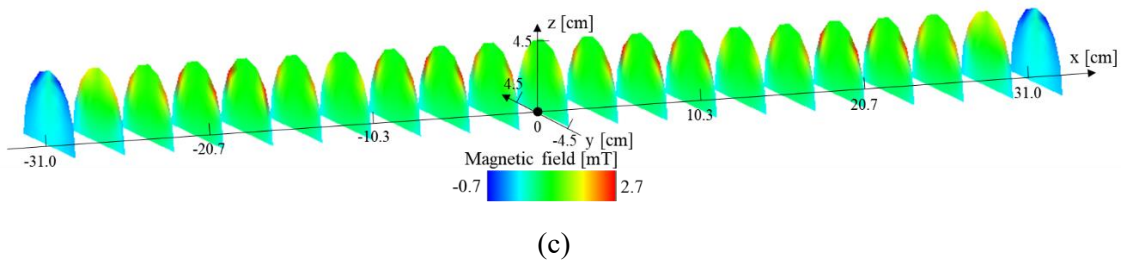
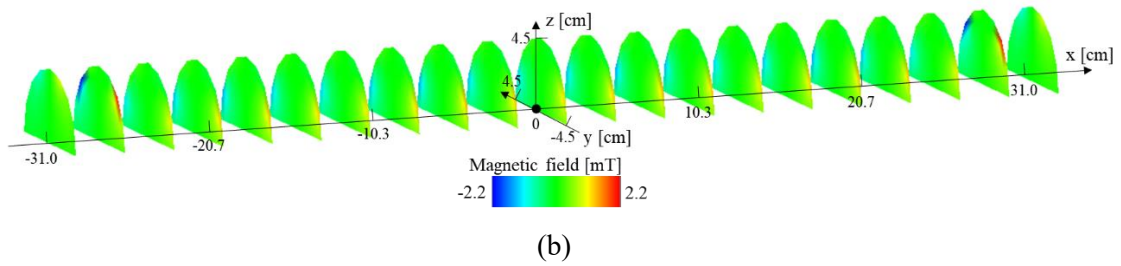
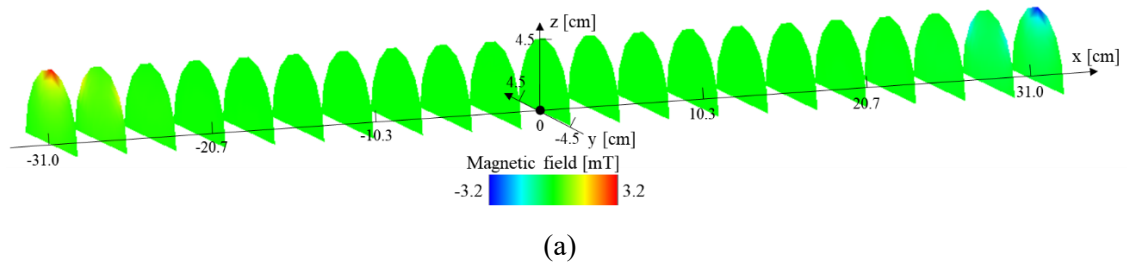


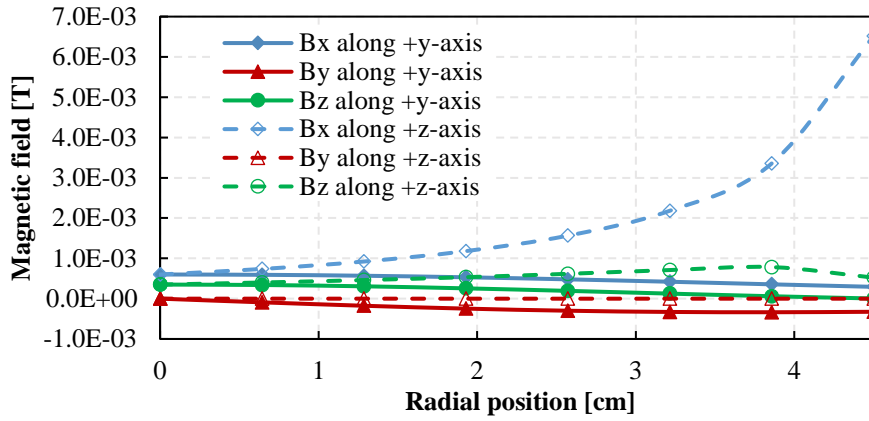
Fig. 3.3.18. (a) X-direction component, (b) y-direction component, (c) z-direction component of magnetic field in the field measuring space at 460 s.

Furthermore, to analyze the magnetic field distribution more accurately, the specific magnitudes of x-direction, y-direction, and z-direction components of magnetic field along the y-axis and z-axis in yz plane are summarized in Fig 3.3.19–3.3.22. The yz planes of $x = -31$ cm, -27.9 cm, -24.8 cm, -21.7 cm, and 0 cm are picked up to study the difference of magnetic field distribution between the coil end part and the straight part.

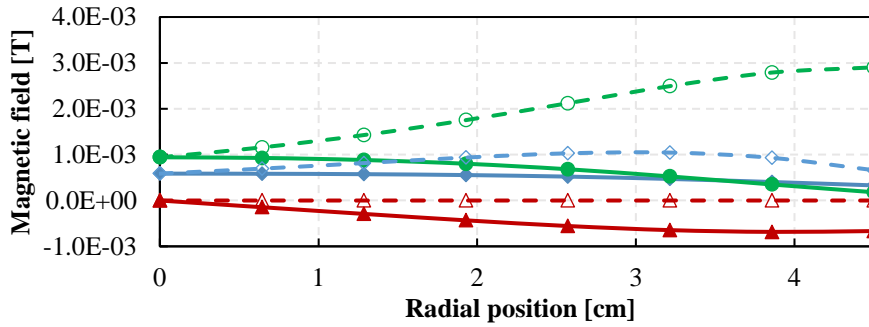
The results verify the observation above that x-direction component increases significantly in

the coil end part, while the y-direction and z-direction increase when it comes to the straight part at any time. In most of the space, the z-direction component dominates the magnetic field and get greater when it is closer to the central area of the coil. The y-direction component mainly appears in the space that close to REBCO tape.

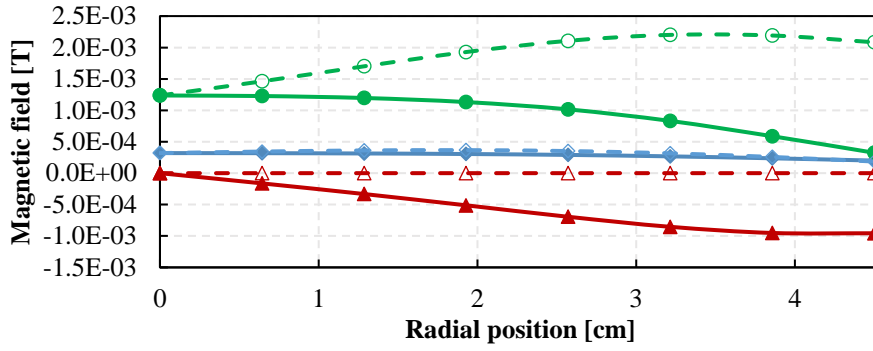
The distribution of x-direction, y-direction, and z-direction components of magnetic field shows similar pattern at different times, namely with different coil current. According to the data, the magnitude of the magnetic field seems in proportion to the coil current, next, it is necessary to study the screening current induced filed at different times. Furthermore, the homogeneity of the magnitude field in this case is not inadequate for the accelerator application, hence common accelerator coil design usually consists of more coils with various arrangements to improve the field homogeneity within the specific space.



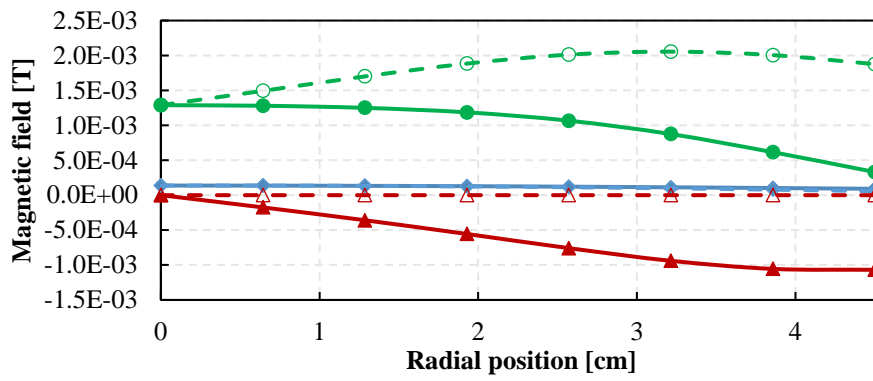
(a)



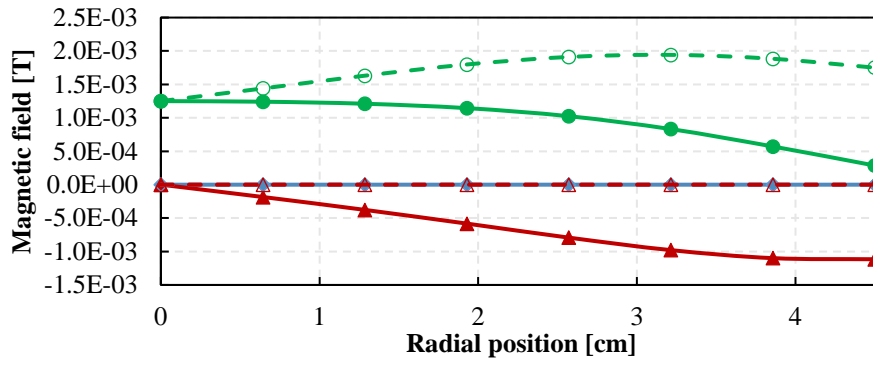
(b)



(c)



(d)



(e)

Fig. 3.3.19. X-direction, y-direction, and z-direction component of magnetic field at 100 s along the y-axis and z-axis at (a) $x = -31.0$ cm, (b) $x = -27.9$ cm, (c) $x = -24.8$ cm, (d) $x = -21.7$ cm, (e) $x = 0$ cm.

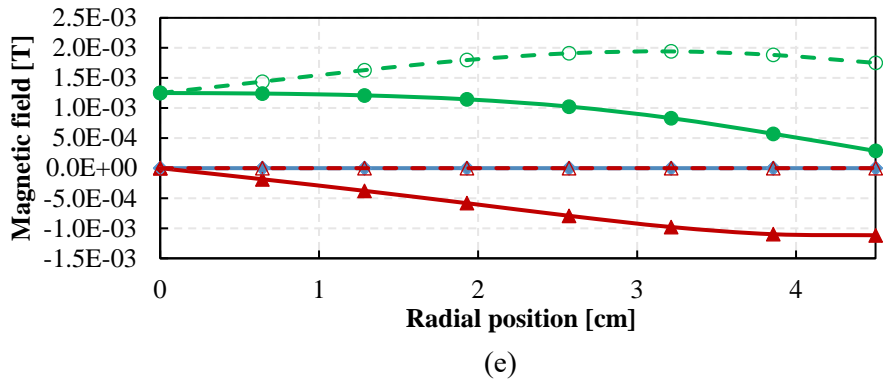
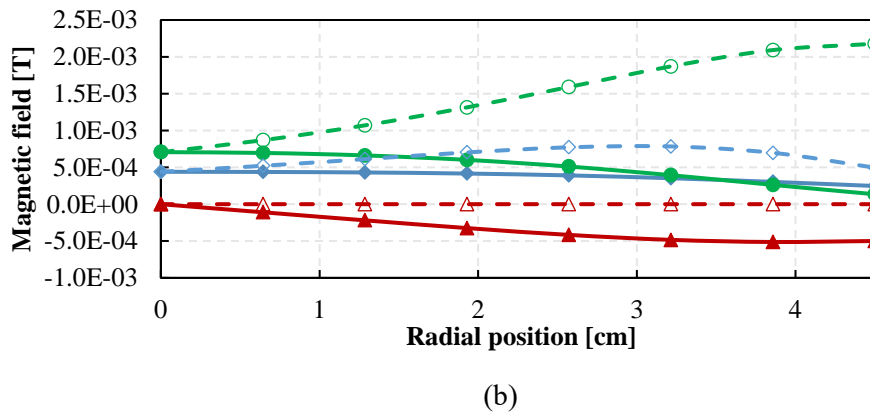
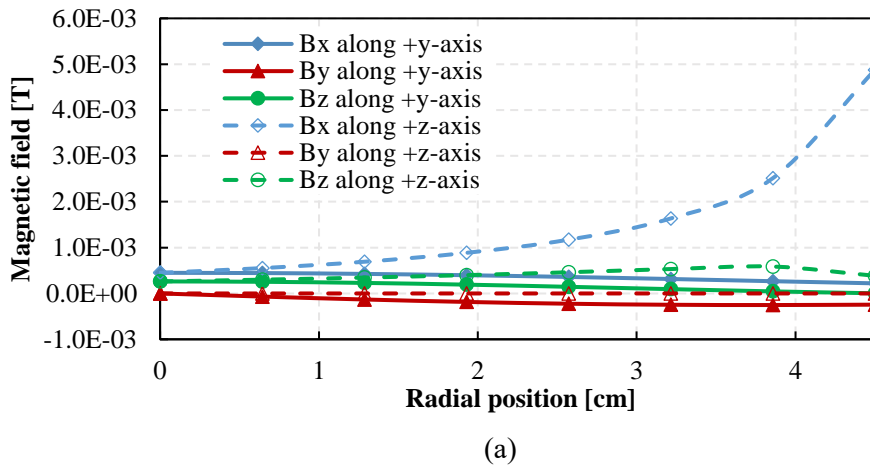
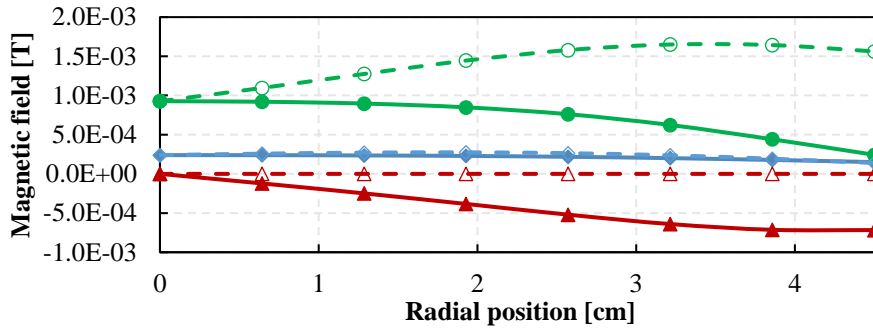
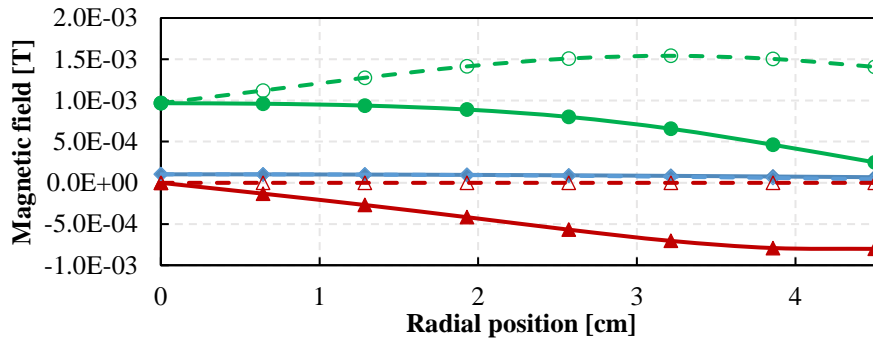


Fig. 3.3.20. X-direction, y-direction, and z-direction component of magnetic field at 520 s along the y-axis and z-axis at (a) $x = -31.0$ cm, (b) $x = -27.9$ cm, (c) $x = -24.8$ cm, (d) $x = -21.7$ cm, (e) $x = 0$ cm.

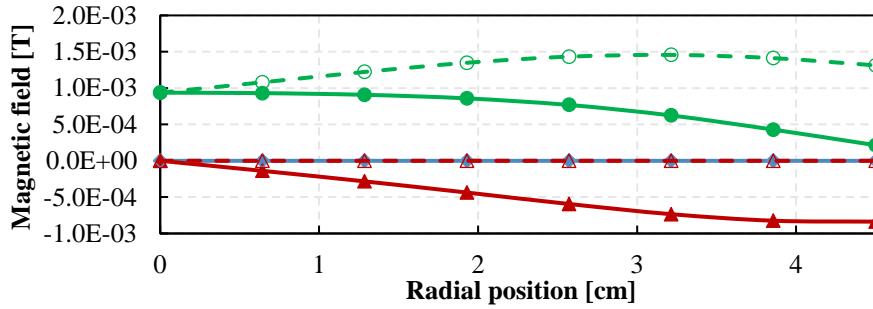




(c)

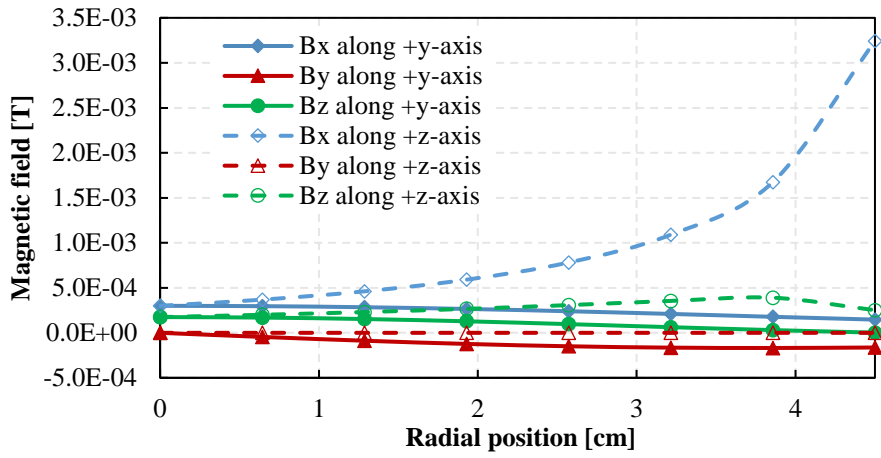


(d)

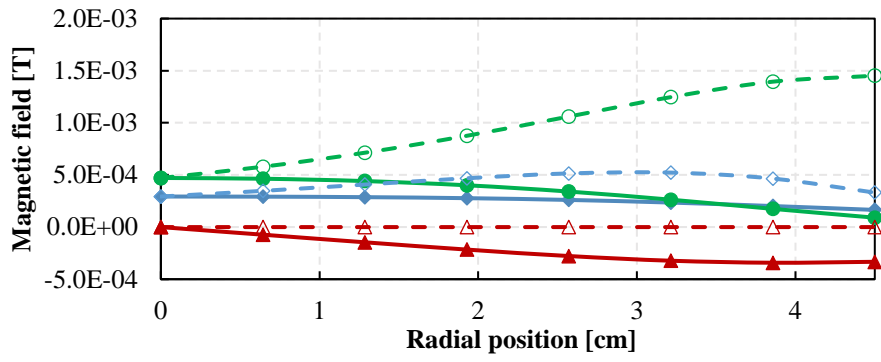


(e)

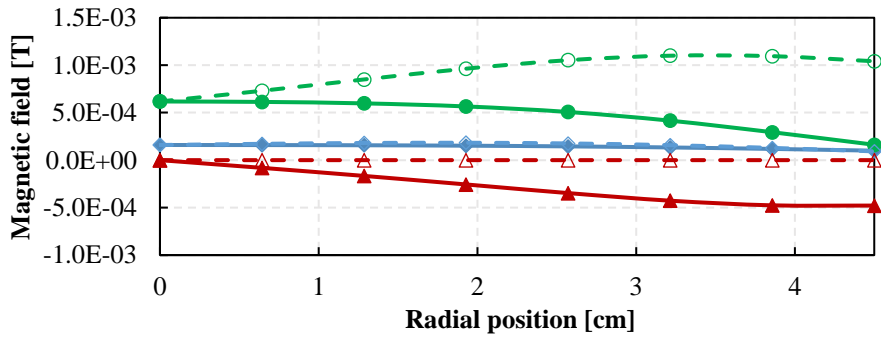
Fig. 3.3.21. X-direction, y-direction, and z-direction component of magnetic field at 845 s along the y-axis and z-axis at (a) $x = -31.0$ cm, (b) $x = -27.9$ cm, (c) $x = -24.8$ cm, (d) $x = -21.7$ cm, (e) $x = 0$ cm.



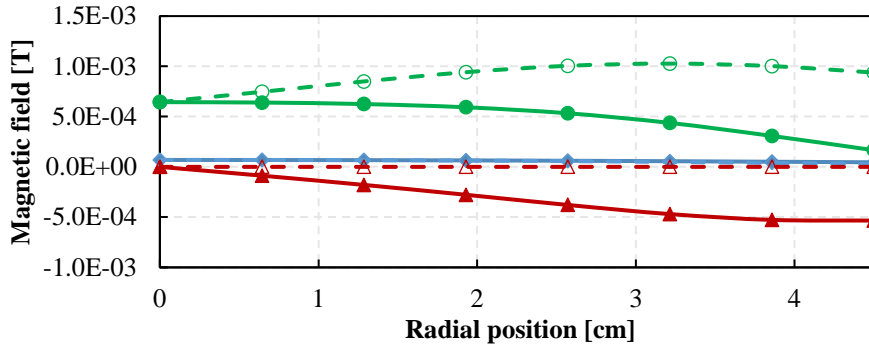
(a)



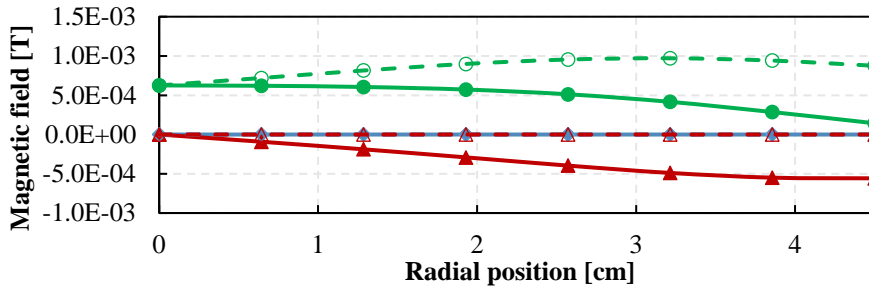
(b)



(c)



(d)



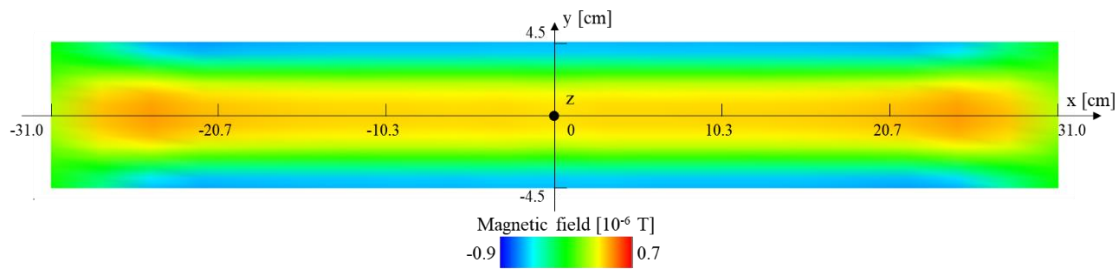
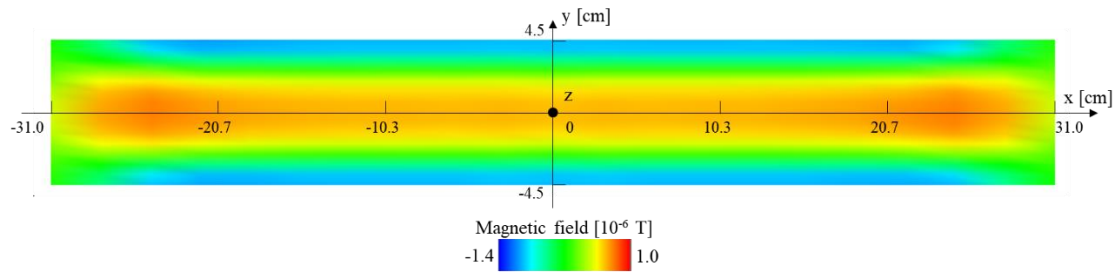
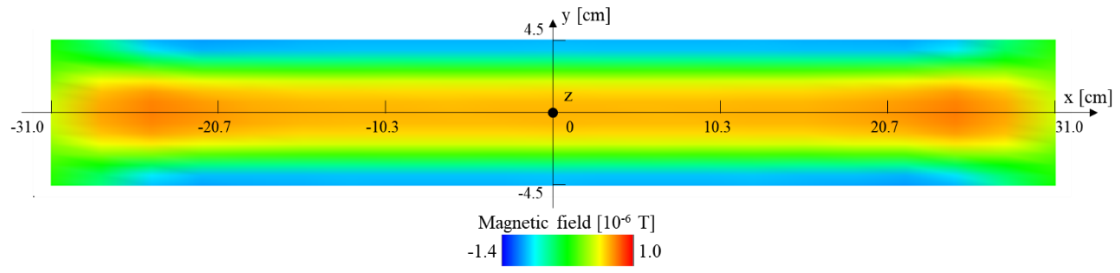
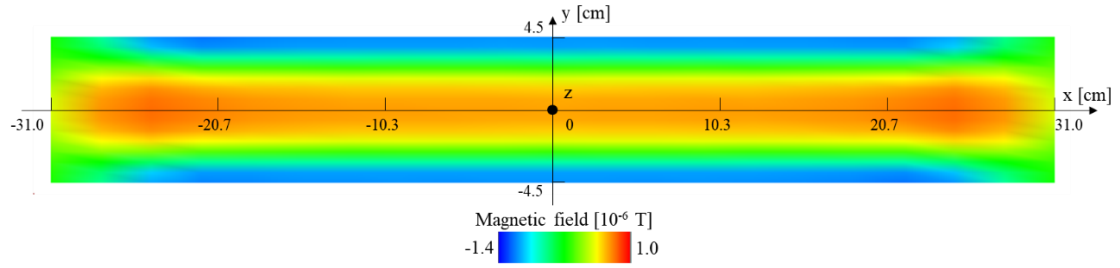
(e)

Fig. 3.3.22. X-direction, y-direction, and z-direction component of magnetic field at 880 s along the y-axis and z-axis at (a) $x = -31.0$ cm, (b) $x = -27.9$ cm, (c) $x = -24.8$ cm, (d) $x = -21.7$ cm, (e) $x = 0$ cm.

Next, the results of screening current induced field distribution are shown below. The distribution of z-direction, x-direction, and y-direction components of screening current induced field in the xy plane ($z = 0$) at certain times are indicated in Fig. 3.3.23–25. The distributions of different direction components show different patterns. The z-direction component increases when it is close to the x-axis and decreases to minus value when it is close to both sides of the measuring area. The x-direction component mainly appears in the coil end parts. The y-direction component mainly appears in the straight part, and shows a positive peak in the area near $y = -3$ cm and a negative peak in the area near $y = 3$ cm. The screening current induced field generally decreases in the process of time and is even reduced in the second cycle: the magnitude of screening current induced field decreases in 300 s from 100 s to 400 s and is even lower after the second ramp-up at 520 s. Additionally, we found that the magnitude of screening current induced field is not in proportion to the coil current: the screening current induced field decreases more greatly than the rate of coil current decrease.

Furthermore, the spatial distributions of x-direction, y-direction, and z-direction components of screening current induced field in the yz plane at certain times are indicated in Fig. 3.3.26–3.3.29. We found that the x-direction component mainly appears in the area of coil end parts and

the y-direction and z-direction components mainly appear in the space close to the REBCO tape because of the coil configuration. Additionally, the y-direction component is weaker than the z-direction component and stronger than the x-direction component. In general, the screening current induced field is much lower in the inner space close to the x-axis.



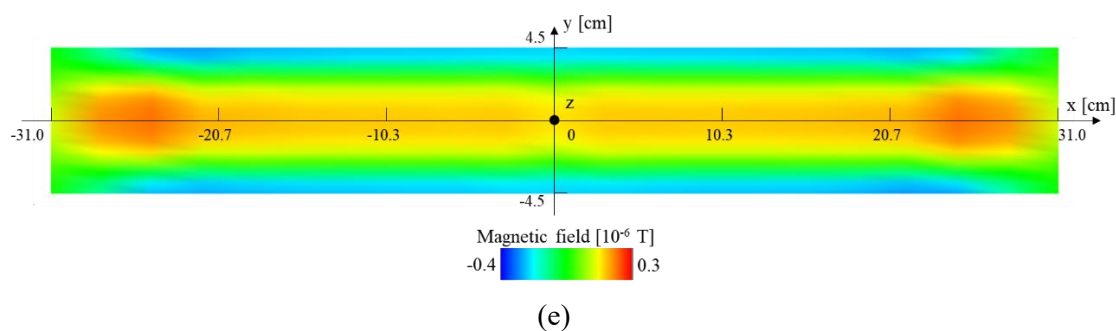
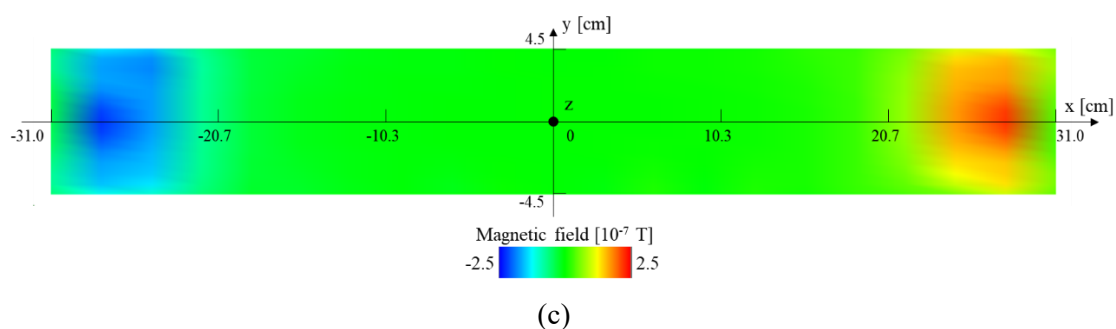
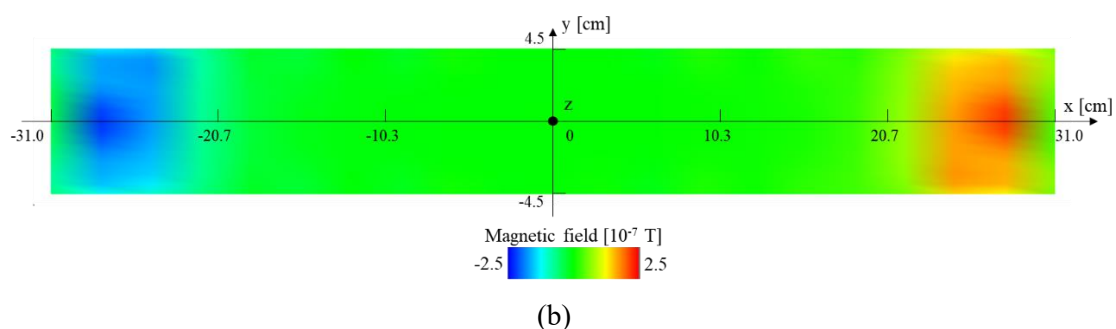
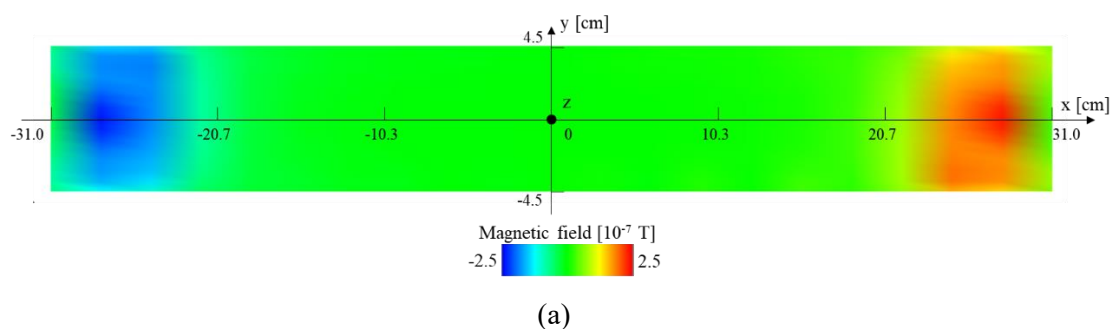


Fig. 3.3.23. Z-direction component of screening current induced field in the xy plane ($z = 0$) at (a) 100 s, (b) 400 s, (c) 520 s, (d) 845 s, (e) 880 s.



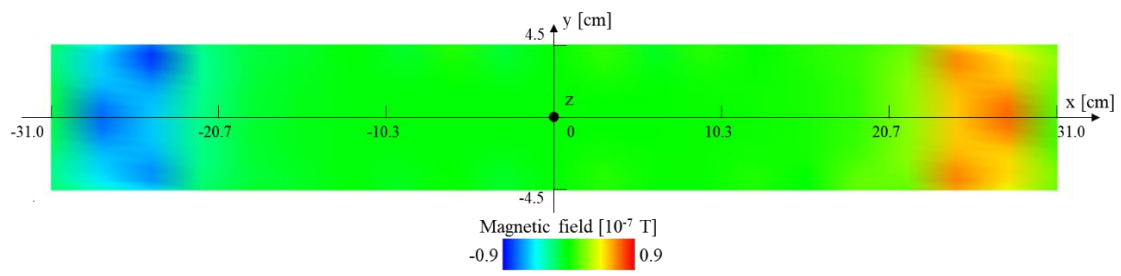
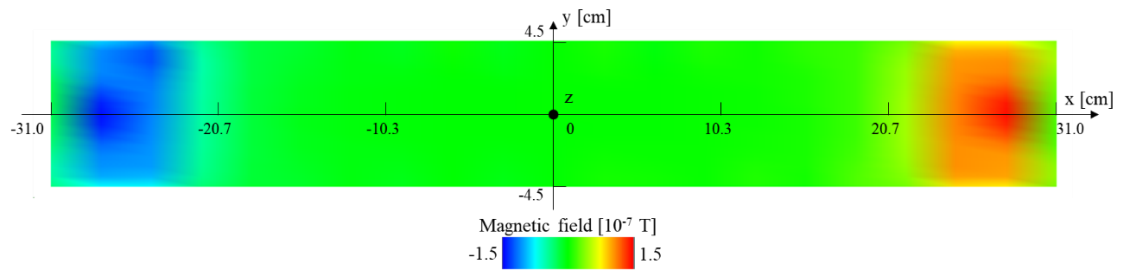
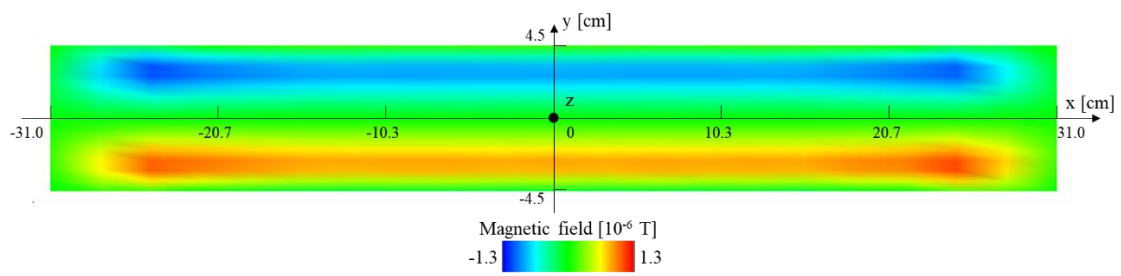
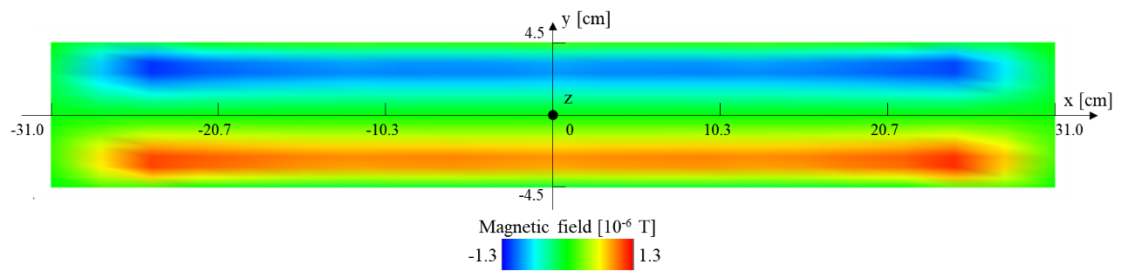
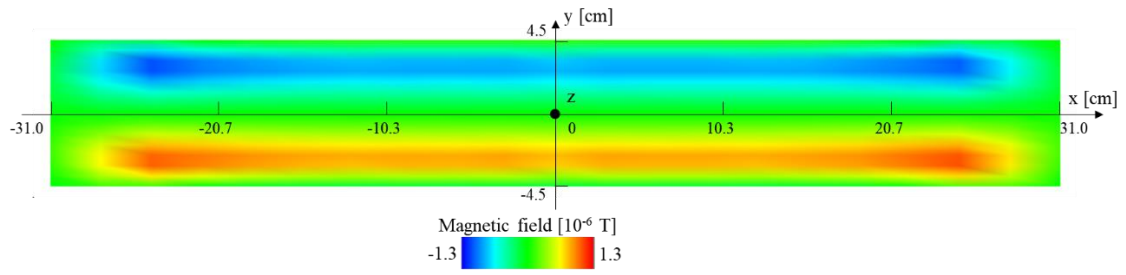
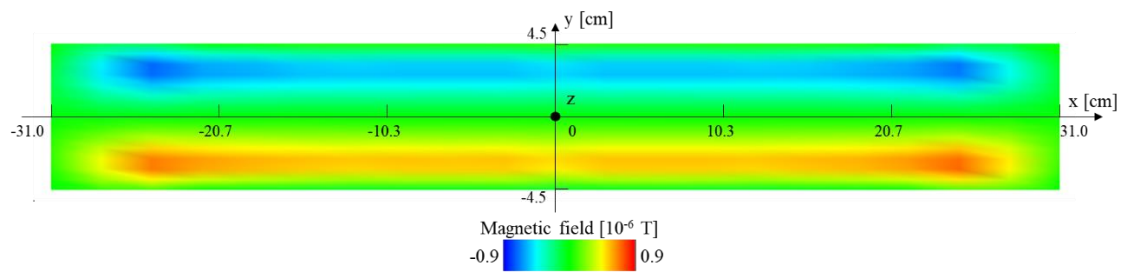


Fig. 3.3.24. X-direction component of screening current induced field in the xy plane ($z = 0$) at (a) 100 s, (b) 400 s, (c) 520 s, (d) 845 s, (e) 880 s.

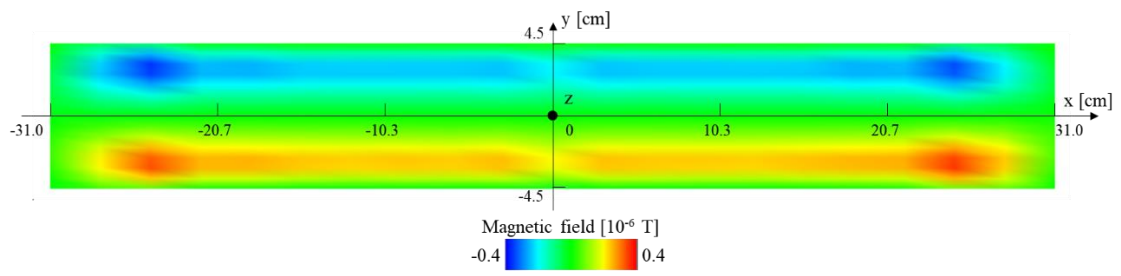




(c)

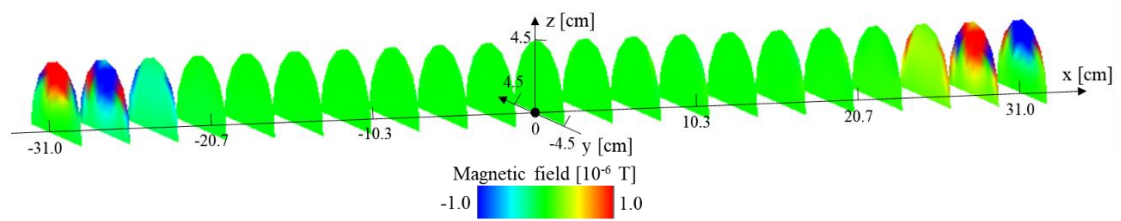


(d)

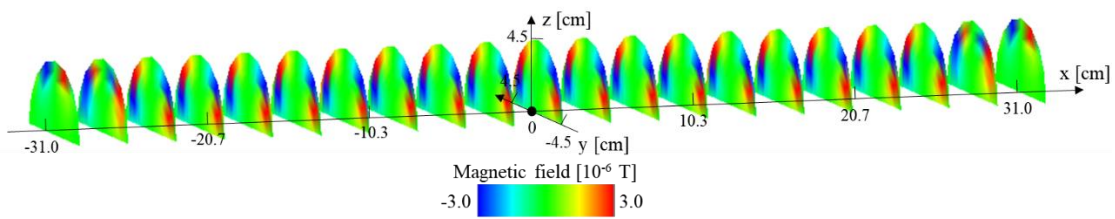


(e)

Fig. 3.3.25. Y-direction component of screening current induced field in the xy plane ($z = 0$) at (a) 100 s, (b) 400 s, (c) 520 s, (d) 845 s, (e) 880 s.



(a)



(b)

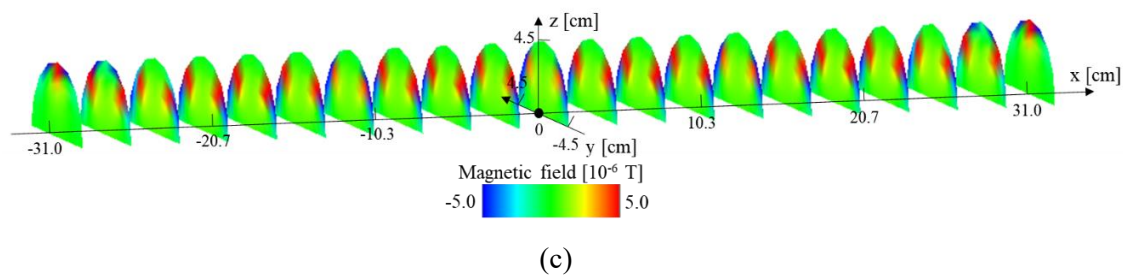


Fig. 3.3.26. (a) X-direction component, (b) y-direction component, (c) z-direction component of screening current induced field in the field measuring space at 100 s.

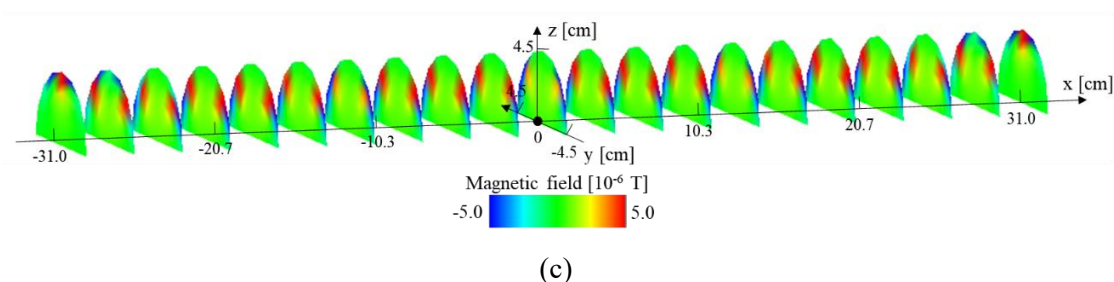
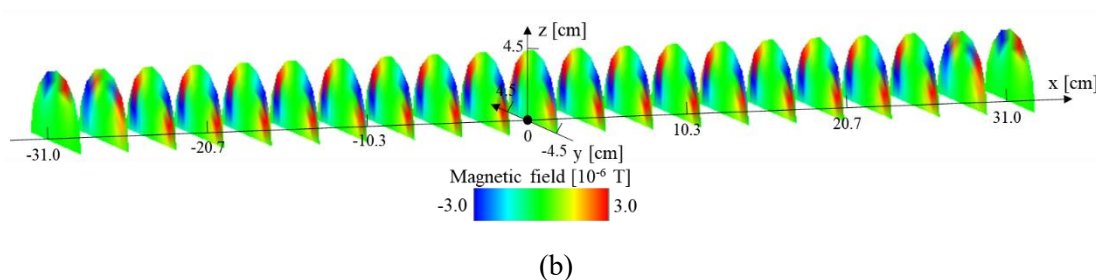
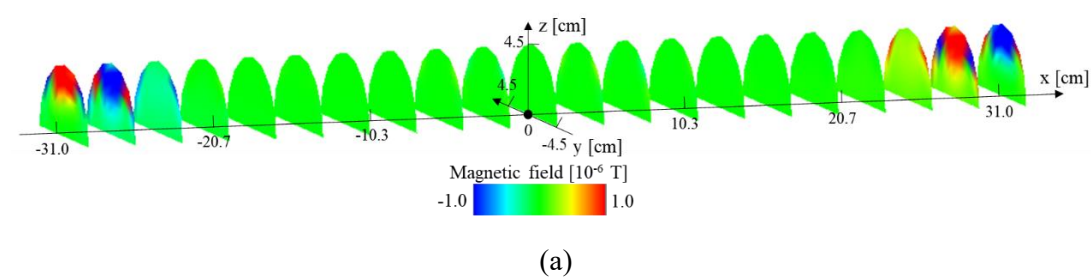
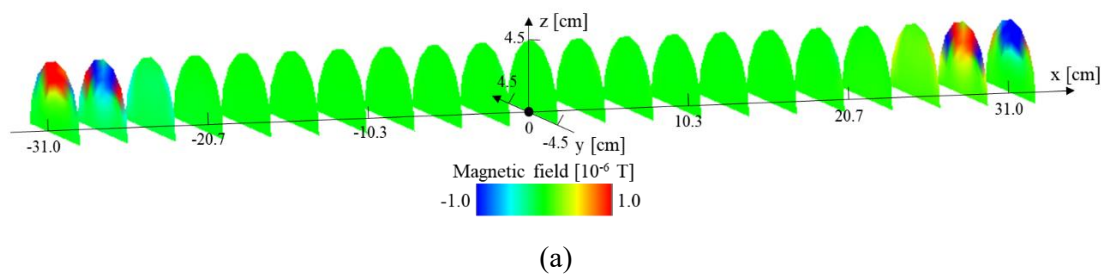
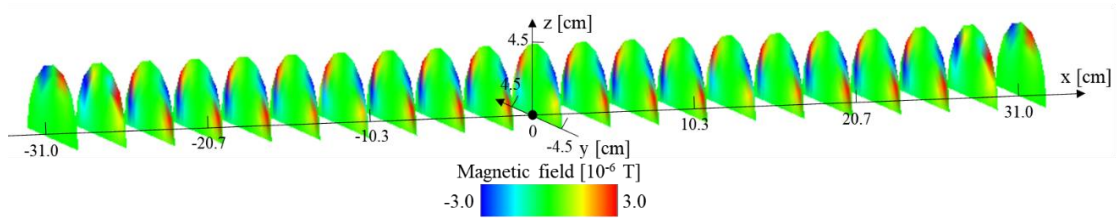
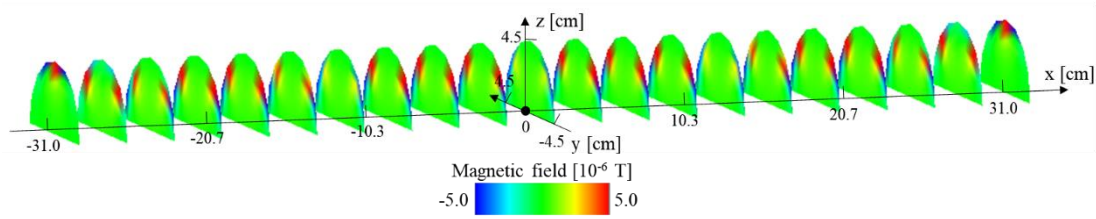


Fig. 3.3.27. (a) X-direction component, (b) y-direction component, (c) z-direction component of screening current induced field in the field measuring space at 520 s.



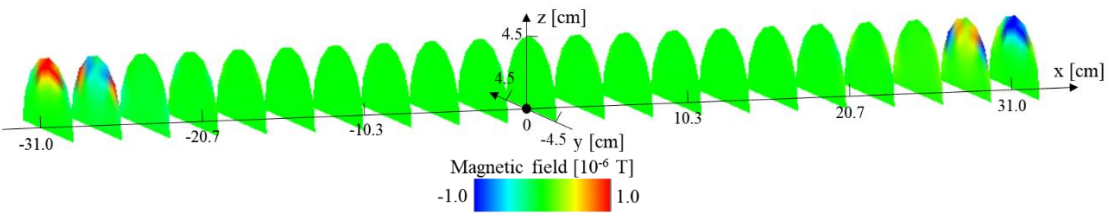


(b)

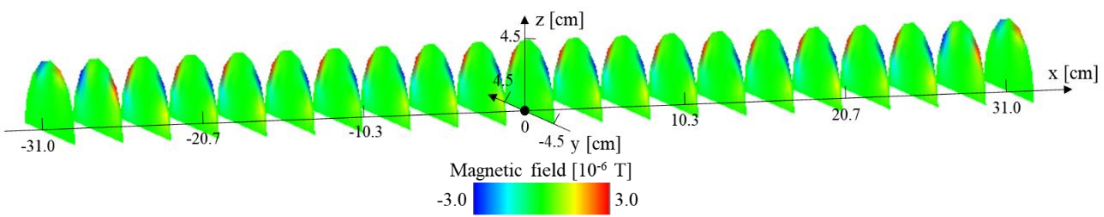


(c)

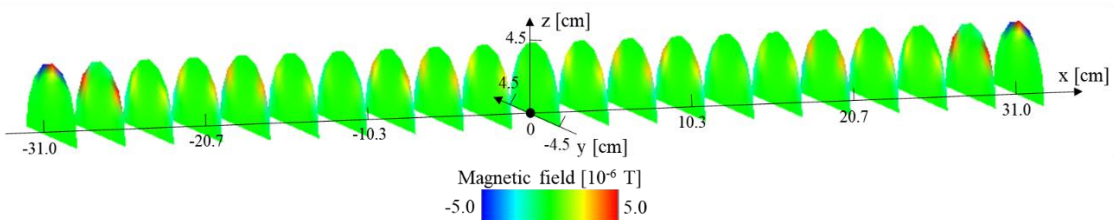
Fig. 3.3.28. (a) X-direction component, (b) y-direction component, (c) z-direction component of screening current induced field in the field measuring space at 845 s.



(a)



(b)



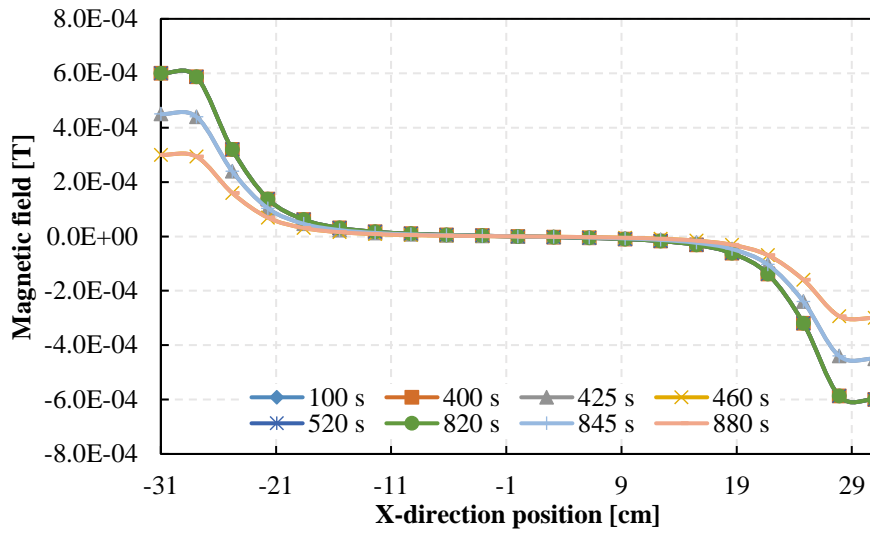
(c)

Fig. 3.3.29. (a) X-direction component, (b) y-direction component, (c) z-direction component of screening current induced field in the field measuring space at 880 s.

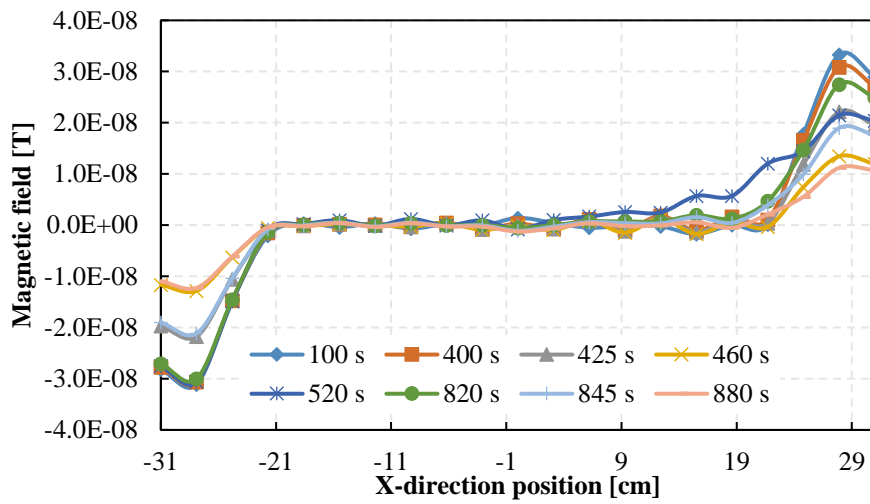
Furthermore, to analyze the distribution of screening current induced field more accurately, the specific data of x-direction, y-direction, and z-direction components along the x-axis, y-axis, and z-axis at certain times are summarized in Fig 3.3.30–3.3.34. In the cases of distribution along y-axis and z-axis, the yz planes of $x = -31$ cm, -27.9 cm, -24.8 cm, -21.7 cm, and 0 cm are chosen to study the difference of screening current induced field distribution between the coil end part and the straight part.

The distribution of magnetic field and screening current induced field along the x-axis ($y = 0$, $z = 0$) is shown in Fig. 3.3.30. The data verify the observation above that x-direction components of both fields enlarge significantly in the area of the coil ends, while the z-direction components increase when it comes to the straight part at any time. The y-direction component is neglectable along the x-axis in comparison with other components. The inhomogeneous distribution of screening current induced field would influence the homogeneity of the magnetic field and needed to be reduced.

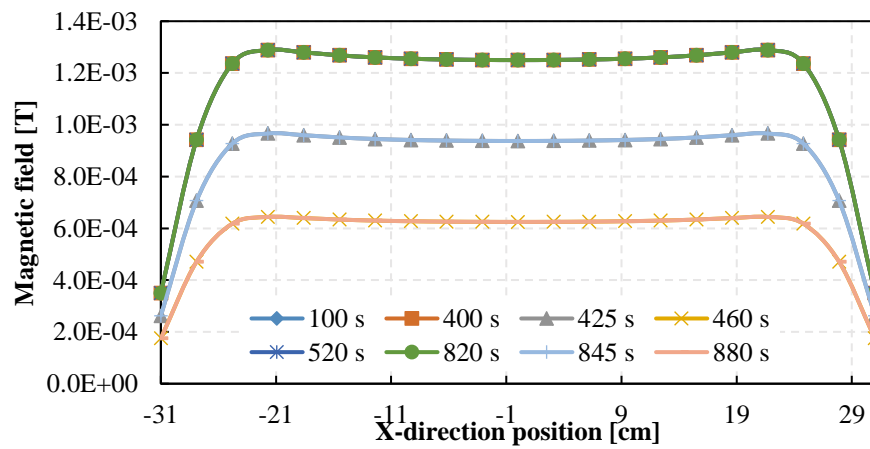
The distribution of screening current induced field along the y-axis and z-axis at certain times is shown in Fig. 3.3.31–3.3.34. The x-direction component mainly appears in the space close to the coil end and becomes neglectable in the straight part. The magnitude of y-direction component increases when it gets closer to the straight part and keeps roughly constant along the x-axis in the straight part because of the coil configuration. The z-direction component has the most complicated distribution. It reaches the peak in the coil end part. On the other hand, in the straight part, it decreases to minus value when the radial position changes from 0 to 4.5 cm, namely from the center to the edge of the measurement space. The magnitude of y-direction and z-direction components slightly decreases in the middle of the straight part at $x = 0$ in comparison with the rest space of the straight part because of the distribution of screening current density. In general, the magnitude of three direction components decreases to roughly half when the current declines from 200 A to 150 A, and further to about 25% when the coil current declines to 100 A.



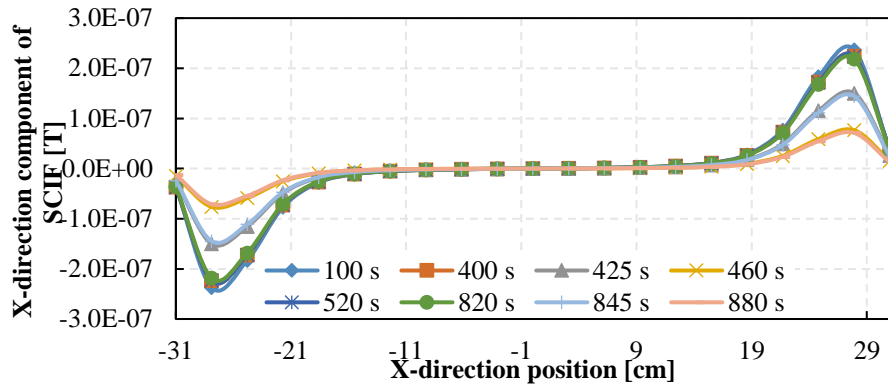
(a)



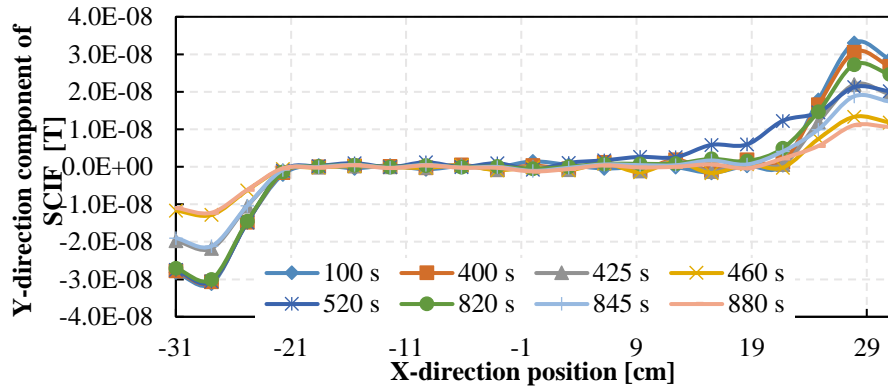
(b)



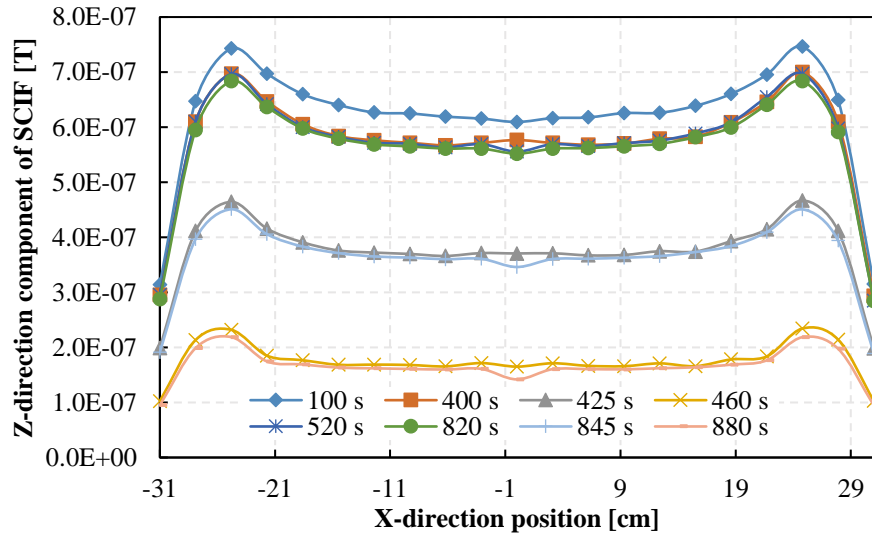
(c)



(d)

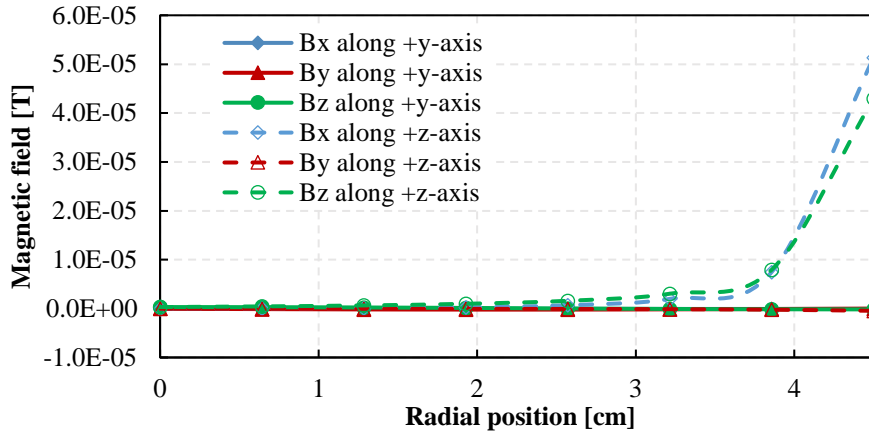


(e)

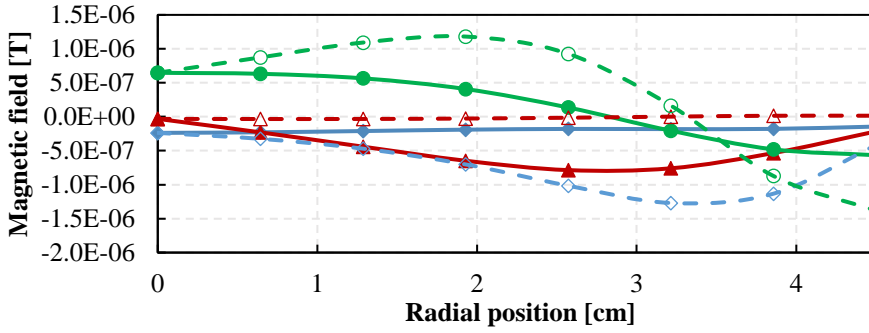


(f)

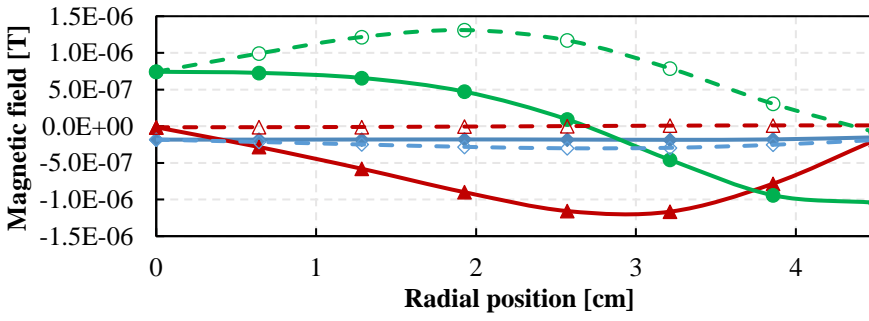
Fig. 3.3.30. (a) X-direction, (b) y-direction, and (c) z-direction component of magnetic field, (d) x-direction, (e) y-direction, and (f) z-direction component of screening current induced field (SCIF) along the x-axis ($y = 0$, $z = 0$) at certain times.



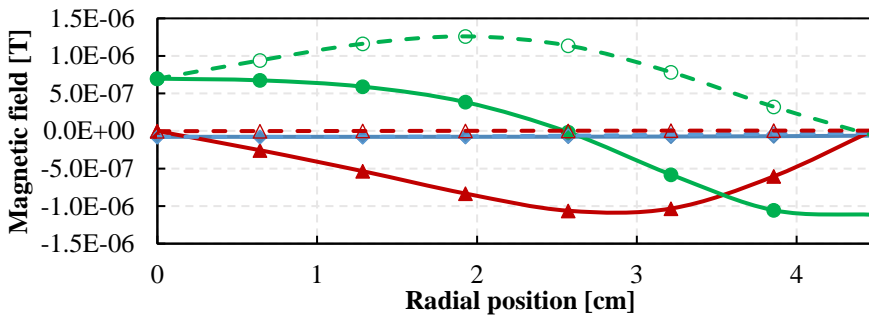
(a)



(b)



(c)



(d)

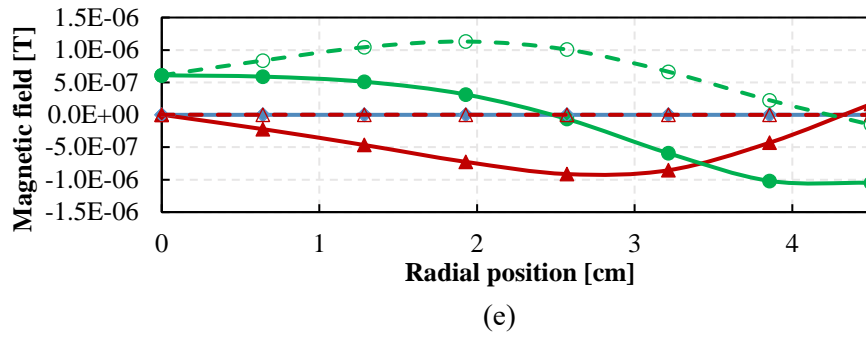
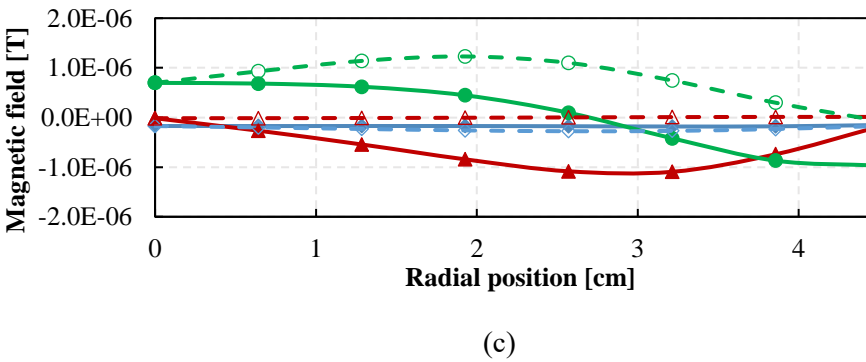
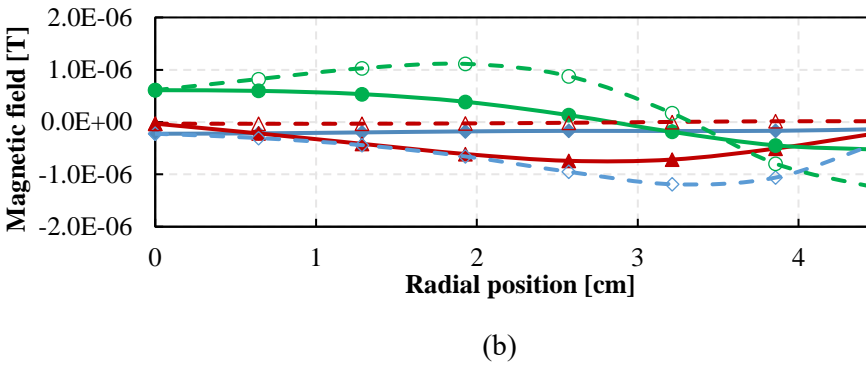
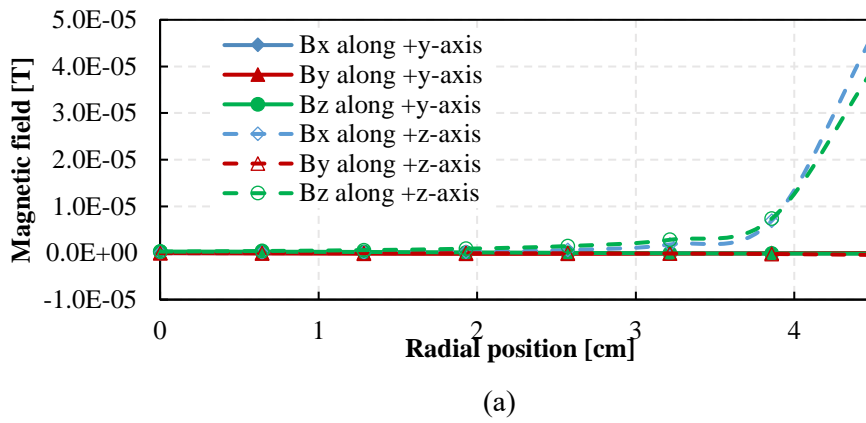
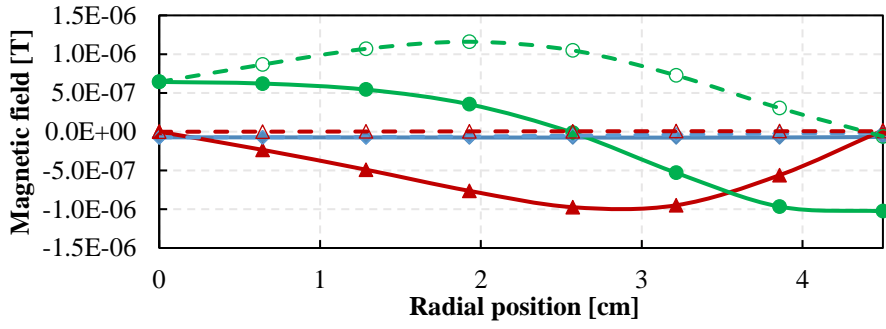
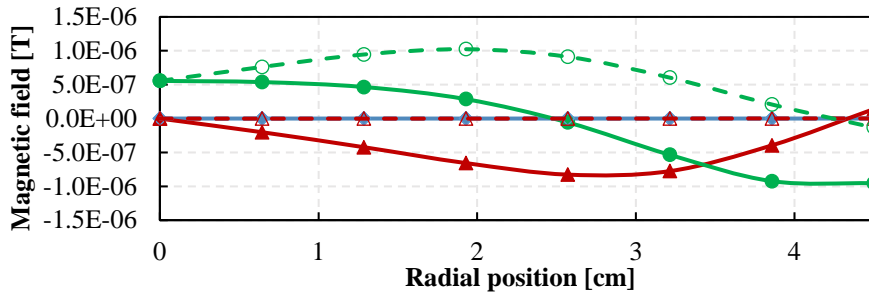


Fig. 3.3.31. X-direction, y-direction, and z-direction component of screening current induced field (SCIF) at 100 s along the y-axis and z-axis at (a) $x = -31.0$ cm, (b) $x = -27.9$ cm, (c) $x = -24.8$ cm, (d) $x = -21.7$ cm, (e) $x = 0$ cm.



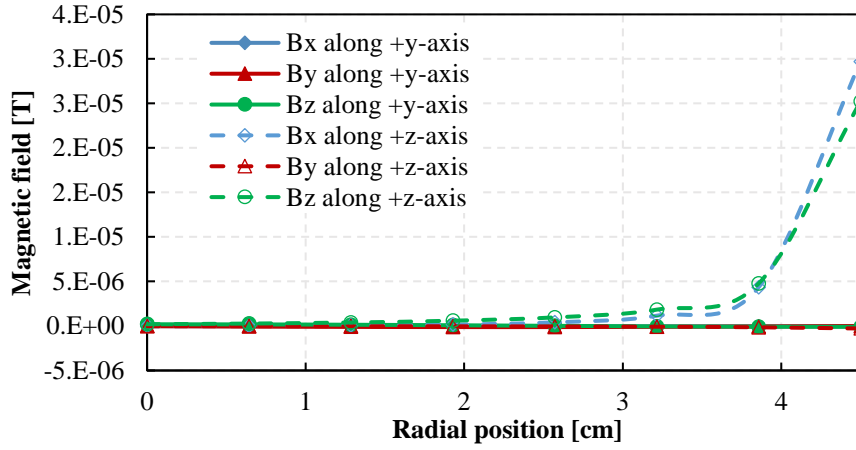


(d)

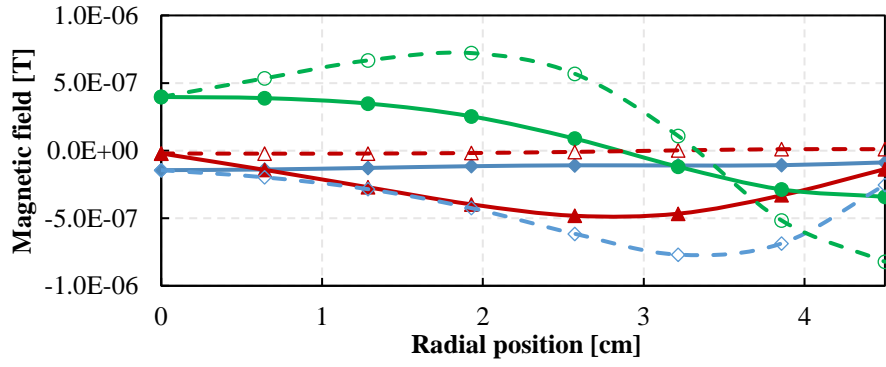


(e)

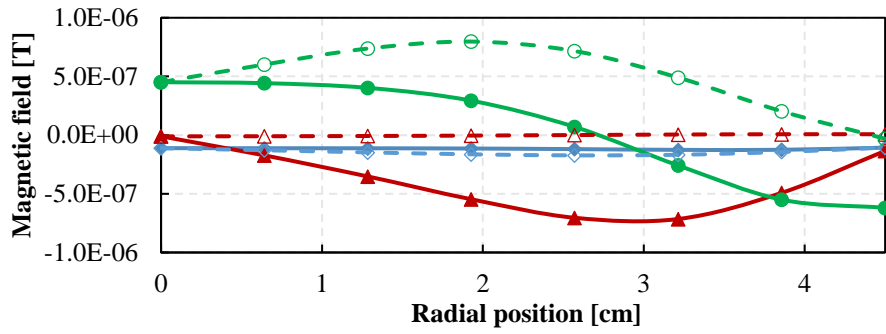
Fig. 3.3.32. X-direction, y-direction, and z-direction component of screening current induced field (SCIF) at 520 s along the y-axis and z-axis at (a) $x = -31.0$ cm, (b) $x = -27.9$ cm, (c) $x = -24.8$ cm, (d) $x = -21.7$ cm, (e) $x = 0$ cm.



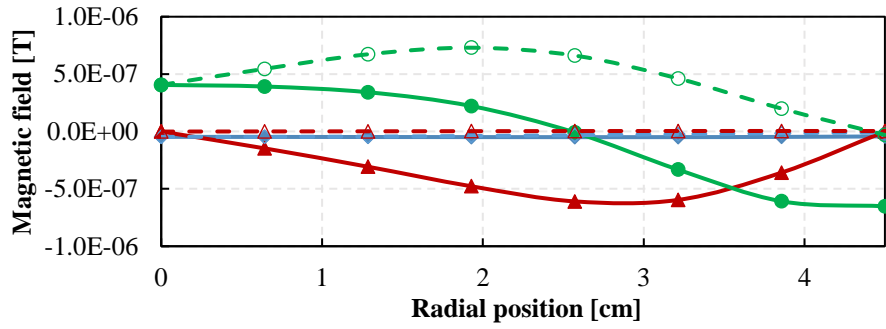
(a)



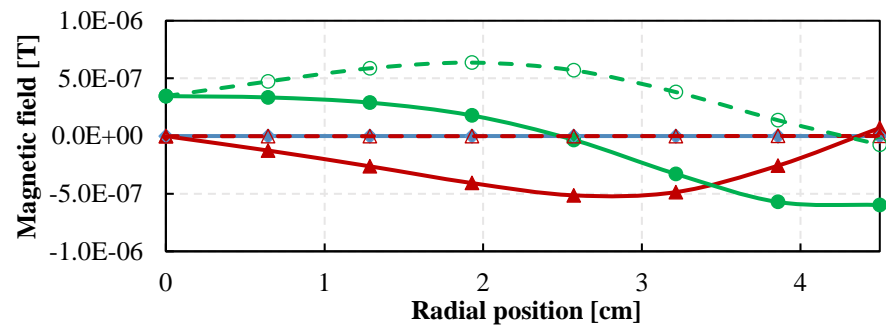
(b)



(c)

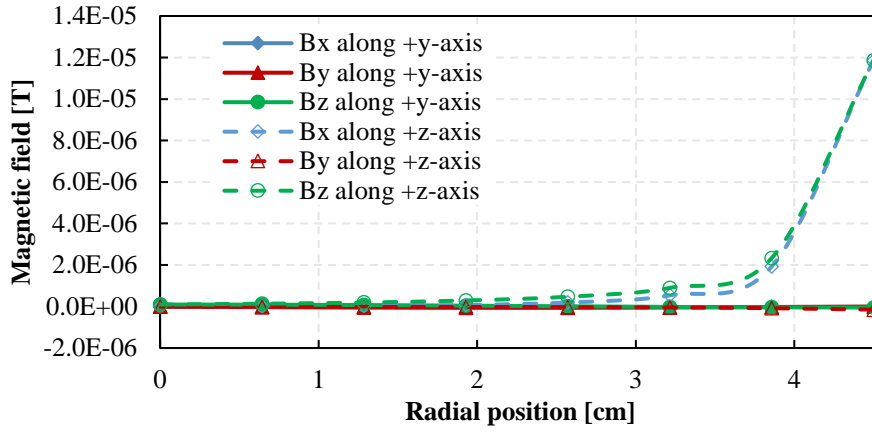


(d)

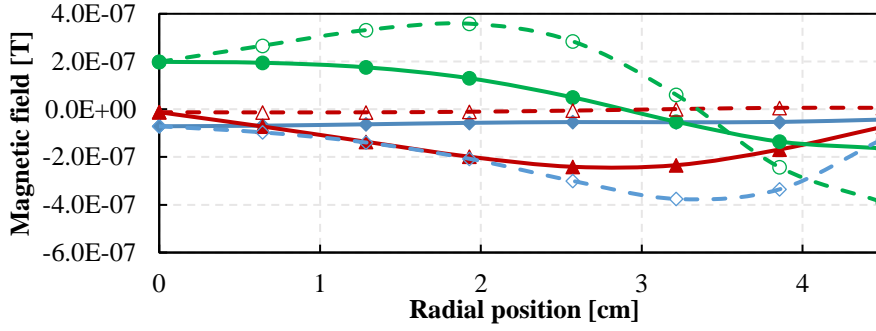


(e)

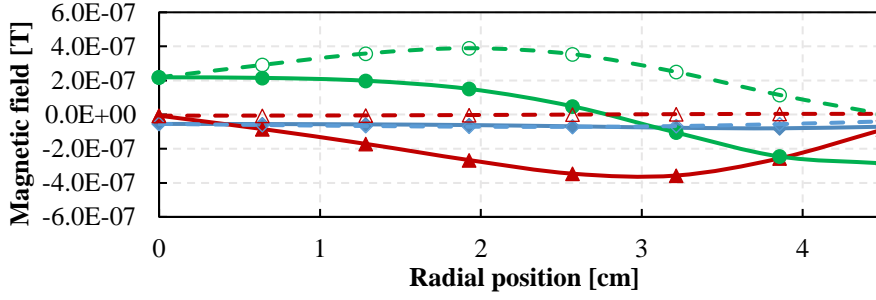
Fig. 3.3.33. X-direction, y-direction, and z-direction component of screening current induced field (SCIF) at 845 s along the y-axis and z-axis at (a) $x = -31.0$ cm, (b) $x = -27.9$ cm, (c) $x = -24.8$ cm, (d) $x = -21.7$ cm, (e) $x = 0$ cm.



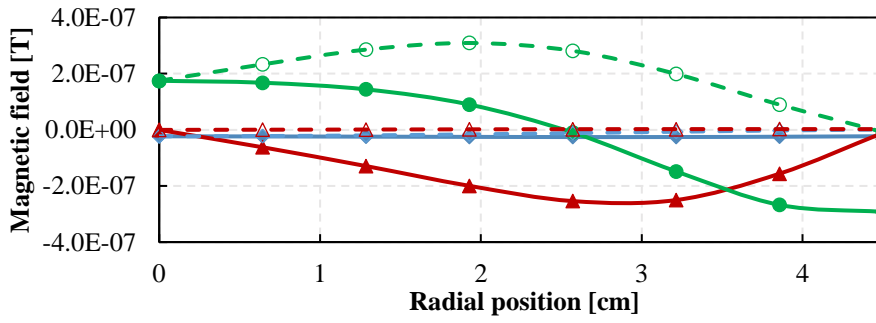
(a)



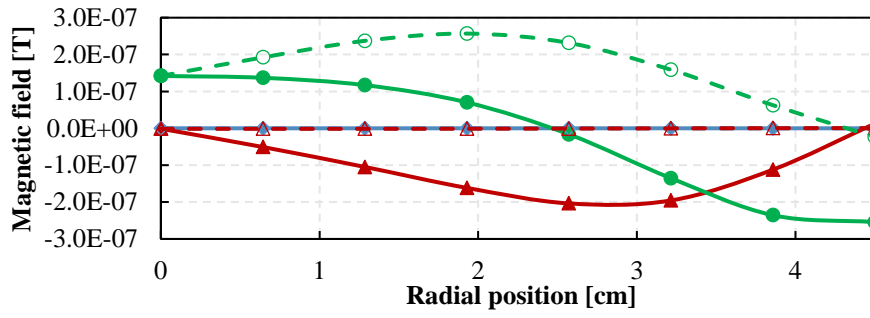
(b)



(c)



(d)



(e)

Fig. 3.3.34. X-direction, y-direction, and z-direction component of screening current induced field (SCIF) at 880 s along the y-axis and z-axis at (a) $x = -31.0$ cm, (b) $x = -27.9$ cm, (c) $x = -24.8$ cm, (d) $x = -21.7$ cm, (e) $x = 0$ cm.

Chapter 4. 3D Heat Transfer Analysis Method

4.1 Analysis Objects and Governing Equation

Finite elements method is utilized to calculate the heat transfer with the 3D temperature distribution. The analysis region of the REBCO tapes coinciding with substrate, cooling characteristics of liquid nitrogen, and heat sources originated in Joule loss in the Ag and superconductor layer are given by the boundary conditions. The coil bobbin and the gap between turns of REBCO conductors are also modelled as shown in Fig. 4.1. The heat transfer between different objects, such as bobbin and REBCO conductor, is also considered in this analysis.

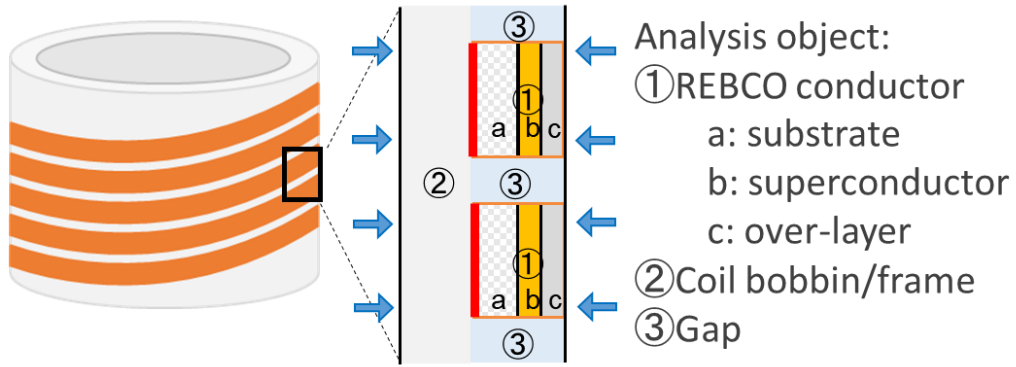


Fig. 4.1. Schematic diagram of the 3D heat transfer analysis model consisting of REBCO conductor, coil bobbin, and gap between conductors.

The 3D governing equation is derived as below.

$$\rho c \frac{\partial T}{\partial t} = \left\{ \frac{\partial}{\partial x} \left(\kappa \frac{\partial T}{\partial x} \right) + \frac{\partial}{\partial y} \left(\kappa \frac{\partial T}{\partial y} \right) + \frac{\partial}{\partial z} \left(\kappa \frac{\partial T}{\partial z} \right) \right\} \quad (4.1)$$

where κ is the thermal conductivity, T is the temperature, ρ is the mass density, c is the specific heat, and Q is the Joule heat. Additionally, the temperature dependence of κ , ρ , and c were considered in the analysis[72]–[75].

The heat flux q can be written as below according to the Fourier's law where \mathbf{n} is the outward normal vector.

$$q = -[\kappa] \frac{\partial T}{\partial \mathbf{n}} = -[\kappa](\mathbf{n} \cdot \nabla T) = \begin{bmatrix} \kappa & 0 & 0 \\ 0 & \kappa & 0 \\ 0 & 0 & \kappa \end{bmatrix} \begin{bmatrix} \frac{\partial T}{\partial x} n_x \\ \frac{\partial T}{\partial y} n_y \\ \frac{\partial T}{\partial z} n_z \end{bmatrix} \quad (4.2)$$

Galerkin method is used for discretization as below where $\{N\}$ is the matrix of weight function.

$$\iiint_V \{N\} \left\{ \frac{\partial}{\partial x} \left(\kappa \frac{\partial T}{\partial x} \right) + \frac{\partial}{\partial y} \left(\kappa \frac{\partial T}{\partial y} \right) + \frac{\partial}{\partial z} \left(\kappa \frac{\partial T}{\partial z} \right) - \rho c \frac{\partial T}{\partial t} \right\} dV = 0 \quad (4.3)$$

The temperature at certain position inside the element can be approximated with $\{N\}$ and nodal temperature $\{T\}_e$

$$T = \{N\}^T \{T\}_e \quad (4.4)$$

For further derivation, equation (4.3) is divided into two terms.

$$\iiint_V \{N\} \left\{ \frac{\partial}{\partial x} \left(\kappa \frac{\partial T}{\partial x} \right) + \frac{\partial}{\partial y} \left(\kappa \frac{\partial T}{\partial y} \right) + \frac{\partial}{\partial z} \left(\kappa \frac{\partial T}{\partial z} \right) \right\} dV \quad (4.5)$$

$$\iiint_V \{N\} dc \frac{\partial T}{\partial n} dV \quad (4.6)$$

Equation (4.7) can be applied to equation (4.5).

$$\iiint_V N \nabla^2 A dV = \iint_S V \nabla A \cdot \mathbf{n} dS - \iiint_V \nabla N \cdot \nabla A dV \quad (4.7)$$

Then,

$$\begin{aligned} & \iiint_V \{N\} \left\{ \frac{\partial}{\partial x} \left(\kappa \frac{\partial T}{\partial x} \right) + \frac{\partial}{\partial y} \left(\kappa \frac{\partial T}{\partial y} \right) + \frac{\partial}{\partial z} \left(\kappa \frac{\partial T}{\partial z} \right) \right\} dV \\ &= \iint_S \{N\} \left\{ \kappa \frac{\partial T}{\partial x} n_x + \kappa \frac{\partial T}{\partial y} n_y + \kappa \frac{\partial T}{\partial z} n_z \right\} dS \\ & - \iiint_V \left\{ \frac{\partial \{N\}}{\partial x} \left(\kappa \frac{\partial T}{\partial x} \right) + \frac{\partial \{N\}}{\partial y} \left(\kappa \frac{\partial T}{\partial y} \right) + \frac{\partial \{N\}}{\partial z} \left(\kappa \frac{\partial T}{\partial z} \right) \right\} dV \\ &= \iint_S \{N\} [\kappa] \frac{\partial T}{\partial \mathbf{n}} dS \\ & - \iiint_V \left\{ \frac{\partial \{N\}}{\partial x} \left(\kappa \frac{\partial \{N\}^T}{\partial x} \right) + \frac{\partial \{N\}}{\partial y} \left(\kappa \frac{\partial \{N\}^T}{\partial y} \right) + \frac{\partial \{N\}}{\partial z} \left(\kappa \frac{\partial \{N\}^T}{\partial z} \right) \right\} dV \{T\}_e \end{aligned} \quad (4.8)$$

The first term can be derived with equation (4.2) as below.

$$\iint_S \{N\} [\kappa] \frac{\partial T}{\partial n} dS = - \iint_S q \{N\} dS \quad (4.9)$$

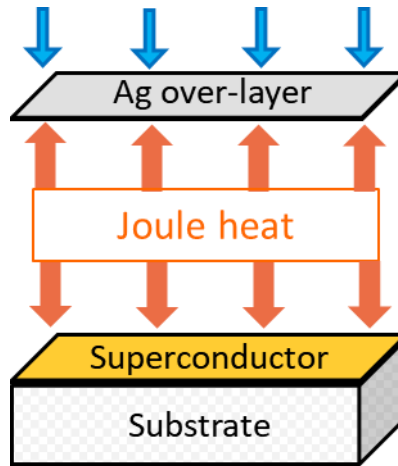
Equation (4.6) can be discretized by inserting (4.4) as below.

$$\iiint_V \{N\} dc \frac{\partial T}{\partial n} dV = \iiint_V \{N\} dc \frac{\partial \{N\}^T}{\partial n} dV \{T\}_e \quad (4.10)$$

Consequently, the governing equation is discretized by Galerkin method as below.

$$\begin{aligned} & \iiint_V \left\{ \frac{\partial \{N\}}{\partial x} \left(\kappa \frac{\partial \{N\}^T}{\partial x} \right) + \frac{\partial \{N\}}{\partial y} \left(\kappa \frac{\partial \{N\}^T}{\partial y} \right) + \frac{\partial \{N\}}{\partial z} \left(\kappa \frac{\partial \{N\}^T}{\partial z} \right) \right\} dV \{T\}_e \\ & + \iint_S q \{N\} dS + \iiint_V \{N\} \{N\}^T dc \frac{\partial \{T\}_e}{\partial n} dV = 0 \end{aligned} \quad (4.11)$$

Next, the terms that influence the boundary conditions are introduced. Generally, regarding the boundary conditions of the thermal problem, four conditions are considered: temperature condition, heat flux condition, heat transfer condition, and heat radiation. In this analysis, heat flux conditions including Joule heat of REBCO conductors and cooling effect of coolant (e.g. liquid nitrogen), and heat transfer conditions between objects are considered. Explanatory diagrams of the boundary conditions considering Joule heat and coolant cooling are shown in Fig. 4.2.



(a)

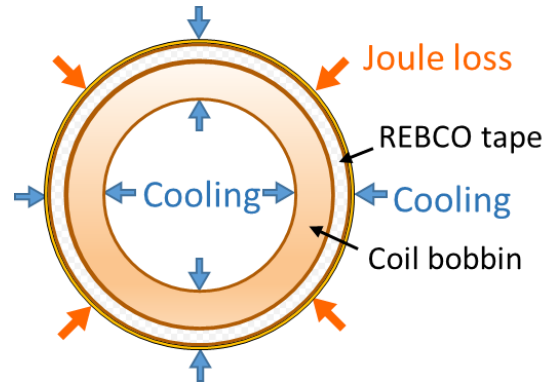


Fig. 4.2. Schematic diagram of the boundary conditions considering (a) Joule heat and (b) coolant cooling.

The heat flux condition is the condition considering the heat flux exchange at the boundary S_1 and defined as equation (4.12). The heat flux q_0 consists of REBCO conductors' Joule heating and the coolant cooling which calculated with coolant's boiling curve. In addition, the Joule heat is calculated in the electromagnetic analysis by $Q = J \cdot E$, where Q is the heating power. The boiling curve is introduced in sector 4.1.3.

$$q = q_0 \quad (4.12)$$

Then the second term in equation (4.11) equals to (4.13).

$$\iint_{S_1} q \{N\} dS = \iint_{S_1} q_0 \{N\} dS \quad (4.13)$$

The heat transfer condition considers the heat flux between solid objects and liquid (e.g. the coolant) and is calculated with the heat transfer coefficient α and liquid temperature T_{fluid} as (4.14). The boiling curve is considered here.

$$\begin{aligned} \iint_{S_2} q \{N\} dS &= \iint_{S_2} \alpha (T - T_{fluid}) \{N\} dS \\ &= \iint_{S_2} \alpha \{N\} \{N\}^T dS \{T\}_e - \iint_{S_2} \alpha T_{fluid} \{N\} dS \end{aligned} \quad (4.14)$$

Consequently, the governing equation (4.11) can be discretized as below,

$$[S] \{T\} + [C] \left\{ \frac{\partial T}{\partial t} \right\} = \{F\} \quad (4.15)$$

where

$$\begin{aligned}
[S] = & \iiint_V \left\{ \frac{\partial \{N\}}{\partial x} \left(\kappa \frac{\partial \{N\}^T}{\partial x} \right) + \frac{\partial}{\partial y} \left(\kappa \frac{\partial \{N\}^T}{\partial y} \right) + \frac{\partial}{\partial z} \left(\kappa \frac{\partial \{N\}^T}{\partial z} \right) \right\} dV \\
& + \iint_{S_2} \alpha \{N\} \{N\}^T dS
\end{aligned} \tag{4.16}$$

$$[C] = \iiint_V dc \{N\} \{N\}^T dV \tag{4.17}$$

$$\{F\} = - \iint_{S_1} q_0 \{N\} dS + \iint_{S_2} \alpha T_{fluid} \{N\} dS \tag{4.18}$$

$[S]$ is the matrix of heat conduction, $[C]$ is the matrix of heat capacity, and $\{F\}$ is the vector of heat flux.

Furthermore, the specific value of interpolation function $\{N\}$ of each element differs depending on the element. In this analysis, hexahedral first-order elements are used for discretization. In the three-dimensional analysis, the integral calculation is performed in the local coordinate system, and the mapping conversion is performed in the whole coordinate system. The formulation of the coordinate system is explained in Section 4.1.2. In addition, Section 4.1.2 also describes the details of the partial differentiation of the interpolation function in the global coordinate system, the derivation of the integral coefficients of the volume integral and the area integral, which are required in the discretization process, and the numerical integration.

For numerical integration, the time derivative term in the transient analysis is approximated with the receding difference of the first order as follows.

$$[S]\{T\}^k + [C] \frac{\{T\}^k - \{T\}^{k-1}}{\Delta t} = \{F\} \tag{4.19}$$

$$\left([S] + \frac{1}{\Delta t} [C] \right) \{T\}^k = \{F\} + \frac{1}{\Delta t} [C] \{T\}^{k-1} \tag{4.20}$$

The superscript of temperature is a time index, and $k-1$ represents the previous time step. Also, Δt is the time step width. Since the node temperature $\{T\}^{k-1}$ of the previous time step is known, the left side of (4.20) contains the unknowns, and the right side is the term of the known quantity. Finally, $\{T\}^k$ is solved with the simultaneous linear equations.

4.2 Galerkin Discretization with Hexahedron First-order Elements

In the 3D heat transfer analysis, formulation in the local coordinate system (p, q, r) is necessary in order to perform integral calculation in the local coordinate system and mapping it to the whole coordinate system. First, the temperature T at an arbitrary point inside the element in the

normalized local coordinate system can be expressed as follows using the scalar interpolation function $\{N\}$.

$$T(p, q, r) = \{N\}^T \{T\}_e \quad (4.21)$$

where $\{N\}$ is defined in the local coordinate system as below ($-1 \leq p, q, r \leq 1$).

$$N_i = \frac{1}{8}(1 + pp_i)(1 + qq_i)(1 + rr_i) \quad (4.22)$$

The schematic diagram of the hexahedron first-order element is shown in Fig. 4.3. Eight interpolation coefficients are necessary for each node in an element and they are defined as below.

$$\{N\} = \begin{bmatrix} N_1 \\ N_2 \\ N_3 \\ N_4 \\ N_5 \\ N_6 \\ N_7 \\ N_8 \end{bmatrix} = \frac{1}{8} \begin{bmatrix} (1-p)(1-q)(1-r) \\ (1+p)(1-q)(1-r) \\ (1-p)(1+q)(1-r) \\ (1+p)(1+q)(1-r) \\ (1-p)(1-q)(1+r) \\ (1-p)(1-q)(1+r) \\ (1+p)(1+q)(1+r) \\ (1-p)(1+q)(1+r) \end{bmatrix} \quad (4.23)$$

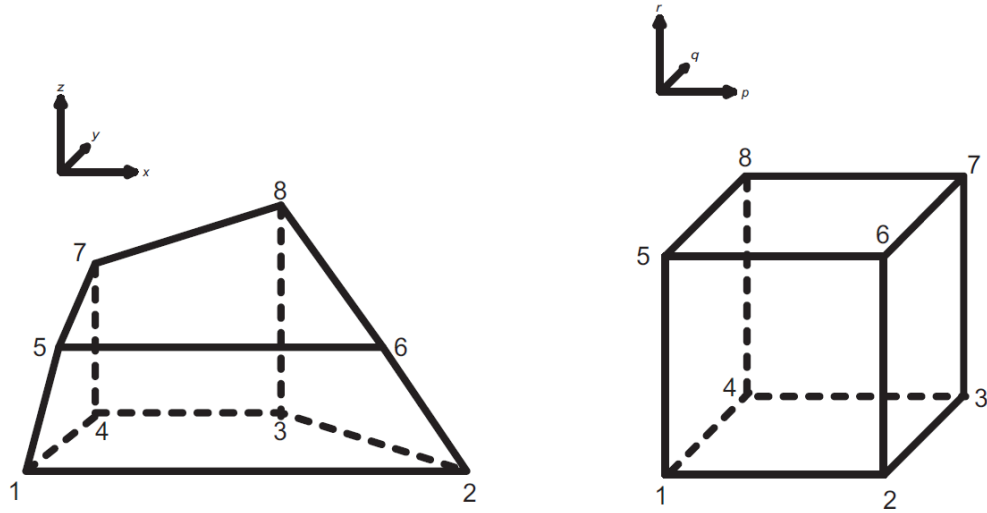


Fig. 4.3. Schematic diagram of the hexahedron first-order element in the global coordinate system (left) and local coordinate system (right).

Next, the partial differential of interpolation function is derived as below.

Partial derivative with respect to p :

$$\begin{aligned}
\frac{\partial N_1}{\partial p} &= -\frac{1}{8}(1-q)(1-r) \\
\frac{\partial N_2}{\partial p} &= \frac{1}{8}(1-q)(1-r) \\
\frac{\partial N_3}{\partial p} &= \frac{1}{8}(1+q)(1-r) \\
\frac{\partial N_4}{\partial p} &= -\frac{1}{8}(1+q)(1-r) \\
\frac{\partial N_5}{\partial p} &= -\frac{1}{8}(1-q)(1+r) \\
\frac{\partial N_6}{\partial p} &= \frac{1}{8}(1-q)(1+r) \\
\frac{\partial N_7}{\partial p} &= \frac{1}{8}(1+q)(1+r) \\
\frac{\partial N_8}{\partial p} &= -\frac{1}{8}(1+q)(1+r)
\end{aligned} \tag{4.24}$$

Partial derivative with respect to q :

$$\begin{aligned}
\frac{\partial N_1}{\partial q} &= -\frac{1}{8}(1-p)(1-r) \\
\frac{\partial N_2}{\partial q} &= -\frac{1}{8}(1+p)(1-r) \\
\frac{\partial N_3}{\partial q} &= \frac{1}{8}(1-p)(1-r) \\
\frac{\partial N_4}{\partial q} &= \frac{1}{8}(1-p)(1-r) \\
\frac{\partial N_5}{\partial q} &= -\frac{1}{8}(1-q)(1+r) \\
\frac{\partial N_6}{\partial q} &= -\frac{1}{8}(1+q)(1+r) \\
\frac{\partial N_7}{\partial q} &= \frac{1}{8}(1+q)(1+r) \\
\frac{\partial N_8}{\partial q} &= \frac{1}{8}(1-q)(1+r)
\end{aligned} \tag{4.25}$$

Partial derivative with respect to r :

$$\begin{aligned}
\frac{\partial N_1}{\partial r} &= -\frac{1}{8}(1-p)(1-q) \\
\frac{\partial N_2}{\partial r} &= -\frac{1}{8}(1+p)(1-q) \\
\frac{\partial N_3}{\partial r} &= -\frac{1}{8}(1+p)(1+q) \\
\frac{\partial N_4}{\partial r} &= -\frac{1}{8}(1+p)(1+q) \\
\frac{\partial N_5}{\partial r} &= \frac{1}{8}(1-p)(1-q) \\
\frac{\partial N_6}{\partial r} &= \frac{1}{8}(1+p)(1-q) \\
\frac{\partial N_7}{\partial r} &= \frac{1}{8}(1+p)(1+q) \\
\frac{\partial N_8}{\partial r} &= \frac{1}{8}(1-p)(1+q)
\end{aligned} \tag{4.26}$$

In the hexahedral element, the global and local coordinates can be transformed with the interpolation function $\{N\}$ and the coordinates of nodes (in xyz coordinate system) $\{x\}_e$, $\{y\}_e$, $\{z\}_e$ as below. Hence, (x, y, z) can be considered to be functions of (p, q, r) .

$$\begin{aligned}
x(p, q, r) &= \{N\}^T \{x\}_e \\
y(p, q, r) &= \{N\}^T \{y\}_e \\
z(p, q, r) &= \{N\}^T \{z\}_e
\end{aligned} \tag{4.27}$$

The relationship between partial differential in xyz coordinate system and the local coordinate system is shown in (4.28).

$$\begin{aligned}
\frac{\partial \{N\}}{\partial p} &= \frac{\partial \{N\}}{\partial x} \frac{\partial x}{\partial p} + \frac{\partial \{N\}}{\partial y} \frac{\partial y}{\partial p} + \frac{\partial \{N\}}{\partial z} \frac{\partial z}{\partial p} \\
\frac{\partial \{N\}}{\partial q} &= \frac{\partial \{N\}}{\partial x} \frac{\partial x}{\partial q} + \frac{\partial \{N\}}{\partial y} \frac{\partial y}{\partial q} + \frac{\partial \{N\}}{\partial z} \frac{\partial z}{\partial q} \\
\frac{\partial \{N\}}{\partial r} &= \frac{\partial \{N\}}{\partial x} \frac{\partial x}{\partial r} + \frac{\partial \{N\}}{\partial y} \frac{\partial y}{\partial r} + \frac{\partial \{N\}}{\partial z} \frac{\partial z}{\partial r}
\end{aligned} \tag{4.28}$$

which can be expressed with matrix

$$\begin{bmatrix} \frac{\partial \{N\}}{\partial p} \\ \frac{\partial \{N\}}{\partial q} \\ \frac{\partial \{N\}}{\partial r} \end{bmatrix} = \begin{bmatrix} \frac{\partial x}{\partial p} & \frac{\partial y}{\partial p} & \frac{\partial z}{\partial p} \\ \frac{\partial x}{\partial q} & \frac{\partial y}{\partial q} & \frac{\partial z}{\partial q} \\ \frac{\partial x}{\partial r} & \frac{\partial y}{\partial r} & \frac{\partial z}{\partial r} \end{bmatrix} \begin{bmatrix} \frac{\partial \{N\}}{\partial x} \\ \frac{\partial \{N\}}{\partial y} \\ \frac{\partial \{N\}}{\partial z} \end{bmatrix} = [J] \begin{bmatrix} \frac{\partial \{N\}}{\partial x} \\ \frac{\partial \{N\}}{\partial y} \\ \frac{\partial \{N\}}{\partial z} \end{bmatrix} \quad (4.29)$$

$[J]$ is the Jacobian matrix that defined as below.

$$[J] = \begin{bmatrix} \frac{\partial x}{\partial p} & \frac{\partial y}{\partial p} & \frac{\partial z}{\partial p} \\ \frac{\partial x}{\partial q} & \frac{\partial y}{\partial q} & \frac{\partial z}{\partial q} \\ \frac{\partial x}{\partial r} & \frac{\partial y}{\partial r} & \frac{\partial z}{\partial r} \end{bmatrix} = \begin{bmatrix} \frac{\partial \{N\}^T}{\partial p} \{x\}_e & \frac{\partial \{N\}^T}{\partial p} \{y\}_e & \frac{\partial \{N\}^T}{\partial p} \{z\}_e \\ \frac{\partial \{N\}^T}{\partial q} \{x\}_e & \frac{\partial \{N\}^T}{\partial q} \{y\}_e & \frac{\partial \{N\}^T}{\partial q} \{z\}_e \\ \frac{\partial \{N\}^T}{\partial r} \{x\}_e & \frac{\partial \{N\}^T}{\partial r} \{y\}_e & \frac{\partial \{N\}^T}{\partial r} \{z\}_e \end{bmatrix} \quad (4.30)$$

In discretization, the partial differentials of interpolation function $\{N\}$ in the global coordinate system are necessary and can be transformed from

$$\begin{bmatrix} \frac{\partial \{N\}}{\partial x} \\ \frac{\partial \{N\}}{\partial y} \\ \frac{\partial \{N\}}{\partial z} \end{bmatrix} = [J]^{-1} \begin{bmatrix} \frac{\partial \{N\}}{\partial p} \\ \frac{\partial \{N\}}{\partial q} \\ \frac{\partial \{N\}}{\partial r} \end{bmatrix} \quad (4.31)$$

Then, the inverse matrix Jacobian matrix is needed in (4.31) which can be derived as below.

$$[J]^{-1} = \frac{1}{\det |J|} \begin{bmatrix} \frac{\partial \{N\}}{\partial p} \\ \frac{\partial \{N\}}{\partial q} \\ \frac{\partial \{N\}}{\partial r} \end{bmatrix} = \begin{bmatrix} \frac{\partial y}{\partial q} \frac{\partial z}{\partial r} - \frac{\partial z}{\partial q} \frac{\partial y}{\partial r} & \frac{\partial z}{\partial p} \frac{\partial y}{\partial r} - \frac{\partial y}{\partial p} \frac{\partial z}{\partial r} & \frac{\partial y}{\partial p} \frac{\partial z}{\partial q} - \frac{\partial z}{\partial p} \frac{\partial y}{\partial q} \\ \frac{\partial z}{\partial q} \frac{\partial x}{\partial r} - \frac{\partial x}{\partial q} \frac{\partial z}{\partial r} & \frac{\partial x}{\partial p} \frac{\partial z}{\partial r} - \frac{\partial z}{\partial p} \frac{\partial x}{\partial r} & \frac{\partial z}{\partial p} \frac{\partial x}{\partial q} - \frac{\partial x}{\partial p} \frac{\partial z}{\partial q} \\ \frac{\partial x}{\partial q} \frac{\partial y}{\partial r} - \frac{\partial y}{\partial q} \frac{\partial x}{\partial r} & \frac{\partial y}{\partial p} \frac{\partial x}{\partial r} - \frac{\partial x}{\partial p} \frac{\partial y}{\partial r} & \frac{\partial x}{\partial p} \frac{\partial y}{\partial q} - \frac{\partial y}{\partial p} \frac{\partial x}{\partial q} \end{bmatrix} \quad (4.32)$$

where

$$\det |J| = \frac{\partial x}{\partial p} \left(\frac{\partial y}{\partial q} \frac{\partial z}{\partial r} - \frac{\partial z}{\partial q} \frac{\partial y}{\partial r} \right) + \frac{\partial y}{\partial p} \left(\frac{\partial z}{\partial q} \frac{\partial x}{\partial r} - \frac{\partial x}{\partial q} \frac{\partial z}{\partial r} \right) + \frac{\partial z}{\partial p} \left(\frac{\partial x}{\partial q} \frac{\partial y}{\partial r} - \frac{\partial y}{\partial q} \frac{\partial x}{\partial r} \right) \quad (4.33)$$

Then, the partial differentials in the global coordinate system are as below.

$$\begin{aligned}
\frac{\partial \{N\}}{\partial x} &= \frac{1}{\det|J|} \left\{ \left(\frac{\partial y}{\partial q} \frac{\partial z}{\partial r} - \frac{\partial z}{\partial q} \frac{\partial y}{\partial r} \right) \frac{\partial \{N\}}{\partial p} + \left(\frac{\partial y}{\partial p} \frac{\partial z}{\partial r} - \frac{\partial z}{\partial p} \frac{\partial y}{\partial r} \right) \frac{\partial \{N\}}{\partial q} + \left(\frac{\partial y}{\partial p} \frac{\partial z}{\partial q} - \frac{\partial z}{\partial p} \frac{\partial y}{\partial q} \right) \frac{\partial \{N\}}{\partial r} \right\} \\
\frac{\partial \{N\}}{\partial y} &= \frac{1}{\det|J|} \left\{ \left(\frac{\partial z}{\partial q} \frac{\partial x}{\partial r} - \frac{\partial x}{\partial q} \frac{\partial z}{\partial r} \right) \frac{\partial \{N\}}{\partial p} + \left(\frac{\partial x}{\partial p} \frac{\partial z}{\partial r} - \frac{\partial z}{\partial p} \frac{\partial x}{\partial r} \right) \frac{\partial \{N\}}{\partial q} + \left(\frac{\partial x}{\partial p} \frac{\partial z}{\partial q} - \frac{\partial z}{\partial p} \frac{\partial x}{\partial q} \right) \frac{\partial \{N\}}{\partial r} \right\} \\
\frac{\partial \{N\}}{\partial z} &= \frac{1}{\det|J|} \left\{ \left(\frac{\partial x}{\partial q} \frac{\partial y}{\partial r} - \frac{\partial y}{\partial q} \frac{\partial x}{\partial r} \right) \frac{\partial \{N\}}{\partial p} + \left(\frac{\partial y}{\partial p} \frac{\partial x}{\partial r} - \frac{\partial x}{\partial p} \frac{\partial y}{\partial r} \right) \frac{\partial \{N\}}{\partial q} + \left(\frac{\partial x}{\partial p} \frac{\partial y}{\partial q} - \frac{\partial y}{\partial p} \frac{\partial x}{\partial q} \right) \frac{\partial \{N\}}{\partial r} \right\}
\end{aligned} \tag{4.34}$$

The transforming coefficient of the integral is defined with (4.35) which is necessary to transform the value obtained in the local coordinate system to the global coordinate system.

$$dxdydz = \det|J| dpdqdr \tag{4.35}$$

In the case of $p = \pm 1$,

$$dS = \sqrt{\left(\frac{\partial y}{\partial q} \frac{\partial z}{\partial r} - \frac{\partial z}{\partial q} \frac{\partial y}{\partial r} \right)^2 + \left(\frac{\partial z}{\partial q} \frac{\partial x}{\partial r} - \frac{\partial x}{\partial q} \frac{\partial z}{\partial r} \right)^2 + \left(\frac{\partial x}{\partial q} \frac{\partial y}{\partial r} - \frac{\partial y}{\partial q} \frac{\partial x}{\partial r} \right)^2} dqdr \tag{4.36}$$

In the case of $q = \pm 1$,

$$dS = \sqrt{\left(\frac{\partial y}{\partial r} \frac{\partial z}{\partial p} - \frac{\partial z}{\partial r} \frac{\partial y}{\partial p} \right)^2 + \left(\frac{\partial z}{\partial r} \frac{\partial x}{\partial p} - \frac{\partial x}{\partial r} \frac{\partial z}{\partial p} \right)^2 + \left(\frac{\partial x}{\partial r} \frac{\partial y}{\partial p} - \frac{\partial y}{\partial r} \frac{\partial x}{\partial p} \right)^2} drdp \tag{4.37}$$

In the case of $r = \pm 1$,

$$dS = \sqrt{\left(\frac{\partial y}{\partial p} \frac{\partial z}{\partial q} - \frac{\partial z}{\partial p} \frac{\partial y}{\partial q} \right)^2 + \left(\frac{\partial z}{\partial p} \frac{\partial x}{\partial q} - \frac{\partial x}{\partial p} \frac{\partial z}{\partial q} \right)^2 + \left(\frac{\partial x}{\partial p} \frac{\partial y}{\partial q} - \frac{\partial y}{\partial p} \frac{\partial x}{\partial q} \right)^2} dpdq \tag{4.38}$$

Consequently, the matrix of heat conduction $[S]$, the matrix of heat capacity $[C]$, and the vector of heat flux $\{F\}$ are derived as below.

$$\begin{aligned}
[S] &= \iiint_V \left\{ \frac{\partial \{N\}}{\partial x} \left(\kappa \frac{\partial \{N\}^T}{\partial x} \right) + \frac{\partial \{N\}}{\partial y} \left(\kappa \frac{\partial \{N\}^T}{\partial y} \right) + \frac{\partial \{N\}}{\partial z} \left(\kappa \frac{\partial \{N\}^T}{\partial z} \right) \right\} dV \\
&\quad + \iint_{S_2} \alpha \{N\} \{N\}^T dS \\
&= \int_{-1}^1 \int_{-1}^1 \int_{-1}^1 \left\{ \frac{\partial \{N\}}{\partial x} \left(\kappa \frac{\partial \{N\}^T}{\partial x} \right) + \frac{\partial \{N\}}{\partial y} \left(\kappa \frac{\partial \{N\}^T}{\partial y} \right) + \frac{\partial \{N\}}{\partial z} \left(\kappa \frac{\partial \{N\}^T}{\partial z} \right) \right\} \det|J| dpdqdr \\
&\quad + \int_{-1}^1 \int_{-1}^1 \alpha \{N\} \{N\}^T Adp dq
\end{aligned} \tag{4.39}$$

$$[C] = \iiint_V dc \{N\} \{N\}^T dV = \int_{-1}^1 \int_{-1}^1 \int_{-1}^1 dc \{N\} \{N\}^T \det|J| dpdqdr \quad (4.40)$$

$$\begin{aligned} \{F\} &= -\iint_{S1} q_0 \{N\} dS + \iint_{S2} \alpha T_{fluid} \{N\} dS \\ &= -\int_{-1}^1 \int_{-1}^1 q_0 \{N\} Adpdq + \int_{-1}^1 \int_{-1}^1 \alpha T_{fluid} \{N\} Adpdq \end{aligned} \quad (4.41)$$

where the integral coefficient $Adpdq$ refers to (4.36)–(4.38) in the case of different surfaces.

Consequently, numerical integration can be conducted with the formulas derived above. In addition, the numerical integration of volume integral and surface integral can be calculated as below, where $f(p, q, r)$ is the integrand, (p_i, q_j, r_k) are the coordinates in the local coordinate system, (W_i, W_j, W_k) are the weight coefficients, and n is the number of division (which is set as 5 in this analysis).

Volume integral:

$$\int_{-1}^1 \int_{-1}^1 \int_{-1}^1 f(p, q, r) dpdqdr = \sum_i^n \sum_j^n \sum_k^n W_i W_j W_k f(p_i, q_j, r_k) \quad (4.42)$$

Surface integral:

$$\int_{-1}^1 \int_{-1}^1 f(p, q) dpdq = \sum_i^n \sum_j^n W_i W_j f(p_i, q_j) \quad (4.43)$$

4.3 Model of Liquid Nitrogen Cooling Effect

In the cases that the REBCO coils are immersed and cooled in liquid nitrogen, the cooling effect is considered as the heat flux boundary condition in the surface that directly contacts the liquid nitrogen. The heat flux q is calculated as below which considers the boiling curve.

$$q = \begin{cases} h_1(T - T_b) & (T - T_b \leq \theta_1) \\ h_1\theta_1 - h_2(T - T_b - \theta_1) & (\theta_1 < T - T_b \leq \theta_2) \\ h_3(T - T_b) + q_0 & (\theta_2 < T - T_b) \end{cases} \quad (4.44)$$

where T is the temperature of the surface, T_b is the temperature of liquid nitrogen, $h_1, h_2, h_3, \theta_1, \theta_2, q_0$ are the parameters that determined in specific boiling curve.

It is difficult to get an accurate boiling curve. The boiling curve and parameters used in this analysis are as below.

$$T_b = 77.3 \text{ K}, \quad h_1 = 10,000 \text{ W/m}^2\text{K}, \quad h_2 = 27,500/7 \text{ W/m}^2\text{K}, \quad h_3 = 200 \text{ W/m}^2\text{K}, \quad \theta_1 = 12 \text{ K},$$

$$\theta_2 = 40 \text{ K}, \quad q_0 = 2,000 \text{ W/m}^2$$

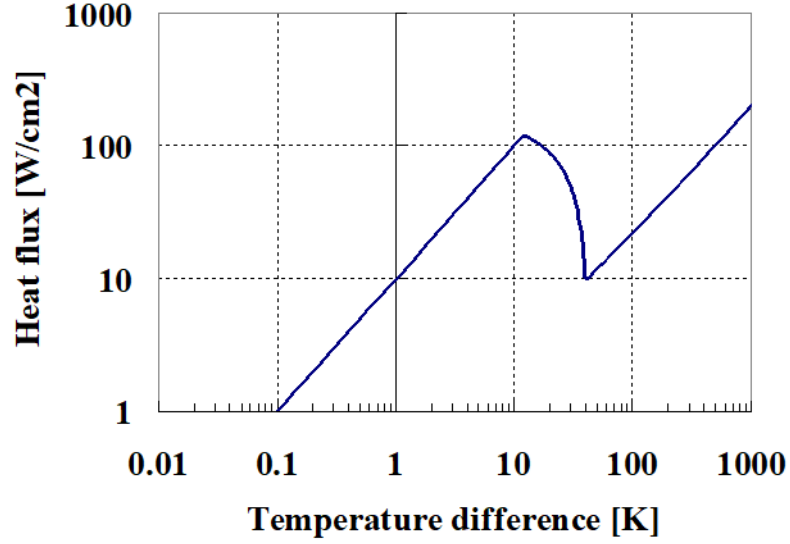


Fig. 4.4. Boiling curve used in this research.

4.4 Coupled Analysis Flowchart

Fig. 4.5 shows the schematic flowchart of the electromagnetic and heat transfer coupled analysis. Heat transfer analysis is coupled to the developed electromagnetic analysis program. The steps showed in red frames are the different steps from traditional 3D electromagnetic analysis using T - Ω formulation. The time step length is variable and is determined according to the analysis results of previous step, such as temperature rise, current change, and so on.

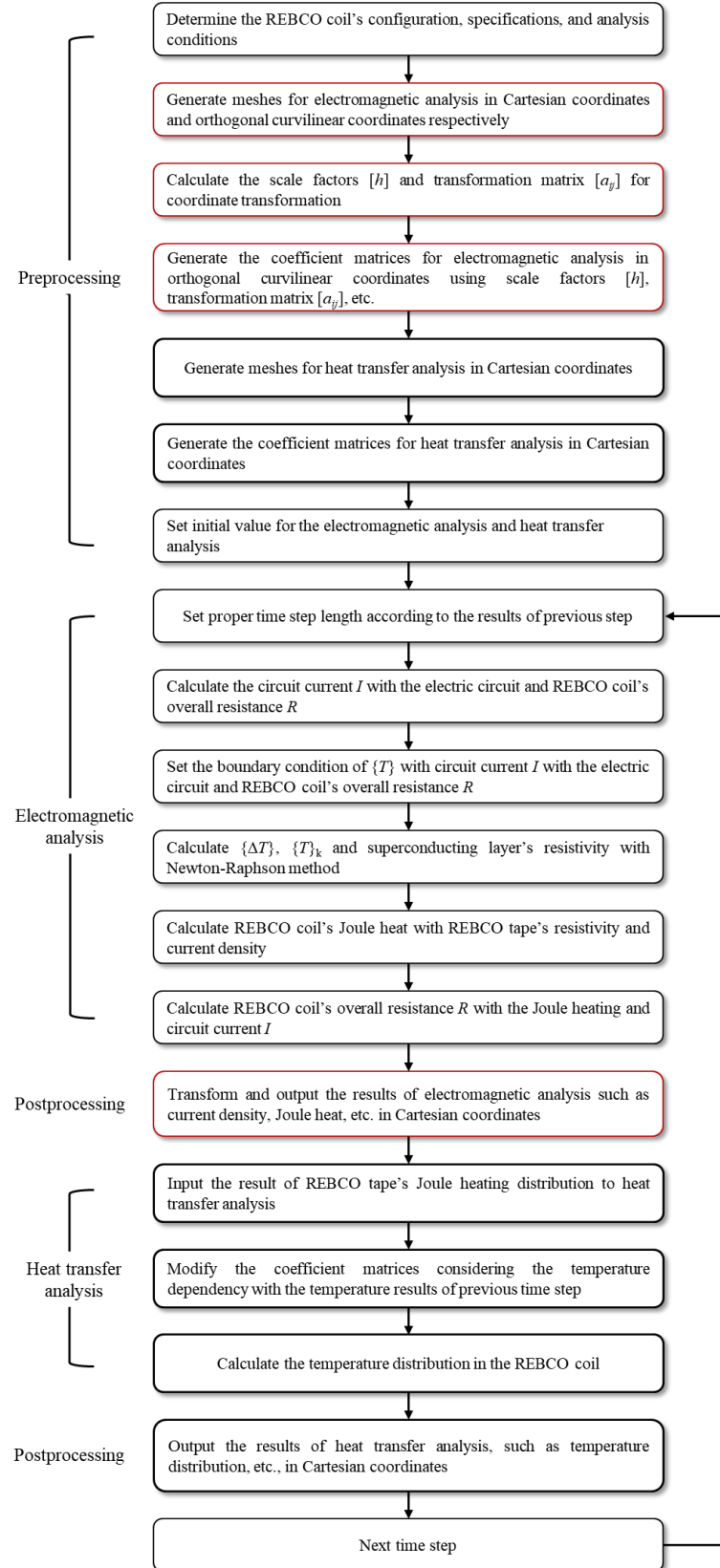


Fig. 4.5. Schematic flowchart of the electromagnetic and heat transfer coupled analysis.

4.5 Verification of the Coupled Analysis

To verify the correctness and accuracy of the coupled analysis model, an over-current simulation was conducted with an over-current of 2000 A and one-meter SF12100 tape [76]. Under the over current condition, REBCO tape's temperature changes dramatically, and consequently affects tape's resistance and current. Therefore, the simulation result of the current is a good reference to verify the accuracy of the coupled analysis. Fig 4.6 summarizes the simulation results which shows good agreement with the experimental results [77]. Although some difference is still observed especially in first 20 ms, it can be improved with more accurate parameters of the simulation model or more accurate models for superconducting properties. In addition, a local degradation of J_C (85% of the rated J_C), which is the same as the experimental tape, was also modelled in the numerical analysis.

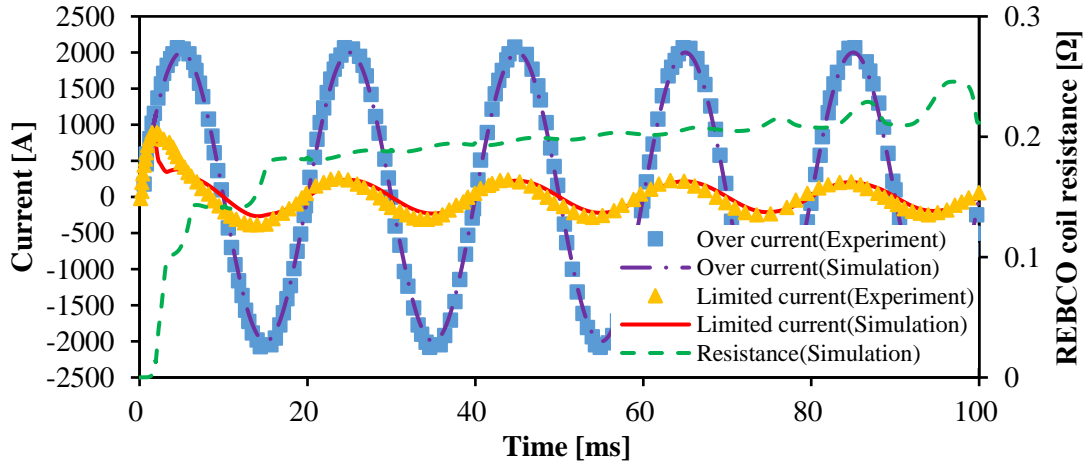


Fig. 4.6. Schematic flowchart of the electromagnetic and heat transfer coupled analysis.

Chapter 5. Case Studies of Electromagnetic and Heat Transfer

Coupled Analysis

5.1 Case Study: REBCO Coil for Resistive SFCL Application

5.1.1 Analysis Conditions

In the resistive type SFCL application, the REBCO coils generate high resistance to limit the overcurrent through the SN transition with a significant temperature rise. A careful design is necessary to generate enough resistance and avoid the quench in the temperature rise. Therefore, the temperature plays an important role when analysing REBCO coils' electromagnetic and thermal behaviors under the overcurrent condition.

In this section, we have analyzed the transient electromagnetic and thermal behaviors of two solenoid REBCO coils under overcurrent: one with uniform J_C distribution and the other with local J_C degradation. The specifications of two REBCO coils and the simulation circuit are summarized in Fig. 5.1 and Table 5.1.

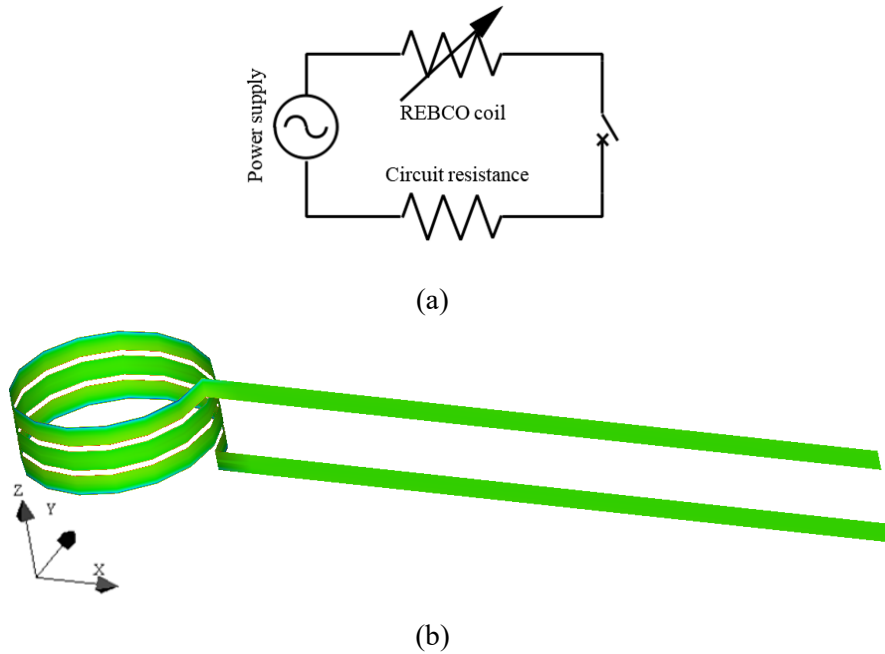


Fig. 5.1. (a) Schematic diagram of overcurrent simulation circuit consists of a power supply, a circuit resistance, and a REBCO coil. (b) 3D electromagnetic model for 3 turn SFCL REBCO coil with current leads. The length of current leads is assumed to be relatively longer than the diameter of REBCO coil to reduce its impact on the electromagnetic behaviors of the REBCO coil.

TABLE 5.1
SPECIFICATIONS OF SFCL REBCO COILS AND CIRCUIT

Properties	Values
Common conditions	
REBCO coil/ Current leads	SuperPower Inc. SF12100
Coil diameter	11 cm
Coil pitch	1.5 cm
Length of current leads	0.4 m per current lead (0.8 m in total)
Cooling method	Immersion cooling in liquid nitrogen
Cooling temperature	77.3 K
Critical current at 77.3 K, self-field	468 A
Ag over-layer thickness	2 μm
Expected overcurrent peak magnitude	2000 A
Over current duration	200 ms
Over current rising speed at the start	1×10^6 A/s
REBCO coil with uniform J_C distribution	
Turns of coil	3
Power-supply voltage	DC 60 V
Circuit resistance	0.03 Ω
REBCO coil with local J_C degradation	
Turns of coil	1
Power-supply voltage	DC 20 V
Circuit resistance	0.01 Ω
JC degraded area	11 mm \times 2.4 mm (in the middle of the coil's longitudinal and width direction)
Degraded JC	117 A (25% of normal JC)

5.1.2 REBCO Coil with Uniform J_C Distribution

Firstly, a REBCO coil with uniform J_C distribution under overcurrent condition was simulated. A 3-turn coil was modelled to consider the influence of solenoid structure and current leads in the analysis. To simulated the overcurrent, a DC power supply source was assumed and the voltage was set to be 60 V in consideration of the tolerance of the REBCO tape.

The transient temperature distribution along the REBCO tape's longitudinal direction is shown in Fig. 5.2. The temperature rise starts from the ends which are connected to the current leads. To investigate the reason, the current density distribution of the whole coil at the peak current (1.1 ms) are shown in Fig. 5.3. A more distinct bias in the current density in the tape width direction is found close to the current leads. Some detailed data is shown in Fig. 5.4. At the current peak, which appears 1.1 ms after fault occurs, the current concentrates to the upper side of REBCO tape that is close to the other current lead. Consequently, this concentration leads to higher Joule heat generation and temperature rise on the upper side. As the magnetic field dependence of critical current is not considered in this model, the bias in the current density distribution is mainly because of the screen current that generated by the rapidly increasing magnetic field of current leads.

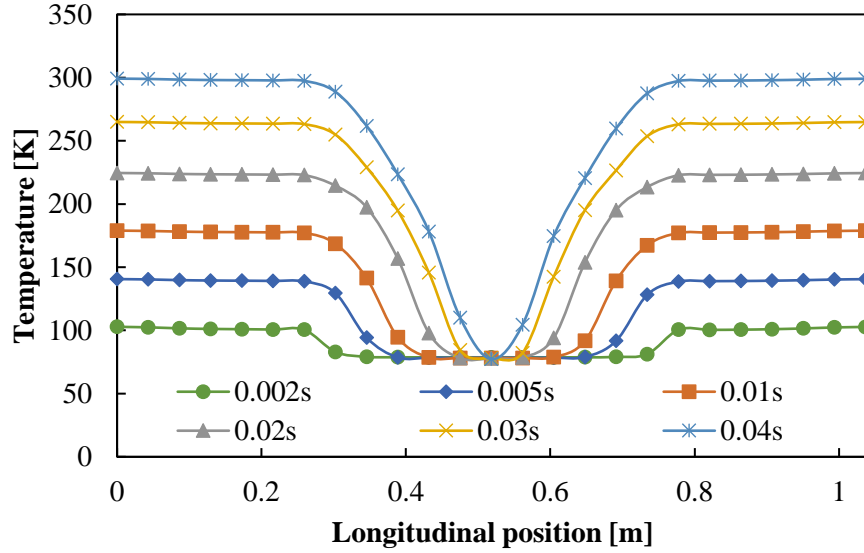


Fig. 5.2. Transient temperature distribution along the tape's longitudinal direction of the SFCL REBCO coil with uniform J_C distribution. The temperature rise starts from the coil ends close to the current leads and the peak temperature rises to 300 K in 0.04 s under the overcurrent.

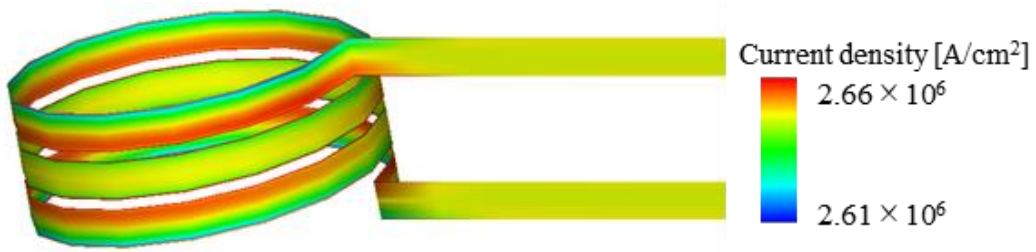
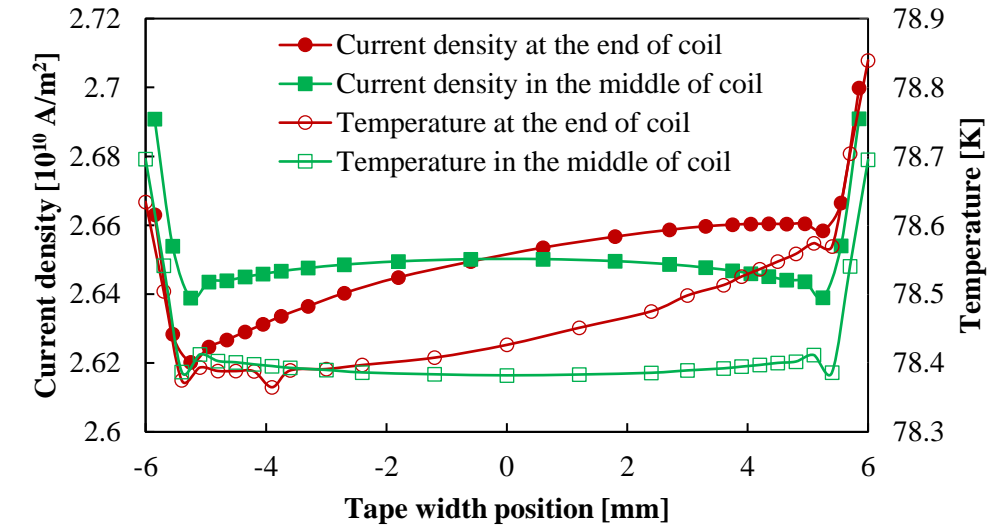
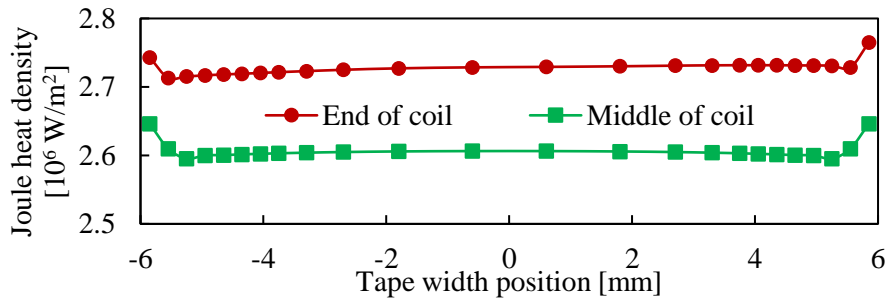


Fig. 5.3. Current density distribution of the SFCL REBCO coil with uniform J_C distribution at the peak current (1.1 ms). An obvious current density distribution bias in the width direction is observed at the coil ends close to the current leads.



(a)



(b)

Fig. 5.4. (a) Current density and temperature distribution; (b) Joule heat density in the tape width direction at the bottom end and in the middle of the REBCO coil with uniform J_C distribution at the peak current (1.1 ms). At the coil end, the current concentrates to the upper side of REBCO tape that is close to the other current lead, which leads to higher Joule heat generation and temperature rise.

5.1.3 REBCO Coil with Local J_C Degradation

Then, to study the influence of J_C degradation on the REBCO coil's electromagnetic and thermal behaviors under overcurrent, a 1-turn coil with local J_C degradation was modelled and simulated, because we found that the number of turns has little influence in this case. Hence, the voltage was set to be 20 V in proportion to the tape length in this case. Moreover, a severe and narrow J_C degradation (25% of normal J_C in $11 \text{ mm} \times 2.4 \text{ mm}$) was assumed in the middle of the coil.

The transient temperature distribution along the REBCO tape's longitudinal direction is shown in Fig. 5.5, and shows that the temperature rises from the J_C degradation area instead of the current leads in comparison with the previous case. The transient current density distribution and Joule heat density distribution of the REBCO coil in the tape width direction are shown in Fig. 5.6. According to the analysis results, it is revealed that the current bypasses the J_C degraded area and flows through the normal J_C area during the rising phase of current, which leads to a higher Joule heat generation. But, soon the current density and Joule heat density distribution turn to uniform because of the thermal conduction and overall temperature rise in the widthwise direction. Therefore, in this case, the hotspot is more likely to occur in the normal J_C area than the J_C degraded area.

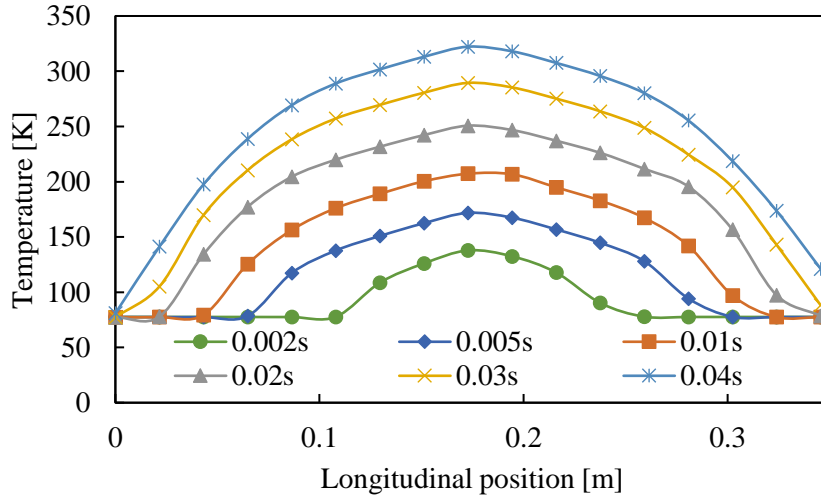
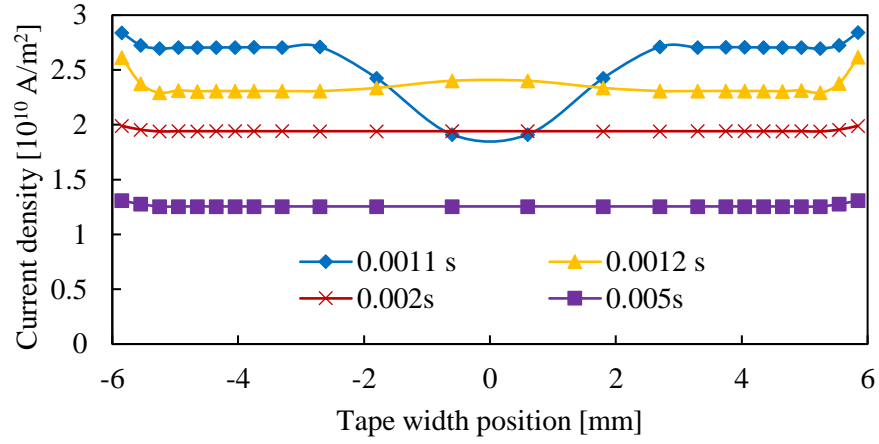
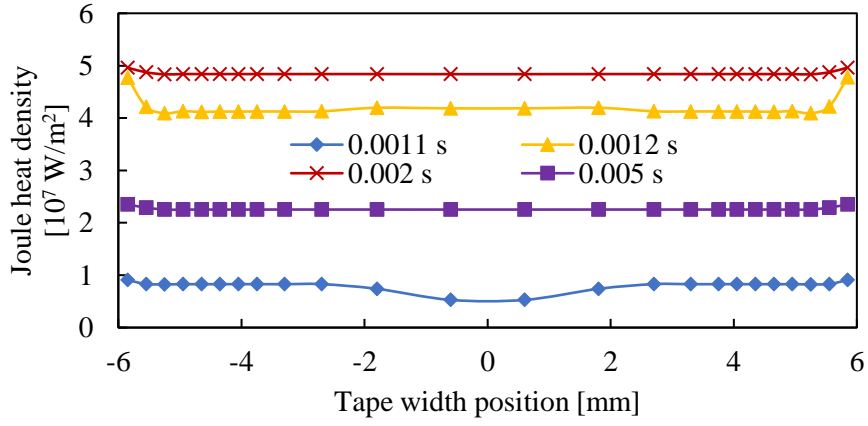


Fig. 5.5. Transient temperature distribution along the tape's longitudinal direction of the SFCL REBCO coil with local J_C degradation. The temperature rise starts from the J_C degraded area in the middle of the coil and the peak temperature exceeds 300 K in 0.04 s under the overcurrent.



(a)



(b)

Fig. 5.6. (a) Current density and temperature distribution; (b) Joule heat density in the tape width direction at the bottom end and in the middle of the REBCO coil with uniform JC distribution at the peak current (1.1 ms). At the coil end, the current concentrates to the upper side of REBCO tape that is close to the other current lead, which leads to higher Joule heat generation and temperature rise.

5.2 Case Study: REBCO Coil for Magnet Application

5.2.1 Analysis Conditions

In the magnet application, quench in the REBCO coils is still a problem that hinders the practical use. A quench usually occurs after an external energy input, such as heat, force, etc., during the normal operation or the excitation process, because such energy input usually results in a temperature rise and decrease in J_C which creates the overcurrent situation. Hence, it is important to investigate the transient electromagnetic and thermal behaviors during such process to find the solution for the quench problem.

In this section, we have analyzed the influence of different energy input power, area, and different time constants of current decrease on the quench of a solenoid REBCO coil. External heat, that lasts 100 ms and is directly input to the surface of the REBCO tape, was assumed to simulate the external energy input. The normal operation current was set to be 60% of I_C . The conventional quench detection and protection scheme were also modelled by the time constant τ of current decrease and the detection voltage in Sector C and D. Namely, once the entire voltage of the REBCO coil reaches the detection voltage (100 mV, in this paper), after a delay time (0.1 s), the circuit current is decreased exponentially with the time constant of τ . The specifications of the REBCO coil and circuit are detailed in Table 5.2. In addition, the silver overlayer and copper stabilizer are treated as one copper layer in the analysis for the simplification of the simulation model, because the silver overlayer is much thinner than the copper layer.

TABLE 5.2
SPECIFICATIONS OF MAGNET REBCO COILS AND CIRCUIT

Properties	Values
REBCO coil/ Current leads	SuperPower Inc. SCS4050
Turns of coil	1
Coil diameter	11 cm
Coil pitch	1.5 cm
Length of current leads	0.4 m per current lead (0.8 m in total)
Cooling method	Immersion cooling in liquid nitrogen
Cooling temperature	77.3 K
Critical current at 77.3 K, self-field	156 A
Ag over-layer thickness	2 μm
Copper stabilizer thickness	20 μm
Operating current	95 A (60% I_C)
Detection voltage	100 mV
Heat input duration	100 ms
Heat input area	11 mm \times 4 mm (11 mm \times 0.8 mm)

5.2.2 Influence of Heat Input Power on Quench

Firstly, several cases of different heat input power density (input power per unit tape surface area) were simulated to investigate the minimum quench energy (MQE) under the assumed conditions. No current decrease was considered here, namely the current was set as constant.

Furthermore, the heat input area was assumed to be full tape width as Fig. 5.7(a).

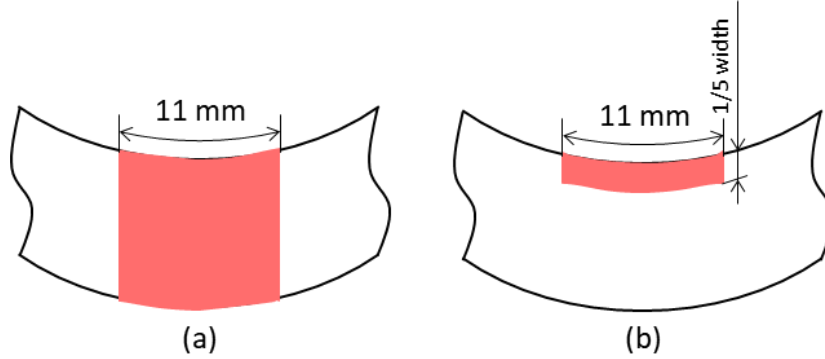


Fig. 5.7. Cases of different heat input area: (a) 11 mm \times 4 mm (full tape width); (b) 11 mm \times 0.8 mm (1/5 tape width).

The results of maximum temperature and entire voltage of the REBCO coil after different heat input are shown in Fig. 5.8. According to the results, the heat input of 8.68 J ($1.984 \times 10^5 \text{ W/m}^2 \times 11 \text{ mm} \times 4 \text{ mm} \times 100 \text{ ms}$) triggers a quench, while the heat input of 8.65 J did not. Therefore, the MQE is considered to be about 8.68 J in this case with constant current. The peak entire voltage of the REBCO coil with heat input of 8.68 J and 8.65 J both have exceeded 100 mV the detection voltage, which reveals that the current may be cut off even in no quench situation if the detection voltage is set as 100 mV, and a higher set value (e.g. 115 mV) would increase the quench detection accuracy in this case.

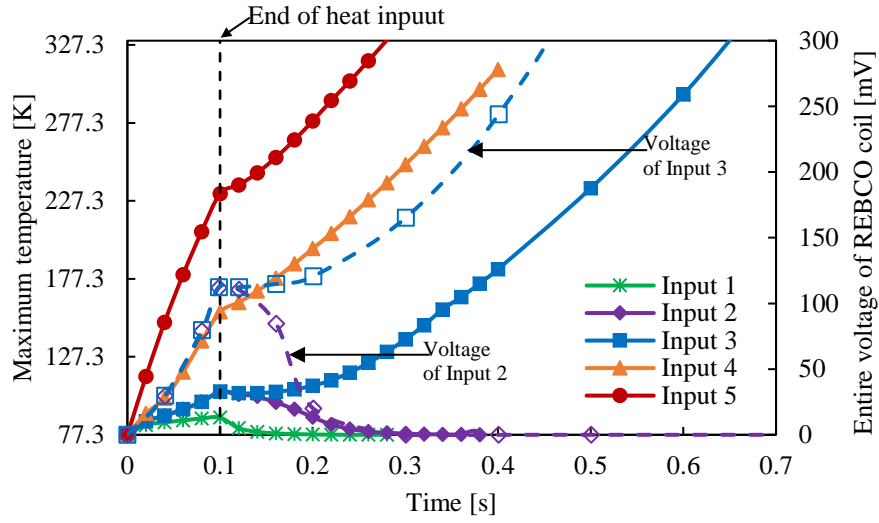
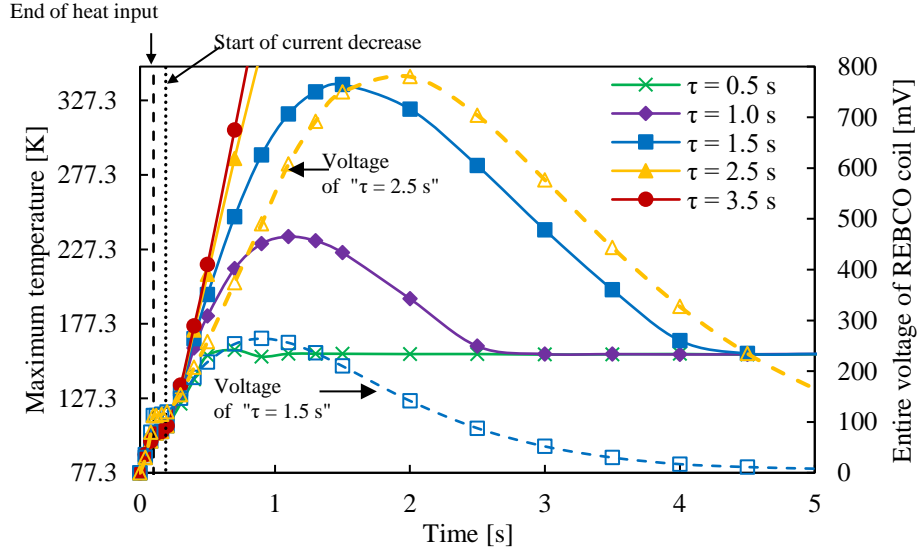


Fig. 5.8. Maximum temperature of the REBCO coil after the heat input with different heat input power density (input power per unit tape surface area): Input 1: 1.44×10^5 W/m²; Input 2: 1.978×10^5 W/m²; Input 3: 1.984×10^5 W/m²; Input 4: 2.88×10^5 W/m²; and Input 5: 5.75×10^5 W/m². Input 1, 2, and 3 lead to a quench. The entire voltages of the REBCO coil under Input 2 and 3 are also shown here.

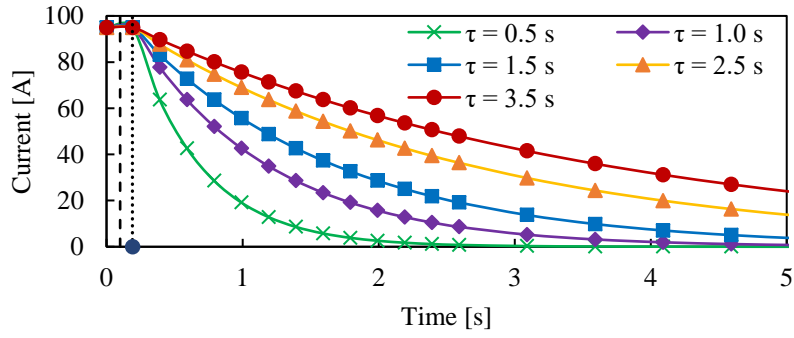
5.2.3 Influence of Time Constant of Current Decrease on Quench

Secondly, the quench detection and protection scheme were considered and the influence of the time constant τ of current decrease was studied. The heat input was set to be 8.68 J (power density: 1.984×10^5 W/m²), and the heat input area was also assumed to be full tape width (Fig. 5.7(a)) as Sector B. Furthermore, the quench detection voltage is set as 100 mV.

Fig. 5.9 shows the results of the maximum temperature of the REBCO coil and the circle current from the heat input with different time constant τ of current decrease. The results indicate that lower time constant could decline the possibility of quench and quench is avoided in the cases of the time constant lower than 1.5 s. In the cases that result in no quench, the temperature rise is limited to the heated area because the Joule heat that generated by the current is not high enough to expand the heating area. Meanwhile, the entire voltages of the REBCO coil in the case of τ is 1.5 s and 2.5 s are also shown in Fig. 5.9. The Joule heat, that continuously generated by the current in the heat input area, hinders the cooling down of the REBCO tape. Namely, cutting off the circuit earlier would achieve a much faster restore of the REBCO coil.



(a)



(b)

Fig. 5.9. (a) Maximum temperature of the REBCO coil and (b) circuit current from the heat input $1.984 \times 10^5 \text{ W/m}^2$ in 100 ms with different time constant τ of current decrease. A quench is avoided when τ is less than 1.5 s. The entire voltages of the REBCO coil with τ of 1.5 s and 2.5 s are also shown here.

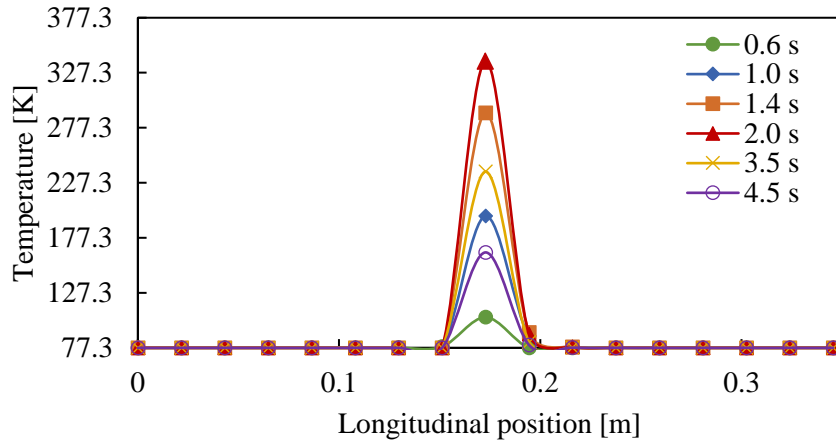


Fig. 5.10. Transient temperature distribution along the REBCO tape's longitudinal direction after the heat input $1.984 \times 10^5 \text{ W/m}^2$ in 100 ms with time constant of 1.5 s. In this case, the peak temperature is 338 K and a quench is avoided. Meanwhile, the temperature rise is limited in the heated area.

5.2.4 Influence of Heat Input Area on Quench

As a further study based on Sector C, we assumed 3 cases of different heat input area with full tape width (Fig. 5.7(a)) or 1/5 tape width (Fig. 5.7(b)) to investigate the influence of the heat input area on the electromagnetic and thermal behaviors. The time constant τ of current decrease was assumed to be 2.5 s. The specifications of 3 cases are shown in Table 5.3. Case C is the reference case which is the same as the case in Sector C. Case A and B have the same reduced heat input area, while the total heat input of Case A and the heat input power density of Case B are the same as Case C.

TABLE 5.3

Case number	Heating input area	Heat input power density	Total heat input
A	11 mm \times 0.8 mm (1/5 tape width -2 mm--1.2 mm)	$9.919 \times 10^5 \text{ W/m}^2$	8.68 J
B	11 mm \times 0.8 mm (1/5 tape width -2 mm--1.2 mm)	$1.984 \times 10^5 \text{ W/m}^2$	1.74 J
C	11 mm \times 4 mm (full tape width)	$1.984 \times 10^5 \text{ W/m}^2$	8.68 J

The results of the transient maximum temperature and entire voltage of the REBCO coil of Case A, B, and C are shown in Fig. 5.11. Even though the heat input in Case C leads to a quench,

the same heat input power density in Case A or the same total heat input in Case B does not result in a quench. The result indicates the importance of the heat (energy) input area when studying the MQE and quench problem. Because the energy input area usually varies from case by case, when designing the quench and protection scheme, the extreme conditions should be considered where a largish energy input area assumption would be preferable. On the other hand, the most common and typical energy input area also should be considered to avoid overdesign in a specific application.

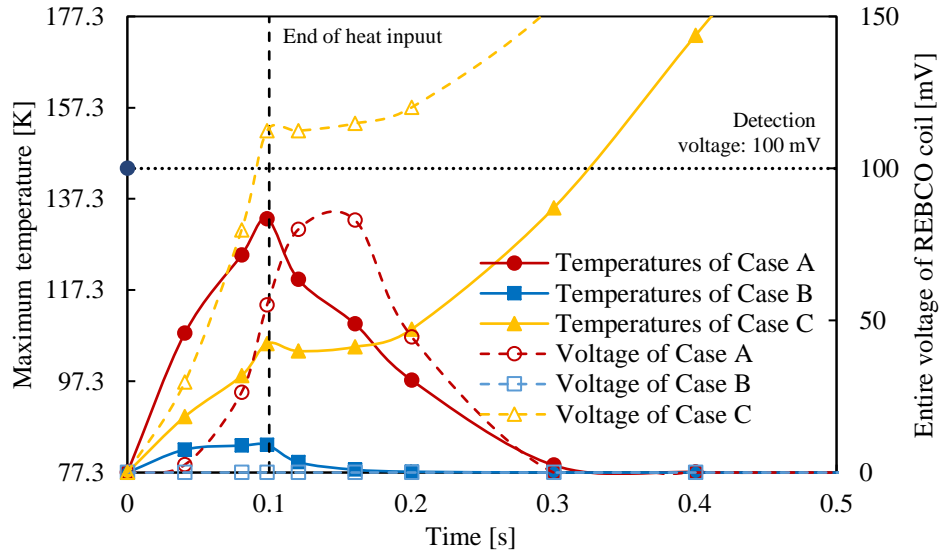
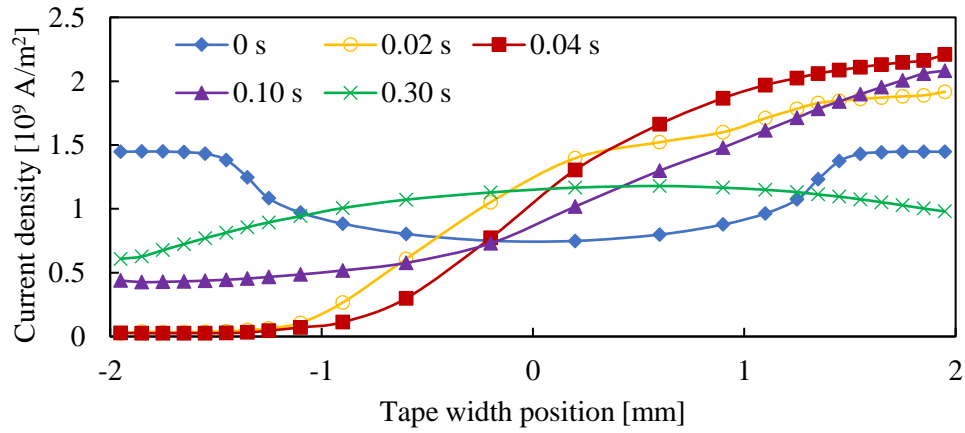


Fig. 5.11. Transient maximum temperature and entire voltage of the REBCO coil in Case A, B, and C. Even though the heat input in Case C leads to a quench, the same heat input power density in Case A or the same total heat input in Case B does not lead to a quench. Furthermore, the peak entire voltages in Case B and C are 85 mV and nearly zero.

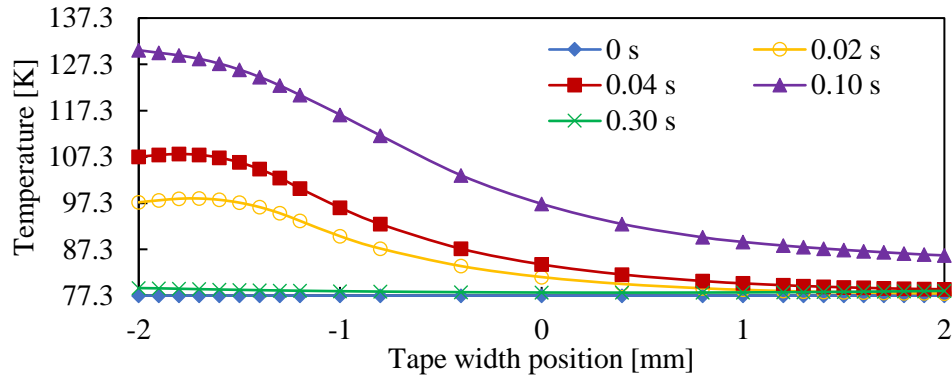
Moreover, in Case C, the entire voltage of the REBCO coil increases rapidly and exceeds the detection voltage (100 mV) during the external heat input, meanwhile the entire voltage in Case B rises more slowly and the peak voltage only reaches 85 mV. The set value of detection voltage as 100 mV shows its practicality in detecting quench here: the quench occurs in the case that the entire voltage exceeds 100 mV. Nevertheless, with this setting of detection voltage, a local temperature rise, which could develop into a quench depending on the heat dissipation conditions, cannot be detected accurately when the heating area is narrow enough (1/5 tape width in this case). Therefore, a couple of staged detection voltage setting is recommended and the actual set value should be decided after exhaustively studying all the possible energy input patterns and quench situations. A lower set value as early-stage detection should be able to detect as much temperature rise as possible and be recorded for review and maintenance. Once the detected voltage rapidly

risks and reaches the higher set value as dangerous stage, it could be judged as a potential quench and triggers the protection. In addition, the speed and magnitude of the voltage rise can be utilized to justify the energy input pattern and evaluate the risk of quench. According to the analysis results, we found that the speed and peak amplitude of voltage rise in the cases of smaller energy input area is much lower than that in the cases of larger energy input area. In the cases of the same energy input area, a critical voltage can also be found to distinguish a possible quench.

For further study on the transient electromagnetic and thermal behaviors, the transient current density and temperature distribution of Case A in the tape width direction in the heat input area are shown in Fig. 5.12. The current density distribution changes rapidly after the start of the heat input: the current density in the heated area decreases to nearly zero while the current concentrates to the opposite side of the tape. The main reason is considered to be the temperature rise bias in tape width direction: the temperature rises rapidly in the heated area and changes the superconductor to normal state first. After the temperature rises in the entire tape width, the decreased current density in the heat input area starts to recover and the current density distribution in the tape width direction becomes more average. However, the current density distribution would not perfectly restore to the initial distribution before heat input. It reveals that the heat input would permanently change the current density distribution, and this fact should be taken into consideration when designing a magnet because the designed magnetic field distribution may change after times of energy input which are even not detected.



(a)



(b)

Fig. 5.12. (a) Transient current density distribution and (b) transient temperature distribution of Case A in the tape width direction in the heated area. The current density distribution changes rapidly after the start of the heat input. At the start of heat input, the current density decreases to nearly zero in the heated area while the current concentrates to the other side of the tape. Then, the decreased current density in the heated area starts to recover and the distribution, which differs from the initial distribution, becomes more average after the temperature rises in the entire tape width.

Chapter 6. Conclusion

The RE (rare earth) $\text{Ba}_2\text{Cu}_3\text{O}_x$ (REBCO)-coated conductor has shown its advantages in various applications such as high field magnet, accelerator, superconducting fault current limiter (SFCL), etc., because of its high critical temperature, critical current density, axial tensile stress, and heat capacity. The developments of such applications using REBCO-coated conductors have become increasingly active in recent years since the commercialization of long-length REBCO-coated conductors. However, some problems are still hindering the practical use of REBCO coils such as quench, AC loss, cooling, cost, and so on.

Experimental and numerical approaches are the main method to study such problems to find the solutions. Although experiments are essential to study the actual physical phenomena and to conclusively verify a certain idea, it is still difficult to measure all the accurate and detailed information such as the current density, electric field, magnetic field, temperature, etc. at a certain point because of the limitation of the measurement technology. Hence, the numerical analysis is necessary and useful in today's research, and has contributed greatly with the detailed analysis. In this thesis, the author focuses on the numerical analysis method especially for the REBCO-coated conductors and coils.

In the research of applications using REBCO-coated conductors, the electromagnetic and thermal behaviors are two of the most important aspects. Because the REBCO-coated conductors have to be cooled to superconductive, and the electromagnetic characteristics of superconductors are functions of the temperature, while the temperature is also affected by the conductor's Joule heat. To study the electromagnetic and thermal behaviors, numerical simulation using equivalent circuit models, finite element method (FEM), etc. has been proposed and widely utilized. Equivalent circuit model of electric circuit elements (and thermal equivalent circuit elements in some cases) is a very fast numerical solution to simulate simple applications of REBCO-coated conductors, meanwhile, the improvement of analysis accuracy, which depends on the parameters of the equivalent circuit, is still a problem especially in the cases with complicated structures. Finite elements method is the most developed and widely used method today, allowing the use of different formulations for electromagnetic analysis: A - V (A : magnetic vector potential; V : electric scalar potential), T - Ω (T : current vector potential; Ω : magnetic scalar potential), H (H : magnetic field), and E (E : electric field). Among them, the T - Ω formulation has shown better convergence in both two-dimensional (2D) and three-dimensional (3D) situations, although extra variables are needed at each node. Some methods, such as the thin plate approximation and the fast multipole method, were proposed to reduce variables and computation load. Because of the importance of thermal analysis, some electromagnetic and heat transfer coupled analysis tools up to 2D have been developed in some research. However, performing a 3D electromagnetic and heat transfer

coupled analysis is still difficult, because the operating characteristics of REBCO-coated conductors are extremely non-linear and strongly affected by the temperature, then the convergence could significantly deteriorate in 3D problems.

In this thesis, the author has developed a three-dimensional electromagnetic analysis method using finite elements method and thin plate approximation for REBCO-coated conductors and coils. Furthermore, the author has applied the electromagnetic analysis method to coupled analysis with heat transfer. Thin plate approximation and coordinate transformation (from Cartesian coordinates system to orthogonal curvilinear coordinate system) are utilized to realize the electromagnetic analysis of REBCO coils, which have 3D structures, in 2D calculation space. The governing electromagnetic equation is given by $\nabla \times (\rho \nabla \times \mathbf{T}) = -\partial \mathbf{B} / \partial t$ (\mathbf{T} : current vector potential; ρ : electric resistivity; \mathbf{B} : magnetic flux density), where \mathbf{T} is defined by $\mathbf{J} = \nabla \times \mathbf{T}$ (\mathbf{J} : current density). With the proposed method, the number of variables is reduced to one-third, namely, only one direction (the normal direction) component of variables is needed in the orthogonal curvilinear coordinate system while three direction components of variables are needed in the Cartesian coordinates system. Therefore, a significant reduction in the computational load is achieved as well as a better convergence property in comparison with normal three-dimensional electromagnetic analysis method. Moreover, no limitation of the REBCO coil shape exists in this method, and REBCO coils with any structures can be modeled and analyzed by simply inputting the Cartesian coordinates of certain REBCO coils. Additionally, a nonlinear E - J relation (E : electric field) as well as the temperature dependence is used for modelling the electromagnetic characteristic of superconductors. In heat transfer analysis, the 3D structure of REBCO coils is modeled and the temperature change is calculated under the condition of Joule heating, heat conduction, heat transfer, and cooling characteristics. In addition, the temperature dependence of thermal characteristics is also considered in the analysis.

Verifications and some case studies are then conducted with the developed analysis program that based on the proposed analysis method. The capability and practicality of the proposed analysis method and developed analysis tool are verified by the results of these verifications and case studies.

Firstly, verifications of the proposed three-dimensional electromagnetic analysis method are conducted by comparing the analysis results with theoretical formula and commercial simulation software JMAG. Good agreement is observed which verifies the correctness and accuracy of the proposed analysis method.

Next, two case studies based on the three-dimensional electromagnetic analysis are conducted and indicate the capability of the developed electromagnetic analysis tool to analyze various electromagnetic characteristics of REBCO coils in any shape. One is an analysis of a solenoid REBCO coil for magnet application, which requires high magnetic field as well as high stability

and homogeneity of the field. The author has modelled a solenoid REBCO coil and assumed some different patterns of excitation to study the magnet field stability and homogeneity with detailed distribution of magnetic field, screening current induced field, current density, and screening current density. The other case study is an analysis of a saddle-shaped REBCO coil for accelerator application, which requires accurate and homogeneous magnetic field with the frequently changing coil current. The author has modelled a saddled-shaped REBCO coil and assumed the change pattern of coil current to study the space magnetic field distribution and the influence of screening current with detailed distribution of magnetic field, screening current induced field, current density, and screening current density.

Moreover, two case studies based on electromagnetic and heat transfer coupled analysis are conducted to study the quench phenomenon in certain applications. One is an analysis of a REBCO coil for resistive type SFCL application, in which quench is a problem because high resistance is generated to limit the overcurrent through the SN transition with a significant temperature rise. The author has analyzed the transient electromagnetic and thermal behaviors of two solenoid REBCO coils under overcurrent: one with uniform critical current density (J_C) distribution and the other with local J_C degradation. The other case study is an analysis of a REBCO coil for magnet application, in which a quench usually occurs after an external energy input during the normal operation or the excitation process. The author has analyzed the influence of different energy input power, area, and different time constants of current decrease on the quench of a solenoid REBCO coil, as well as the electromagnetic and thermal behaviors before and after the quench.

References

- [1] Y. Yanagisawa *et al.*, “Operation of a 400MHz NMR magnet using a (RE:Rare Earth)Ba₂Cu₃O_{7-x} high-temperature superconducting coil: Towards an ultra-compact super-high field NMR spectrometer operated beyond 1GHz,” *Journal of Magnetic Resonance*, vol. 249, pp. 38–48, Dec. 2014, doi: 10.1016/j.jmr.2014.10.006.
- [2] S. Iguchi *et al.*, “Advanced field shimming technology to reduce the influence of a screening current in a REBCO coil for a high-resolution NMR magnet,” *Supercond. Sci. Technol.*, vol. 29, no. 4, p. 045013, 2016, doi: 10.1088/0953-2048/29/4/045013.
- [3] S. Noguchi *et al.*, “Optimal configuration design of MRI REBCO magnet taking into account superconducting layer,” in *2016 IEEE Conference on Electromagnetic Field Computation (CEFC)*, Nov. 2016, pp. 1–1, doi: 10.1109/CEFC.2016.7815982.
- [4] G. A. Kirby *et al.*, “Accelerator-Quality HTS Dipole Magnet Demonstrator Designs for the EuCARD-2 5-T 40-mm Clear Aperture Magnet,” *IEEE Transactions on Applied Superconductivity*, vol. 25, no. 3, pp. 1–5, Jun. 2015, doi: 10.1109/TASC.2014.2361933.
- [5] M. Noe and M. Steurer, “High-temperature superconductor fault current limiters: concepts, applications, and development status,” *Supercond. Sci. Technol.*, vol. 20, no. 3, p. R15, 2007, doi: 10.1088/0953-2048/20/3/R01.
- [6] G. Zhang, H. Wang, Q. Qiu, Z. Zhang, L. Xiao, and L. Lin, “Recent progress of superconducting fault current limiter in china,” *Supercond. Sci. Technol.*, 2020, doi: 10.1088/1361-6668/abac1f.
- [7] A. M. Campbell, “An Introduction to Numerical Methods in Superconductors,” *J Supercond Nov Magn*, vol. 24, no. 1–2, pp. 27–33, Jan. 2011, doi: 10.1007/s10948-010-0895-5.
- [8] Y. Ichiki and H. Ohsaki, “Numerical analysis and design of fault current limiting elements using large-size YBCO thin films,” *Physica C: Superconductivity and its Applications*, vol. 463, pp. 1168–1171, Oct. 2007, doi: 10.1016/j.physc.2007.03.453.
- [9] S. Sugita and H. Ohsaki, “Numerical analysis of AC losses in REBCO thin film for coated conductor and fault current limiter,” *Physica C: Superconductivity*, vol. 392–396, pp. 1150–1155, Oct. 2003, doi: 10.1016/S0921-4534(03)00784-6.
- [10] S. Noguchi, R. Itoh, S. Hahn, and Y. Iwasa, “Numerical Simulation of Superconducting Coil Wound With No-Insulation NbTi Wire,” *IEEE Transactions on Applied Superconductivity*, vol. 24, no. 3, pp. 1–4, Jun. 2014, doi: 10.1109/TASC.2013.2287909.
- [11] F. Sirois and F. Grilli, “Potential and limits of numerical modelling for supporting the development of HTS devices,” *Supercond. Sci. Technol.*, vol. 28, no. 4, p. 043002, 2015, doi: 10.1088/0953-2048/28/4/043002.
- [12] F. Grilli, “Numerical Modeling of HTS Applications,” *IEEE Transactions on Applied Superconductivity*, vol. 26, no. 3, pp. 1–8, Apr. 2016, doi: 10.1109/TASC.2016.2520083.

- [13] C.-H. Bonnard, F. Sirois, C. Lacroix, and G. Didier, "Multi-scale model of resistive-type superconducting fault current limiters based on 2G HTS coated conductors," *Supercond. Sci. Technol.*, vol. 30, no. 1, p. 014005, 2017, doi: 10.1088/0953-2048/30/1/014005.
- [14] T. Wang *et al.*, "Analyses of Transient Behaviors of No-Insulation REBCO Pancake Coils During Sudden Discharging and Overcurrent," *IEEE Transactions on Applied Superconductivity*, vol. 25, no. 3, pp. 1–9, Jun. 2015, doi: 10.1109/TASC.2015.2393058.
- [15] F. Grilli *et al.*, "Finite-element method modeling of superconductors: from 2-D to 3-D," *IEEE Transactions on Applied Superconductivity*, vol. 15, no. 1, pp. 17–25, Mar. 2005, doi: 10.1109/TASC.2004.839774.
- [16] Y. Ichiki and H. Ohsaki, "Numerical analysis of AC losses in YBCO coated conductor in external magnetic field," *Physica C: Superconductivity*, vol. 412, pp. 1015–1020, Oct. 2004, doi: 10.1016/j.physc.2004.01.122.
- [17] M. Nii, N. Amemiya, and T. Nakamura, "Three-dimensional model for numerical electromagnetic field analyses of coated superconductors and its application to Roebel cables," *Supercond. Sci. Technol.*, vol. 25, no. 9, p. 095011, 2012, doi: 10.1088/0953-2048/25/9/095011.
- [18] R. Brambilla, F. Grilli, and L. Martini, "Development of an edge-element model for AC loss computation of high-temperature superconductors," *Supercond. Sci. Technol.*, vol. 20, no. 1, pp. 16–24, Nov. 2006, doi: 10.1088/0953-2048/20/1/004.
- [19] J. W. Barrett and L. Prigozhin, "Electric field formulation for thin film magnetization problems," *Supercond. Sci. Technol.*, vol. 25, no. 10, p. 104002, Sep. 2012, doi: 10.1088/0953-2048/25/10/104002.
- [20] H. Ueda, M. Fukuda, K. Hatanaka, T. Wang, A. Ishiyama, and S. Noguchi, "Spatial and Temporal Behavior of Magnetic Field Distribution Due to Shielding Current in HTS Coil for Cyclotron Application," *IEEE Transactions on Applied Superconductivity*, vol. 23, no. 3, pp. 4100805–4100805, Jun. 2013, doi: 10.1109/TASC.2012.2234813.
- [21] P. Tixador, G. David, T. Chevalier, G. Meunier, and K. Berger, "Thermal-electromagnetic modeling of superconductors," *Cryogenics*, vol. 47, no. 11–12, pp. 539–545, Nov. 2007, doi: 10.1016/j.cryogenics.2007.08.003.
- [22] H. K. Onnes, "Further experiments with liquid helium. C. On the change of electric resistance of pure metals at very low temperatures etc. IV. The resistance of pure mercury at helium temperatures," in *Through Measurement to Knowledge: The Selected Papers of Heike Kamerlingh Onnes 1853–1926*, H. K. Onnes, K. Gavroglu, and Y. Goudaroulis, Eds. Dordrecht: Springer Netherlands, 1991, pp. 261–263.
- [23] W. Meissner and R. Ochsenfeld, "Ein neuer Effekt bei Eintritt der Supraleitfähigkeit," *Naturwissenschaften*, vol. 21, no. 44, pp. 787–788, Nov. 1933, doi: 10.1007/BF01504252.
- [24] F. London, H. London, and F. A. Lindemann, "The electromagnetic equations of the

- supraconductor,” *Proceedings of the Royal Society of London. Series A - Mathematical and Physical Sciences*, vol. 149, no. 866, pp. 71–88, Mar. 1935, doi: 10.1098/rspa.1935.0048.
- [25] J. Bardeen, L. N. Cooper, and J. R. Schrieffer, “Microscopic Theory of Superconductivity,” *Phys. Rev.*, vol. 106, no. 1, pp. 162–164, Apr. 1957, doi: 10.1103/PhysRev.106.162.
- [26] J. Bardeen, L. N. Cooper, and J. R. Schrieffer, “Theory of Superconductivity,” *Phys. Rev.*, vol. 108, no. 5, pp. 1175–1204, Dec. 1957, doi: 10.1103/PhysRev.108.1175.
- [27] “Journal of Experimental and Theoretical Physics.” <http://www.jetp.ac.ru/cgi-bin/e/index/e/5/6/p1174?a=list> (accessed Dec. 31, 2020).
- [28] M. D. Ainslie, “Transport AC loss in high temperature superconducting coils,” Thesis, University of Cambridge, 2012.
- [29] K. Marken, “1 - Fundamental issues in high temperature superconductor (HTS) materials science and engineering,” in *High Temperature Superconductors (HTS) for Energy Applications*, Z. Melhem, Ed. Woodhead Publishing, 2012, pp. 1–31.
- [30] “CCAS - Coalition for the Commercial Application of Superconductors.” <http://www.ccas-web.org/superconductivity> (accessed Dec. 31, 2020).
- [31] J. G. Bednorz and K. A. Müller, “Possible high T_c superconductivity in the Ba–La–Cu–O system,” *Z. Physik B - Condensed Matter*, vol. 64, no. 2, pp. 189–193, Jun. 1986, doi: 10.1007/BF01303701.
- [32] M. K. Wu *et al.*, “Superconductivity at 93 K in a new mixed-phase Y–Ba–Cu–O compound system at ambient pressure,” *Phys. Rev. Lett.*, vol. 58, no. 9, pp. 908–910, Mar. 1987, doi: 10.1103/PhysRevLett.58.908.
- [33] X. Li *et al.*, “The Development of Second Generation HTS Wire at American Superconductor,” *IEEE Transactions on Applied Superconductivity*, vol. 19, no. 3, pp. 3231–3235, Jun. 2009, doi: 10.1109/TASC.2009.2020570.
- [34] “Home Page | SuperPower.” <http://www.superpower-inc.com/> (accessed Jan. 04, 2021).
- [35] W. Witzeling, “Computation of screening currents in superconducting persistent current devices,” *Cryogenics*, vol. 16, no. 1, pp. 29–32, Jan. 1976, doi: 10.1016/0011-2275(76)90283-6.
- [36] Ph. Vanderbemden *et al.*, “Behavior of bulk high-temperature superconductors of finite thickness subjected to crossed magnetic fields: Experiment and model,” *Phys. Rev. B*, vol. 75, no. 17, p. 174515, May 2007, doi: 10.1103/PhysRevB.75.174515.
- [37] 信也長谷部 and 快男鹿野, “静磁界解析における t - Ω 法と新しい電流モデルとの関係,” *電気学会論文誌. a, 基礎・材料・共通部門誌*, vol. 110, no. 9, pp. 555–560, 1990, doi: 10.1541/ieejfms1990.110.9_555.
- [38] L. Quéval, K. Liu, W. Yang, V. M. R. Zermeno, and G. Ma, “Superconducting magnetic bearings simulation using an H-formulation finite element model,” *Supercond. Sci. Technol.*, vol. 31, no. 8, p. 084001, Jun. 2018, doi: 10.1088/1361-6668/aac55d.

- [39] Z. Hong, A. M. Campbell, and T. A. Coombs, “Numerical solution of critical state in superconductivity by finite element software,” *Supercond. Sci. Technol.*, vol. 19, no. 12, pp. 1246–1252, Oct. 2006, doi: 10.1088/0953-2048/19/12/004.
- [40] C. P. Bean, “Magnetization of Hard Superconductors,” *Phys. Rev. Lett.*, vol. 8, no. 6, pp. 250–253, Mar. 1962, doi: 10.1103/PhysRevLett.8.250.
- [41] Y. B. Kim, C. F. Hempstead, and A. R. Strnad, “Critical Persistent Currents in Hard Superconductors,” *Phys. Rev. Lett.*, vol. 9, no. 7, pp. 306–309, Oct. 1962, doi: 10.1103/PhysRevLett.9.306.
- [42] P. W. Anderson, “Theory of Flux Creep in Hard Superconductors,” *Phys. Rev. Lett.*, vol. 9, no. 7, pp. 309–311, Oct. 1962, doi: 10.1103/PhysRevLett.9.309.
- [43] J. Rhyner, “Magnetic properties and AC-losses of superconductors with power law current—voltage characteristics,” *Physica C: Superconductivity*, vol. 212, no. 3, pp. 292–300, Jul. 1993, doi: 10.1016/0921-4534(93)90592-E.
- [44] M. Nii, N. Amemiya, and T. Nakamura, “Three-dimensional model for numerical electromagnetic field analyses of coated superconductors and its application to Roebel cables,” *Supercond. Sci. Technol.*, vol. 25, no. 9, p. 095011, 2012, doi: 10.1088/0953-2048/25/9/095011.
- [45] Y. Ichiki and H. Ohsaki, “Transient Electromagnetic Phenomena during Current Limiting Process in YBCO Thin Film,” *J. Phys.: Conf. Ser.*, vol. 43, no. 1, p. 942, 2006, doi: 10.1088/1742-6596/43/1/230.
- [46] “Superconductivity - 3rd Edition.” <https://www.elsevier.com/books/superconductivity/poole/978-0-12-409509-0> (accessed Jan. 04, 2021).
- [47] J. Šouc, E. Pardo, M. Vojenčiak, and F. Gömöry, “Theoretical and experimental study of AC loss in high temperature superconductor single pancake coils,” *Supercond. Sci. Technol.*, vol. 22, no. 1, p. 015006, Nov. 2008, doi: 10.1088/0953-2048/22/1/015006.
- [48] F. Gömöry, M. Vojenčiak, E. Pardo, M. Solovyov, and J. Šouc, “AC losses in coated conductors,” *Supercond. Sci. Technol.*, vol. 23, no. 3, p. 034012, Feb. 2010, doi: 10.1088/0953-2048/23/3/034012.
- [49] M. Vojenčiak, F. Grilli, S. Terzieva, W. Goldacker, M. Kováčová, and A. Kling, “Effect of self-field on the current distribution in Roebel-assembled coated conductor cables,” *Supercond. Sci. Technol.*, vol. 24, no. 9, p. 095002, Jul. 2011, doi: 10.1088/0953-2048/24/9/095002.
- [50] E. Pardo, M. Vojenčiak, F. Gömöry, and J. Šouc, “Low-magnetic-field dependence and anisotropy of the critical current density in coated conductors,” *Supercond. Sci. Technol.*, vol. 24, no. 6, p. 065007, Apr. 2011, doi: 10.1088/0953-2048/24/6/065007.
- [51] 一木洋太, “数値解析に基づく超電導薄膜限流素子の大容量化に関する研究,” 東京大学博士論文, 2007.

- [52] 畑山明聖 and 櫻林徹, 工学・物理のための基礎ベクトル解析. 東京: コロナ社, 2009.
- [53] 梶島岳夫, 乱流の数値シミュレーション, 改訂版. 東京: 養賢堂, 2017.
- [54] 杉田晋哉, “超電導薄膜を用いた抵抗形限流素子の数値解析に関する研究,” Mar. 2003, Accessed: Dec. 11, 2020. [Online]. Available: https://repository.dl.itc.u-tokyo.ac.jp/index.php?active_action=repository_view_main_item_detail&page_id=28&block_id=31&item_id=2243&item_no=1.
- [55] W. T. Norris, “Calculation of hysteresis losses in hard superconductors carrying ac: isolated conductors and edges of thin sheets,” *J. Phys. D: Appl. Phys.*, vol. 3, no. 4, pp. 489–507, Apr. 1970, doi: 10.1088/0022-3727/3/4/308.
- [56] E. H. Brandt and M. Indenbom, “Type-II-superconductor strip with current in a perpendicular magnetic field,” *Phys. Rev. B*, vol. 48, no. 17, pp. 12893–12906, Nov. 1993, doi: 10.1103/PhysRevB.48.12893.
- [57] E. H. Brandt, “Superconductors of finite thickness in a perpendicular magnetic field: Strips and slabs,” *Phys. Rev. B*, vol. 54, no. 6, pp. 4246–4264, Aug. 1996, doi: 10.1103/PhysRevB.54.4246.
- [58] H. Ueda *et al.*, “Evaluation of Magnetic-Field Distribution by Screening Current in Multiple REBCO Coils,” *IEEE Transactions on Applied Superconductivity*, vol. 25, no. 3, pp. 1–5, Jun. 2015, doi: 10.1109/TASC.2014.2371133.
- [59] M. Tsuda, R. Takano, H. Miura, D. Miyagi, T. Matsuda, and S. Yokoyama, “Suitable Excitation Condition in Overshooting Process for Suppressing Magnetic Field Attenuation in Y-Based Coated Conductor Coils,” *IEEE Transactions on Applied Superconductivity*, vol. 27, no. 4, pp. 1–5, Jun. 2017, doi: 10.1109/TASC.2016.2642582.
- [60] Y. Yanagisawa *et al.*, “Effect of coil current sweep cycle and temperature change cycle on the screening current-induced magnetic field for Ybco-coated conductor coils,” *AIP Conference Proceedings*, vol. 1434, no. 1, pp. 1373–1380, Jun. 2012, doi: 10.1063/1.4707063.
- [61] T. Feder, “Accelerator school travels university circuit,” *Physics Today*, vol. 63, no. 2, pp. 20–22, Feb. 2010, doi: 10.1063/1.3326981.
- [62] “Two circulating beams bring first collisions in the LHC,” *CERN*. <https://home.cern/news/press-release/cern/two-circulating-beams-bring-first-collisions-lhc> (accessed Jan. 09, 2021).
- [63] Y. Nagai and Y. Hatsukawa, “Production of ^{99}Mo for Nuclear Medicine by $^{100}\text{Mo}(n,2n)^{99}\text{Mo}$,” *J. Phys. Soc. Jpn.*, vol. 78, no. 3, p. 033201, Mar. 2009, doi: 10.1143/JPSJ.78.033201.
- [64] “重粒子線治療研究部 - 量子科学技術研究開発機構.” <https://www.qst.go.jp/site/qms/1885.html> (accessed Jan. 09, 2021).
- [65] A. W. Chao, K. H. Mess, M. Tigner, and F. Zimmermann, *Handbook of Accelerator Physics and Engineering*, 2nd ed. WORLD SCIENTIFIC, 2013.
- [66] H. Maeda and Y. Yanagisawa, “Recent Developments in High-Temperature Superconducting Magnet Technology (Review),” *IEEE Transactions on Applied Superconductivity*, vol. 24, no. 3,

- pp. 1–12, Jun. 2014, doi: 10.1109/TASC.2013.2287707.
- [67] H. Ueda *et al.*, “Evaluation of Magnetic-Field Distribution by Screening Current in Multiple REBCO Coils,” *IEEE Transactions on Applied Superconductivity*, vol. 25, no. 3, pp. 1–5, Jun. 2015, doi: 10.1109/TASC.2014.2371133.
- [68] M. C. Ahn, T. Yagai, S. Hahn, R. Ando, J. Bascunan, and Y. Iwasa, “Spatial and Temporal Variations of a Screening Current Induced Magnetic Field in a Double-Pancake HTS Insert of an LTS/HTS NMR Magnet,” *IEEE Transactions on Applied Superconductivity*, vol. 19, no. 3, pp. 2269–2272, Jun. 2009, doi: 10.1109/TASC.2009.2018102.
- [69] Y. Sogabe and N. Amemiya, “AC Loss Calculation of a Cosine-Theta Dipole Magnet Wound With Coated Conductors by 3D Modeling,” *IEEE Transactions on Applied Superconductivity*, vol. 28, no. 4, pp. 1–5, Jun. 2018, doi: 10.1109/TASC.2018.2793668.
- [70] B. Auchmann and S. Russenschuck, “Coil end design for superconducting magnets applying differential geometry methods,” *IEEE Transactions on Magnetics*, vol. 40, no. 2, pp. 1208–1211, Mar. 2004, doi: 10.1109/TMAG.2004.824710.
- [71] 曾我部 友輔, “高温超伝導マグネットの粒子加速器応用に向けた交流損失および遮蔽電流磁界に関する研究.”
- [72] J. Lu, E. S. Choi, and H. D. Zhou, “Physical properties of Hastelloy® C-276™ at cryogenic temperatures,” *Journal of Applied Physics*, vol. 103, no. 6, p. 064908, Mar. 2008, doi: 10.1063/1.2899058.
- [73] H. Fujishiro, M. Ikebe, T. Naito, K. Noto, S. Kohayashi, and S. Yoshizawa, “Anisotropic Thermal Diffusivity and Conductivity of YBCO(123) and YBCO(211) Mixed Crystals. I,” *Jpn. J. Appl. Phys.*, vol. 33, no. 9R, p. 4965, Sep. 1994, doi: 10.1143/JJAP.33.4965.
- [74] M. Zhang, K. Matsuda, and T. A. Coombs, “New application of temperature-dependent modelling of high temperature superconductors: Quench propagation and pulse magnetization,” *Journal of Applied Physics*, vol. 112, no. 4, p. 043912, Aug. 2012, doi: 10.1063/1.4747925.
- [75] D. R. Smith and F. R. Fickett, “Low-Temperature Properties of Silver,” *J Res Natl Inst Stand Technol*, vol. 100, no. 2, pp. 119–171, 1995, doi: 10.6028/jres.100.012.
- [76] K. Qian, T. Shiratani, Y. Terao, and H. Ohsaki, “Three-Dimensional Thermal Analysis of an SFCL REBCO Coil Immersed in Liquid Nitrogen,” *J. Phys.: Conf. Ser.*, vol. 1054, no. 1, p. 012078, 2018, doi: 10.1088/1742-6596/1054/1/012078.
- [77] S. Kar, X.-F. Li, V. Selvamanickam, and V. V. Rao, “Current distribution mapping in insulated (Gd,Y)BCO based stabilizer-free coated conductor after AC over-current test for R-SFCL application,” *IOP Conf. Ser.: Mater. Sci. Eng.*, vol. 171, no. 1, p. 012118, 2017, doi: 10.1088/1757-899X/171/1/012118.

List of Publications

1. Papers

- [1] K. Qian, T. Shiratani, Y. Terao, and H. Ohsaki, "Three-Dimensional Thermal Analysis of an SFCL REBCO Coil Immersed in Liquid Nitrogen," *J. Phys.: Conf. Ser.*, vol. 1054, no. 1, 012078, 2018.
- [2] K. Qian, Y. Terao, and H. Ohsaki, "Three-Dimensional Electromagnetic and Thermal Field Coupled Analysis of Different Types of REBCO Coils under Overcurrent Conditions," *IEEE Transactions on Applied Superconductivity* (under review).

2. International Conferences

- [3] K. Qian, H. Ohsaki, M. Tomita. "Fault Current Analysis of DC Electric Railway Feeding Systems using Superconducting Power Cables", 17th International Conference on Electrical Machines and Systems (ICEMS2014), DS1H3-17, China, October 2014.
- [4] D. Kumagai, K. Qian, H. Ohsaki, M. Tomita. "Feasibility Study of Superconducting Fault Current Limiters for DC Electric Railway Feeding Systems", 12th European Conference on Applied Superconductivity (EUCAS 2015), France, September 2015.
- [5] K. Qian, Z. Guo, Y. Terao and H. Ohsaki, "Electromagnetic and thermal design of superconducting fault current limiters for DC electric systems using superconducting," *2017 20th International Conference on Electrical Machines and Systems (ICEMS)*, Sydney, NSW, 2017.
- [6] K. Qian, T. Shiratani, Y. Terao and H. Ohsaki, "Three-Dimensional Thermal Analysis of an SFCL REBCO Coil Immersed in Liquid Nitrogen," The 30th International Symposium on Superconductivity (ISS2017), Tokyo, Japan, APP3-1, December 2017
- [7] K. Qian, Y. Terao and H. Ohsaki, "Three-Dimensional Electromagnetic and Thermal Field Coupled Analysis of REBCO Coils Considering Local Performance Degradation", 2018 Applied Superconductivity Conference (ASC 2018), 1LPo2B-04, Seattle, U.S.A., October, 2018.
- [8] K. Qian, Y. Terao and H. Ohsaki, " Three-Dimensional Electromagnetic and Thermal Coupled Analysis of an SFCL REBCO Coil Immersed in 65 K Liquid Nitrogen," The 31th International Symposium on Superconductivity (ISS2018), Tsukuba, Japan, APP5-3, December, 2018
- [9] K. Qian, Y. Terao and H. Ohsaki, " Electromagnetic and Thermal Coupled Analysis of an SFCL REBCO Coil Immersed in Liquid Nitrogen Considering Boiling Phenomenon," The 32th International Symposium on Superconductivity (ISS2019), Kyoto, Japan, APP4-5, December, 2019

- [10] ○K. Qian, Y. Terao and H. Ohsaki, “Three-Dimensional Electromagnetic and Thermal Field Coupled Analysis of Different Types of REBCO Coils Under Overcurrent Conditions”, 2020 Applied Superconductivity Conference (ASC 2020), Wk2LPo1B, Tampa, U.S.A., June, 2020.
- [11] ○K. Qian, Y. Terao and H. Ohsaki, " Three-Dimensional Electromagnetic and Thermal Field Coupled Analysis of Different Types of SFCL REBCO Coils Immersed in Liquid Nitrogen," The 33th International Symposium on Superconductivity (ISS2019), Tsukuba, Japan, AP8-5, December, 2020.

2. Internal Conferences

- [12] ○銭 可楨, 大崎 博之, 富田 優: “超電導ケーブルを導入した直流電気鉄道き電系における短絡事故電流の解析”, 第 89 回 2014 年度春季低温工学・超電導学会, 2P-p15, 東京都, 2014 年 5 月.
- [13] ○銭 可楨, 大崎 博之, 富田 優: “超電導ケーブルを導入した直流電気鉄道き電系における事故電流対策の検討”, 第 90 回 2014 年度秋季低温工学・超電導学会, 1P-p26, 福島県, 2014 年 11 月.
- [14] ○銭 可楨, 郭 卓然, 寺尾 悠, 大崎 博之, 富田 優: “超電導ケーブルを導入した直流電気鉄道き電系向け超電導限流器の電磁的および熱的設計”, 第 94 回 2017 年度春季低温工学・超電導学会, 1P-p18, 東京都, 2017 年 5 月.
- [15] ○銭 可楨, 白谷 俊樹, 寺尾 悠, 大崎 博之: “超電導限流器用 REBCO コイルの三次元電磁界・熱伝導場連成解析”, 第 95 回 2017 年度秋季低温工学・超電導学会, 1P-p06, 高知県, 2017 年 11 月.
- [16] ○白谷 俊樹, 銭 可楨, 寺尾 悠, 大崎 博之: “超電導限流器用 REBCO コイルの三次元過渡熱解析”, 第 95 回 2017 年度秋季低温工学・超電導学会, 1P-p07, 高知, 2017 年 11 月.
- [17] ○銭 可楨, 白谷 俊樹, 寺尾 悠, 大崎 博之: “超電導限流器用 REBCO コイルの三次元過渡熱解析 —線材特性による限流性能と温度上昇への影響—”, 第 96 回 2018 年度春季低温工学・超電導学会, 2P-p15, 東京都, 2018 年 5 月.
- [18] ○銭 可楨, 寺尾 悠, 大崎 博之: “過電流下 REBCO コイルの三次元電磁界・熱伝導場連成解析”, 第 99 回 2020 年度春季低温工学・超電導学会, 1P-p24, 2020 年 7 月.
- [19] ○銭 可楨, 寺尾 悠, 大崎 博之: “薄板近似を用いた REBCO コイルの三次元電磁界・熱伝導場連成解析”, 第 100 回 2020 年度秋季低温工学・超電導学会, 1P-p02, 京都, 2020 年 12 月.

Acknowledgements

I am here to thank the people who have contributed, either directly or indirectly, to this doctoral thesis.

Firstly, I must express my uttermost gratitude to my supervisor, Prof. Hiroyuki Ohsaki. I may not finish my work without his kind advice, patient guidance, and warm support throughout the duration of my research. He did not only give me important hints on my research, but also taught me how to consider and solve problems. Furthermore, I would like to thank him again for allowing me the freedom to explore my own ideas and keep patient even when I lost the direction in my research.

Secondly, I would like to thank Dr. Yutaka Terao, the assistant professor in Ohsaki Lab. Thank you for your kind advices on both research and everyday life. I am also thankful for your hard work to make the mood in the lab more positive and happier.

Then, I would like to thank the secretary Ms. Suzuki for her perfect work to support my research. I must also thank all the members of Ohsaki Lab especially Takahiro Akahori. Thank you for sharing my work in the laboratory operation and I also enjoyed the unique communication with you. I will never forget my student life with every member: Yusuke Terachi, Yiqi Ba, Zhuoran Guo, Sho Tanaka, Weilu Kong, Shiye Fang, Toshiki Shiratani, Toshiki Shimomura, Yuta Miura, Yukimasa Hirota, Shun Iwatsuki, Akihisa Seta, Reo Takamizo, Wataru Akada, Masataka Shimizu, Xiang Zhang, Mikito Kato, Takayuki Mashimo, Hisashi Enokida, Takuya Miki, Tobias Tymosch, Yang Gao, Daniel Heideman, Doa Jamil, Yusuke Ishida, Yosuke Iwata, Beier Qu, Ryotaro Mimura, Takemi Onoue, Hiroki Saito, ARITHAT THANAKULITTHIRAT.

Finally, I must thank all of my family and friends for their love and support. My parents, Wei Qian and Yajun Chen, have supported me in all of my pursuits and encouraged me to achieve my dream. My wife, Yinyu He, has supported me wholeheartedly even in my hardest times, and without her help and encouragement, I would never have achieved all that I have so far. My daughter, Xili Qian, is an angel to me and always exceeds my expectations.